

General Disclaimer

One or more of the Following Statements may affect this Document

- This document has been reproduced from the best copy furnished by the organizational source. It is being released in the interest of making available as much information as possible.
- This document may contain data, which exceeds the sheet parameters. It was furnished in this condition by the organizational source and is the best copy available.
- This document may contain tone-on-tone or color graphs, charts and/or pictures, which have been reproduced in black and white.
- This document is paginated as submitted by the original source.
- Portions of this document are not fully legible due to the historical nature of some of the material. However, it is the best reproduction available from the original submission.

THE MOMENTUM TRANSFER OF INCOMPRESSIBLE TURBULENT
SEPARATED FLOW DUE TO CAVITIES WITH STEPS

TEES-1086-TR-77-02

by

ROBERT E. WHITE AND DAVID J. NORTON

NASA CR:

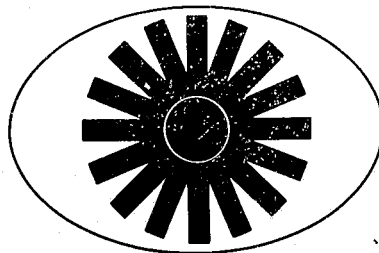
151590

(NASA-CR-151590) THE MOMENTUM TRANSFER OF
INCOMPRESSIBLE TURBULENT SEPARATED FLOW DUE
TO CAVITIES WITH STEPS (Texas Engineering
Experiment Station) 261 p HC A12/MF A01

N78-15437

CSCL 20D G3/34

Unclas
57841

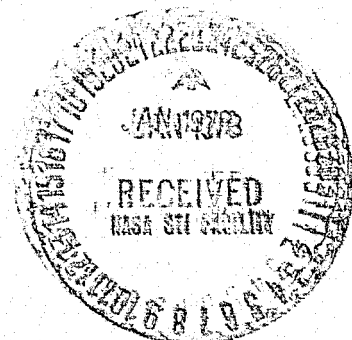


TEES

TEXAS ENGINEERING EXPERIMENT STATION
TEXAS A & M UNIVERSITY
COLLEGE STATION TEXAS 77843

December 1977

Prepared for
NASA, Johnson Space Center
Aerodynamics & Entry Section
Houston, Texas



THE MOMENTUM TRANSFER OF INCOMPRESSIBLE TURBULENT
SEPARATED FLOW DUE TO CAVITIES WITH STEPS

TEES-1086-TR-77-02

by

ROBERT EARL WHITE
and
DAVID JERRY NORTON

prepared by
Texas Engineering Experiment Station
College Station, Texas

to

NASA, Johnson Space Center
Houston, Texas

December, 1977

ABSTRACT

The Momentum Transfer of Incompressible Turbulent
Separated Flow Due to Cavities with Steps

An experimental study was conducted using a plate test bed having a turbulent boundary layer to determine the momentum transfer to the faces of step/cavity combinations on the plate. New experimental data were obtained from configurations including an isolated configuration and an array of blocks in tile patterns. A momentum transfer correlation model of pressure forces on an isolated step/cavity was developed with experimental results to relate flow and geometry parameters. Results of the experiments reveal that isolated step/cavity excrescences do not have a unique and unifying parameter group due in part to cavity depth effects and in part to width parameter scale effects. Drag predictions for tile patterns by a kinetic pressure empirical method predict experimental results well. Trends were not, however, predicted by a method of variable roughness density phenomenology. Data presented will be helpful in testing formal numerical solutions over a step/cavity excrescence, and correlations permit drag predictions on like configurations.

ACKNOWLEDGEMENTS

Specific acknowledgement is given to Dr. Spencer Baen of TEES at Texas A&M and to Mr. Ernie Hillje and Mr. Jim Young of NASA-JSC who monitored the experimental program. The experimental program was supported by NAS Contract 9-11303. Their financial support is gratefully acknowledged.

The authors are indebted to Mr. Joe Brusse and Mr. John Ribbe for their superb work on design and construction of the test plate, the cavity model, and the probing systems. Thanks are due to Mr. Robert Carr for his assistance with instrumentation. Thanks are also due to Mrs. Gay Pridgeon and Mrs. Janis Sloan for help in typing this report.

TABLE OF CONTENTS

	PAGE
INTRODUCTION	1
LITERATURE SURVEY	7
Cavity Flow	7
Turbulent Jet Boundary Formation and Impingement	29
Forward-Facing Step Flow	34
Rearward-Facing Step Flow	46
Flat-Plate Turbulent Boundary Layer Vis-a'-vis Velocity Profile	48
STEP/CAVITY GEOMETRY DESCRIPTIONS	55
STEP/CAVITY MODEL CATEGORY DESCRIPTIONS	57
Forward Step Flow	61
Cavity Flow	63
Rearward Step Flow	67
ANALYTICAL DEVELOPMENT	70
Separated Jet Kinetic Pressure Formulas	74
Pressure Data Formulas	82
EXPERIMENTAL APPARATUS AND PROCEDURE	87
Cavity Model and Cavity Apparatus	90
Tiled Surface	99
Anemometry	100
Pressure Instrumentation	103
RESULTS AND DISCUSSION	104
Pressure Measurements	104
Velocity Profiles	114
Correlation of Momentum Transfer	125
Surface Hot-Film Measurements	138
CONCLUSIONS AND RECOMMENDATIONS	152
REFERENCES	156
APPENDIX A TILED SURFACE DRAG PREDICTIONS	165
APPENDIX B PRESSURE SURVEYS	192
APPENDIX C VELOCITY SURVEYS	231

LIST OF TABLES

TABLE		PAGE
1	ESDU correlation coefficients	72
A-1	Element drag properties	169

LIST OF FIGURES

FIGURE		PAGE
1	Schematic of geometry	6
2	Sketch of stepped cavity and step flows	11
3	Representative cavity drag coefficient.	21
4	Step/cavity categories.	59
5	Test geometry matrix.	60
6	Rear view of test plate with stepped multiple tiles (right) and step/cavity model (left) in place.	88
7	Anemometer hot film probes installed on traversing mechanisms at rear of test plate (splitter plate seen).	88
8	View of test plate through tunnel walls	88
9	Step/cavity model on side from rear removed from test bed.	91
10	Model mechanisms as seen from below	91
11	Plan view of model at $\beta = 45^\circ$ (cavity floor removed).	91
12	Plan view of step/cavity model at $\beta = 90^\circ$ (cavity floor removed).	93
13	Fore pressure orifice and Preston tube port plane detail.	93
14	Aft pressure orifice, Preston tube port, and surface hot film port plan detail	93
15	Model rearward facing step pressure orifice detail.	94
16	Corner pressure orifice detail with adjustable step block removed	94
17	Stepped cavity model in situ with velocity traversing probe mechanism arm behind.	96
18	Stepped tile surface showing tile gaps with probe mechanism arm showing	96
19	Probe mechanism drive unit without arm (position potentiometer on: limit switches not visible).	96
20	Hot film instrumentation (mechanisms drive controller at right)	101

LIST OF FIGURES (continued)

FIGURE		PAGE
21	Pressure transducer instrumentation (Scanivalve controller at left)	101
22	Pressure integral; $b = 0.50$ inch, $\beta = 0^\circ$, rear position, $Q = 20$ psf.	105
23	Pressure integral; $b = 0.15$ inch, $\beta = 0^\circ$, rear position, $Q = 20$ psf.	106
24	Pressure integral; $b = 0.50$ inch, $\beta = 0^\circ$, forward position, $Q = 20$ psf.	107
25	Pressure integral; $b = 0.15$ inch, $\beta = 0^\circ$, forward position, $Q = 20$ psf.	108
26	Pressure integral; $b = 0.50$ inch, $\beta = 45^\circ$, rear position, $Q = 20$ psf.	109
27	Pressure integral; $b = 0.15$ inch, $\beta = 45^\circ$, rear position, $Q = 20$ psf.	110
28	Pressure integral; $b = 0.50$ inch, $\beta = 45^\circ$, forward position, $Q = 20$ psf.	111
29	Plate skin friction coefficient, C_f	116
30	Velocity profile correlation; $Q = 5$ psf, front and rear positions	118
31	Velocity profile correlation; $Q = 10$ psf, front and rear positions.	119
32	Velocity profile correlation; $Q = 20$ psf, front and rear positions.	120
33	Velocity profile correlation; $Q = 40$ psf, front and rear positions.	121
34	Velocity survey repeatability between different entry dates; $Q = 20$ psf, rear position	123
35	Turbulence intensity survey repeatability; $Q = 20$ psf, rear position	124
36	Depth effect on level cavity velocity survey; $Q = 20$ psf, rear position	126
37	Depth effect on level cavity turbulence intensity survey, $Q = 20$ psf, rear position	127

LIST OF FIGURES (continued)

FIGURE		PAGE
38	Level cavity drag coefficient for various d/b	128
39	Width parameter scale effects on stepped cavity correlation, $d = 0.10$ inch	130
40	Width parameter scale effects on stepped cavity correlation, $d = 0.25$ inch	131
41	Width parameter scale effects on stepped cavity correlation, $d = 0.50$ inch	132
42	Width parameter scale effects on stepped cavity correlation, $d = 0.75$ inch	133
43	Width parameter scale effects on stepped cavity correlation, $d = 1.00$ inch	134
44	Correlation slope and intercept width parameter scale effects on stepped cavities	136
45	Depth component effect on level cavity unification para- meter correlation with boundary layer/width coupling. . .	137
46	Forward-facing step correlation	139
47	Rearward-facing step correlation to h/δ	140
48	Rearward-facing step correlation to $\log(hU_T/\nu)$	140
49	Surface sensor mean and RMS components for a forward- facing step	142
50	Surface sensor RMS components for a stepped cavity; $b = 0.50$ inch, $Q = 20$ psf, rear position.	144
51	Surface sensor RMS components for a stepped cavity; $b = 0.15$ inch, $Q = 20$ psf, forward position	146
52	Surface sensor RMS component for a stepped cavity; $b = 0.50$ inch, $Q = 20$ psf, forward position	147
53	Effect of position aft of rearward-facing step corner on surface sensor mean and RMS components at different tunnel Q	148
54	Effect of different cavity gap depths on mean and RMS sensor voltage components; $Q = 20$ and 40 psf	148

LIST OF FIGURES (continued)

FIGURE		PAGE
55	Effect of tunnel Q on surface sensor for a rearward-facing step; sensor 8 step heights behind step	150
56	Mean and RMS sensor components for different aft positions with a backward-facing step	150
A-1	Average skin friction coefficient compared to empirical method predictions.	183
A-2	Average displacement thickness prediction compared to experiment for tiled surfaces - dependency on Reynolds number.	190
A-3	Comparison of average skin friction by variable roughness density phenomenology to experiment - dependency on Reynolds number	190
B-1	Cavity model surface pressure coefficients; $h = b = 0.0$, $\alpha = \beta = 0^\circ$, reference orifice ahead of model.	193
B-2	Cavity model surface pressure coefficients; $h = b = 0.0$, $\alpha = 0^\circ$, $\beta = 45^\circ$, reference orifice ahead of model	194
B-3	Step/cavity wall pressure coefficients for various steps and cavity gap depths; $b = 0.5$ inch, $\beta = 0^\circ$, rear position.	196
B-4	Step/cavity wall pressure coefficients for various steps and cavity gap depths; $b = 0.15$ inch, $\beta = 0^\circ$, rear position.	206
B-5	Step wall pressure coefficients; $\beta = 0^\circ$, rear position.	214
B-6	Step wall pressure coefficients; $\beta = 45^\circ$, rear position.	215
B-7	Step/cavity wall pressure coefficients for various steps and cavity gap depths; $b = 0.5$ inch, $\beta = 45^\circ$, rear position	216
B-8	Step/cavity wall pressure coefficients for various steps and cavity gap depths; $b = 0.15$ inch, $\beta = 45^\circ$, rear position.	219
B-9	Step/cavity wall pressure coefficients for various steps and cavity gap depths; $b = 0.15$ inch, $\beta = 0^\circ$, forward position.	222

LIST OF FIGURES (continued)

FIGURE		PAGE
B-10	Step/cavity wall pressure coefficients for various steps and cavity gap depths; $b = 0.5$ inch, $\beta = 0^\circ$, forward position.	225
B-11	Step/cavity wall pressure coefficients for various steps and cavity gap depths; $b = 0.5$ inch, $\beta = 45^\circ$, forward position.	228
C-1	Velocity survey; $Q = 5$ psf	232
C-2	Turbulence intensity; $Q = 5$ psf.	233
C-3	Velocity survey; $Q = 10$ psf.	234
C-4	Turbulence intensity; $Q = 10$ psf	235
C-5	Velocity survey; $Q = 20$ psf.	236
C-6	Turbulence intensity; $Q = 20$ psf	237
C-7	Velocity survey; $Q = 40$ psf.	238
C-8	Turbulence intensity; $Q = 40$ psf	239
C-9	Velocity survey behind a $b = 0.5$ inch level cavity; rear position, $Q = 10$ psf.	240
C-10	Turbulence intensity behind a $b = 0.5$ inch level cavity; rear position, $Q = 10$ psf	241
C-11	Velocity survey behind a $b = 0.065$ inch level cavity; rear position, $Q = 20$ psf	242
C-12	Turbulence intensity behind a $b = 0.065$ level cavity; rear position, $Q = 20$ psf	244
C-13	Velocity survey behind a $b = 0.5$ inch level cavity; rear position, $Q = 40$ psf	245
C-14	Turbulence intensity behind a $b = 0.5$ inch level cavity; rear position, $Q = 40$ psf	246

NOMENCLATURE

A	wall-law logarithm term constant multiplier
A_{tile}	tile surface area
A'	wall-law logarithm term dimensional constant multiplier
a	turbulent jet spread parameter of Tollmien
a', b', c', d'	jet shear layer cubic coefficients
B	wall-law additive constant
B'	wall-law additive dimensional constant
b	cavity gap width
C_D	drag coefficient
$C_{D_{\text{ind}}}$	independent drag coefficient
$C_{D,p}$	pressure drag coefficient
C_{D^*}, C_{τ^*}	drag coefficient, defined by $2C_D/C_f$
C_f	skin friction coefficient
C_p	pressure coefficient
C_{p_0}	Preston tube pressure coefficient
C_p^+	uncorrected pressure coefficient
C_1, C_2	ESDU correlation constants
D	drag, diameter
d	cavity depth
f	frequency
G	universal shape parameter
H	shape parameter
h	step height
h_{eff}	effective step height

k	protuberance roughness height
k_s	sand grain roughness height
\bar{k}	effective roughness height
l	Prandtl mixing length
M	correlation curve slope
M_e	Mach number at the boundary layer edge
N	correlation curve intercept
n	power-law exponent constant
Q	tunnel reference dynamic pressure setting
q	kinetic pressure
R	Reynolds number
S	basic area
S_{tile}	tile associated surface area
s	cavity span
U, \bar{U}	mean velocity - axially directed
U_τ	friction velocity
u'	fluctuating axial velocity component
V	mean velocity - normally directed, voltage
v'	fluctuating normal velocity component
W_i	pressure coefficient weighting factor
x_c	axial coordinate from cavity front corner
\bar{x}_r	step induced separation distance
y	normal coordinate
y_o	boundary layer roughness height in turbulent flow
α	model test bed plate pitch angle
β	cavity model skew angle

Δ	defect thickness
ΔM	momentum increment defined by Eq. (52)
Δm	mass increment
$\Delta U_1/U_\tau$	decrement due to surface roughness
$\Delta U_2/U_\tau$	decrement due to pressure gradient
Δx	distance to protuberance
Δy	pressure orifice separation distance
$\Delta()$	increment
δ	boundary layer thickness
δ^*	displacement thickness
ϵ_M	eddy diffusivity
η	jet similarity parameter of Tollmien
θ	momentum thickness
κ	von Karman's constant
Λ	correlation factor, defined on Fig. 45 (p. 137)
λ	specific roughness ratio based on surface area
λ_k	specific roughness ratio based on projected area
μ	dynamic viscosity
μ_t	eddy viscosity
ν, ν	kinematic viscosity
ξ	jet similarity parameter of Görtler
Π	Cole's wake parameter
ρ	density
σ	turbulent jet spread parameter of Görtler
τ, τ_{xy}	shear stress
ϕ	EDSU friction correlation parameter

Ψ	ESDU compressibility correlation parameter
ψ	stream function
Ω	vorticity
$\int c_p$	momentum transfer weighted coefficient
$\sqrt{u'^2}/\bar{u}$	turbulence intensity

Subscripts

avg	mean temporal average
ds	dividing stream line
e	boundary layer edge
eff	effective
F	forward-facing
h	height
max	maximum
p	pressure
R	rearward-facing
ref	reference
rms	root-mean-squared
S	viscous sublayer
T	turbulent
x	axial coordinate
y	normal coordinate
θ	momentum thickness
1,2	forward position and rearward position, respectively

INTRODUCTION

In addition to the appearance of cavities on aircraft surfaces (at bay doors, around wheel covers, between fixed and movable wing surfaces), cavities occur in jet and rocket propulsion system assemblies at pipe joints, in the bed of rivers and streams, on the surface of land masses, in fluid amplifiers, and within air conditioning ducts. Cavities in some of the systems or designs mentioned above have short transverse dimensions compared to the width or they are three-dimensional features. Examples are narrow bays and port holes. A general characterization of three-dimensional turbulent separated flow is not always possible due to the complexities of the flow; however, certain salient characteristics can be qualified by using simple two-dimensional models and characteristic experimental data.

At present, a relevant application of cavities in an air-vehicle design may be seen on the NASA sponsored Space Shuttle where large areas of the outer skin of the orbiter are covered with thermal protection tiles. The ceramic coated tiles on the orbiter serve as insulation to withstand reentry heating for the metallic skin below. When heated by air friction the tiles expand and, unless tiles are separated one from another, mechanical stresses may result in tile cracking and consequential failure. By separating tiles, however, aerodynamic drag is aggravated and orbiter entry performance is affected.

In addition to being separated, flat tiles on a curved under-skin and inherent manufacturing tolerances cause misalignment of tiles and consequently steps between tiles results. Steps on the surface of a plate

The citations on the following pages follow the style of the AIAA Journal.

within a tangential flow field results in increased tangential force which, for an aircraft, means an increase in drag force by a momentum transfer mechanism. The drag producing characteristics of cavities and cavities with steps and, more generally, the momentum transfer to these via pressure on the cavity/step walls and its prediction is the subject of this writing.

The research described herein builds upon experimental studies conducted in October 1974 and February 1975 in the 7 x 10 foot Low Speed Wind Tunnel at Texas A&M University. Because of the current development of a reusable space shuttle orbiter by the United States, it was necessary to quantify the drag effects caused by thermal insulation tiles attached to the orbiter body and wing surfaces. In experimental wind tunnel studies conducted at Texas A&M, arrays of tiles with gaps and with steps were tested on the surface of a test bed. The test bed containing the arrays was along and spanning the width of the tunnel. The tiles, being separated, produce a multiple cavity arrangement.

In addition to quantifying the flow and skin friction effects of the multiple cavity/tile arrangement, extensive and fundamental experimental studies on isolated cavities on the test bed were conducted concomitant to the multiple cavity experiments. In addition to presenting and expanding the analysis on the multiple cavity experimental research, the bulk of work and the topic of this research will be on analysis of the details of flow over and forces on an isolated cavity. This report will determine the detailed features of flow over narrow, isolated, stepped and level cavities.

The complexity of flow over and within step/cavities and interaction of the flow with the adjacent incompressible turbulent boundary layer and

the stream above precludes an analytical solution to the general step/cavity problem. Therefore, arguments based on phenomenological analytical models have been utilized to give insight and provide correlations. This approach provides guidelines and by using abundant basic experimental data it provides a basis to relate to other applications and/or similar problems.

This investigation considers both the rearward and forward steps and defines the pressure and drag on the step/cavity surfaces. An analysis is presented for the effects of flow at a skew to a single cavity and the result of the complementary experimental study for flow over multiple cavities is analyzed and may be referred to in conjunction with the isolated cavity studies.

The measurement of wall pressure from experiments conducted on an isolated step/cavity reveal that two different regimes or types of separated flow are exhibited. One type resembles base flow with negative pressure on the backward-facing step and on the opposite cavity wall. The wall pressures are essentially constant.

The other type of flow observed has two categories. Wall pressures are greater than the base flow category (a rearward-step/cavity). The simple forward step and the forward-step/cavity flow and pressure appear to be determined by a different mechanism than backward steps. Use of experimental observation assists in step/cavity pressure force prediction by different approaches based on step/cavity geometry. This scheme allows a tractable analytical analysis for cavities with steps. For deep cavities the flow regimes are mutually exclusive. Therefore, dichotomous analytical models are used to assess the effects on the rearward step and on the forward step in an open cavity. By combining analytical models

and experimental observations to evaluate particular cavity geometry in the flow, a wide range of geometries may be considered. Analytical evaluations developed for comparison rely on the combination of simple models for flow over a step to include, primarily, flow impinging on the step wall across a surface cavity. Other analytical methods used with multiple cavity experimental studies form a part of the overall research program. What may be referred to as steady, two-dimensional analysis will be used with three-dimensional effects which appear being correlated to existing test data. The skewed cavity analysis is in this category.

In the past, much boundary-layer research has been conducted in the area of protuberance, roughness, and cavity flow-field analysis. Although there is consensus that cavity and step drag prediction may be based on fundamental boundary layer parameters, disagreement of experimental measurements and failure of analytical models to describe the momentum transfer to steps or cavities has not been put on a firm basis. Many practical configurations have been ignored: data for cavities with steps is practically nonexistent and a void is filled with the findings of this research.

A review of existing data and theories will support and assist in the understanding of the momentum transfer mechanism. Investigations on the nature of the flow over cavities have presented simple models for the purpose of giving qualitative or quantitative features and in most instances accompanying experimental data are used in conjunction with analytical models for comparison. To now there have been some investigations of the separation and reattachment of an incompressible turbulent boundary layer over open level cavities within a plane and with cavity wall faces normal to the flow but no treatise includes the effect of unlevel surfaces

across narrow gaps (referred to as stepped cavities) and skewed cavity wall faces.

The scope and the extent of this research is primarily restricted to narrow cavities and to steps beneath an incompressible turbulent boundary layer. Sizes considered for cavities and steps are from the same to one smaller order of magnitude in length, b or h , as the boundary layer thickness, δ . Data for these geometries fill a void in existing data and show detailed pressure data for what is believed to be here-to-fore untested geometries. In the discussions to follow several geometrical and flow parameters are required to define a step/cavity configuration and its size. Flow parameters are designated customary symbols if possible, but because geometrical parameter symbols are not standardized these are designated. Geometrical characteristics and definitions for cavities and steps are shown with symbols on Fig. 1. Because of its familiarity, the U.S. Customary System of units will be used where necessary.

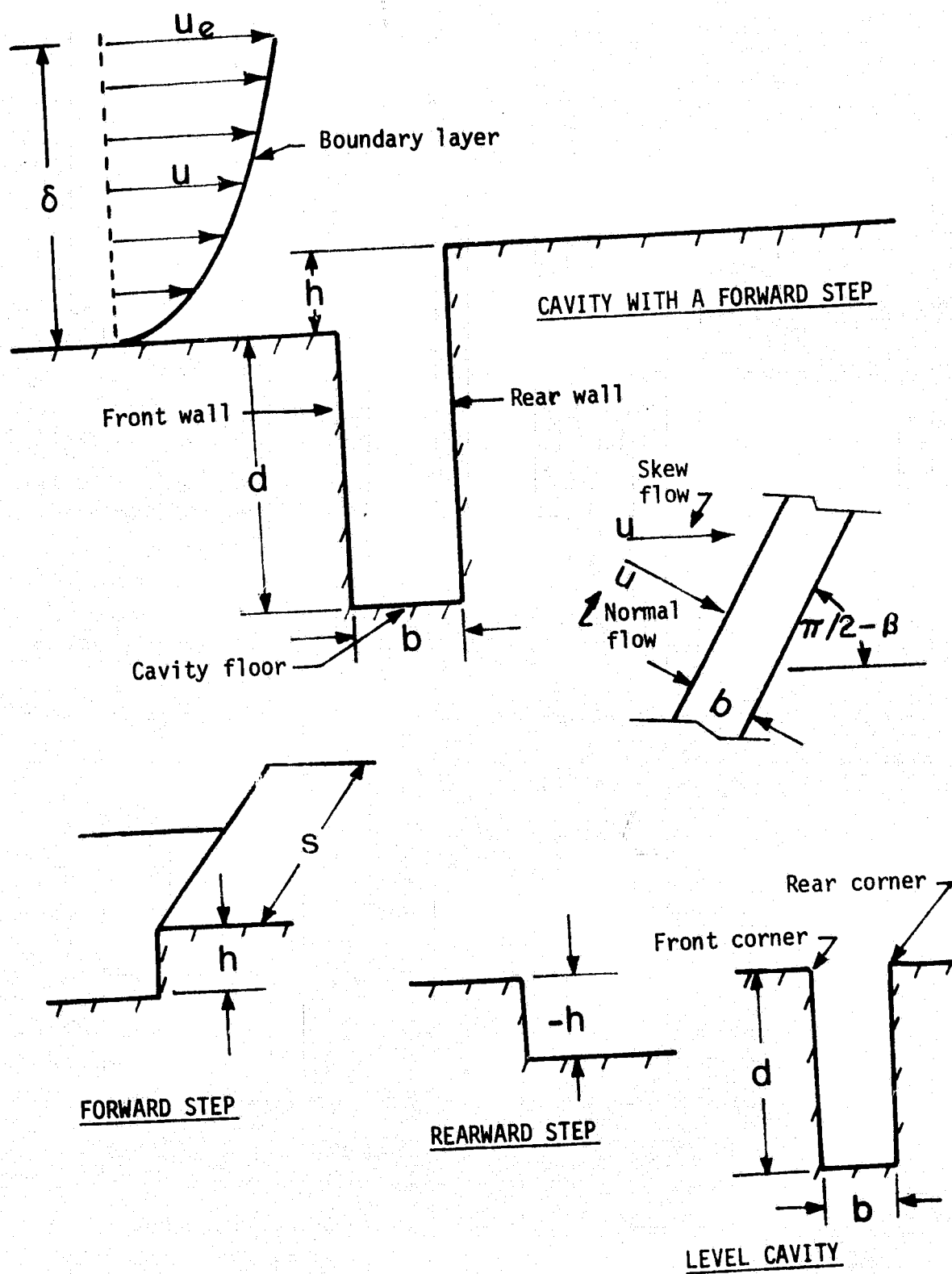


Fig.1 Schematic of geometry.

LITERATURE SURVEY

To enumerate the totality of turbulent boundary layer research or even the many facets of separated flow caused by cavities and steps would be an unthinkable task. Even so, some of the pertinent research stands out as being basic to characterization for the boundary layer flow field encountered in the course of the present study. Of particular interest are six topics described generally by the following:

1. Flow of a boundary layer over an embedded rectangular cavity and effects on the cavity and its flow field.
2. Turbulent jet boundary formation and impingement.
3. Flow over a forward-facing step.
4. Flow over a rearward-facing step.
5. Flat plate turbulent boundary layer flow vis-a-vis the velocity profile.
6. The flat plate turbulent flow over a roughened surface.

Of particular interest are investigations where the pressure and velocity field are described or predicted as well as designation of parameters characteristic of the boundary layer, a cavity, and/or a step.

Cavity Flow

The description of flow in a rectangular level cavity has been described on numerous occasions by researchers of boundary layer and acoustic phenomena. Pertinent investigations include the effects of a turbulent boundary layer; although, laminar or unsheared uniform flow

prior to the forward, separation corner show similarities to turbulent flow with regard to vortex formation within the cavity. Roshko¹ reports measurements of pressure on cavity wall and floor surfaces and gives mean velocity measurements in and before the cavities (b/δ constant). Wall and floor static pressure measurements for d/b from 0.75 to 2.5 are given in addition to cavity floor static and pitot pressures at the center of the floor for shallow cavities ($d/b < 0.14$). Static pressure on the $s/b=8.0$ model at the center of the cavity floor and pitot pressure at the rear corner for $0 \leq d/b \leq 2.5$ are presented. The latter shows a hysteresis loop for $1.1 < d/b < 1.9$ and intermittent scatter which Roshko also noticed in floor measurements for $0.5 < d/b < 0.9$ and for $d/b > 2.0$. All pertinent data were for $U_e = 75$ fps although a few mid-floor pressures were reported at $U_e = 200$ fps. Mean velocity profiles before and behind the cavity (b fixed at 4.0 inch) show the approaching boundary layer to be turbulent with $\delta \approx 0.87$ inches; thus, the cavities are wide with $\delta/b = 0.22$. Mean velocity profiles perpendicular to and very near the cavity floor or walls with $d/b = 1.0$ reveals a boundary layer type flow within, which further away develops into a single unsymmetrical vortex executing, according to Roshko, solid-body rotation. Roshko concludes that the pressure and drag force on a level cavity depends strongly on the boundary layer structure even though the single large stable vortex for the square cavity is not so dependent. Also, the total drag depends almost entirely on the pressure forces by roughly two orders of magnitude greater than friction forces and the friction forces on the floor may actually contribute a small thrust. The contribution to

drag from the change in friction on the surface behind the cavity (determined by extrapolating velocity profiles to the surface) is relatively small. Roshko predicts that pressure forces result from transport of momentum into the cavity, and the main contribution to drag force on the cavity is at the top of the downstream forward-facing wall. He also predicts that pressures on this wall are important to sound production at high speed and reported intermittencies are due to excitation of different states of stable vortices within the cavity. In a similar study, Fox^{2,3} conducted experiments on a two-dimensional body of elliptical nose (major to minor axis of 3.0) mounted midway between walls of a wind tunnel: solid blockage was 68% of the tunnel. Immediately (1.1 inch) behind the body nose was a half-thickness rectangular cut-out giving a constant $d=2.05$ inches. Testing at 160 fps gave a laminar boundary layer at the forward corner with $\delta/d = 0.019$. A range of cavities were tested ($0.25 \leq b/d \leq 1.75$) for this wide cavity ($0.011 \leq \delta/b \leq 0.076$). Cavity aspect ratio, s/b , ranged from 2.5 to 17.6 which, according to Mau] and East⁴, could have three-dimensional cellular flow especially near the cavity floor. At all speeds between 160 fps and 600 fps, Fox found a unique pressure distribution for $b/d = 1.50$ but different from Roshko's results and not having the intermittencies of Roshko's data. A large value of drag coefficient results from pressure integration of Fox's data at $b/d = 1.5$ being on the order of $C_{D,p} = 0.15$ based on area bs . This is an order of magnitude greater than other data found for level cavities. Fox concludes that for $b/d < 1.25$ the pressure and flow in a cavity is governed primarily by the b/d ratio and secondarily by boundary layer

parameters such as the boundary layer thickness. For $b/d \gtrsim 1.75$ this is also true according to Fox and in between $b/d \approx 1.25$ and 1.75 the secondary parameters dominate. Similar velocity profiles could be obtained in the separated shear-layer jet-mixing zone for $b/d = 1.75$ by shifting the y coordinate; however, this did not occur for $b/d = 1.0$. Within a square cavity the vortical motion predicted by Roshko was also found by Fox. The appearance was found to conform to the cavity walls and floor as opposed to being round except near the center and this feature is brought out in Fig. 2 where instead of a large single vortex, a double vortex for the deeper cavity with $d/b \approx 2.0$ is shown. Fox attributes differences between his results and Roshko's to the thicker boundary layer of Roshko. Also, three-dimensional results quoted by Maul and East ($\delta/b \approx 0.21$) are attributed by Fox to the boundary layer depth and its relationship to d/b . With regard to the hysteresis and intermittencies observed by Roshko, Maul and East predict these are caused by the appearance of one or the other of two possible cell flow states and the sudden collapse of cell flow, respectively. Flow conditions were different from Roshko's so the effects of Reynolds number or other viscous flow parameters were not included by Maul and East. They do, however, indicate the importance of b/d (even for large span cavities) to the stability and mode of vortex cells structure within the cavity and the resulting effects cell structure may have on the flow and all pressure within a cavity. Regions of two-dimensional flow occur in particular zones of d/b , though without span and boundary layer structure taken into account the zones are not clearly defined.

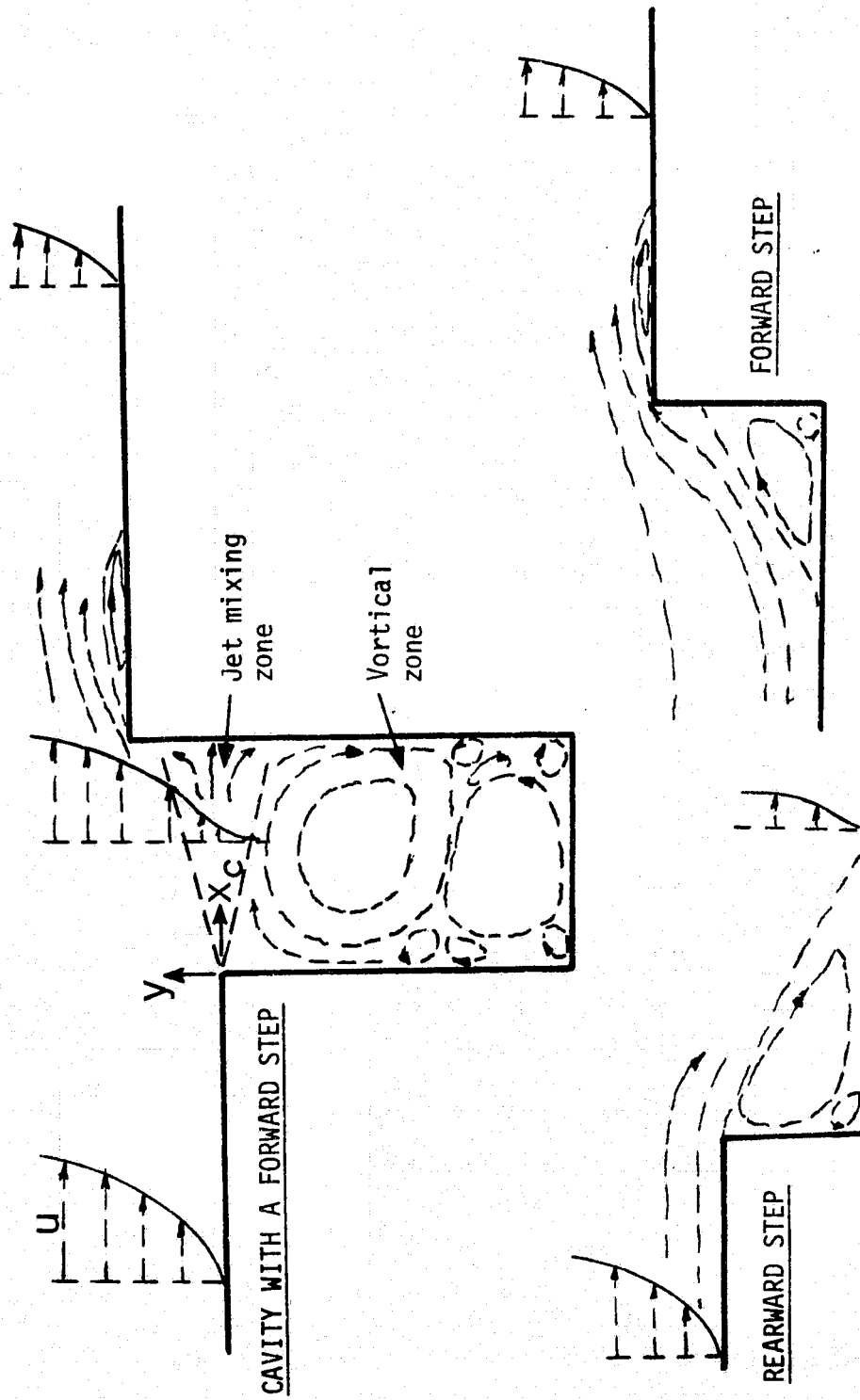


Fig. 2 Sketch of stepped cavity and step flows.

The occurrence of acoustic resonance by a cavity leads to great increases in drag above what is found for a quiescent cavity. Studies conducted on the unsteady and acoustic emission phenomenon from cavities and the mechanisms are numerous. Some of these studies are presented by Krishnamurty⁵, Plumbee et al⁶, Quinn⁷, Rossiter⁸, Karamecheti⁹, McGregor¹⁰, McGregor, White and Fenton^{11, 12, 13}, Bilanin and Covert¹⁴, Hardin and Mason¹⁵, Rockwell¹⁶, and Sarohia¹⁷, to name several. Krishnamurty⁵ tested several cavities from deep to shallow over a range of Mach numbers from 0.25 to 1.50 and gives additional data that show cavity acoustic radiation to $M = 2.55$ for both laminar and turbulent approach boundary layers. The two dimensional cavities resonate at a dominant frequency and higher harmonics and represent a conversion of aerodynamic shear energy into acoustic energy. No radiation was noticed below $M = 0.4$. The frequency of cavities was found to be inversely proportional to cavity width, b , and depends on the boundary layer structure, the cavity depth, and the Mach number as well as b . Radiation appeared to be more intense for laminar flow ahead of the cavity so it is not a turbulent phenomenon alone. Plumbee et al⁶ associated the phenomenon with instability of the separated turbulent boundary layer at the cavity forward corner. Because a single predominant frequency and harmonics are observed, the resonance is not so much a function of the boundary layer turbulence but rather of its separation. Deep cavities were reported to have a depth mode excited while shallow ones had a width mode excited. Quinn⁷ described the waves found in a partially covered cavity within a duct as acoustic waves and not

Helmholtz resonance. Quinn shows the frequency to depend on b for the deep cavities tested but not the boundary layer type. Conclusions about the Helmholtz resonance with his experimental apparatus is doubted.

One of the earlier attempts to model the unsteady pressure fluctuations in cavities came as a result of an experimental study by Rossiter⁸ with shallow and deep slots in which unsteady pressures occur. Both random and periodic fluctuation were found to occur. In his study, Rossiter described the periodic fluctuations as being related to the acoustic edge-tone phenomenon as reported on by Karamcheti⁹ and this predominated in deep slots. No net drag coefficient was given; however, a model for periodic pressure frequency if and when it occurred was presented in terms of a Strouhal parameter as

$$fb/U_e = (m - \gamma_v)/(Ma/c + 1/k) = f(M, R_e) \quad (1)$$

In the formula above b is the slot length; m , the mode number, takes on integer values (1, 2, 3, etc.); γ_v ($= 0.25$) is an experimentally determined vortex spacing factor of shed vortices over the rear edge prior to acoustic pressure impulse initiation from the edge; k ($= 0.35$ to 0.66) is a constant giving the speed of the shed vortices over the cavity relative to the edge-stream velocity, U_e ; M is the Mach number of the free stream; a is the speed of sound in the free-stream; and c is the speed of sound in the cavity (subsonically, $a \approx c$). In Rossiter's experiments the boundary layer thickness was on the same order to one order of magnitude smaller than slot depth and was one order of magnitude less than the slot width, b . Random pressure

fluctuations were predominant for shall cavities and periodic for deep cavities. The magnitude of random fluctuations were found to be proportional to the kinetic pressure at the edge of the boundary layer, q_e , and appeared to be broad banded and at more than one frequency. The magnitude of pressure amplitude for periodic waves was to be proportional to the boundary layer thickness, δ . These had a narrow band with harmonics and an r.m.s. pressure as great as 0.35 times the free-stream kinetic pressure. Within the cavity, random type pressure fluctuations were more intense near the forward-facing wall upper reaches and the greatest appear to be at the reattachment point of the shear layer for the open type cavity.

McGregor¹⁰ associated the resonance with shear layer deflection. Because of the momentum dissipation within the cavity the shear layer deflection outward from the cavity was greater than the deflection inward so as to conserve mass flow to and from the cavity. No resonance was found by McGregor below $M = 0.4$, however. McGregor speculates that the additional drag was accounted for by parameters relating flow and geometry as

$$C_D = C_D(y_i/b, M_e, \delta/b, d/b) \quad (2)$$

where y_i is the extent of the shear layer deflection into the cavity at resonance and M_e is the Mach number at the edge of the boundary layer. Further, data show that increasing y_i/b results in increased drag whereas increasing M_e or δ/b cause decreases in drag due to resonance. Depth effects were not investigated in McGregor's study and boundary layers were thin ($\delta/b \approx 0.3$ and smaller). Similar results^{11, 12, 13}

show that Rossiter's model for frequency at resonance agrees with the experimental results well and, in addition, heat transfer from a resonating cavity is greater than for the same wetted area of flat plate. Bilanin and Covert¹⁴ arrive at Rossiter's formulation for frequency (Strouhal number) analytically and suggest that excitation of two or more discrete frequencies that are not harmonic are observed during resonance. These correspond to two or more vortex sheet displacement modes. Resonance at low Mach numbers is not predicted. Hardin and Mason¹⁵, using potential flow theory, represent the jet shear layer as discrete rectilinear vortices by which noise (resonance) of a cavity may be investigated. Though inviscid, their analysis shows that a steady state solution predicts a large relatively stable vortex within the cavity and vorticity shed downstream. A broad-band noise is predicted which has been recorded experimentally near wheel cavities during aircraft landing. Results were not, however, compared to experimental data nor is the connection to the drag mechanism mentioned. Rockwell¹⁶, using a semiempirical analysis based on hydrodynamic stability theory, extended Bilanin and Covert's¹⁴ analysis to predict cavity frequencies caused by amplified disturbances to a shear layer of finite momentum thickness with continuous velocity profile rather than the discontinuous one proposed by Bilanin and Covert. Though momentum transfer to cavities was excluded, the importance of momentum thickness, θ , in the shear layer and its growth was emphasized. The growth is significant to shallow cavity flow. There is no way, however, to predict if oscillations will occur and how severe they might be based on the preceding boundary layer

and the cavity geometry. Sarohia¹⁷ conducted a series of experiments using hot-wire anemometry techniques to determine the phase and frequency content of oscillations in a level cavity on an axisymmetric body at low speeds (< 80.0 fps). Characteristic lengths (b , d , and δ) were small and the boundary layer ahead of the cavities was laminar. For a given cavity width, b , data show that as the momentum thickness prior to separation increases, it is changed less within the cavity. By comparing to results obtained by East¹⁸, Sarohia concludes that lower frequencies for a given mode of oscillation occur in turbulent boundary layer flow over a cavity than in laminar flow. Further, oscillations tend to increase the growth rate of the free shear layer Reynolds stress term, $-\rho u'v'$. Based on the experiments of East¹⁸, it is probable the tests during the present program may attain a first mode transverse (longitudinal) resonance. East obtained a Strouhal number first mode of approximately 0.3 where $b = 1.0$ inch and $\delta = 0.8$ inch. Plumbee et al⁶ predict a depth or normal mode resonance when $d/b > 1.0$ if resonance in fact occurs. The fundamental depth mode Strouhal number is predicted to be

$$fd/a = 0.25/\{1 + P(b/d)^Q\} \quad (3)$$

where $P \approx 0.65$ and $Q \approx 0.75$. This Strouhal number is predicted to be between 0.1 and 0.22. In his study on wheel well resonance, Yu¹⁹ tested NACA 0018 airfoils of 2.5 and 10.0 feet chords. For the smaller, $d = 3.0$ inch and b was varied from 1.2 to 6.0 inch and for the larger, $d = 1.0$ foot and b from 0.4 feet to 2.0 feet. Testing was in the Ames low speed 7 X 10 foot wind tunnel. The cavity forward corner was at

approximately quarter chord; however, no boundary layer depth was reported for either model. Yu, using experimental data, determined the Strouhal number to be

$$fb/U_{\infty} = \bar{a}/R_e + \bar{b} \log R_e + \bar{c} \quad (4)$$

where $\bar{a} = 0.142 \times 10^5$, $\bar{b} = -0.032$, and $\bar{c} = 0.591$ for deep cavities and $\bar{c} = 1.171$ for shallow cavities. Incremental drag coefficient (for the 10 foot chord wing) between the wing with a cavity and the wing without a cavity were shown varying with Mach number and with Reynolds number. For a given depth, shallow cavities had more drag (based on wing reference area) than deep cavities. Also, a discontinuity in incremental drag coefficient at $R_e = 2.0 \times 10^6 (= U b/\nu)$ shows the demarcation between deep and shallow cavities to be at approximately $b/d = 1.5$. When based on cavity width, b , Yu's conclusion about drag is invalid except for very shallow cavities. Similar and additional findings to those mentioned above may be found in the works of Mabey²⁰ and of Heller and Bliss.²¹

Numerical solutions for cavity flow are in their infancy, yet finite difference solutions such as by Borland²² show some promise. Borland solves the inviscid Euler equations. Chin et al²³ numerically solve a reduced form of the Navier-Stokes equations for a square cavity. Prandtl mixing length and an empirical spread parameter were used to obtain solutions; however, a preceding boundary layer was not considered. Solutions in the cavity are good compared to data of Roshko¹ and Fox². Computer processor time was about 25 minutes on a CDC 6400 for one case.

It would be advantageous to have a scheme (theoretical or empirical) to predict when resonance would occur based on cavity geometry and boundary layer structure. Also, a method to predict increases in cavity drag with resonance that was reliable and general to geometry is needed. These do not exist but a resonating cavity is known to increase drag and thus be a source "error" in steady state momentum transfer and drag analysis.

A typical shortcoming of studies on oscillations of flow over level cavities is that no determination is made of the effects oscillations have on temporal mean momentum transfer or drag. Also typical is testing or analysis with thin boundary layer (small δ) relative to cavity width, b , and depth, d ; whereas, many practical applications where cavities occur have deep boundary layers with narrow cavities ($\delta/b > 1$). Narrow cavities occur, for example, on the space shuttle thermal protection system, in atmospheric flow over land masses, and at the interface of aircraft skin joints. The experiments by East¹⁸, however, had velocities and boundary layer thicknesses comparable to those of the present experimental program. Also, other studies have been conducted beside those giving cavity pressure by Roshko¹, Fox², and Rossiter⁸. Some give only experimental results for cavity drag and/or steady flow theory of a phenomenological type. Examples may be seen in the works of Weighardt²⁴, Tillman²⁵, Tani et al²⁶, Hoerner²⁷, Charwat et al²⁸, Gaudet and Winter²⁹, Haugan and Dhanak³⁰, Norton and White^{31, 32} and Schlichting³³.

Chang³⁴ presents the data of Weighardt, Tillman, and Tani and gives data from a score of other experimental and theoretical works

related to flow separation.

Using a beam mounted plate, Weighardt and Tillman measured the change in drag between a plate with a cavity and without a cavity. There is embedded within these coefficients an effect due to smooth plate drag change caused by changes in viscous shear stress on the plate ahead of and behind the cavity. Much of the data shown by Hoerner²⁷ and Schlichting³³ on protuberance and cavity drag was determined from tests by Weighardt, Tillman, and co-workers and the often used concept of mean kinetic pressure and mean velocity to generalize drag coefficients of protuberances was introduced by Weighardt. Since boundary layer velocity on smooth plates used by Weighardt and Tillman followed a near 1/7th power form (i.e. $n = 7$), they defined the mean dynamic pressure for protuberances by

$$q_{eff} = \frac{1}{h} \int_0^h q(y) dy \quad (5)$$

which, for an $n = 7$ power-law exponent profile, becomes

$$q_{eff} = q_e \left[\frac{7}{9} \left(\frac{h}{\delta} \right)^{2/7} \right] ; h \leq \delta \quad (6a)$$

or

$$q_{eff} = q_e \left[1 - \frac{2}{9} \frac{\delta}{h} \right] ; h \geq \delta \quad (6b)$$

Mean velocity could be similarly determined by

$$U_{eff} = \frac{1}{h} \int_0^h U(y) dy \quad (7)$$

which permits generalized Reynolds number to be defined. Thus,

$$C_{D_{ind}} = \frac{\Delta D}{q_{eff} S} \quad (8)$$

where S is the flow-normal frontal area and

$$R_{h,eff} = U_{eff} \frac{h}{\nu} \quad (9)$$

respectively. According to Tillman, referencing to q_{eff} and $R_{h,eff}$ eliminates boundary layer velocity profile form effect and Reynolds number effects on drag coefficient for protuberances. However, with cavities, it appears that several regimes (not all stable) of flow are possible so in drag measurements on cavities, no suitable height was used for defining $C_{D_{ind}}$; thus, Weighardt and Tillmann present drag coefficient based on q_e and $s \cdot b$. Representative drag coefficient data shown in Fig. 3 indicates a single drag maximum occurs for $d/b \approx 0.1$ to 0.3 for the fairly long groove-shape cavities. Photographs of the vortical-flow streams in a $d/b = 2.0$ level cavity appear to be very similar to vortex streams for a stepped cavity depicted in Fig. 2. Of photographs by Weighardt and shown by Chang³⁴, there is, for a cavity with $d/b = 1.0$, one large vortex zone present. For shallow cavities there may not be a single large vortex and for $d/b < 0.1$: there is a reattaching shear layer that separated as a free jet turbulent wake flow from the upstream, forward corner boundary. For shallow cavities, small vortices are expelled from the downstream rear corner into the boundary layer wake or into the main stream. A demarcation of cavity flow regimes is noted when breadth to depth ratio, b/d , is reduced. Charwat et al²⁸ have shown that for a shallow cavity the separated wake attaches to the floor, and distinct

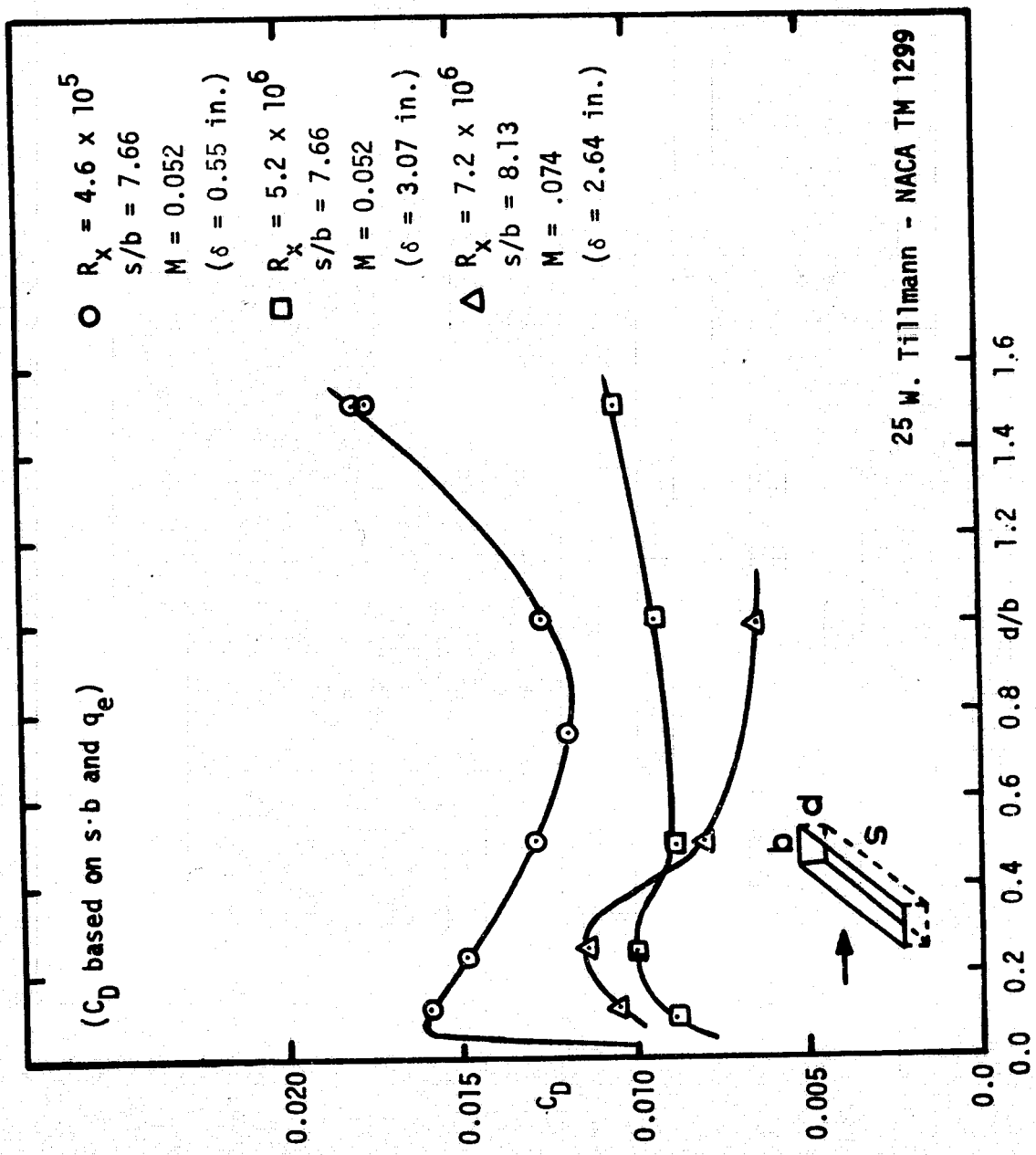


Fig.3 Representative cavity drag coefficient.

wakes appear as a separation wake behind the rearward-facing step and as a recompression wake ahead of the forward-facing step formed by the cavity back wall. The cavity is closed. As b/d is decreased the diffusing separation wake bridges the cavity entirely and forms an open cavity. With increasing or decreasing b/d for a level cavity, closing and opening is affected by δ/d and hysteresis is indicated. Critical closure occurs when the separation wake merges with the recompression wake. As would be expected, a step/cavity opens or closes differently than a level cavity; however, Charwat²⁸ shows that in supersonic flow the ratio of closure breadth to depth bears a near linear relationship to the ratio of forward facing cavity wall length $(d+h)$ to depth, d . Shallow level cavities have more uniform pressure on the recompression face compared to deep cavities, and narrow cavities (large δ/b) have a lower pressure gradient on the recompression face than do wide cavities because of a decreased mixing parameter $U(y=0)/U_e$. The mass-exchange model of Charwat³⁵ suggests that for resonating cavities the net rate of momentum added to the cavity gives the drag increment per unit cavity span over and above the steady state cavity drag. This momentum increment is

$$\Delta M = \rho \int_{-y_i}^{y_o} U^2 dy - \rho \tilde{U}^2 (y_o + y_i) \quad (10)$$

where y_o and y_i are the distances the shear layer is deflected outward and inward, respectively. The velocity \tilde{U} is the velocity at $y = 0$ in the shear layer. Charwat assumes $y_o = y_i$. A constant density is assumed. The mass added per unit span during a half-cycle pulsation is then

$$\Delta m = \rho \int_0^{y_0} U dy - \rho \tilde{U} y_0 \quad (11)$$

The velocity U is assumed to be

$$U = \tilde{U} + y[dU/dy]_{y=0} \quad (12)$$

where $[dU/dy]_{y=0}$ may be found from the shape of the steady state shear layer profile. Conservation of mass is not to be had with this model since, as McGregor¹⁰ shows, $y_i \neq y_0$. This results because the velocity of mass expelled must be less than the inflow velocity because of shear stresses acting on the injected mass by cavity walls. A more tenable model gives the momentum increment

$$\Delta M = [dU/dy]_{y=0} \{ \tilde{U}(y_0^2 - y_i^2) + \frac{1}{3} [dU/dy]_{y=0} (y_0^3 + y_i^3) \} \quad (13)$$

where

$$y_0 = [(\tilde{U}/[dU/dy]_{y=0})^2 + 2U y_i/[dU/dy]_{y=0} - y_i^2]^{\frac{1}{2}} - \tilde{U}/[dU/dy]_{y=0} \quad (14)$$

It is necessary, however, to know y_i and as no reliable theory is available, y_i must be determined by experiment during resonance. Generally, y_i is proportional to separated shear layer width and inversely proportional to $[dU/dy]_{y=0}$. It is also a function of Mach number. The theory of Bilanin and Covert¹⁴ or of Rockwell¹⁶ may be useful in giving y_i , however, with some experimentally determined measurements still necessary.

Gaudet and Winter²⁹ present phenomenological correlations for drag of various forms of protuberances and cavities. Direct drag measurements by a strain-gage balance were capable of measuring some

of the effects on skin friction before and behind excrescences. Of particular interest here were measurements on cavities. For long cavities (s large) three models were tested ($b/d = 1, 2, \text{ and } 3$). Cavities were wide ($d/\delta = 0.03$) where at $M = 0.2$, $\delta \approx 7.1$ inches. The cavities, in the transition region between deep and shallow, gave small drag increments for their balance and no effects for variation of b/d on drag could be discerned. Cavity drag was correlated by analogy to step correlations. Results for long rectangular level cavities referenced to flat plate skin friction coefficient are

$$C_D/C_f = 2 \log U_\tau b/\nu - 2 \quad (15)$$

valid over the range $10 < U_\tau b/\nu < 10^3$; however, data were not presented. Equation (15) gives fair agreement for drag data of "square holes" ($s/b = 0.4, 1.0, \text{ and } 2.5$). Data for circular holes of diameter D correlate to a different form. Namely,

$$C_D/C_f = C_1 (U_\tau D/\nu)^{C_2} \quad (16)$$

where C_1 depends strongly on Mach number and hole depth d while C_2 depends mainly on Mach number. In incompressible flow, $C_2 \approx 0.31$ while C_1 varies cyclically from approximately 0.15 to 1.0. Data are shown for d/D from 0.04 to 1.5. Additional data for circular holes are presented by Schlichting³³. Oil-flow patterns for circular holes show an extremely complicated three-dimensional flow exists. It is also speculated the flow is unstable.

Haugan and Dhanak³⁰ investigated steady flow over level deep cavities and developed a model for drag determination based on a

solution of the separated jet diffusion model introduced by Tollmien³⁶. Turbulent shear stress or Reynolds stress with incompressible boundary layer assumptions and a negligible pressure gradient axially in the jet mixing zone (see Fig. 2) was expressed by

$$\tau = \rho (a^3/2) x^2 \left| \frac{\partial U}{\partial y} \right| \frac{\partial U}{\partial y} \quad (17)$$

This follows by having assumed momentum eddy diffusivity to be

$$\epsilon_M = \frac{1}{2} a^3 x^2 \left| \frac{\partial U}{\partial y} \right| \quad (18)$$

and

$$\tau = \rho \epsilon_M \frac{\partial U}{\partial y} \quad (19)$$

As shown by Abramovich³⁷, the same form of momentum equation

$$U \frac{\partial U}{\partial x} + V \frac{\partial U}{\partial y} = a^3 x^2 \frac{\partial U}{\partial y} \frac{\partial^2 U}{\partial y^2} \quad (20)$$

results by Prandtl mixing-length theory. The later turbulent model proposed by Görtler based on new theory of Prandtl for turbulent shear and using Boussinesq's analogy to laminar flow gives, as shown by Abramovich,

$$U \frac{\partial U}{\partial x} + V \frac{\partial U}{\partial y} = \chi k x U_r \frac{\partial^2 U}{\partial y^2}$$

The velocity profile from this is an error function in terms of $\xi = \sigma y/x = y/x \sqrt{2\chi k}$. Haugan and Dhanak's solution makes use of the similarity parameter given by

$$\eta = y/ax \quad (21)$$

where $a = 0.12$ was chosen. The solution to Eq. (20) is based on satisfying boundary conditions giving continuous velocity and gradient

in the y-direction where the free jet mixing zone and the boundary layer above it join and by experimental observation that the local turbulent shear stress is near a maximum at $y = 0.0$. By letting the stream function be

$$\psi = aU_e x f(\eta) \quad (22)$$

Eq. (20) becomes

$$f'''' + f = 0 \quad (23)$$

or

$$U/U_e = f'(\eta) = k_1 e^{-\eta} + k_2 e^{-\eta/2} \cos(\sqrt{3}\eta/2) + k_3 e^{-\eta/2} \sin(\sqrt{3}\eta/2) \quad (24)$$

where k_1, k_2, k_3 are "local" constants dependent on x/b and δ/b .

Level cavity drag coefficient is based on a control volume analysis and is given by

$$C_D = \bar{\tau}_{y=0} / \frac{1}{2} \rho U_e^2 \quad (25)$$

McGregor¹⁰ assumed a cubic for velocity profile in the free jet and a boundary layer given by a 1/7th power law profile.

Thus, for

$$U = \alpha_0 + \alpha_1 y + \alpha_2 y^2 + \alpha_3 y^3 \quad (26)$$

and boundary conditions at $y = y_u$, the upper edge of the free jet

$$U_u = U_e (y/\delta)^{1/n}, \quad U'_u = \partial U_u / \partial y; \quad y_u \leq \delta$$

$$U_u = U_e, \quad U'_u = 0; \quad y_u \geq \delta$$

and at $y = y_L$, the lower edge of the non-symmetrical free jet.

$$U_L = 0 \quad U'_L = 0 \quad (27)$$

then α_0 , α_1 , α_2 , and α_3 are determined. With τ by Eq. (17) evaluated at the midline as considered by Haugen and Dhanak, then

$$C_D \approx a^3 (\alpha_1 b / 2U_e)^2 \quad (28)$$

since

$$\partial U / \partial y_{y=0} = \alpha_1 \quad (29)$$

McGregor compares predicted drag coefficients to data and predictions of Haugen and Dhanak ($\delta/b < 0.6$). Both the Haugen and Dhanak theory and McGregor's theory underpredict Haugen and Dhanak's data but show the correct trend. Drag coefficients were determined by integrating wall pressure measurements. Neither prediction model is capable of giving drag on step/cavity configurations nor are they capable of predicting wall pressures for level cavities.

In previous studies, Norton and White^{31,32} studied multiple level cavity effects on a test plate covered with tiles. Velocity profiles before and after a series of cavities permitted momentum loss to be computed simply where no pressure gradient existed. Level cavities were found to have small drag compared to stepped cavities. By modifying Hoerner's²⁷ method to account for multiple tiles on the test surface and using data presented by Hoerner, they showed good agreement and trends for multiple cavity arrangements. This work has been extended and includes an analysis with the more general log-law boundary layer. Results of this are presented in Appendix A.

This multiple cavity analysis is similar to some aerospace industry practices³⁸ although no single scheme for drag estimation on surfaces with cavities, steps, or more general roughnesses can be found or recommended. Because the research^{31,32} is directly related to the present study more description will be given further on in the text.

Employing the stream function, Chapman³⁹ reduced the momentum and energy equations for laminar cavity flow with a uniform approaching stream to an ordinary differential equation. Transforming to a nondimensional x, ψ coordinate system and using a similarity parameter of nondimensional stream function divided by the square root of the nondimensional x -coordinate, solutions were numerically obtained in Chapman's analysis; however, no velocity or heat transfer experiments were compared. Later, Chung and Viegas⁴⁰ addressed Chapman's problem with interest on the heat transfer in the region where the free-shear jet wake reattached to the forward-facing downstream wall. The region was assumed to be an inviscid, incompressible, but rotational flow so that $\nabla^2 \psi = -\Omega(\psi)$ where Ω is the vorticity. Pressure distribution on the level cavity forward-facing wall were computed; however, differences between the pressure distribution presented and pressure distribution observed for incompressible turbulent flow lead one to the conclusion that the mathematical flow models of Chung and Viegas and of Chapman need to be improved to account for momentum transfer to the cavity. The numerical solution by Chin et al²³ for a uniform turbulent flow over a $b/d = 1.0$ cavity show good agreement to measurements^{1,2,3} within the mid-cavity vortical zone (Fig. 2). Velocity profiles in the free shear layer are in good agreement with Fox's³ data but show

deviations near the back wall. Space is too limited to give an exposition on Chin's solution; however, results look encouraging for the finite difference scheme. Parametric curves are not shown in sufficient number to predict the momentum transfer to the cavity or cavity drag and computation schemes were not available at this writing to investigate the computer program capabilities. A similar statement may be made relative to the scheme used by Adams⁴¹ for open level cavities.

Turbulent Jet Boundary Formation and Impingment

The separated turbulent jet-wake mixing zone description has proved useful if not necessary to parametric modeling separated flow over level cavities^{2,3,6,10,23}. The jet boundary is also useful to modeling separated flow over steps, fences, and plates. Confirming models by comparison to experimental measurements may, however, be difficult. It is probable that existence of time dependent three-dimensional flow as encountered in cavity experiments requires determination of the experimental mean momentum transfer mechanism to an excrescence or an indentation by time and spatial pressure integration (shear drag being an order of magnitude smaller)⁴².

Previously reported is unsteady flow as observed in cavities. In steady two-dimensional flow, a feature of level cavities, forward-facing steps, and cavities with forward-facing steps is that the dividing streamline surface generally stagnates somewhere on the forward-facing wall. This may not be true, however, for three-dimensional flow. For level cavities, Kistler and Tan⁴² found that shear stress alone at a transverse station does not permit prediction

of drag when three-dimensional steady effects are present. Because of this, it is speculated that a free jet impingement model of the flow which incorporates prediction of pressure forces would be more general and applicable to a wide variety of geometries than correlations using force balance data. Even with the new generation of computers, correlations are necessary since numerical solutions fall short or are not feasible.

Pressure forces appear to be determined mainly by the flow near the upper extent of the forward-facing wall where pressure gradients are greatest; therefore, it is germane to review aspects of the characteristics of free-jet diffusion as this concerns free-jet impingement on a forward-facing wall.

Following Tollmien's³⁶ solutions for free turbulent expansion, there has been a deluge of research concerning free turbulent shear flow. Much of the earlier works (prior to 1958) have been recorded by Abramovitz³⁷, Pai⁴³, Rajaratnam⁴⁴, White⁴⁵, and Schlichting³³. Other noted works include the discussions by Batchelor⁴⁶ and the discussions and experiments of Liepmann and Laufer.⁴⁷ Three concepts prevailed for analysis of turbulent jets during that time: the constant mixing length theory of Tollmien, the constant exchange coefficient theory of Gortler, and the inductive theory of turbulence by Reichardt. The three are classified as phenomenological as opposed to statistical theories. Reichardt's theory is based only on mean velocity measurements and actually is an empirical interpolation formula. Both Tollmien's and Gortler's solutions predict mean velocity in a turbulent free jet very well; however, as shown by Liepmann and Laufer⁴⁷, both

theories can predict turbulent shear stress 25% higher than measurements. In addition, the mixing length and the exchange coefficient were not constant across the mixing region as proposed by Tollmien and Görtler, respectively.

Recently, Elassar and Pandelfini⁴⁸ and Islam⁴⁹ examined several models for eddy viscosity for shear stress prediction. A particularly interesting finding of Elassar and Pandolfini was that it requires different mixing lengths in similar and nonsimilar free jets. At that time additional theory on statistical properties of turbulence were gaining ground. Particularly, expressing the turbulent shear stress with an eddy viscosity model having the intermittency factor, discussed by Corrsin and Kistler⁵⁰, Townsend⁵¹, and Hinze⁵², had received application but primarily by way of correlating existing data⁵³. Recently, attention has been given to the development of models and prediction of mean velocity, shear stress, and heat transfer in free shear layers under a supersonic stream.⁵⁴

The error function velocity profile derived by Görtler is widely used; however, several considerations need to be taken into account in using Görtler's free shear layer formula. Features of the flow which need to be taken into account are:

1. Profiles are not similar or locally similar immediately after separation (with or without a boundary layer in the viscous flow). Camarata⁵⁵ discusses upstream boundary layer effects.
2. With geometry aligned coordinate axes, mean velocity profiles must be shifted or aligned (usually about the half-velocity point). Truncation of profiles is used prior to similarity flow when an

initial boundary layer is present.

3. Similar profiles are not expected in flow where downstream walls or obstructions may influence the flow.

These considerations also apply to other approximations used to represent free jet mean velocity profiles. Therein lies a disadvantage of classical formulas, implied need for rigorous numerical solutions to a system of differential equations with appropriate boundary conditions.

Several of the most recent numerical concepts and formulations are embodied in NASA SP-321⁵⁶. Solutions to free turbulent flows are compared and most of the significant literature on the subject are reviewed. Several concepts for closure (relating turbulent shear stress to mean flow) of the defining differential equations are given in the conference papers⁵⁶ and notable is the predominate use of differential numerical solutions as opposed to integral methods. Some years before, the Stanford conference papers⁵⁷ mainly had integral methods for use in boundary layer problem analysis.

Turbulent boundary layer flow developed on a smooth plate separates before an isolated step or from the front corner of a rearward facing wall of a cavity. With separation there forms a free asymmetric or detached shear layer. In two-dimensional flow over a flat surface this free asymmetric jet will reattach to the downstream forward-facing wall for a forward-facing step or level cavity. The reattachment occurs at some point on the forward facing wall and is said to impinge on the wall. Analyses have been made to define the velocity field above and the pressure on a flat plate when

either a planar or circular turbulent symmetric jet impinges on the plate. Gauntner et al⁵⁸ conducted a survey of methods used to predict the normal impingement of a symmetrical jet. Classical potential flow solutions for impingement are presented; however, it is suggested that these inviscid, irrotational solutions do not suffice. An inviscid but rotational solution for symmetric jet impingement is developed by Tani and Komatsu⁵⁹; however, application to impingement of a free turbulent asymmetric jet may not be deduced from this work. Tani and Komatsu required measured constants to fit a power series form for velocity along the jet centerline. In asymmetric jets, no characteristic centerline may easily be defined even though the stagnation streamline on a forward facing step has been found to intercept the wall at near perpendicular. Johnson⁶⁰ shows that potential flow solutions for pressure distribution give first order accuracy in the near vicinity of stagnation. For an asymmetric jet the dividing streamline stagnates although the pressure differs from maximum pressure on the receiving wall. This pressure distribution is observed and can be supported by considering shear gradient. To first order it is expected that pressure on the forward-facing wall varies parabolically with distance along the wall from the maximum pressure point.

Near the back wall of a cavity or a forward-facing step the streamlines of the turbulent incompressible free jet are known to turn and diverge about the dividing or separation streamline². Because the dividing streamline is curved in the presence of the wall which allows for pressure gradients, the jet streamlines at wall impingement are associated with velocity profiles which impinge at an angle.

Although the dividing streamline has been observed to stagnate at a near normal to the wall, the asymmetric free turbulent shear layer approaches the wall at an oblique. Little research has been done on wall pressure distribution for oblique impingement and no literature considers oblique impingement of an asymmetric free turbulent jet on a half plane. Oblique impingement of an asymmetrical plane jet having attained similarity was studied by Beltaos⁶¹. Data reveal that the pressure distribution at the receiving plane is skewed and that the stagnation streamline (located at y_{pds} on the plate) is offset from the intercept of the incident jet centerline. Offset was empirically determined in terms of incident angle, and the pressure distribution based on offset coordinates follows a Gaussian form. Parameters defining the flow considered by Beltaos include the mean kinematic momentum of the plane jet at a nozzle exit, distance to the plate, impingement angle, and density. By relating or extrapolating these to a cavity forward-facing wall the dimensionless groups which appear in Beltaos's work become $p/(\rho U_e^2/2)$, b/δ , n , and $(y_{p_{max}} - y_{p_{ds}})/b$. For a forward-facing step the parameter groups become $p/(\rho U_e^2/2)$, h/δ , n , and, layers, $(y_{p_{max}} - y_{p_{ds}})/h$. As will be described later, b alternatively may be related to an effective height of the rear-most cavity wall.

Forward-Facing Step Flow

As with turbulent, free jets produced at separation, flow over a forward-facing step relies on empirical quantities to define the flow field. In order to describe the momentum transfer in a phenomenological way and to provide meaningful correlation of measured pressure forces,

dimensionless groups of flow and geometric parameters are required. In general, the flow parameters for correlation should be those which can be obtained with knowledge of the turbulent boundary layer at the spatial position of the step were no step present. Considerable experimental research (testing mainly) has been reported for steps on flat surfaces having an incompressible turbulent boundary layer. Because forward-facing steps have a significant effect on the pressure over the surface prior to the step in incompressible flow, much of the research on flow over a forward-facing step has been on prediction of separation ahead of the step. Bradshaw and Galea⁶² conducted experiments in a channel on a large step ($h = 1.75 \delta$) to determine criterion for separation point. Of prime interest was the effect on an equilibrium turbulent boundary by a step and how forced, sudden separation occurs. A relatively thick boundary layer ($\delta \approx 1.3$ inch) was tested. Also, rather large static pressure gradients (approximately 0.2 percent per inch of the dynamic pressure) were encountered on the smooth test plate reaching approximately fourteen boundary layer heights ahead (when steps were not in place). These pressure gradients had to be considered to analyze findings. Separation was found to occur at approximately 1.2 step heights ahead of the step for the large step ($\delta/h \approx 0.5$). Good and Joubert⁶³ investigated the flow over a series of bluff thin plates on a smooth wall having a turbulent boundary layer. Reasoning as did Bradshaw and Galea⁶² that separation was induced upstream in the manner described by Stratford and

Townsend*, Good and Joubert hypothesized that plate drag coefficient could best be correlated by wall parameters as opposed to mean kinetic pressure proposed by Tillmann²⁵ and as presented by Hoerner²⁷. It was noted⁶² that major stress gradient changes and total pressure changes are confined mainly to the inner part of the boundary layer stream-lines. As mentioned previously, Tillman assumed a power-law velocity profile with $n = 7$. Hoerner's analysis was confined to $n = 6$ power-law profiles (reference profiles) existing in the absence of the protuberance. With Stratford-Townsend ideas, Good and Joubert reasoned that correlation could be based on assuming reference mean velocity profiles having inner layer variables characteristic of "equilibrium layer" log-law reference profiles or

$$U/U_\tau = A \ln yU_\tau/\nu + B \quad (30)$$

The less general analysis by Tillmann²⁵ considered

$$U/U_e = (y/\delta)^{1/7} \quad (31)$$

Thus, Tillman derived the mean kinetic pressure form used for Eqs. (5) - (8). In the independent parameter group used for correlation of step drag by Tillman²⁵, Weighardt²⁴, and Hoerner²⁷, inner wall-law variables do not appear; however, Reynolds number effects could be accounted for by proper choice of n . Using the parameters of Eq. (30), Good and Joubert considered drag coefficient for thin plates to be expressed by

*Stratford and Townsend presented a sequence of papers in Journal of Fluid Mechanics between 1959 and 1962. Reference to these will be found in the papers by Bradshaw and Galea⁶² and by Good and Joubert⁶³.

$$C_D = C_f f(hU_\tau/\nu, U_\tau/U_e) \quad (32)$$

or, in the notation of Ref. 63, a new coefficient from Eq. (32) follows

$$C_{D_\tau} = 2C_D/C_f. \quad (33)$$

Arguing as Ref. 63, Plate⁶⁴ uses $C_* (=C_{D_\tau})$ and addresses protuberances on a rough surface. In a more general situation, the velocity profile may be described as given by Coles in Volume II of the Stanford Conference Papers⁵⁷.

$$U/U_\tau = (1/\kappa) \ln(yU_\tau/\nu) + B + (\pi/\kappa)W(y/\delta) \quad (34)$$

so that

$$C_D/C_f = f(hU_\tau/\nu, U_\tau/U_e, \pi) \quad (35)$$

or alternatively

$$C_D/C_f = f(hU_\tau/\nu, h/\delta, \pi) \quad (36)$$

In addition to the drag coefficient correlation, C_{D_τ} , for plates normal to the flow as given by Good and Joubert, extensions of inner layer based C_D/C_f are developed by Gaudet⁶⁵ and by Gaudet and Winter²⁹ for other isolated roughness or protuberance shapes. The correlations are similar in form to that of Eq. (15); constants are different. Good and Joubert show that pressure drag on the front face of a bluff plate may be correlated in the same manner as plate front- and back-face net pressure drag providing the connection to forward-facing steps drag correlation.

As part of the experimental program of Ref. 63, the upstream

influence of the bluff plates tested at a Reynolds number of 1×10^7 was determined to be

$$\Delta x/h = 15(h/\delta)^{-0.7} \quad (37)$$

where the value of δ at the site of the plates was approximately 2.3 inches and h/δ was from approximately 0.053 to 1.709. For flow over a flat plate with no pressure gradient, Eq. (37) may be useful in locating surface static pressure or piezometer holes: holes should be forward of the distance given by Eq. (37) or out of the sphere of influence of forward-facing step protuberances. For the plates tested, Good and Joubert find

$$C_D/C_f = (1/2)C_{D_\tau} = 138.5 \log (hU_\tau/\nu) - 134 \quad (38)$$

below $hU_\tau/\nu = 10^3$.

Equation (38) may be compared to the formula for square ridges (Ref. 29)

$$C_D/C_f = 150 \log (hU_\tau/\nu) - 190 \quad (39)$$

Also, for drag coefficient on the thin plate forward face of Ref. 63

$$C_D/C_f = 62.5 \log (hU_\tau/\nu) - 60.5 \quad (40)$$

between $hU_\tau/\nu \approx 10^2$ and 10^4 . For the back surface of the plate

$$C_D/C_f = 76 \log (hU_\tau/\nu) - 73.5 \quad (41)$$

below $hU_\tau/\nu \approx 10^3$. Deviations from straight line correlation with $\log (hU_\tau/\nu)$ above 10^3 are apparently due to the back face; however, tunnel blockage was disregarded.

Gaudet and Winter²⁹ have

$$C_D/C_f = 60 \log (hU_\tau/\nu) - 80 \quad (42)$$

for forward-facing steps and

$$C_D/C_f = 16 \log (hU_\tau/\nu) - 6 \quad (43)$$

for rearward-facing steps. For a nominal $hU_\tau/\nu = 10^3$, Eq. (42) and Eq. (40) differ by 27.0 percent; however, Gaudet and Winter measured drag directly with a balance and Good and Joubert integrated pressures on plate surfaces.

Consistent with Eq. (34) and Eq. (36), Ref. 63 writes

$$C_D/C_f = C_1 \log (hU_\tau/\nu) + C_2 + C_3 \phi(h/\delta) \quad (44)$$

for zero pressure gradient. Use of Eq. (44) above $h/\delta \approx 0.4$ is necessary because C_D/C_f could not be correlated with only hU_τ/ν for the bluff plate. Even so, drag on the front face of the plate was found to be dependent on hU_τ/ν as mentioned previously: the back face of the plate causes Eq. (44) to be used above $h/\delta \approx 0.4$. Front-face pressure distribution could not be correlated with hU_τ/ν alone but require functions of y/h which were not linear and not unique. Effects of h/δ are evident and pressure distribution normalized by maximum pressure on the forward-facing wall show effects of the character of the separation region between the face and the stretch of floor ahead. With regard to flow over a bluff plate in a pressure gradient, Ref. 63 gives a basis for drag correlation; however, results are not unified or tractable and remain beyond the scope of the

present study. A different approach to account for the effects of pressure drag on a forward step by correlation with a pressure gradient present is proposed by Nash and Bradshaw⁶⁶. It appears that using actual mean velocity profiles as reference profiles permits inclusion of wall-law similarity parameters and thus suitable momentum transfer correlation in parametric form.

Many additional experimental studies have been conducted to determine the drag of forward facing steps. One of these by Pallister⁶⁷ concerns the drag for both forward- and rearward-facing steps, ridges, and holes. This study confirms generally the analysis by Gaudet and Winter²⁹ and by Gaudet et al⁶⁵ and consequently that of Good and Joubert⁶³ for the drag on the forward face of a plate. Principally, confirmation is due to correlation of C_D/C_f to hU_τ/ν . Experiments were conducted with a floor mounted drag balance so some effect in the friction drag component is present in the data. A typical finding of these tests was that for forward steps much smaller than the boundary layer height the effects on pressure extend many step heights upstream. In fact, for the small step, this distance is greater than for the large step on a step height basis with steps much greater than the height of the viscous sublayer. Unlike the analysis of Gaudet and Winter⁶⁵, however, the test plate velocity profiles exhibited a form indicative of a rough wall. Because of this, the value used for C_f was not as determined by direct reading but had to be adjusted to account for roughness in order to agree with similar analyses found in Refs. 29 and 65.

Numerous other sources of experimental measurements and analyses on forward facing steps have appeared recently. Most relate to and generally confirm those described previously. For example, Kovalenko and Nesterovich⁶⁸ examine steps at transonic and supersonic speeds basing drag on effective kinetic pressure in the manner by which Tillmann²⁵ analyzes low-speed step-flow drag. Swept or skewed finite steps are shown to have drag which depends on the square of the cosine of the angle of skew. Wu and Chen⁶⁹ test very shallow cavities and find that disturbances created upstream of a step suppress or enhance separation at the downstream step. Surface pressure was found to stabilize more rapidly than velocity profile after disturbance upstream. Pressures appear to relax inward while velocity profiles appear to relax out from the surface before the forward step. One may also conclude that actual velocity profiles would better serve step momentum transfer correlation studies where profiles are available as opposed to an idealization of the boundary layer prior to influence by the forward step.

Many recent studies have considered supersonic speeds. Some of the characteristics of flow over a forward step may be seen in the work of Czarnecki and Jackson⁷⁰ and Chang³⁴. High speed flows exhibit some of the characteristics of low speed flows as might be expected since flow in the wall region before the step is subsonic.

In conjunction with the effects a forward-facing step has on flow before the step face and with the flow in the immediate vicinity of the step face, researchers have studied the flow field immediately behind the upper corner of the step face. Ota and Itasaka⁷¹

experimentally studied flow reattachment and redevelopment downstream of a blunt plate. Their findings indicate that reattachment occurs from 4.0 to 5.0 plate thicknesses downstream whereas the velocity profile requires approximately 20.0 plate thicknesses to redevelop into a flat plate profile. Ota and Itasaka's experiments may be viewed as a limiting case study where the approaching boundary layer is of zero thickness.

An accumulation of studies by Robertson and Taulbee⁷² and Taulbee and Robertson⁷³ on a flat plate having a forward-facing step give data and a theoretical model with which to predict the flow field. Although their attention is placed on the flow approaching the step and the flow redevelopment aft of the step, little emphasis is placed on the step face pressure determination. Nor is the relationship of the step to boundary layer height and other boundary-layer velocity profile parameters related to the flow in the separation bubble. To fully determine the influence downstream of the step it is necessary to provide the relationship between the flow across the plane of the step and the action within the separation bubble initiated at the upper back corner of the step. Taulbee and Robertson⁷³ found by experiments on a large step ($\delta/h \approx 0.5$) that the characteristics of the outer part of the approaching turbulent boundary layer were suitable for use in theoretical analysis of the flow field over the step. Measurements of experimental pressure and velocity data for $\delta/h \approx 1.40$ were also compared with the theoretical (numerical) solutions obtained by finite difference solutions based on their frozen upstream vorticity model; however, agreement was not as good as comparisons at $\delta/h \approx 0.5$.

The rotational flow analysis of Ref. 67 is apparently useful for large steps only and does predict the separation bubble ahead of the step when the step is large. Experimental studies of subsonic flow over a forward-facing step on a flat plate (no pressure gradient) with a turbulent boundary layer have, in most instance, been limited to smooth surfaces before the step. As previously mentioned, Plate⁶⁴ extends the drag correlation analysis idea presented by Good and Joubert⁶³, Eq. (32). The coefficient C_D/C_f was found to be essentially a function of hU_t/ν for $h/\delta \leq 0.4 + 0.5$ or for $h U_t/\nu \leq 10^3$. Raju, Loeser, and Plate⁷⁴ sought to establish the importance of U_t/U_e with, however, a tunnel blockage given by

$$C_D = C_{D,\text{uncorrected}}(1-h/H_t)^{2.85} \quad (45)$$

where H_t is the wind tunnel uniform jet height perpendicular to the flat plate surface before the step (fence) obstruction. Good and Joubert⁶³ did not correct for blockage: Raju, Loeser, and Plate corrected Good and Joubert's data to compare with their own. Experiments conducted in Ref. 74 considered rough surfaces before their fence. For this, then, the functional correlation relationship is

$$C_D/C_f = f(h/y_o, U_t/U_e) \quad (46)$$

Experiment showed, however, that the dependence on U_t/U_e was of no importance.

Theoretical studies of flow over a forward-facing step by Bitte and Frost⁷⁵ consider three different methods. As did Taulbee and Robertson⁷³, Bitte and Frost required the use of numerical solution.

Though their studies do not lead directly to correlations of momentum transfer parameter groups as they depend on sets of boundary layer parameter groups, they do permit systematic variation of parameters in stipulated order of magnitude. The best of the numerical solutions are in agreement with some experimental data where particular emphasis was placed on the structure of flow streamlines. Their inviscid free streamline model based on rotational inviscid flow over a fence requires several empirically determined parameters and is not applied to a forward-facing step. Nevertheless, streamlines near the front face and pressure on the face resemble those of a simple step quite well. The velocity approaching the step face is, however, not representative of boundary layer flow. A second solution approach using a representative boundary layer and inviscid solution pressure distribution is presented by Bitte and Frost⁷⁵. Closure was attained using mixing length and main emphasis was placed on velocity profiles behind a fence (thus not representing forward-face conditions with their results). A third approach by Bitte and Frost was based on two-dimensional Navier-Stokes equations. Three different turbulence models were used: an eddy viscosity model, a turbulence kinetic-energy model, and a two-equation model with a transport equation for the turbulence length scale. The equations of motion are posed in terms of stream function and vorticity to eliminate pressure terms. To relate the effective viscosity to mean flow parameters the mixing length concept of Prandtl was used as an eddy viscosity model. This is

$$\mu_t = \rho \ell^2 ((\partial U / \partial y)^2 + (\partial V / \partial x)^2)^{1/2} \quad (47)$$

where ℓ , the mixing length, is linearly related to y , y_0 , x , and h depending on position in the flow field. The turbulent kinetic-energy model uses

$$\mu_{\text{eff}} = \mu + \mu_t = \rho K^{1/2} \ell C_\mu \quad (48)$$

where K is the mean kinetic energy of the velocity fluctuations and ℓ was taken by Bitte and Frost to be the same as that in the eddy viscosity model. This analysis requires a third partial differential equation (in addition to the equation relating the stream function, ψ , and vorticity, Ω , and the equation for transport relating ψ , Ω , and μ_{eff}). The quantity C_μ is inversely proportional to the turbulent Reynolds number.

In the two-equation model the foregoing equations are used except the mixing length is formulated in terms of a partial differential transport equation. The details of the formulations may be found in the report of Bitte and Frost. Numerical formulation used "upwind differencing" for convection terms and iterative successive substitution solution. Both the numerical aspects and comparison to experiment reveal that the last of the solutions, the two-equation model, is most representative of mean and turbulent quantities. Aspects of parametric investigations by Bitte and Frost shall be discussed in a later section. Of particular interest are the results for the flow just aft of the corner although no experimental and theoretical comparisons were given.

Rearward-Facing Step Flow

Of particular interest to the present study are correlations which successfully predict the pressure on the rearward-facing wall of a down step. For down steps submerged in a turbulent boundary layer, the pressure on the wall is essentially a constant the magnitude of which is dependent on the characteristics of the boundary layer ahead of the step.²⁹ For incompressible flow, Eq. (43), developed by Gaudet and Winter²⁹, is said to agree with data taken by Weighardt but not with that of Tani et al.²⁶ In Gaudet and Winter's report, however, they fail to show their data or that of others but claim that considerable scatter exists. Based on correlations for forward-facing steps and claims of greater scatter in data used for developing Eq. (43) than for developing Eq. (42), Weighardt's data may be 50% lower than what Eq. (43) prescribes for C_D/C_f . Hoerner⁷⁶, using an effective kinetic pressure concept, Eq. (5), gives

$$C_D = 0.18 (h/\delta)^{1/3} \quad (49)$$

which shows agreement to experimental data of Weighardt up to $h/\delta = 0.5$. Experimental drag coefficient data shown by Hoerner is at most 17% different from values given by Eq. (49). Results of the present study will be compared to predictions given by Eq. (43) and Eq. (49) in a later section.

Analytical as opposed to correlation schemes have been developed and notable are the works of Nash⁷⁷, McDonald⁷⁸, and Tanner^{79,80} for prediction of base pressure. The methods have been compared to experimental data and they are known to give reasonably good base

pressure predictions. Due, however, to the limited scope of this report as it addresses the backward-facing step, no attempt will be made to improve upon or to extend the methods of Nash, McDonald, or Tanner. For incompressible flow with a turbulent boundary layer, the methods of Nash⁷⁷ and Tanner^{79,80} may be best suited to analysis and limiting values for base pressure will be given the data analysis. Several other analytical schemes, as well as the above, are given by Chang³⁴ and Tanner⁷⁹. Suggestions for their computational use are presented. Empirical formulas, such as for separated velocity profile given by Görtler³⁷, or a sinus formula⁷⁹ are typical in all analytical methods.

In a comprehensive review and analysis Kaul and Frost⁸¹ provide two methods by which backward-facing steps may be analyzed. The first of the two methods uses the two-equation approach of Bitte and Frost⁷⁵ solving numerically equations for vorticity, stream function, turbulent kinetic energy, and turbulence length scale formulated in finite differences. The second scheme employs an approximate integral technique solving the integral horizontal momentum equation with specified empirical relationships and an assumed velocity profile in the recirculation region behind the step. Before the step down, a power-law profile is assumed. At separation over the step corner the assumed error function mixing region profile is matched to a polynomial of fifth order in the recirculation region. Details for solution are clearly indicated.

To summarize, theoretical solutions show encouraging results when compared to experiment, however, easily manageable solution, integral

or differential, do not yield base pressure coefficient without considerable empirical detail. For this reason, correlation of boundary layer parameters and geometry features remain important if not necessary to the fundamental understanding of the rearward-facing step momentum transfer.

Flat-Plate Turbulent Boundary Layer Vis-a-Vis Velocity Profile

For the purpose of correlating experimental pressure measurements to boundary layer parameters it is desirable to have mean velocity profiles that scale to an easily recognizable formula. For the flat plate flow considered in this study the fully developed turbulent profiles expressible in logarithmic or power-law form provide the necessary formulas. Although as-tested velocity profiles may be used to correlate and, in fact, may be more suitable since they represent actual flow conditions, there is need to compare tested and formulated velocity profiles. Smooth flat-plate velocity formulas introduced previously in Eqs. (30), (31), and (34) are generally accepted as representative of the profile formulas for smooth surface turbulent boundary layer flow. As described by Reynolds⁵⁷, these same profiles serve other functions in methods used to predict a more general turbulent flow by means of integral, flow equation solution. The concepts necessary to development of representations of the mean velocity field may be seen in the required texts on the subject of turbulent flow by Schlichting³³, White⁴⁵, Hinze⁵², Plate⁶⁴, and Townsend⁵¹. With regard to flow over rough surfaces or surface disparities, no one text seems to thoroughly dispose of the subject

but many review and research papers cover aspects of this subject. A brief paper review may be seen in Ref. 31.

In his discussions, Clauser^{82,83} describes the universality of the equilibrium-defect profile with no pressure gradient present or, except very near the wall,

$$(U - U_e)/U_\tau = g(y/\delta) \quad (50)$$

With a pressure gradient present the history of the boundary layer is, of course, remarkably sensitive to pressure gradient. But, by maintaining a constant balance of pressure force on the boundary layer and wall shear stress, a constant history is retained in the boundary layer. Clauser⁸³ introduced the chart for experimental determination of turbulent skin friction based on logarithmic velocity distribution in the form of U/U_e vs. R_y with C_f as a parameter. Validity of this chart, for smooth walls at least, is based on Ludwig and Tillman⁸⁴ findings that even for flow in a pressure gradient a universal curve exists near a smooth wall. According to Clauser this is given by Eq. (30) with $A=2.43$ and $B=4.90$. Clauser shows also that since the boundary layer height, δ , is difficult to define, other typical length parameters may be better suited to evaluate velocity profiles. The displacement thickness

$$\delta^* = \int_0^\infty [1 - (U/U_e)] dy \quad (51)$$

and momentum thickness

$$\theta = \int_0^\infty [1 - (U/U_e)] U/U_e dy \quad (52)$$

for incompressible flow are not as well suited as the defect thickness.

given by

$$\Delta = \int_0^{\infty} (U_e - U)/U_{\tau} dy \quad (53)$$

Since $U_{\tau}/U_e \equiv \sqrt{C_f/2}$,

$$\delta^* = \sqrt{C_f/2} \Delta \quad (54)$$

and

$$\theta = \sqrt{C_f/2} (1 - G \sqrt{C_f/2}) \Delta \quad (55)$$

where the universal profile shape parameter,

$$G = \int_0^{\infty} [(U_e - U)/U_{\tau}]^2 d(y/\Delta) \quad (55)$$

So, the shape parameter $H = \delta^*/\theta$ becomes

$$H = 1/(1 - G \sqrt{C_f/2}) \quad (56)$$

Clauser found that for no pressure gradient $G = 6.8$ and $\Delta/\delta = 3.6$ independent of Reynolds number and C_f .

In his report on the effects of roughness Hama⁸⁵ reviews the flat plate boundary layer velocity profiles with particular emphasis on his experiments with a plate roughened by a wire screen. The effect of screens on mean velocity profiles and skin friction coefficient is given. The type of roughness tested by Hama may be categorized generally as a distributed roughness similar to the sand grain roughness investigated by Nikuradse and described by Schlichting^{33,86} and White⁴⁵. Categories of roughness types and modes of flow over roughness are delineated by Norton and White³¹.

For the smooth plate within the viscous zone ($0 \leq yU_\tau/\nu \leq 32.5$) Hama prescribes a velocity distribution in terms of a semi-empirical relationship containing an incomplete elliptic integral of the first kind. This is different from the relationship usually considered and given by

$$U/U_\tau = y U_\tau/\nu \quad (57)$$

Although Eq. (57) proves useful due to its simplicity, Hama's⁸⁵ relationship provides smooth blending into the logarithmic or overlap region of the boundary layer. In the overlap region for flow over a rough surface with equilibrium pressure gradient, Clauser⁸³ shows that two forms apply: the first being independent of pressure gradient and the second independent of roughness. These are

$$U/U_\tau = 2.43 \ln y U_\tau/\nu - (\Delta U_1/U_\tau) + 4.9 \quad (58)$$

and

$$(U - U_e)/U_\tau = 2.43 \ln (y/\Delta) - (\Delta U_2/U_\tau) + 0.6 \quad (59)$$

respectively. In Eq. (58), $\Delta U_1/U_\tau$, a function of $k U_\tau/\nu$, is the shift in vertical ordinate due to roughness and $\Delta U_2/U_\tau$ is the shift in vertical ordinate due to pressure gradient from the constant pressure line on the U/U_τ vs. $\ln y U_\tau/\nu$ curve. The validity of Eqs. (58) and (59) for a smooth plate with no pressure gradient is given by Hama as being for

$$yU_\tau/(\delta^*U_e) \leq 0.045 \quad (60)$$

and

$$yU_{\tau}/\nu \geq 32.5 \quad (61)$$

In the outer part of the boundary layer Hama gives the empirical formula

$$(U_e - U)/U_{\tau} = 9.6 (1 - y/\delta)^2 \quad (62)$$

valid for

$$0.15 \leq y/\delta \leq 1 \quad (63)$$

where

$$\delta = 0.30 \delta^* U_e/U_{\tau} \quad (64)$$

Equation (64) compares to the more recent formula due to Coles and given by White⁴⁵

$$\delta = 0.26 \delta^* U_e/U_{\tau} \quad (65)$$

and to the older, power-law relationship

$$\delta = \delta^* (1+n) \quad (66)$$

Based on numerous studies with flow over a flat plate having what is termed a fully rough surface, Hama concludes that the local friction coefficient, C_f , is independent of Reynolds number for constant value of δ^*/k and/or θ/k where k is the roughness height. In his experiments Hama showed universality of Eqs. (56), (59) and (62). However, because of the type of roughnesses tested, the pertinent geometrical dimension of roughness was restricted to height even though spacing of roughness elements was suggested as an important factor. Further, six other possible values for A and B for use with

Eq. (30) which lead to reliable surface resistance formulas are attributable to scatter in experimental data. Bettermann⁸⁷ experimented on rectangular bars of various spacing (spacing along the flat plate) in the flow direction. Using the form of Eq. (58) with, however, $A = 2.43$ and $B = 5.2$, Betterman gives

$$\Delta U_l / U_\tau = 2.43 \ln k U_\tau / \nu + C \quad (67)$$

where C is a constant dependent on λ , the ratio of the total surface area to the roughness surface area as seen from above. Dvorak⁸⁸ gives the following

$$C(\lambda) = 17.53(0.706 \ln \lambda - 1) \quad (68)$$

for $\lambda \leq 4.68$ and

$$C(\lambda) = -5.95(0.479 \ln \lambda - 1) \quad (69)$$

for $\lambda > 4.68$.

These correlations consider more data than originally considered by Bettermann who did not include data correlation for $\lambda > 5.6$. Dvorak briefly describes the transitionally rough regime but did not find sufficient data to clearly define this type of flow. The logarithmic polynomial fit to Hama's⁸⁵ data over the narrow range of λ as given by Dvorak may provide some knowledge of $\Delta U_l / U_\tau$ in the transitional regime, but, because of dependence on λ , accurate description requires further study.

As described by Simpson⁸⁹, Furaya et al⁹⁰, and Norton and White³², the consideration of additional types of roughness elements requires a more general interpretation of λ such that λ or λ_k is the total

surface area as seen from above divided by the roughness frontal area. Simpson further points out that the height coordinate is measured at an intermediate point between the surface and a roughness crest so as to satisfy Eq. (59) and that use of Eq. (68) or Eq. (69) is contingent on the flow between individual roughness elements being of an open cavity flow or of a closed cavity flow type, respectively. Also, as k/λ or k/δ increases, slight departure from the form of Eqs. (68) and (69) was noted. Furuya et al.⁹⁰ show results for cylinders on a flat plate that give a density effect by Eq. (68) for $\lambda_k \leq 4.68$ but by

$$C(\lambda) = -9.68(.294 \ln \lambda - 1) \quad (70)$$

for $\lambda \geq 4.68$. The reason for this difference is not explored. Additional information about the effects protuberences have on the velocity profile are given by Perry et al.⁹¹ Flow patterns in level cavities are also shown in Ref. 91.

STEP/CAVITY GEOMETRY DESCRIPTION

To systematically correlate experimental data to prediction by an analytical math model derived using geometrical, boundary layer, and separated flow parameters, it is necessary to examine, tentatively, the flow about cavities and steps as it is presently envisioned. A sketch of typical flow patterns is shown in Fig. 2 which, with geometry of Fig. 1, permits a discussion of flow over cavities and steps. Step/cavity flows will be further categorized in more detail in a following section after presenting basic terminology necessary to describe what is meant by a deep cavity, a narrow cavity, an open cavity, and a closed cavity. A deep cavity is one having $d/b \gtrsim 1.0$ and a narrow cavity has $\delta/b > 1.0$. For a wide cavity $\delta/b < 1.0$. An open cavity is deep enough so there is not attachment of the jet boundary shear zone to the cavity floor: closed cavities have reattachment. A skewed cavity is one to which the boundary layer approaches other than perpendicular to the walls ($\beta \neq 0.0$). An additional distinction of cavities is to describe a cavity as being shallow. To be shallow (or long as referred to by some researchers) a cavity has $b/d > 3.0$. Thus, transition between a deep and a shallow cavity occurs for $1.0 \lesssim b/d \lesssim 3.0$. A long cavity is defined here as one having s/b and $s/d \gtrsim 10$ although this does not imply, necessarily, two dimensional flow in the cavity. It is remarked that the above descriptions of cavity terms apply to level cavities. However, for cavities with steps, forward-facing or rearward-facing, or when cavity skew is great, the above-mentioned terms may not always be adequate. For a level cavity with $\beta \neq 0.0$ it is reasonable to apply the definitions using $b \cos \beta$ instead of b . For cavities with steps the definitions may be applied

but should be done so with reservation. An immersed step/cavity or an immersed step is defined by $h/\delta < 1.0$, although this description as it applies to rearward-facing steps, by itself, is an inadequate description. Finally, large cavities have b , d and s much greater than δ and large steps have h much greater than δ , Δ , or another suitable length scale of the approaching boundary layer.

STEP/CAVITY MODEL CATEGORY DESCRIPTIONS

Because of the scope and complex formulations necessary to develop a general numerical solution to the class of separated boundary layer flows considered - boundary layer flow over steps and cavities - it is intended to present semi-empirical or phenomenological theory. Arguments will be presented to develop a simple phenomenological model to permit correlation of step and cavity wall pressure forces from kinetic pressure on an approaching boundary layer and a step-induced separated wake. This will require prediction models using an empirical formulation for describing expansion of a separated turbulent jet wake. Additional geometry will be described at that time. To establish the time-average mean velocity profiles for kinetic pressure prediction, proposed flow models will be in agreement with experimental observations. Observations from past research in the numerous literature on step and level cavity flow fields aids in determining the general features, particularly geometry, of the configurations of steps and cavities tested. Choice of this analysis scheme is based on the success had in predictions of forces obtained in concomitant tests during the test program. The attending tests had multiple step/cavities produced by separated and alternately raised and lowered tiles on the test plate in the same test environment. The isolated step/cavity test model to be analyzed here has a range of geometries nearly the same as the tile steps and gaps when compared to boundary layer length parameter dimensions, and the test facilities were identical. Further, the range of velocities, Reynolds numbers, transport and thermodynamic properties of the airflow were the same. Some results of the tile tests have been previously described^{31,32} and predictions are

presented in Appendix A.

Based on geometries considered and the magnitude of flow parameters obtained in tests, it is possible to present schematically the classes of step/cavity flow that may be encountered. Figure 4 shows seven configurations ($\beta = 0.0$ unless stated otherwise) of the possible flow conditions as they are envisioned. These are further separated into three categories. All are characterized by an approaching smooth-surface, incompressible turbulent boundary layer shown in an undisturbed state as though no step/cavity were present. In addition, all are characterized by a step or a step and a cavity. The scales for these geometrical features are exaggerated slightly in proportion though not unduly as will be shown in sketches of the scaled geometry described later. As a precursor, however, the reported geometry matrix with mean velocity profiles is shown in Fig. 5. Other features of the idealized flow are depicted in Fig. 4 (except in one category) by a separated flow with a velocity profile after separation characterized principally by the diffusing jet wake, the extent and growth of which are indicated schematically.

Before proceeding with the development of the analytical flow models for correlating measured pressure forces, features of the configurations shown schematically in Fig. 4 will be categorically discussed.

Characteristic of all flow configurations with step and cavities in a boundary-layer flow is the appearance of single or multiple energy dissipating separation bubbles with cells. These bubbles contain one or more vortex cells and thus have reversed flow. Each rotates as an eddy core and is energized by the main stream through a shear layer zone. Eddy cells may not all contact the main stream directly through the separated shear layer. Typical of these types of cells are the small corner eddies

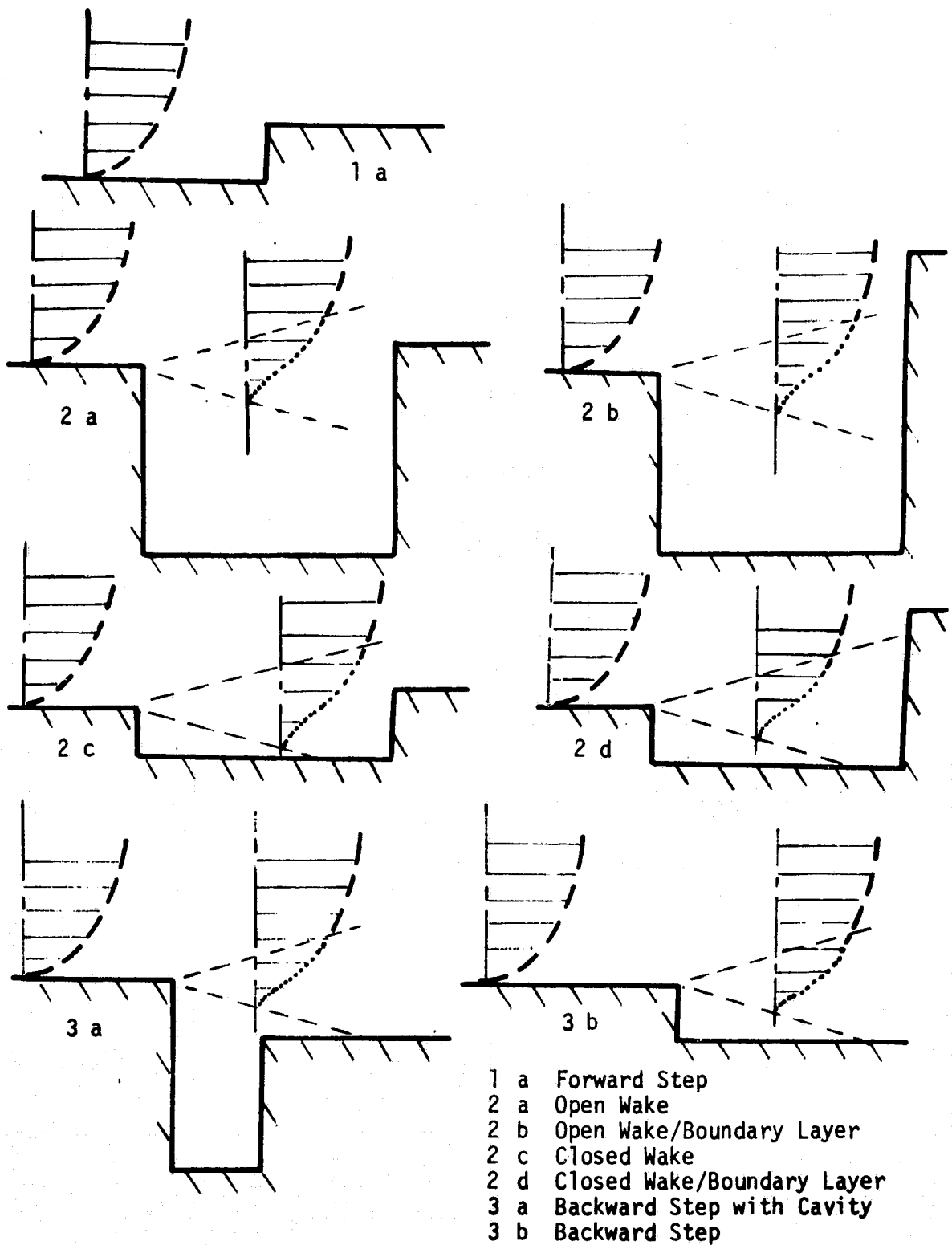


Fig.4 Step/cavity categories.

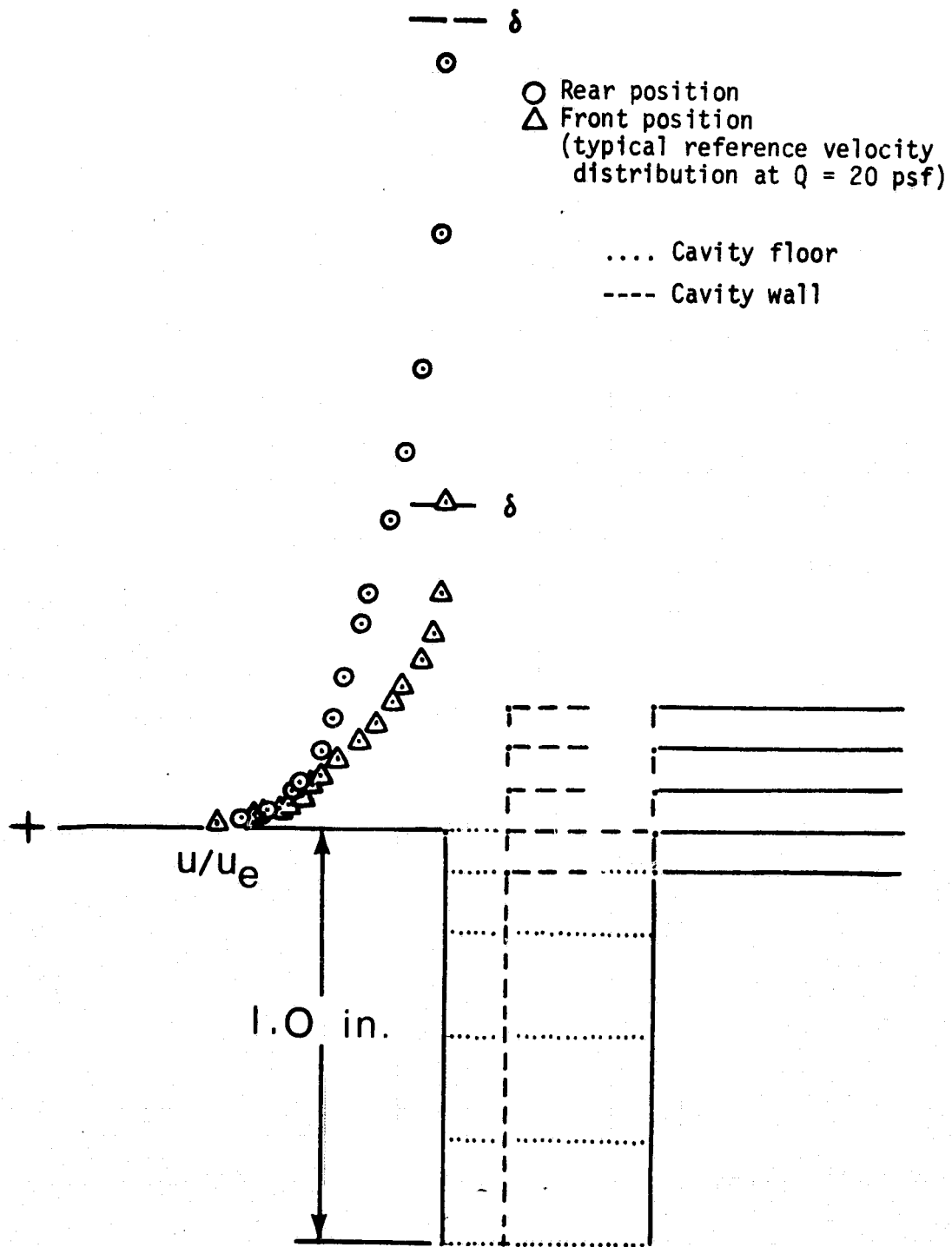


Fig.5 Test geometry matrix.

(corner rollers) which obtain energy from a larger surrounding cell(s). Multiple larger cells may also be found in deep cavities in addition to corner eddies. As with all separation phenomena, the viscosity of the fluid and an adverse pressure gradient instigate the separation. It will be assumed for discussion that the flow features are steady (unsteady flow and resonance has been observed most often with high speed flow), incompressible, and represented by temporal mean quantities of the turbulent flow.

Forward Step Flow

When fluid flows over a significant length of plate preceding the forward step (Fig. 2 and Fig. 4) and the turbulent boundary layer that forms immerses the step, a separated flow is initiated by the diminished velocity gradient at the plate surface. The separated region extends back to and up the step face. The stream confining the separation cell reattaches at a point up the step face. Flow outside the standing eddy (separation cell as it is referred to here) accelerates up and over the step until, at the step corner or edge, flow again separates to produce an extended separation bubble followed downstream by outer stream boundary layer reattachment and redevelopment. The corner separation cell exhibits reversed flow down the step face. In the cell is a near constant pressure on the wall and step. The corner cell, predominantly made up of one large vortex, has been characteristically observed to stretch forward from 0.6 to 1.2 of the step height. The extent of the cell up the step face is approximately 0.4 to 0.7 of the step height. The boundary of the corner cell is defined by solid surfaces and a detached dividing streamline which is slightly curved. This cell appears to be a cylindrical sector

with adjoining straight sides in two-dimensional flow ($s/h \gg 1$) and the lengths defining the straight sides of the cell are governed by the structure of the approaching boundary layer roughness length scale, y_0 , typically introduced through the relationship governing a velocity profile

$$U/U_\tau = (1/\kappa) \ln ((y-y_0)/y_0) \quad (71)$$

The length y_0 is proportional to ν/U_τ for the smooth wall. Plate⁶⁴ and Good and Joubert⁶³ report that the effect of the step on upstream pressure is felt approximately $15(\delta/h)^{7/4}$ before the step, but experiments presented by Taulbee and Robertson⁷³ indicate distances may be slightly greater for step heights which are greater than the boundary layer height, δ , that would exist on the plate at the position of the step without a step. On the step faces within the cell, pressure is approximately constant. For outer flow, above the stagnating separation streamline and toward the upper corner on the step, pressure imposed immediately above the attachment point may increase above the stagnation point pressure of the dividing streamline due to higher total pressure ascribed to reattaching main flow of greater velocity. This pressure gradient could be sustained by shear stress gradients in the region. Even so, pressure rapidly drops toward the upper corner due to flow acceleration from outward curvature. Increasing y_0 results in increasing the extent of the corner cell whereas the maximum vorticity in the cell tends to decrease with increasing y_0 .

Finally, at the step edge and immediately beyond, the flow must again separate with reattachment downstream. Increasing the roughness length scale results in a decreased aft separation bubble length as indicated by Bitte and Frost⁷⁵; however, for the present study, the flow beyond the step face is of no immediate concern to the present problem

discussion and model development for correlating momentum transfer to step faces by pressure forces. It is interesting, nevertheless, that the upper corner bubble length decreases from approximately five times the step height, according to Ota and Itasaka⁷¹, for incompressible flow with zero roughness length ($y_0 = 0.0$) given by a uniform, isotropic, shear-free flow onto a blunt plate. For values of $y_0 \gtrsim 0.10$ with a turbulent boundary layer, the bubble length to reattachment length step height approaches one third. This is thought to occur because increasing roughness height increases turbulence production and turbulence length scale. Quantitative evaluation of the reattachment length may be seen in the analysis of Bitte and Frost⁷⁵ and in Ota and Itasaka⁷¹ where also the length required to establish the equilibrium smooth flat plate turbulent boundary layer is discussed. This length is astoundingly greater than reattachment length, differing by an order of magnitude.

Cavity Flow

The number of different possible flow situations which may exist within flow over a cavity is known to be greater than those found for flow over a single forward-facing step. Similarities exist, however, when viewed from the point that vortical cells are established ahead of the forward-facing wall. Not only, however, does the possibility exist for large cells to form adjacent to the floor but also it is possible for cells to form one on top of another. It appears that by adding another dimension, the cavity depth, the number of possible flow situations which might be modeled for analysis increases to include at least those indicated 2a, 2b, 2c, and 2d in Fig. 4. Unfortunately, since no photographic records were found for stepped cavities that were, generally, more narrow than the boundary layer is deep, it remains somewhat of a supposition as

to the true nature of the flow for a step height (h), cavity width (d), and cavity length (s) in the general range of those addressed by the present study.

Pictorial representations of, velocity measurements within, and wall pressure measurements around level cavities^{1,2,4,28,30,34} as well as wall pressure measurements of the present study reveal that the dominant features are controlled by the step/cavity geometry as opposed to the shape and thickness of the boundary layer. For a cavity with a forward step the marked exception should be for the step cavity with $h/b \gg 1.0$ as there will be a step height beyond which the stepped/cavity differs little from the forward step. In this case, separation of the boundary layer and formation of the free shear layer occur in advance of the cavity front corner. In the matrix shown in Fig. 5 (dashed lines indicating rear corner position; dotted lines indicating cavity floor position) the narrowest cavity with a corresponding large step should be of this type.

It has been observed that below some level in a deep cavity (deep types 2a and 2b in Fig. 4) the pressures on front and rear walls are nearly the same, the small differences being due to complex vortex type flow (shown in Fig. 2) within the lower depths of the cavity. At the greater depths pressures may be slightly less than the static pressure of the oncoming subsonic flow, but generally, pressures are analogous to a too large, static, surface pressure tap as described by Roshko¹ - the pressure is slightly higher than static. There is an exception to this, however, for cavities with a rearward step (3a shown in Fig. 4) where deep cavity pressures are lower than static. For the forward step, cavity pressures in the lower part of the cavity may be significantly higher

than oncoming flow static pressure.

Higher up and near the cavity opening (types 2a and 2b) pressures on the front wall change little from pressure found in deeper parts of the cavity; however, there appears to be two possible mechanisms which are important. First, for the level cavity, the slight rearward step, and the cavity with a forward-facing step, pressures on the front cavity wall are determined and dominated by flow effects on the rear wall. Second, cavity pressures are representative of typical subsonic base pressure behind a simple step when the cavity has a rearward step front wall that extends above the rear cavity wall by significantly more than what the shear layer can spread before reattachment to the surface of the cavity. Type 3a in Fig. 4 exemplifies this situation. Thus, the front wall represents a relatively constant pressure surface differing from a simple step when the boundary layer or the free shear layer is intercepted by the cavity rear wall.

Finally, the remaining region in types 2a and 2b is the highest part of the rear wall which may be slightly below the level of the front corner, level across the cavity, or stepped above the front corner. Here the boundary layer or the free shear layer is most influenced and pressures in the region of the rear wall rise significantly and decrease again as the flow expands around the rear corner made by this wall and the following plate surface behind the cavity. For a deep cavity with a forward step, the pressure increases from the point where the shear layer dips into the cavity to reach a maximum pressure on the wall face - above this, flow accelerates or expands around the cavity rear corner. The distinction between 2a and 2b depicted in Fig. 4 is actually obscure. In 2a the shear layer wake intercepts the forward-facing wall and streamlines of the

oncoming boundary layer that has been slightly affected by the diffusion process ride up and over a shear zone. Type 2b shows that the shear layer wake and the overriding boundary layer flow are affected to a greater degree by virtue of a greater step height or narrower cavity width. It is anticipated that the recompression vortex and buffer zone between the shear layer wake and the flow within the cavity are more highly energized given a cavity width for type 2b than for type 2a.

In high speed flow, a distinction between open and closed cavities is more easily identifiable when compared to the opening and closing in low speed flow with a thick turbulent boundary layer. Charwat et al²⁸ were able to distinguish the cavity width defining the two different stable states of stepped cavity flow by photographs. Although an unstable intermediate type of flow was revealed, a critical width was found. This critical width is the width at which the flow separating from the cavity front corner just reattaches to the cavity floor. Following reattachment, separation immediately occurs and a recompression wake forms to impinge on and flow over the forward-facing back wall of the cavity. The separation cells behind the backward-facing wall and before the forward-facing wall are essentially isolated one from another. For widths greater than the critical, an attached boundary layer reforms on the cavity floor. The representations 2c and 2d in Fig. 4 are for the flow conditions where reattachment occurs on the cavity floor. Some detail, both experimental and theoretical, has been previously described in review of cavity flow literature. As may be seen in the matrix shown in Fig. 5, the wide level cavity configuration ($b = 0.5$ inch) is probably a bit too wide to be like 2c of Fig. 4. Furthermore, the wide cavity with a forward-facing step ($h \geq 0.1$ inch) probably does not have a floor-attached separation shear

layer.

Rearward Step Flow

Flow over a backward-facing step is characterized by several features which distinguish it from but relate it to similar types of separation such as near the trailing edge of an airfoil. Shear and turbulence influences of the flow over the preceeding surface is responsible for the wide range of distances found to the point of reattachment aft of the step. The up-stream history of a turbulent boundary layer appears to have more influence on the position of reattachment and behavior of flow on a rearward-facing step than on a forward-facing step.

Before the step, streamlines are directed nearly parallel to the surface: the same may be said for reattachment aft of the downstep on the lower surface behind. Unlike flow over an airfoil, the point of separation is fixed by the geometry. Flow separates from the upper corner of the step. The dividing streamline from the upper corner separates an entrapped separation bubble having one predominant vortex cell for the two-dimensional, turbulent, steady flow considered. Between the step face and the surface behind a small corner eddy appears. A free shear layer thickened by turbulence appears and develops at separation. Further, spreading occurs on either side of the dividing stream line. In the shear layer wake the fluctuating component of velocity is high. At reattachment of the dividing streamline, that part of the mass flow entrained has completely been returned to the recirculating cell; however, the position aft of the step face where replenishing begins is unknown. Within the shear layer the turbulence intensity and shear stress are insensitive to initial boundary layer height before the step. Immediately below the step corner and over the step face the pressure (base pressure)

which is responsible for nearly all the drag exerted on the step, is practically constant. This static pressure exists along the lower corner and back approximately three to four step heights as well as over much of the recirculation zone cell. As reattachment is approached the pressure increases (it is above ambient at reattachment) and continues to increase beyond free-stream static reaching a maximum difference at approximately a step height behind the reattachment point. This overshoot is accounted for by the concave curvature of streamlines during the reattachment and equilibrium boundary layer reformation. Attainment of ambient pressure occurs before the boundary layer is again in an equilibrium state following the form given by Eq. (34).

Other particularities have been discussed previously (Refs. 28, 77, 80, and 81); however, with regard to the present study, the data of Tani et al²⁶ and data presented by Chang³⁴ and by Kaul and Frost⁸¹ form a basis to which results for the present experiments may be compared. Representations 3a and 3b of Fig. 4 indicate schematically the type of base flow involved. In Fig. 4 the type of flow depicted by 3a is little affected by the presence of the cavity. Using the matrix shown in Fig. 5 it is seen that unless the cavity width is such that the separated shear layer spreads into the cavity before the forward-facing cavity wall, reattachment is expected to occur aft of the cavity. Because of the reattachment point position, the cavity should cause only slight modifications to the separation cell. This proves to be the case as will be shown in a later section. Because of the limited rearward-facing step and step/cavity configurations tested (see Fig. 5) it may aptly be said that the momentum transfer to these configurations is indicative of flow given by something between a weak perturbation ($h/\delta \ll 1.0$) and a strong

perturbation ($h/\delta = O(1.0)$). It is certain that an overwhelming perturbation ($h/\delta \gg 1.0$) as defined in Kaul and Frost⁸¹ does not occur.

ANALYTICAL DEVELOPMENT

There has been notable success in correlating drag of bluff bodies immersed in a turbulent boundary layer. Characteristically, correlation flow parameters are those at the site of the obstruction if the obstruction (generally, on a smooth plate) were to be removed. The boundary layer (its parameters and properties) on the unobstructed replacement surface is referred to as the reference boundary layer. Hoerner,²⁷ using a collection of data, Plate,⁹² using Wieghardt²⁴ data, and Good and Joubert⁶³ have shown that bluff protuberances, backward-facing steps, and sharp-edged plates correlated total or pressure drag to the boundary layer parameters successfully.

Hoerner employs a $n = 6$ (power-law) reference boundary layer with constant δ/x to determine the mean kinetic pressure over protuberance height (see Appendix A). The mean pressure is then divided by the free-stream kinetic pressure and multiplied by an independent drag coefficient to obtain a drag coefficient for the immersed body. Hoerner's analysis gives

$$C_D \sim (h/\delta)^{2/6} \quad (72)$$

Plate's analysis for bluff-plate form drag obtains the correlation for drag coefficient based on free-stream velocity and plate height with the correlation parameter h/δ . Plate's analysis gives $C_D \sim (h/\delta)^{2/7}$; however, bluff plate drag dependence on U_τ/U_e is evident when Good and Joubert use Plate's scheme on their experimental data. To improve Plate's scheme, Good and Joubert correlate C_{D_τ} ($= 2C_{D,p}/C_f$) for sharp-edged plates normal to the stream via the inner-law parameter hU_τ/ν : C_f and U_τ were determined from a reference profile found in their study to be of

the general logarithmic type.

The analysis of Good and Joubert is like that found in the parametric charts of RAS ESDU 73028⁶⁵. In Ref. 65 correlation is given by

$$C_D/C_f = \phi - \psi \quad (73)$$

where C_D includes inseparable form and friction drag effects due to steps or ridges. The values of ϕ and ψ are determined by

$$\phi = C_1 \log(R_h (1.0 + 0.178 M_e^2)^{-1.3}) - C_2 \quad (74)$$

and

$$\psi = -C_1/2 \log(C_f/2) \quad (75)$$

ESDU correlation in the form of parametric charts are based on extracting ϕ and ψ from experiment; however, there is considerable extrapolation in the charts. Chart construction is based on the premise that

$$C_D/C_f = C_1 \log(hU_\tau/\nu) - C_2 \quad (76)$$

The ESDU correlations in Ref. 65 are further described by Gaudet and Winter²⁹ and unlike tests on the bluff plates used by Good and Joubert (δ/h from ~ 0.05 to ~ 2.3), the protuberance heights for ESDU correlations were approximately 0.03δ . Force-balance data were used and some friction drag change from the reference condition was unavoidable. Cavity drag correlations were for narrow span, shallow, rectangular holes and not strictly representative of cavities considered in the present study. A summary of correlation constants at $M_e \approx 0.2$ is given in Table 1.

TABLE 1 ESDU correlation coefficients

Forward Step:	$C_1 = 60$	$C_2 = -80$
Rearward Step:	$C_1 = 16$	$C_2 = -6$
Rectangular Hole: ($h \leftarrow b$)	$C_1 = 2$	$C_2 = -2$

The Hoerner,²⁷ Plate,⁹² Good and Joubert,⁶³ and ESDU⁶⁵ correlations agree well for steps in the lower half of the boundary layer. However, inconsistencies exist in the data correlations because no delineation is always made of whether total drag or form drag appears. The result is that drag data, total and form, are often shown together and used to establish correlation to an ill-defined drag coefficient. Although restricted to bluff bodies or protuberances immersed in the boundary layer, the success obtained in correlating protuberance drag with length and flow parameters suggests that some of the same parameters and other parameters may be used to develop correlations of step/cavity or cavity form drag.

Correlation of form drag on a step/cavity or cavity has not been concisely put on the basis of knowledge of the characteristics of a general immersing boundary layer. As in the case of simple steps with no cavity, particularly the backward-facing step, analytical solutions for form drag independent of experimentally determined separated flow or shear layer detachment lengths and pressure or velocity measurements are not possible at present; therefore, empiricism is necessary to predict momentum transfer.

Because flow separates at the forward corner of most cavities, more than just the reference boundary layer is required to define form drag

of step/cavity or level cavity roughness elements. The elements characterizing the free-jet boundary also need to be included. Thus, instead of using the step height, h , a new height h_{eff} , based on step height and the extent of the spread of the separated boundary jet can be employed. The form drag may then be correlated with mean kinetic pressure over the effective height, h_{eff} . This concept assumes that a separated jet boundary expands into a region of constant density and static pressure. Imparted to the hypothetical surface (a forward-facing surface of height h_{eff}) is momentum referred to as mean kinetic pressure. It is given by the temporal mean velocity squared as averaged in the integral sense over h_{eff} . Based on experimental evidence of the extent of separation ahead of a simple forward-facing step or on the reattachment length behind a rearward-facing step (this being approximately seven times the step height for the latter), exceptions are expected in the applicability of using such a model. The mean kinetic pressure concept of Hoerner is an extension of the method which adapts a momentum equation in integral average form to shear layer profiles at a boundary layer represented by a power-law profile. The formulation to be developed herein will attempt to correlate the kinetic pressure using knowledge of boundary layer profiles and separated jet expansion processes. Limitations to the use of this correlation model will be described following development of the model.

To define the kinetic pressure at the forward-facing step/cavity wall in the manner similar to that for the forward-facing step, it is necessary to define the form of a semi-free jet wake. This requires a model for jet shape prediction based on satisfying the boundary conditions. The model will include empirical constants from observations of jet wake structure. The most promising model and constants were deduced from the

works of Haugen and Dhanak³⁰ and of McGregor¹⁰ where theoretical analyses of level cavities exhibited reasonable agreement with measured drag. The experimental results of Haugen and Dhanak (used also by McGregor) were, however, for values of $\delta/b < 0.6$, and step/cavity experimental data in incompressible flow for open cavities is apparently nonexistent except for the data obtained in this test program.

Separated Jet Kinetic Pressure Formulas

Turbulent jet boundary velocity profiles for a uniform flow prior to separation was first investigated by Tollmien³⁶ using Prandtl mixing length concepts. Later Görtler (see Ref. 37) studied free jet expansion using Prandtl's constant eddy viscosity model. Although both theories agree well with experiments conducted by Liepmann and Laufer,⁴⁷ mathematical complexities with Tollmien's or Görtler's formulations occur when a boundary layer shear profile as opposed to a uniform stream precedes a cavity front corner. The results of Haugen and Dhanak rely on experimental measurements and do not appear to give valid velocity profiles at the downstream forward-facing step. A polynomial form for velocity will be developed to satisfy boundary conditions and limit empirical constants to a minimum. The use of a cubic obtained conservation of axial momentum locally to within the accuracy of velocity squared measurements. This conservation required proper choice of separated jet wake parameters. The free jet parameters are those determined experimentally for cavity flow and they reflect the nature of a cavity velocity distribution by including parameters pertinent to cavities with the sole exception of cavity depth. Correlations of kinetic pressure force to measured pressure force permit the depth influence to be included.

The velocity distribution over the cavity for the jet wake appearing with forward step separation is approximated by the cubic form

$$U/U_r = a + b\xi + c\xi^2 + d\xi^3 \quad (77)$$

where

$$\xi = \sigma y/x_c \quad (78)$$

and σ , an empirical similarity spreading parameter used first by Görtler in incompressible flow of a free jet boundary, has been found to be approximately 12.0 for free expansion of a jet. This parameter σ is inversely proportional to the constant, a , used by Tollmien and by Haugen and Dhanak where their similarity coordinate is defined by

$$\eta = y/ax_c \quad (79)$$

An often used empirical constant characterizing the structure of a free jet is $a = 0.09$ (Abramovich³⁷); however, Haugen and Dhanak³⁰ and McGregor¹⁰ get better agreement between theory and experiment when the value $a = 0.11$ is used. From Tollmien's analysis the outer limit of the jet boundary zone (where $U = U_e$) is finite and given by

$$y = 0.0882x_c \quad (80)$$

So, to provide an upper bound on the jet, Tollmien's jet spread zone boundary is modified slightly to account for finite cavity depth and a forward-facing wall which confine the jet wake. Multiplying the constant 0.0882 by the spreading constant ratio 0.11/0.09 obtains

$$y = 0.108x_c \quad (81)$$

as the limit defining the outer edges of the jet spread. For computation

of kinetic pressure at $\beta = 0$, the gap width, b , replaces x_c .

Abramovich³⁷ presents two original but different solutions for the free-jet wake problem of a turbulent flow. The two are those as given by Tollmien who used Prandtl mixing length concept ($\ell = a^{3/2} x_c / \sqrt{2}$) and as given by Görtler who used virtual or apparent kinematic viscosity analysis of Prandtl's second hypothesis. The two give a different form of the shear stress. Namely

$$\tau_{xy} = \rho a^{3/2} x_c^2 \left| \frac{\partial U}{\partial y} \right| \left| \frac{\partial U}{\partial y} \right| \quad (82)$$

according to Tollmien and

$$\tau_{xy} = \rho x_c U_r \frac{\partial U}{\partial y} / (4\sigma^2) \quad (83)$$

according to Görtler. From Görtler's analyses ($\sigma = 13.47$) the outer edge corresponds to $\xi = 1.3$ at $U/U_r = 0.998$ (Görtler's solution must be adjusted to fit experimental data and is not immediately applicable for this reason).

Boundary conditions are specified by magnitude matching and gradient matching the jet wake and the boundary layer into which the jet diffuses with the assumption that the boundary layer is unaffected by the separated flow except at and below the upper edge of the jet wake. In addition, $U/U_r \approx 0$ at the lower edge of the jet wake and based on Haugen and Dhanak data $U/U_r \approx 0.48$ to 0.54 at $\eta = 0.0$. The value of U_r is determined by the undisturbed boundary layer profile where $y/x_c = y/b = 0.108$.

Several jet wake velocity profiles may be considered beside the cubic form chosen. Haugen and Dhanak's formula

$$U/U_r = U_e/U_r (k_1 e^{-\eta} + k_2 e^{\eta/2} \cos(\frac{\sqrt{3}}{2} \eta) + k_3 e^{\eta/2} \sin(\frac{\sqrt{3}}{2} \eta)) \quad (84)$$

did not match the experimental reference boundary layers well. They³⁰ determined the three constants k_1, k_2, k_3 by matching velocity and velocity gradient to a one-seventh power-law boundary layer profile and by requiring $\partial^2(U/U_r)/\partial n^2 = 0$ at $n = 0.0$ (corresponding to a maximum shear stress at $y = 0.0$). Also Haugen and Dhanak give an additional solution to represent the vortex in the cavity in the vicinity of the jet. Their solution is incomplete and incapable of predicting pressure at the cavity walls.

Görtler's shear stress is modified by using U_r instead of U_e when the outer edge of the jet mixing zone is within the boundary layer. Görtler's solution is given by

$$U/U_r = 1/2(1 + \operatorname{erf} \xi) \quad (85)$$

This, however, leads to a discontinuity in $\partial U/\partial y$ at the outer edge of the jet mixing zone. Other forms such as the sinus form

$$U/U_r = 1/2[1 + \sin\{\pi(y + .108x_c)/(2 \times .108x_c) - \pi/2\}] \quad (86)$$

agree very well with Görtler's solution when $\sigma = 14.5$, suggested by Plate, is used in Görtler's solution. This form is like Cole's wake function of the outer layer in equilibrium boundary layer analysis. Hyperbolic tangent and exponential forms were tried based on analyses of other types of free jet flow but are not advantageous or mathematically suitable by being transcendental or giving a poor gradient fit to the boundary layer/jet interface. Therefore, the cubic form was adopted because of its simplicity and because the boundary conditions associated with determining the constants approximate experimental observations.

In the boundary layer that adjoins the jet it is assumed that

$$U/U_e = A' \ln y + B' \quad (87)$$

At the forward-facing wall of the step/cavity the reference velocity at the jet/boundary layer interface occurs for $x_c = b$ (when $\beta = 0$) and $y = 0.108 b$ or

$$U_r/U_e = A' \ln 0.108 b + B' \quad (88)$$

Further, in the boundary layer above the cavity

$$\left. \frac{\partial(U/U_e)}{\partial y} \right|_{y=0.108 b} = A'/0.108 b \quad (89)$$

With this information it is possible to determine the four constants in the jet wake profile: a' , b' , c' , and d' . At $\eta = 0$, U/U_r in the jet wake is 0.48 to 0.54. The correct value must be determined iteratively to conserve mean-velocity based momentum between that at $x_c = b$ and that at $x_c = 0$; therefore, $a' = \text{constant}$. At the lower extreme of the jet wake $\eta = (1/a)(-0.108)$ and $U/U_r = 0.0$. Using the boundary layer velocity at the jet-wake upper extreme gives the second condition for determining b' , c' , and d' . Finally, matching slopes at the jet-wake/boundary-layer interface obtains the third required condition. When combined, the three conditions may be solved simultaneously to yield b' , c' , and d' .

Appropriate values of A' and B' may be found by experimental measurements as was accomplished in the present study using linear least square curve fitting in the independent parameter $\ln y$ throughout the log-law portion of the undisturbed, reference, mean-velocity profile. Also, the values of A' and B' are related to the constants A and B of the inner boundary-layer relationship

$$U/U_\tau = A \ln yU_\tau/\nu + B \quad (30)$$

by

$$A' = A \sqrt{C_f/2} \quad (90)$$

and

$$B' = \sqrt{C_f/2} (A \ln U_\tau/\nu + B) \quad (91)$$

where yU_τ/ν is nondimensional. Establishing values of A' and B' when it is known the velocity profile (referenced to shear velocity) is an equilibrium profile permits evaluations without experimental velocities.

The shear velocity, U_τ , can be related to friction coefficient of the undisturbed, reference flow by using boundary layer edge velocity, U_e , from specified or potential flow solution. The inner viscous shear layer is not included, having been assumed extremely thin compared to other significant geometry lengths, and has not been considered in any literature reviewed concerning turbulent jet boundaries. It is thought the viscous sublayer rapidly vanishes because of the adverse pressure gradient at separation on the upstream cavity corner.

Application may now be made of the mean dynamic pressure or kinetic pressure concept. This takes the form

$$q_{eff} = [1/2 \rho U_{e,eff}^2]^{-1} \int 1/2 \rho U^2 dy \quad (92)$$

where for $\beta = 0$

$$h_{eff} = h + 0.108 b \quad (93)$$

and the integral limits are from $-0.108 b$ to h .

Because b is defined as the perpendicular distance across the cavity, a different form must be used for $\beta \neq 0$. This requires that the distance

across the cavity be replaced by $b/\cos \beta$, the kinetic pressure force be resolved to the drag direction, and U_r/U_e be determined at the greater length $b/\cos \beta$. This procedure is based on two-dimensional flow with no turning for step/cavities at a skew to the oncoming flow. This gives for the kinetic pressure equation

$$q_{\text{eff}} = \frac{\cos \beta}{h + \frac{0.108 b}{\cos \beta}} \int_{\frac{-0.108 b}{\cos \beta}}^h \left(\frac{U \cos \beta}{U_e} \right)^2 dy \quad (94)$$

or

$$q_{\text{eff}} = \frac{\cos^4 \beta}{h \cos \beta + 0.108 b} \int_{\frac{-0.108 b}{\cos \beta}}^h \left(\frac{U}{U_e} \right)^2 dy \quad (95)$$

Limitations and restrictions on the foregoing formulation occur for several reasons. If the lower jet boundary impinges on the surface beyond the forward-facing step corner the analysis is void as it is for the simple backward-facing step. If the jet reaches to the cavity floor (impinges on the floor surface) and a closed cavity is formed, the model is expected to be invalid. In this case, the superposition of base pressure and kinetic pressure on the forward-facing wall may be used. Backward-facing step pressure in these situations are to be described by other means or formulations.

In general, reattachment of an incompressible boundary-layer flow over the backward-facing step occurs at approximately 7.0 step heights down stream of the step face. By this analysis, jet impingement occurs at 9.28 step heights. In Tollmien's analysis the turbulent jet spreads above into a constant velocity turbulent flow and below into quiescent

fluid. There are no transverse boundaries after the uniform flow separates from the forward-plane/step-face corner. The jet intercepts or impinges on a hypothetical plane parallel and h below the forward plane at $5.44h$ from the step face. Without restrictions downstream this is approximately the forward limit of turbulent jet reattachment even though reattachment is more complicated due to entrainment and replacement of mass to the reversed flow vortex cell.

A final limitation may be imposed because separated flow appears before a forward-facing step. This separation cell extends forward. Thus, for step/cavities where the step is forward-facing and $h \cos \beta / b \gtrsim 1.70$, useful or accurate correlation of measured pressure and kinetic pressure may be questionable.

In summary, it is remarked that by exactly obtaining conservation of axial momentum based on the mean-velocity squared then

$$\int_{\frac{-0.108 b}{\cos \beta}}^h (U/U_e)^2 dy = \int_0^h (U/U_e)^2 dy \quad (96)$$

when $h \gtrsim 0.108 b / \cos \beta$. Recall that integrations are performed at $x_c = b / \cos \beta$. Further, separated jet-wake velocity profiles are not expected to be similar profiles precisely in the variable proportional to y/x_c because the forward edge at the cavity step is preceded by a shear or boundary layer velocity profile. Nor is precise similarity in y/x_c expected because there is a finite depth and forward-facing wall which must influence the jet spreading after the edge. Thus, the analysis may not be likened to that of Tollmien or Görtler exactly but doing so provides a tractable parameter by which correlation of experimental data

is possible without extensive analytical solutions.

Finally, a kinetic pressure analysis of the type proposed is thought to be restricted, from the point of acceptable geometry, by consideration of the range of step height to cavity width ratio allowed. Namely,

$$[\bar{x}_r \cos \beta]^{-1} \gtrsim h/b \gtrsim 0.108/\cos \beta \quad (97)$$

where \bar{x}_r is between 0.6 and 1.2 and describes the extent ahead of a step whereupon a separated flow may be expected. Several configurations tested did not meet the above criteria but it is not surprising that step/cavities not meeting the aforementioned criteria lend themselves to correlation because of the momentum balance and applicability to forward steps without cavities. Also, cavity depth to width ratio is restricted by

$$d/b \gtrsim 0.108/\cos \beta \quad (98)$$

so as to have an open cavity type of flow. For a shallow or wide cavity the separated jet wake may reattach to the cavity floor. The closed cavity may be analyzed for drag by considering the cavity as rearward- and forward-facing steps; however, by the present scheme, it would be necessary to have velocity profile measurements within the cavity. These were not obtained nor, incidentally, was a closed cavity tested; therefore, the formulation for a velocity profile for kinetic pressure prediction necessitates consideration of an appropriate separated jet wake (jet boundary) and the kinetic pressure of the adjoining and associated boundary layer above the jet.

Pressure Data Formulas

Pressure- or form-drag coefficient on step/cavity walls has been

predicted from experimental pressure measurements at the walls by numerically integrating with quadrature formulas the net pressure coefficient component acting in the axial or drag coordinate direction. For open cavities at $\beta = 0$ pressure forces are dominant and at smaller values of β , where three-dimensional flow can be significant, pressure forces are indicative of drag when pressures at the cavity side walls are included and pressure forces are resolved into the drag coordinate direction. When β is large, closed cavities may more appropriately be referred to as shallow slots. Slots will not be analyzed and allowing $\beta = 45^\circ$ probably approaches the limit where it becomes necessary to account for floor as well as wall shear forces in drag coefficient determination. For $\beta \approx 0$ the drag may be represented by the pressure or form drag and for a two-dimensional step/cavity (step height h and cavity depth d) a pressure drag coefficient per unit span may be described by

$$C'_{D,p} = \cos \beta / (h+d) \int_{-d}^h (C_{p,F} - C_{p,R}) dy \quad (99)$$

Being two-dimensional, cavity side walls are excluded and these pressure terms do not appear in the preceding formula. Quantities $C_{p,F}$ and $C_{p,R}$ result from pressures on the forward- and rearward-facing walls, respectively. For no cavity and a forward-facing step, the wall is merely the step face and $C_{p,R} = 0.0$. For no cavity where there is a rearward-facing step $C_{p,F} = 0.0$. The quantity $\cos \beta$ resolves pressure forces in the drag direction where only $\alpha = 0$ is considered.

There is some doubt as to whether $C'_{D,p}$ truly reveals the nature of stepped cavities because of the geometry variations and flow characteristics involved. Because of this doubt, it is necessary to modify the

C-2

pressure drag coefficient formula to represent the different geometries. In all geometry arrangements $y = 0$ corresponds to the coordinate upward and perpendicular from the test bed surface preceding the step/cavity. This allows the following definitions of pressure drag coefficient consistent with convention and present definitions of geometric parameters:

a) Forward-facing step (no cavity):

$$C_{D,p} = \cos \beta / h \left(\int_0^h C_{p,F} dy \right) \quad (100)$$

b) Rearward-facing step (no cavity, h negative):

$$C_{D,p} = \cos \beta / h \left(\int_0^h C_{p,R} dy \right) \quad (101)$$

c) Level cavity (no step)

$$C_{D,p} = \cos \beta / b \left(\int_{-d}^0 (C_{p,F} - C_{p,R}) dy \right) \quad (102)$$

d) Forward-facing step (with cavity)

$$C_{D,p} = \cos \beta / b \left(\int_{-d}^h C_{p,F} dy - \int_{-d}^0 C_{p,R} dy \right) \quad (103)$$

e) Rearward-facing step (with cavity)

$$C_{D,p} = \cos \beta / b \left(\int_{-d}^h C_{p,F} dy - \int_{-d}^0 C_{p,R} dy \right) \quad (104)$$

Because numerical quadrature formulas were used to compute integrals in the five preceding formulas and because step/cavity pressure orifices were evenly spaced ($\Delta y = 0.05$ inches) it is possible to represent drag

coefficients in consistent and convenient form. This is done by summing all pressure coefficients with the appropriate quadrature weighting coefficient and designating dy by Δy . Doing so gives

$$C_{D,p} \approx C(h, \beta, b) \sum C_{p,i} W_i \Delta y \quad (105)$$

or

$$C_{D,p}/C(h, \beta, b) \approx \sum C_{p,i} W_i \Delta y \equiv \int C_p dy \quad (106)$$

or, defining a momentum transfer "force" coefficient,

$$\sum C_{p,i} W_i \equiv \int C_p \quad (107)$$

Open-ended fourth-order quadrature over $2\Delta y$ was used to start integration when three or more pressure orifices at a wall were exposed or open to the flow environs. Two orifices were the minimum required for integration with tested geometries permitting only trapezoidal approximation over $2\Delta y$ (so too the last Δy in three exposed orifice configurations). With multiple orifices exposed (four or more), fifth order close ended quadrature was used to continue integrations over $2\Delta y$ increments. Therefore, the quantities $\int C_p$ are generally fourth-order with extrapolation only from the step/cavity upper corner to the first pressure orifice down the step or cavity wall. The quantity $\int C_p$ of Eq. (107) represents the nondimensional force normal to and accumulated over both cavity walls. A positive value indicates rearward directed force but normal to step/cavity walls and not in the drag coordinate direction except when $\beta = 0$. Configurations satisfying criteria given previously permit correlation using parametric formulas. That is, it should be possible to correlate the following quantities:

$$\cos^2 \beta / 0.108 \Delta y \int_{\cos \beta}^h (U/U_e)^2 dy \quad (108)$$

and

$$1/\Delta y \int C_p dy \equiv \int C_p \quad (109)$$

where Δy is chosen for convenience and has been selected on the basis of pressure orifice spacing. In general Δy may be any convenient length characteristic of configuration geometry and serving as a consistent reference area per unit span across the flow.

EXPERIMENTAL APPARATUS AND PROCEDURE

To simulate conditions that exist on most water and flight vehicles, particularly surfaces of large airborne craft at subsonic speeds, this experiment was designed to obtain large Reynolds numbers in the Texas A&M 7 x 10 foot low-speed wind tunnel. The 10 foot wide test bed plate model was mounted with side wall seals between the tunnel walls and secured to the pivot-pitch mechanism behind and slightly below the trailing edge by quarter inch plates referred to as a splitter plate. Entry through the tunnel roof required the 11 foot long plate be made in two halves bound together at the splitter plate by machine screws. Since the splitter plate extended above and below the test plate surface, the splitter plate served as a barrier down the center of the plate either side of which different test surface materials could be laid with minimal interference and yet tested at identical tunnel conditions. The test bed plate model was nominally 6 inches thick, the frame of which consisted of welded aluminum alloy beam members in the shape of a box structure. Plates extending down from sides of the frame were drilled to accept pins through the pitch mechanism pivot axis. Two tunnel floor mounted frames extended upward to provide support for pivot pins. These three-piece frames are seen lighted at the lower left- and right-hand sides of Fig. 6. The protruding splitter plate with securing screws is shown in Fig. 7 while a rear-side view of the test bed plate giving further detail of the pivot frame and splitter plate is shown in Fig. 8. With the test bed plate horizontal, the upper, level surface was 35.0 inches from the tunnel ceiling.

Overall length of the test bed plate was 132.0 inches. The leading

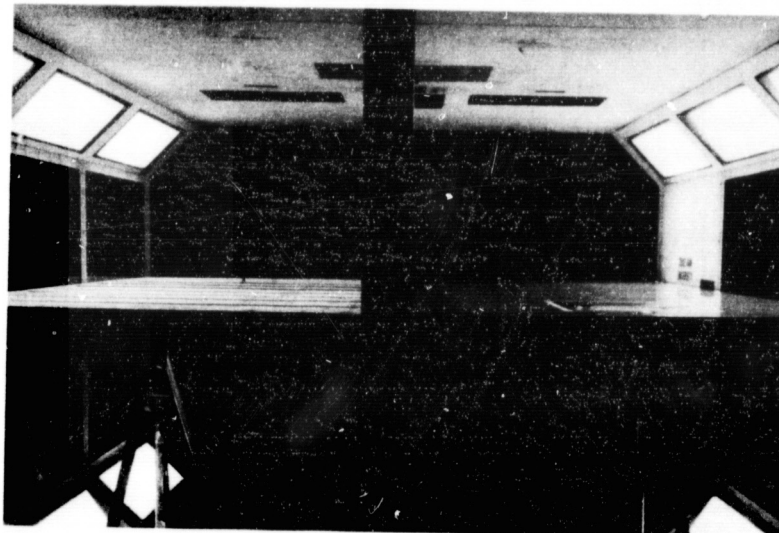


Fig. 6 Rear view of test plate with stepped multiple tiles (right) and step/cavity model (left) in place.

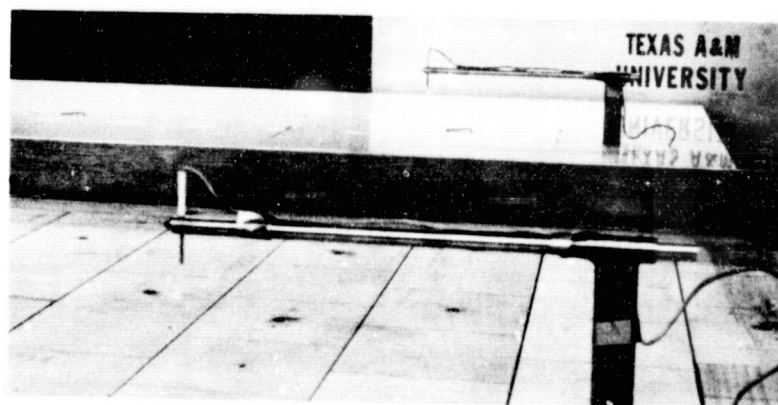


Fig. 7 Anemometer hot film probes installed on traversing mechanisms at rear of test plate (splitter plate seen).

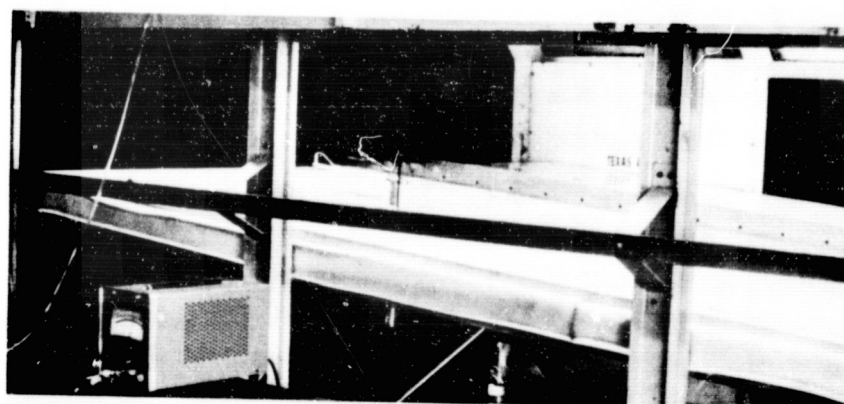


Fig. 8 View of test plate through tunnel walls.

edge section extended 12.0 inches back and was drooped. A 3.0 inch diameter aluminum tube provided the leading edge with only slight curvature in the lower surface skin tangent to the tube and the lower surface of the plywood covering the box frame underside. A cambered smooth sheet of aluminum rolled to be tangent to the leading edge tube attached 12.75 inches back from the leading edge to the upper flat surface. The splitter plate projected outward from the leading edge section all around and continued projected back beyond the blunt trailing edge below to the pitch mechanism connection plate. A 2mm boundary layer transition wire 20° up and around the leading edge radius assured turbulent flow over the test bed plate. The trip wire spanned the entire length of the leading edge.

On the starboard side of the splitter plate was a smooth flat surface covered with Formica over plywood. Starting 21.5 inches to the right of the splitter plate on this smooth side were two 20 inch square removable sections. The forward edge of the front removable section was 22.75 inches behind the leading edge while the forward edge of the rear removable section was 100.0 inches behind the leading edge. The outline of the rear removable section is seen on the far side of Fig. 7. The step/cavity model, to be described later is seen in place in the rear position in Fig. 6. Small additional openings 4.0 inches behind each removable section were provided for an anemometer hot film probe traversing mechanism arm.

Before describing the port side of the test bed plate model, the step/cavity model referred to previously and its instrumentation will be described since it relates to experiments conducted on the starboard or smooth side of the test bed plate model.

Cavity Model and Cavity Apparatus

The cavity model consisted of a 20 inch square aluminum block to replace either the front or the rear removable sections in the Formica test bed. Adjustment bolts on the bottom four corners permitted leveling of the block in the Formica test bed. These long bolts are visible in Fig. 9. Within the block was an 18 inch diameter disk which was locked in place during testing but could be rotated through 360 degrees. On this disk were mounted several devices necessary to the establishment of a variable width, variable depth cavity one side of which could be stepped. The devices are shown in profile on Fig. 9, and from below in Fig. 10. Cavity gap width and step height were set by manual adjustment whereas the cavity depth could be controlled with the wind tunnel in operation. As seen in Fig. 10, a wide thin bar (depth bar) with threaded ends was retained by sprocketed bolts. A chain around these sprockets also passed over a sprocketed electric motor (upper center of Fig. 10). Chain tension and bar position were determined by a potentiometer, also sprocketed, and shown in the upper right of Fig. 10. Safety/stop switches to prevent overrun are seen below and to the left of the bar in Fig. 10. Two-piece, various-width plates of solid nylon (0.0625, 0.15, 0.25, and 0.50 inches) each 12.0 inches in span could be attached to the depth bar. By operating the motor, the cavity depth (to within 0.005 inch) could be changed. The upper surface of the nylon plates also serve as the level floor of the cavity as well as the cavity width spacer. The 12.0 inch span cavity, as seen from above the test bed plate, is shown in Fig. 11. In Fig. 11, the disk is rotated 45° to the flow direction: a nylon plate may not be seen within the cavity in Fig. 11. Visible in Fig. 11,

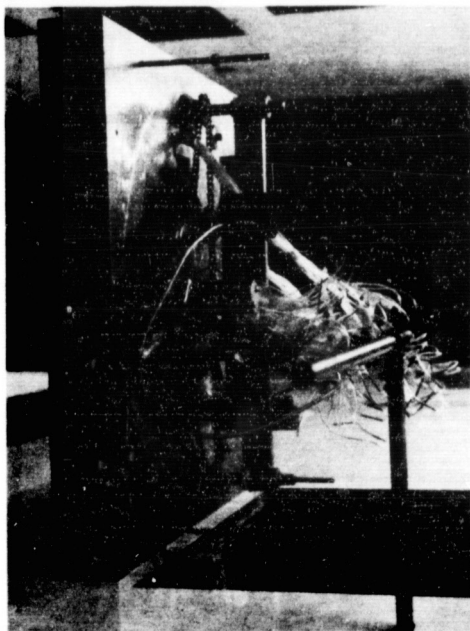


Fig. 9 Step/cavity model on side from rear removed from test bed.

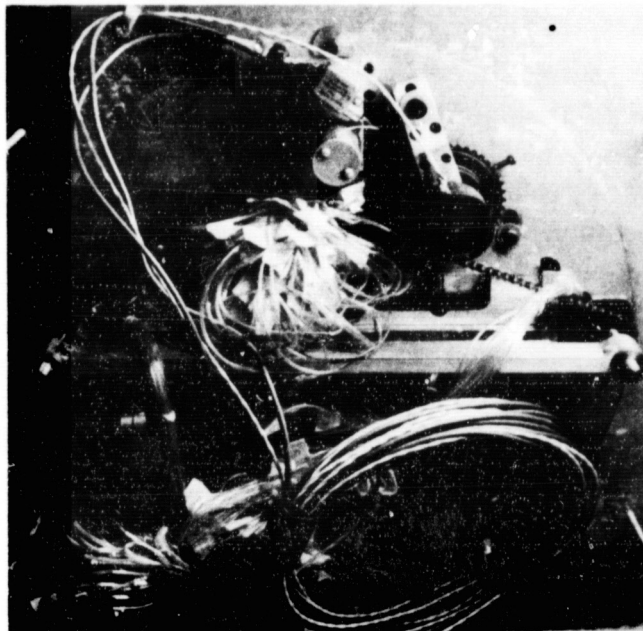


Fig. 10 Model mechanisms as seen from below.

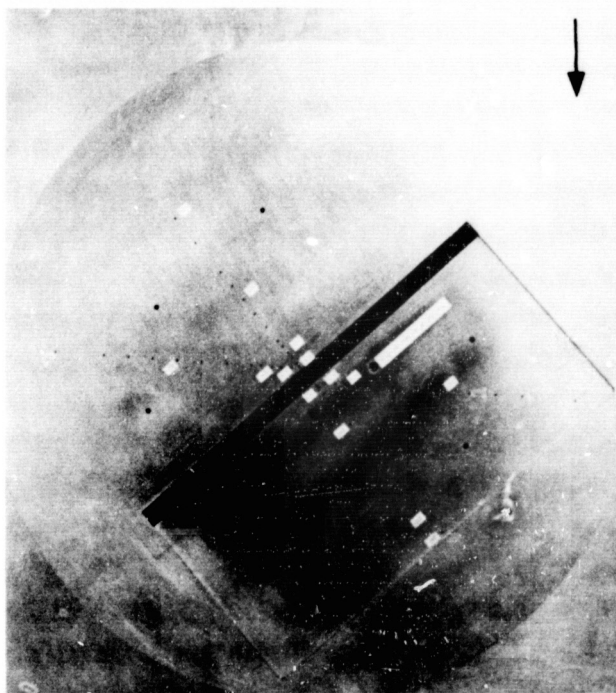


Fig. 11 Plan view of model at $\beta=45^\circ$ (cavity floor removed).

however, are a number of orifices and the outline of a 5.5 x 12 inch adjustable step block. The step block has been recessed in Fig. 11 for definition. By shimming beneath the block, step height could be adjusted. In the flush position, all aluminum surfaces were lapped to insure a smooth surface. The details of all orifices on the model upper surface are shown in Figs. 12, 13, and 14. Flow direction with the cavity perpendicular to the tunnel axis is indicated by arrows on the figures. Fig. 12 represents a very deep cavity with a cavity width of 0.5 inch and 0.1 inch rearward-facing step. In Fig. 13 pressure orifices 301 through 313 are aligned perpendicular with the cavity span while 401 through 412 are at a 45° skew to the cavity. The three larger holes provided openings for Preston tubes used in calculating skin friction coefficient (see Ref. 93 for Preston tube formulas). Preston tubes were 0.122 inch O.D. Fig. 14 shows pressure orifices continuing with 314 through 326 toward the rear of the step/cavity model and orifices 413 through 424 at a 45° skew. With the cavity-containing disk skewed at 45° the 400-series pressure orifices align with the flow. Also shown on Fig. 14 are three openings for Preston tubes and a single larger opening through which a sheathed TSI 1268 (0.06 inch O.D.) flush mount hot film sensor element was inserted. Pressure orifice locations are discernible by comparison to the 6.0 inch scale shown in Fig. 14.

On both cavity faces and at both end (side) walls a series of pressure orifices were drilled and tubulated. Definition of the rearward-facing step orifices may be seen in Fig. 15. Orifices in line were 0.1 inch apart. The first orifice in the set 101 through 115 was number 101 and is 0.05 inch from the front corner. With the block in place as shown in Fig. 12, pressure orifices 1 through 15 were across from orifices 101

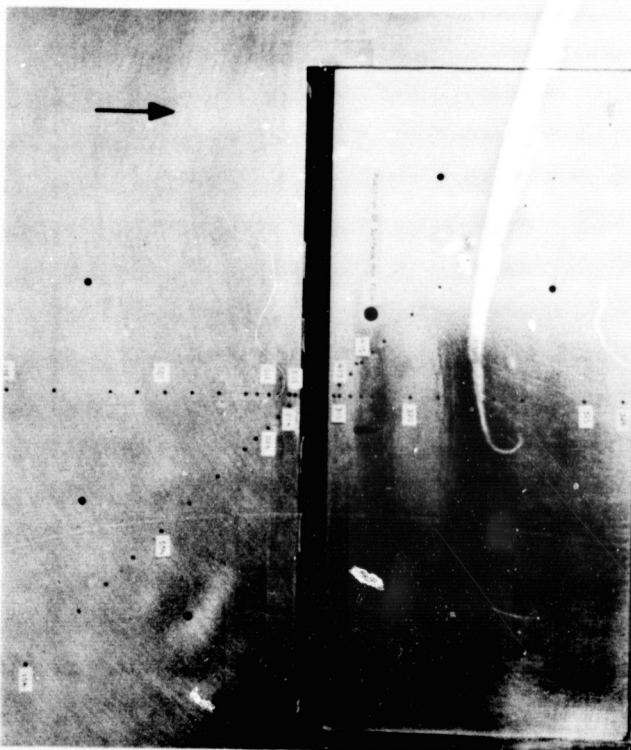


Fig. 12 Plan view of step/cavity model at $\beta=90^\circ$ (cavity floor removed).

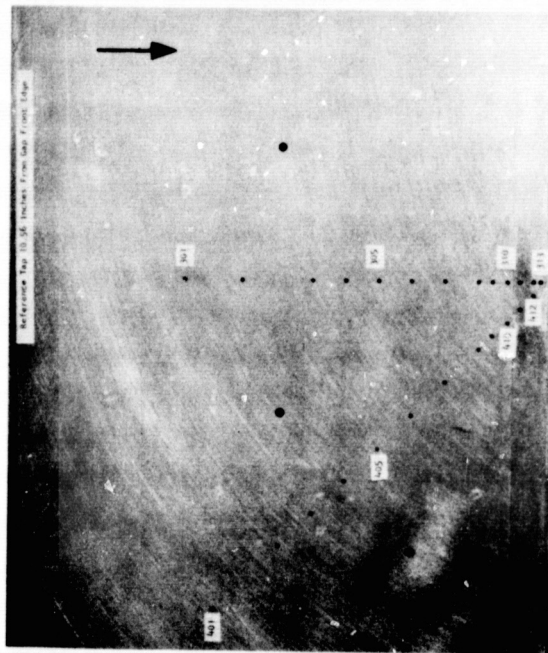


Fig. 13 Fore pressure orifice and Preston tube port plan detail.

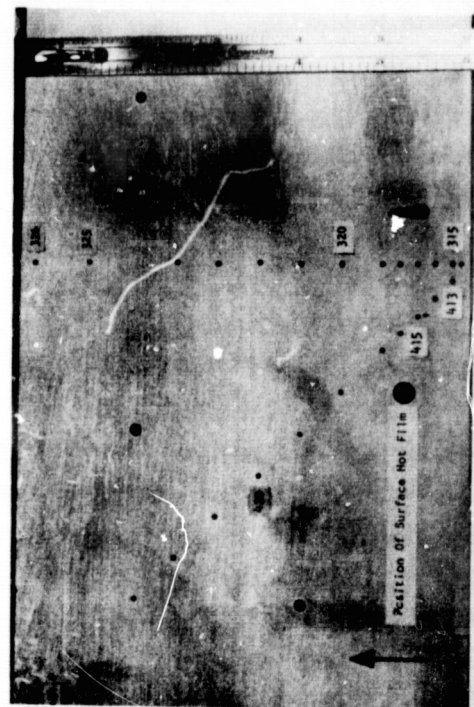


Fig. 14 Aft pressure orifice, Preston tube port, and surface hot film port plan detail.

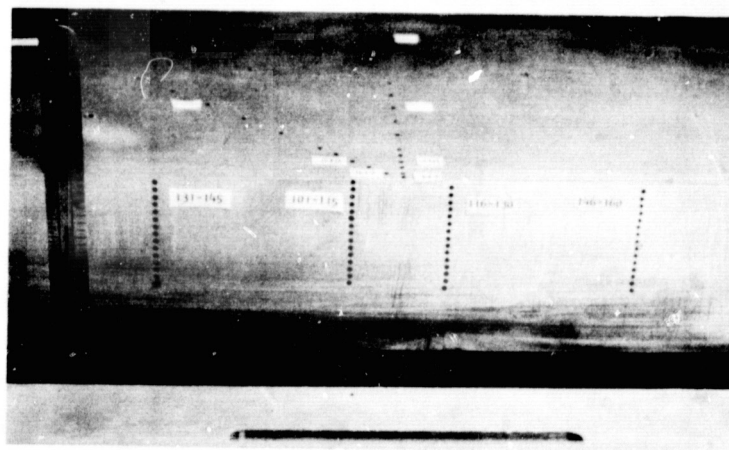


Fig. 15 Model rearward facing step pressure orifice detail.

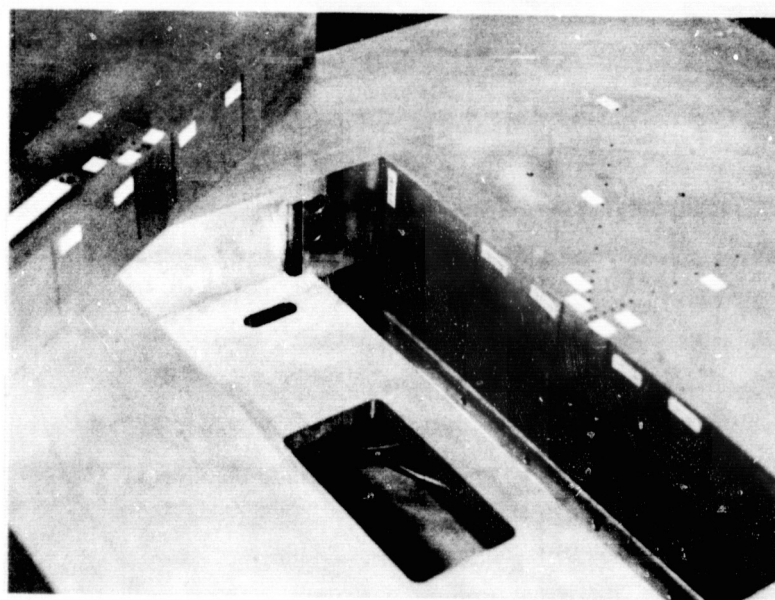


Fig. 16 Corner pressure orifice detail with adjustable step block removed.

through 115. Pressure orifices 116 through 130 and 16 through 30 have the same relationship of being across the cavity; however, pressure orifice 16 was 0.1 inch down from the rear corner. Orifices 131-145 and 146-160 on the rearward facing wall and their counterparts, 31-45 and 46-60 on the forward-facing wall were 0.01 inch apart down the faces, spread to either side of the cavity center span, and start 0.01 inch down from the cavity corners. The adjustable step block is shown removed in Fig. 16 to expose detail of side wall pressure orifices numbered 216-230. Orifices 201-215 on the opposite side of the cavity span are in the end (side) wall/rearward-facing wall corner each series starting 0.078 inches down from the forward corner. The orifices are 0.1 inch apart. Shown on Fig. 16 is a drilled plate (5 holes), integral with the depth bar, for securing the nylon cavity-width-spacing depth plates. Also shown is an access cutout for routing block Preston and pressure orifice plastic tubes leads and sensor film wires to instrumentation. Shims for adjusting block height were laid on the surface through which the access cutout was made. Adjustment for height ranged from 0.1 inch below the cavity model surface to 0.3 inch above the surface. On sides and behind the block in a stepped or recessed position, modeling clay was used to provide smooth transition surfaces to the disk surface. The step/cavity model is shown in place in the rear position in Fig. 17. The traversing mechanism arm is seen in Fig. 17. An oblique view of the arm with hot film probe sting installed is shown on Fig. 18. In Fig. 18, the probing mechanism is on the tiled surface in the forward position. The tile surface shown and other tile surface arrangements will be described in a later section. In Fig. 17, the step is shown with a 0.3 inch step. Forward-facing step pressure orifices are revealed in addition to a



Fig. 17 Stepped cavity model in situ with velocity traversing probe mechanism arm behind.

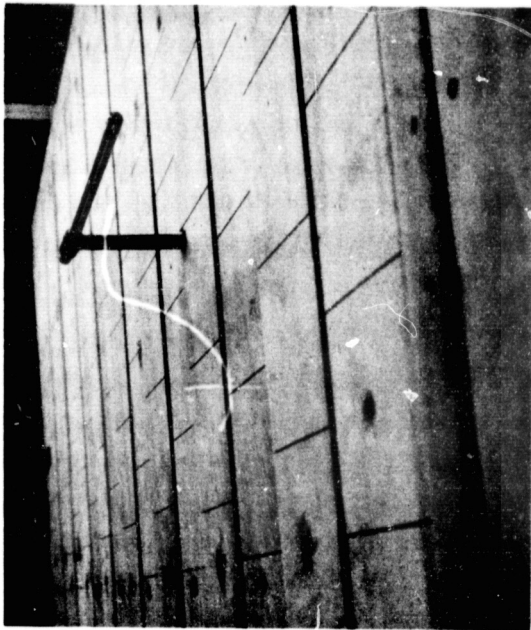


Fig. 18 Stepped tile surface showing tile gaps with probe mechanism arm showing.

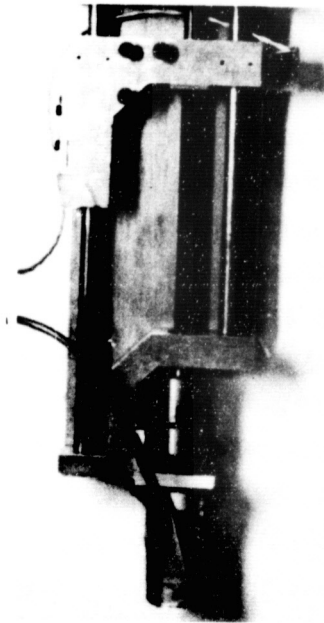


Fig. 19 Probe mechanism drive unit without arm (position potentiometer On: limit switches not visible).

ORIGINAL PAGE IS
OF POOR QUALITY

Preston tube ahead of the stepped cavity. The static pressure orifice used in conjunction with the Preston tube shown is immediately beside the Preston tube as was the arrangement with all Preston tubes on the model surface, on the smooth Formica surface, and on the tiled surface. On each side of the splitter plate (removable sections in place on the Formica smooth surface) 20 additional static pressure orifices were provided. Further discussion and a full set of measurements using the inline surface pressure orifices are given by Norton and White in Refs. 31 and 32. With the step/cavity model in the rear position with the cavity perpendicular to the flow ($\beta = 0^\circ$), the cavity front corner was 110.1 inches from the leading edge of the test bed plate. In the forward position the cavity front corner at $\beta = 0^\circ$ was 33.6 inches aft of the test bed plate leading edge. All stepped cavity tests were made with the test bed plate horizontal ($\alpha = 0^\circ$).

To make boundary layer measurements, two probe traversing mechanisms were built to attach beneath the test bed plate. Figure 19 shows the drive unit for the probe mechanism arm and probe sting unit. The hot film probe holder and the arm/sting units are shown in the rear position in Fig. 7. Probe mechanism bolts to the underside of the test bed plate were through the light colored aluminum block shown in the right-hand side of Fig. 19. The probe arm bolted to a right angle piece with three machine screws attached. A geared, 10 turns Bourns 10K potentiometer. Between two angle piece is shown with wire connection in the lower right of Fig. 19. A stationary rack gear provided drive to the potentiometer. Between two slide bars a drive screw through the angle piece provides traversing mechanism drive and positioning. Position was repeatable to ± 0.001 inch. As with the gap depth drive, a Globe Industries 24 volt DC motor provided

power. This motor, with a flexible rubber coupling to the drive screw, is seen at the left in Fig. 19.

Plastic tube leads from the step/cavity model, seen in bundles in Figs. 9 and 10, and free stream static reference pressure leads were routed beneath the test bed plate to a 48S2-197 Scanivalve (45 port). Reference pressure was from a pressure orifice 10.6 inches in front of the cavity front corner with the model in the rear position. The reference pressure orifice with the model in the rear position may be seen in Fig. 17. Reference orifice was 12.7 inches in front for the forward position. The orifice is slightly ahead of the model in the Formica surface. As described later, pressure coefficients presented for this study were corrected finally to the mean free-stream static pressure along the model ($h = 0, b = 0$) in the flow direction. Pressure coefficient referenced in this way was confirmed by static-probe pressure measurements off of the model surface in the manner free stream velocity (U_{∞} or U_e at $\alpha = 0^\circ$) was determined.

All pressures recorded were routed through the Scanivalve to a ± 0.5 psid Validyne transducer excited to give approximately 0.06 volts per mm H₂O and calibrated against a TEM Engineering Ltd. Betz type manometer. Transducer pressure calibrations were found to be linear in output voltage and the TEM manometer is readable to 0.1 mm H₂O pressure. Tunnel velocity was set by tunnel dynamic pressure using a ± 0.5 psid Statham pressure transducer. Tunnel conditions were closely monitored and recorded for data reduction. Off-center cavity pressures were very close to identical depth sets of cavity wall pressure measurements and scanning of centered pressure orifices proceeded as 1-15, 16-30, 101-115, 116-130. Scanning in this manner was intended to reveal drift; however, no drift in

transducer voltage recordings was found for any of the tests. Off center pressure orifices (31-45, 46-60, 131-145, and 146-160) and corner orifices (216-230, and 201-215 to the right) were selectively recorded with orifices higher up wall faces usually used. Well over 200 pressure orifices were provided; however, many cavity pressure orifices were not exposed to the flow environment upon being covered by the nylon depth/space plates.

Tiled Surface

Shown in Fig. 18 is one of four configurations tested on the port side of the test bed plate (to the left of the splitter plate as seen from behind). The tiles were produced by slotting boards and were nominally 5.94 inches square. Slot depths were sawed 0.75 inch deep. Tiles were Magnolia wood which provided sharp, clean corners and were sanded smooth but not finished with chemical coating. Thin aluminum sheet backed the tiles against the test bed box frame structure. Screws holding the removable tile boards were covered with clay during tests. By shimming alternate row sets of tile boards, steps between the alternating pattern tile boards were produced. The tiled side of the test bed started 24.0 inches aft of the leading edge. Immediately aft of the 12 inch leading edge section was a 12.0 inch sanded Magnolia plank followed by the first tile board. For the raised (stepped) tile configurations, even numbered tiled boards were shimmed either 1/16 inch or 1/8 inch. In one configuration, tile boards were cut to lay at 45° skew to the flow direction. In all, four configurations were tested and for later reference the configurations are designated as follows:

1. Case A - no steps, tile boards normal to the flow
2. Case B - no steps, tile boards skew at 45°

3. Case C - 1/16 inch steps up and down, boards normal to the flow

4. Case D - 1/8 inch steps up and down, boards normal to the flow

In all configurations, the distance between tiles was 1/16 inch. The tile arrangements were designed to simulate the skin bonded thermal protection system (TPS) tiles found over large areas of the Space Shuttle Orbiter to withstand re-entry thermal heating. Because of curved surfaces on the orbiter, the TPS tiles, separated for thermal expansion to avoid mechanical loads to brittle tiles, are expected to have height mismatches. The TPS tile mismatches result in unavoidable steps which, because protruberances result in an effective increase in friction drag, degrade glide performance on the return leg of the orbiter mission. Acoustical tiles in high temperature exhaust systems of jet engines bear a resemblance to multiple tile arrangements also. In an exhaust system with tiles, power losses might be expected.

Each tile in a row from front to back was provided with a pressure orifice. The second tile board and fourth from last tile board were used for boundary layer surveys employing a traversing mechanism like that used on the smooth side of the test bed. The five Preston tubes used on the smooth side proved useful whereas, Preston tubes on the tiles side did not yield useful information for local friction drag coefficient estimation. Results of the tiles surface tests are shown in Appendix A as well as in Refs. 31 and 32.

Anemometry

The instrumentation used for hot film anemometry is shown in Fig. 20. To measure the true rms fluctuating component with a hot film probe horizontal to the test bed surface and perpendicular to the flow, a Thermo-

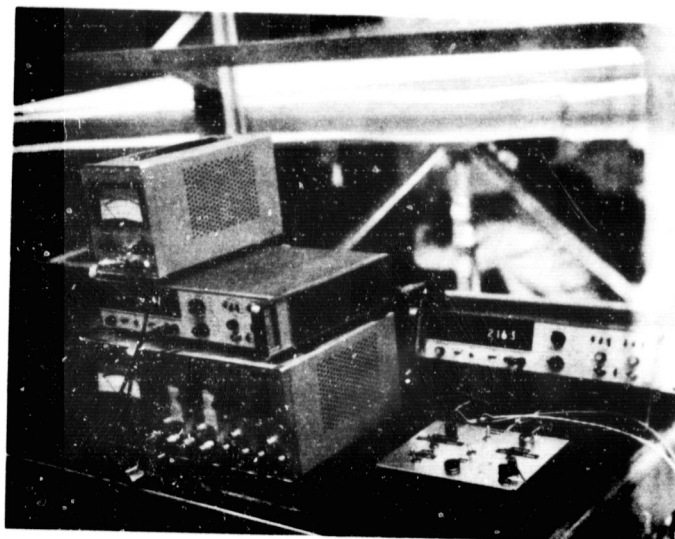


Fig. 20 Hot film instrumentation (mechanisms drive controller at right).

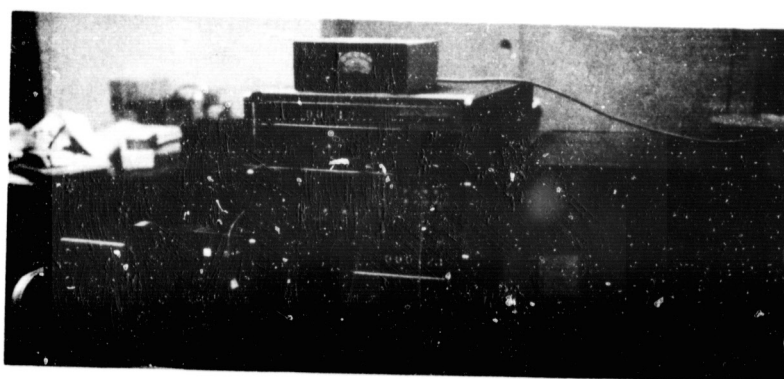


Fig. 21 Pressure transducer instrumentation (Scanivalve controller at left).

Systems Inc. (TSI) Model 1060 true rms voltmeter was used. Time constant averaging interval and range were manually set to obtain steady readings in the upper end of the meter scale. Generally, 10 second averaging was used. The TSI 1060 is shown in the upper left of Fig. 20. For mean velocity, a Hewlett-Packard 5326 B Timer-Counter DVM was used as a voltmeter with digital output. Both the TSI 1060 and the HP 5326 B were supplied voltage from a 1050 series TSI constant temperature anemometer having a TSI 1051-6 monitor and power supply and 1054 B linearized anemometer module. Probes were matched to control resistors. Boundary layer probe sensors were TSI 1218-20 hot films without wall contact pins. Each probe sensor was calibrated against a pitot static tube routed to the TEM manometer. The flush mount sensor (TSI 1268) element mentioned in conjunction with the cavity model block was also wired to the three instruments shown on the left of Fig. 20. The surface sensor was approximately .75 inches behind the rear corner of the forward-facing wall. To the right in Fig. 20 are shown instruments used to control and monitor probe mechanisms and cavity depth mechanism position. The HP 5326 B in DVM mode gave digital position voltage scheduled to correspond to desired physical position of the probe mechanism or the cavity depth. The switch unit (below in Fig. 20) permitted selection of device (two at a time), direction (up or down), and jogging to obtain accurate positioning. Initial position of boundary layer probe sensors was determined by feeler-gage type spacers. Micrometer calibration with the DVM was to within ± 0.001 inch repeatable, and limit switches on the traversing mechanism prevented overrun. Depth gage micrometer calibration was used on the step/cavity nylon depth plate and plate drive.

Pressure Instrumentation

Pressure transducer and Scanivalve instrumentation are shown in Fig. 21. To the left is the solenoid controller (Scanco CTRLR/S2-S6). In the center from top to bottom are P-Ducer OSC carrier amplifier (Scanco POCA 3), HP-3460A DVM, HP-2515A high speed digital scanner, and a HP-2401A IDVM. To the right in Fig. 21 is a paper tape digital recorder (HP 562A). Tapes from the recorder provided scan port number and transducer voltage in addition to wind tunnel run number, date, and other identification information. Tape data was transferred to computer cards for data reduction with necessary model and wind tunnel information to provide geometry and pressure coefficients at each desired pressure orifice. Appendix B gives the results of pressure orifice survey data for the numerous configurations of the step/cavity test program. Figures in Appendix B are self explanatory with all but actual cavity width revealed on the unique plotting scheme. Future developments in and of step/cavity models will require experimental pressure coefficient information with the detail as shown in figures of Appendix B. This also applies to velocity survey profiles shown in Appendix C. This information will be discussed in a later chapter.

RESULTS AND DISCUSSION

The assemblage of experimental data for this study falls into one of two main categories. First, there are data derived from pressure measurements. Second, there are data derived from velocity measurements. Pressure measurements were made along solid surface boundaries primarily above and on the test bed plate (above with a pitot-static tube) and at rearward- and forward-facing walls of the step/cavity model. Velocity measurements were made above the test bed plate either without step/cavities present or immediately behind one or several cavities or stepped cavities. A unique type of velocity or more aptly shear stress measurement with a flush, hot-film sensor element is included though in principle the hot-film sensor as used herein is more nearly related to relative surface, convection heat transfer by mean and turbulent processes. The intention in presenting flush, hot-film sensor results is to relate indirectly the relative linearized signal voltage to the separation flow processes and momentum transfer processes. Quantification of shear stress or separation was not intended although this has been accomplished with the same or similar instruments by several researchers.⁹⁴⁻¹⁰¹ Momentum correlations follow presentation of pressure and velocity experimental results.

Pressure Measurements

The result of pressure measurements are shown in Figs. 22-28 where the numerical weighted function for pressure integral, Eq. (109), serves to scale pressure force in a nondimensional manner. Magnitude and resolution is achieved on carpet-plot graphs by connecting integral values of $\int C_p$ with lines. Trends are revealed but it is not proposed that tests at intermediate points in the test matrix would give results that fall on

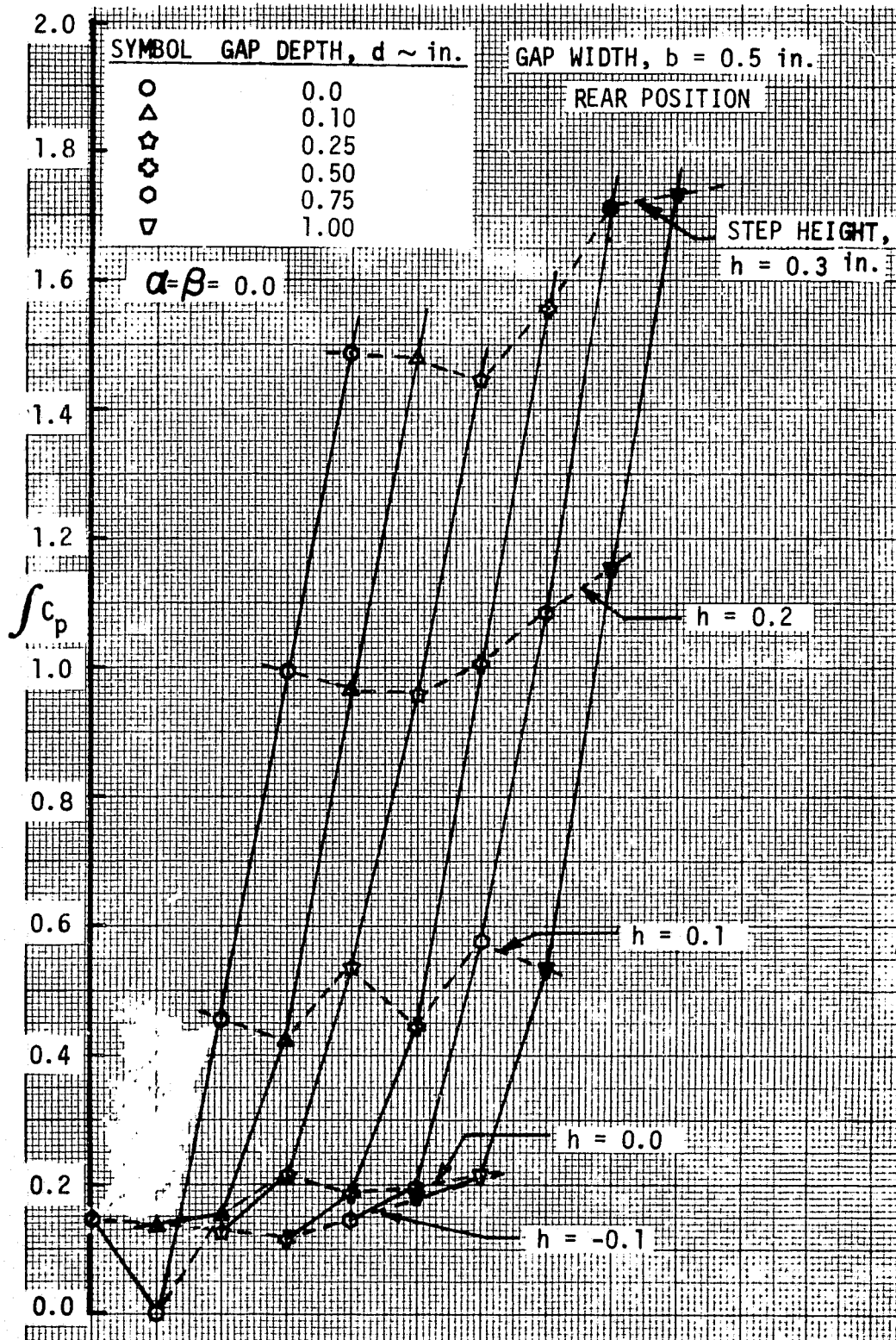


Fig. 22 Pressure integral; $b=0.50$ inch, $\beta=0^\circ$, rear position, $Q=20$ psf.

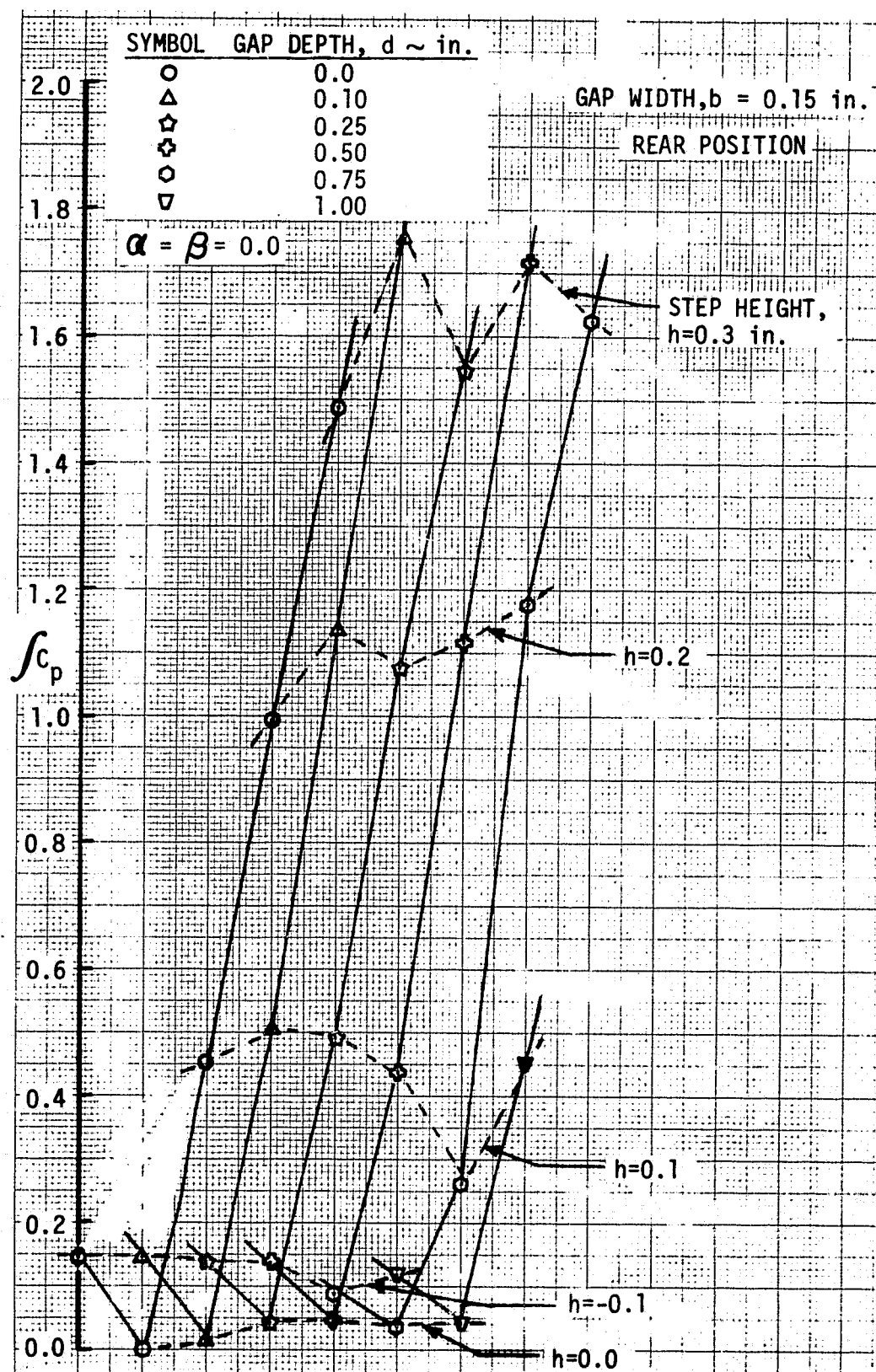


Fig. 23 Pressure integral; $b=0.15$ inch, $\beta=0^\circ$, rear position, $Q=20$ psf.

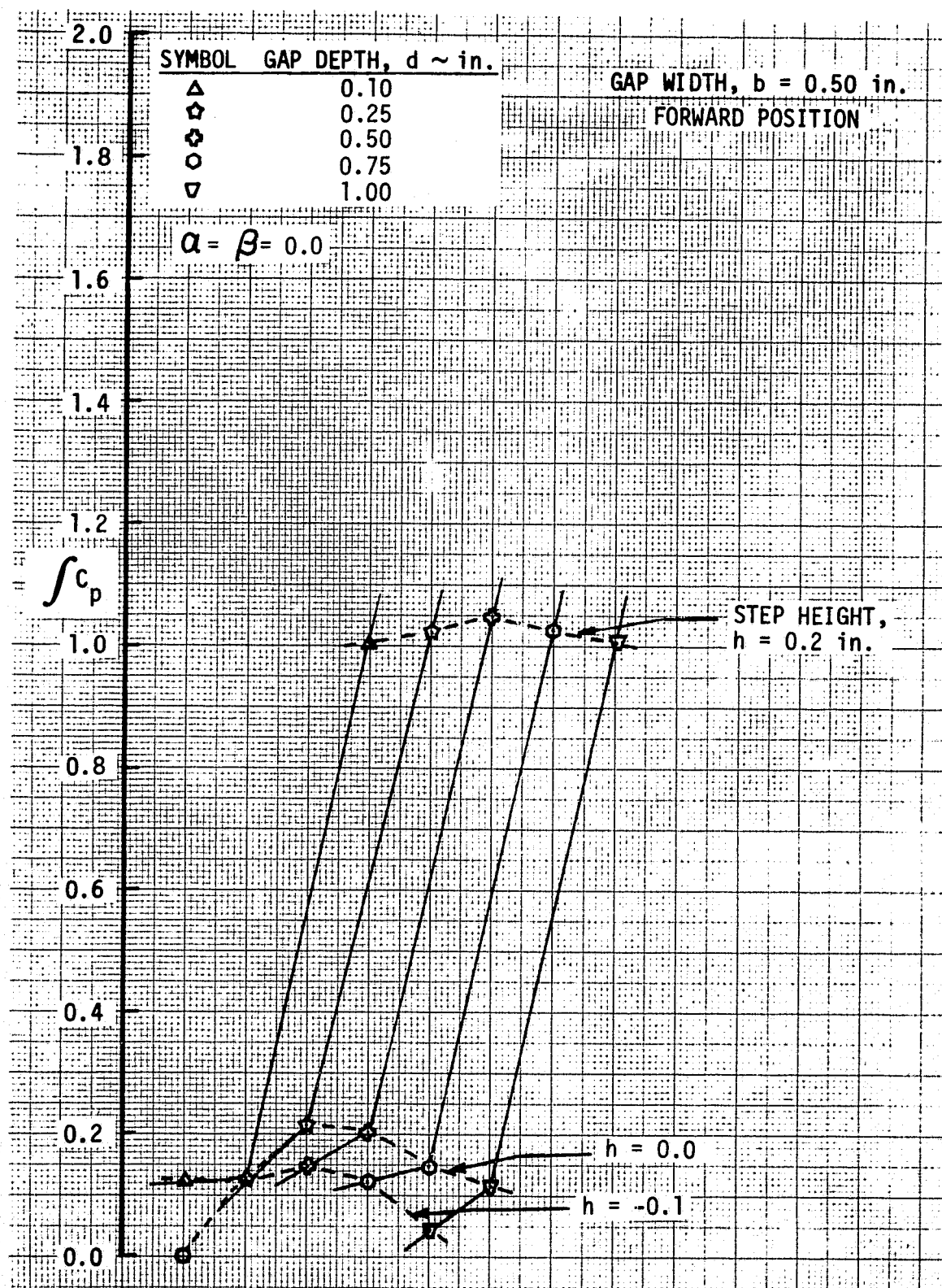


Fig. 24 Pressure integral; $b=0.50 \text{ inch}$, $\beta=0^\circ$, forward position, $Q=20 \text{ psf}$.

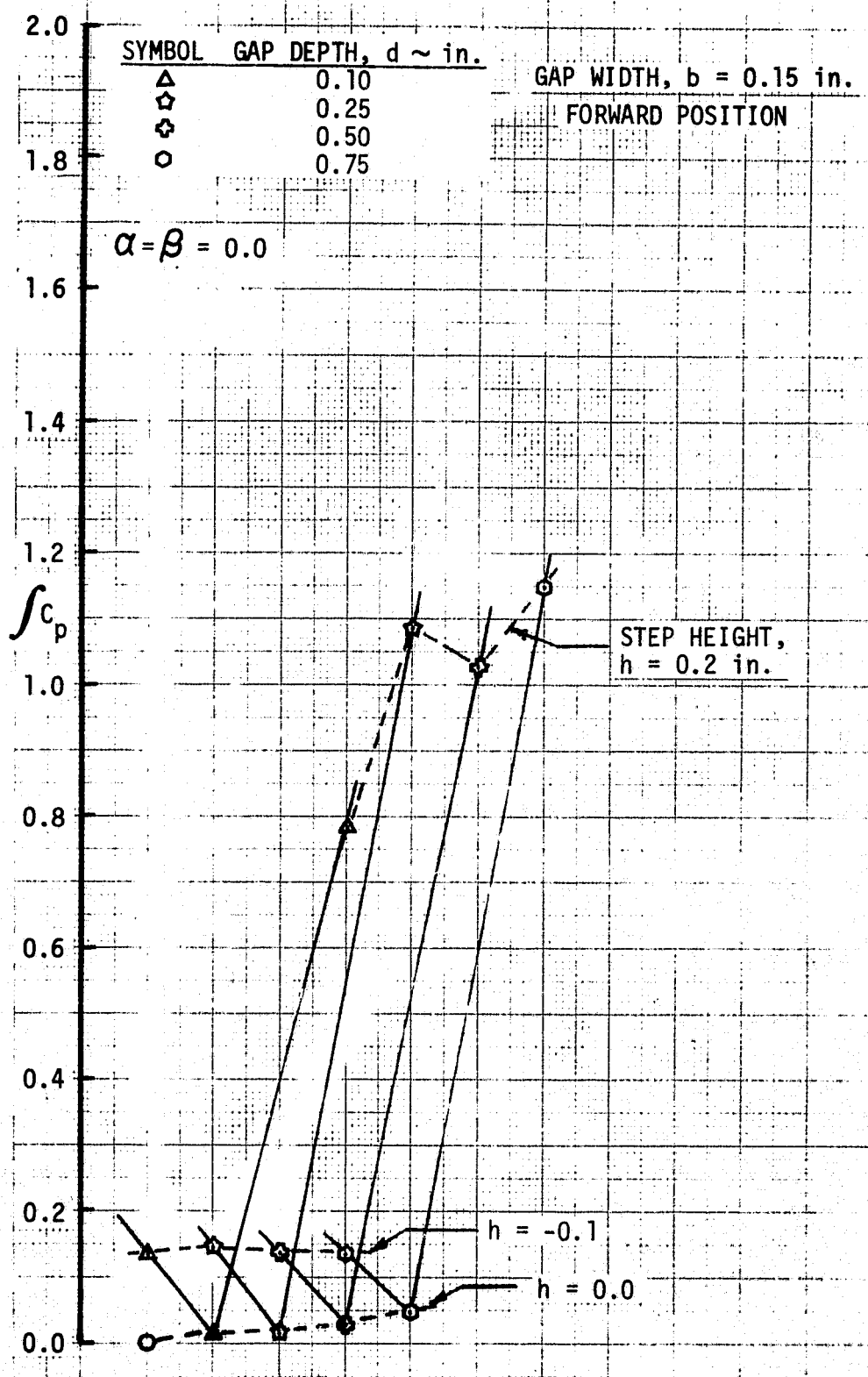


Fig. 25 Pressure integral; $b=0.15$ inch, $\beta=0^\circ$, forward position, $Q=20$ psf.

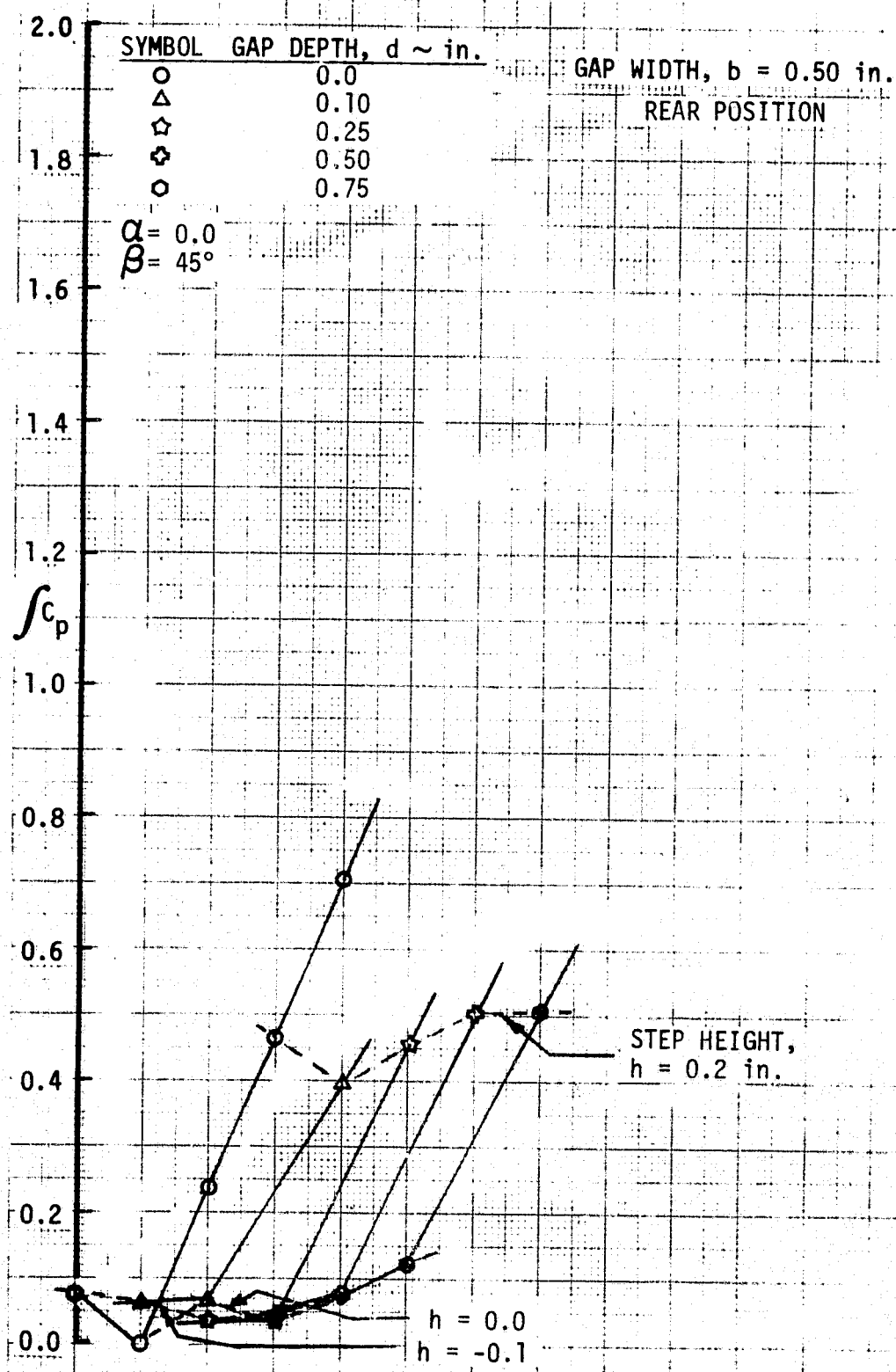


Fig. 26 Pressure integral; $b=0.50$ inch, $\beta=45^\circ$, rear position, $Q=20$ psf.

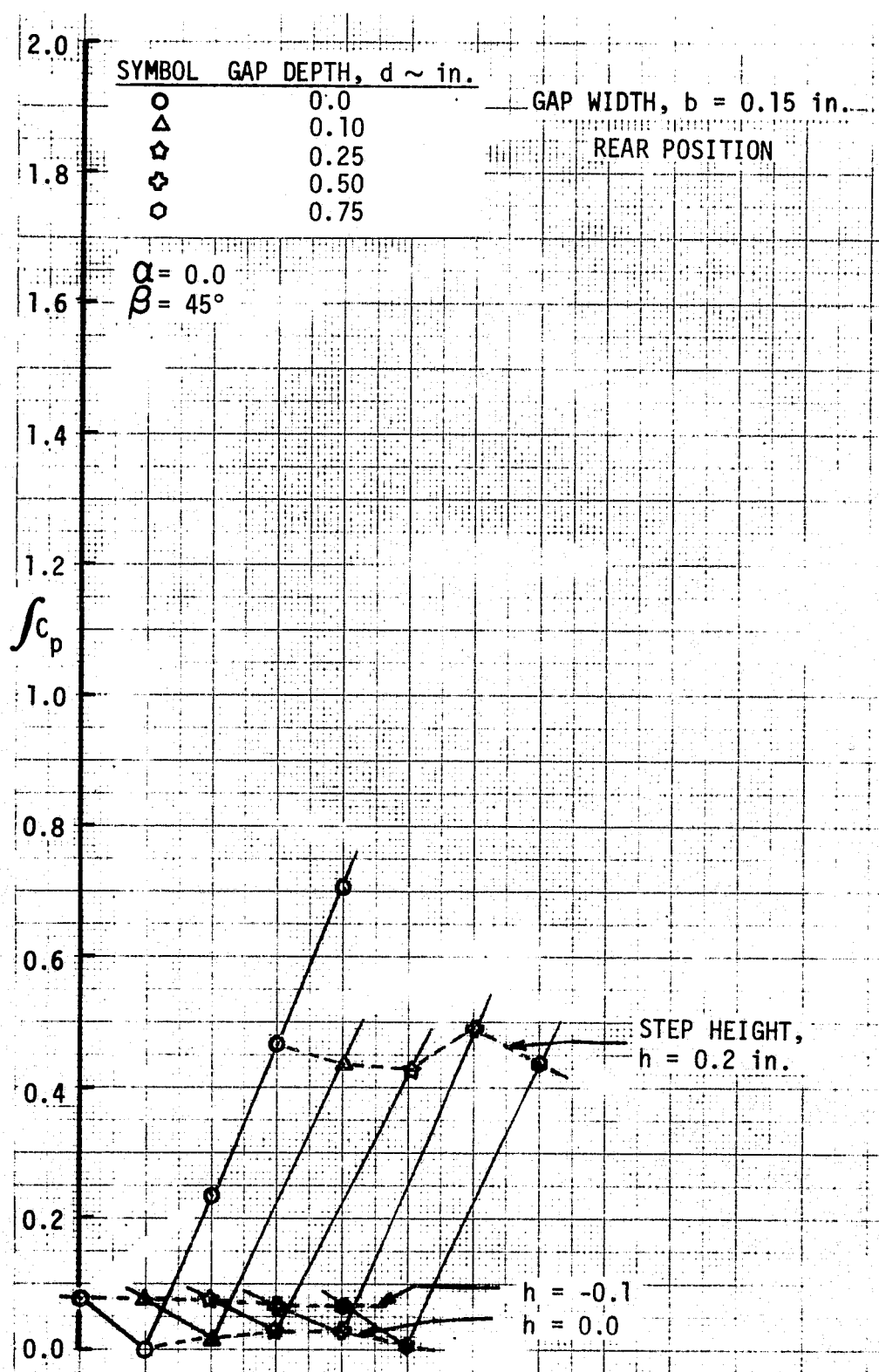


Fig. 27 Pressure integral; $b=0.15$ inch, $\beta=45^\circ$, rear position, $Q=20$ psf.

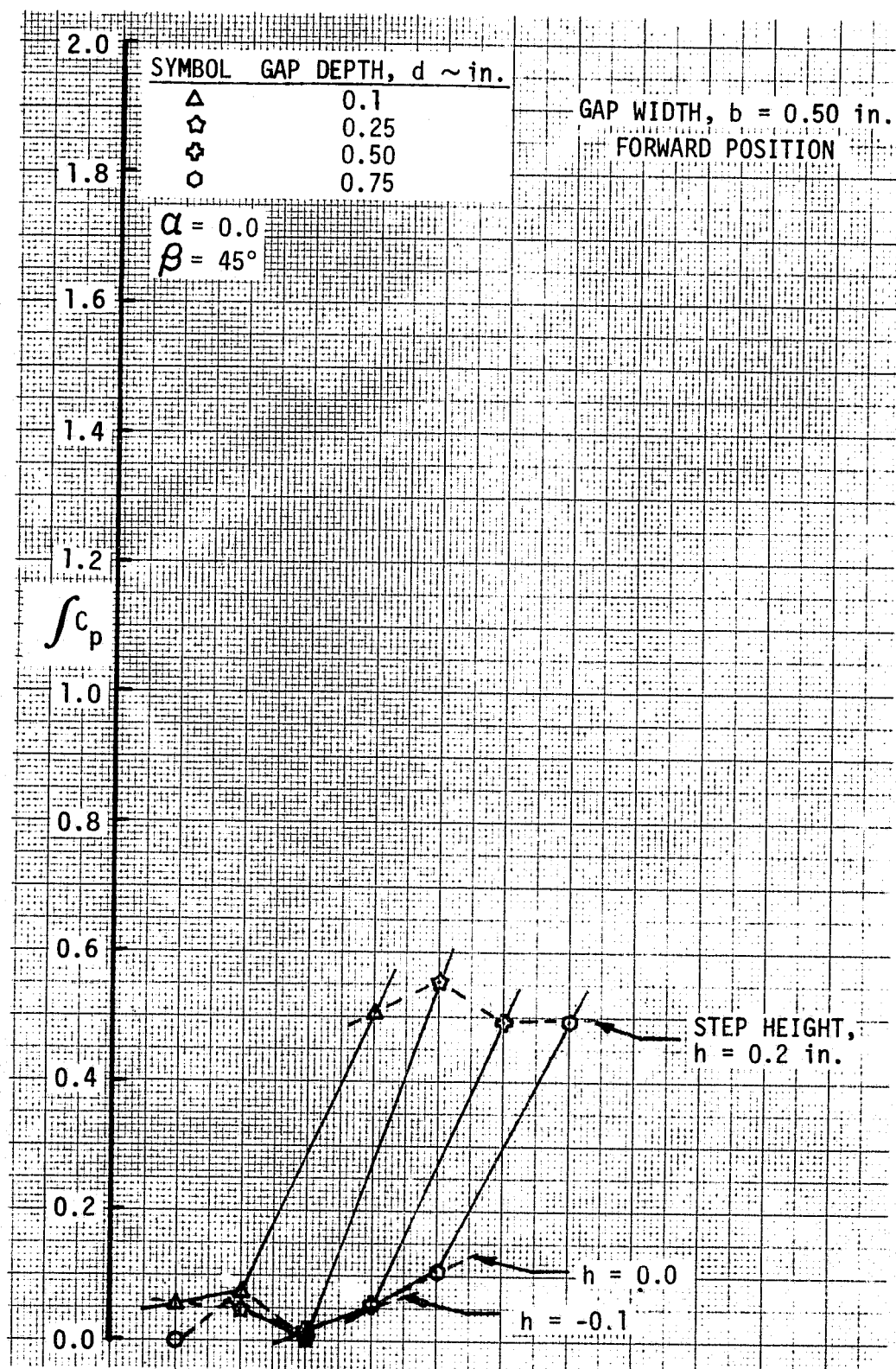


Fig. 28 Pressure integral; $b=0.50$ inch, $\beta=45^\circ$, forward position, $Q=20$ psf.

line construction. The trends shown in Fig. 22 predict a near linear increase in momentum transfer for step heights from 0.1 to 0.2 and from 0.2 to 0.3 inches. For these step/cavity configurations, the gap width is 0.5 inch and may thus be considered to transition from shallow to deep as depth increases. Cavities may not be considered wide since $\delta/b > 1.0$. For the largest steps ($h = 0.2$ and $h = 0.3$ inch) some increase in momentum transfer appears to occur where $b/d \approx 2.0$. For $h = 0.1$ inch there appears to be erratic change with increasing cavity depth yet the trend is still to higher momentum transfer with increasing depth. For $h = 0.0$ (level cavity) and $h = -0.1$ inch (backward step or base flow) $\int C_p$ magnitudes are small. When the cavity depth is between 0.1 inch and 1.0 inch the transfer of momentum to the level cavity is slightly greater than that to the backward-facing step with a cavity. This is not unexpected on the basis that there is shear-layer deflection into the cavity and consequential impingement on the forward-facing cavity wall. For the more narrow cavity the result is different as revealed in Fig. 23. For the $b = 0.15$ inch cavity data of Fig. 23, the separated shear-layer deflects slightly into the cavity to provide little momentum transfer to the cavity forward-facing wall. The $h = -0.1$ inch configuration pressure integral of Fig. 23 is only slightly different from the $h = -0.1$ result of Fig. 22: this indicates that the flow does not reattach until it has passed over the cavities which are of different widths.

Similar trends in $\int C_p$ occur for stepped/cavities described on Fig. 23 as the trends that occur for those stepped/cavities described on Fig. 22 with $h = 0.2$ or 0.3 inches; although, one particular spurious point for $h = 0.1$ inch and $d = 0.75$ inch occurs. The reason for this is unknown; however, cavity pressure coefficient distribution for this configuration

shown in Appendix B does not appear to be peculiar. Anomalies may be enhanced or accentuated by the numerical integration scheme.

Step/cavity pressure integrations for the model in the forward position on the test bed plate shown in Figs. 24 and 25 are very similar to pressure integrations for the model in the rear position. In Fig. 24, however, the trend appears to be toward decreasing momentum transfer with increasing cavity depth and is believed to be a depth effect related to the flow conditions of the approaching boundary layer. In Fig. 25, trend similarity to the rear position 0.15 inch cavity gap (Fig. 23) is evident although the pressure integral at $b/d = 1.5$ for $h = 0.2$ inch is 20% lower than for the same geometry in the rear position. No data smoothing was used so unusual scatter in the data, though small, may be the cause of the aforementioned low value of pressure integral for $h/d = 2.0$ on Fig. 25.

The momentum transfer to a skewed cavity ($\beta = 45^\circ$) in the rear position on the test bed plate is represented on Figs. 26 and 27 by the pressure integrals for discrete configurations. The pressure integrals are shown for $\beta = 45^\circ$ with the step/cavity in the forward position on Fig. 28. By comparing Figs. 22 and 26, Figs. 23 and 27, and Figs. 24 and 28, the effect of step/cavity skew may be seen. Momentum transfer is reduced for the skewed step/cavity compared to perpendicular step/cavity yet the trend is the same. For the $b = 0.50$ inch stepped/cavity configuration with $h = 0.2$ inch, a slight decrease in pressure integral near $d = 0.10$ to 0.25 is seen in both Figs. 22 and 26. The relationship between the momentum transfer on a level cavity and on a 0.10 inch step down is the same for $\beta = 45^\circ$ as seen for $\beta = 0^\circ$. For $b = 0.15$, data at $\beta = 0^\circ$ and $\beta = 45^\circ$ (shown on Figs. 23 and 27, respectively) show the $h = -0.1$ inch backward facing stepped/cavity to have a slightly larger

momentum transfer to the cavity from the flow over the step/cavity excrecence than that with $h = 0.0$ inch. For the $\beta = 45^\circ$ configuration with $h = 0.2$ inch the increase in $\int C_p$ with increasing depth is not apparent as this trend is with the $\beta = 0^\circ$ and $b = 0.15$ inch step/cavity described on Fig. 23. The pressure integrals given on Fig. 28 ($b = 0.50$ inch, $\beta = 45^\circ$, and the model in the forward position) are similar to the $\beta = 0^\circ$ counterpart shown in Fig. 24. With the step/cavity at a skew to the oncoming flow, momentum transfer to the cavity walls by pressure forces is reduced from the amount found with step/cavities across the direction of the flow.

Though slight inaccuracies are undoubtedly introduced by the numerical integration formula being applied directly to pressure measurement data, it is probable that data smoothing and conditioning would possibly mask some genuine yet unelucidated phenomena. Finally, the pressure integral defined by Eq. (109) permits momentum transfer for stepped and unstepped cavities to be compared on the same basis without resorting to definition of drag coefficient. By using $\int C_p$ the relative magnitude of pressure force exerted on step/cavity walls is seen to be dominated by the step height for the 0.1, 0.2, and 0.3 inch steps; however, cavity depth and cavity gap width have an effect and in some instances appear to reduce the pressure force to a level below that of the step-without-a-cavity pressure force.

Velocity Profiles

Wind tunnel testing was conducted during two different time periods separated by several months. During the first entry, preliminary cavity model pressure studies and detailed velocity surveys were

made. During the second entry, detailed cavity model pressures were made. To verify initial findings, velocity surveys were repeated during the second entry when detailed cavity model pressures were made. To instrumentation accuracy, velocity surveys were repeated during the second entry for all repeated condition.

Mean and RMS fluctuating velocity profiles were established for the smooth Formica side of the test-bed plate at the site where step/cavity model excrescences were later to be deployed. Unperturbed velocity profiles serve as step/cavity reference velocity profiles. Also, the tiled surfaces of the test bed plate were surveyed at approximately the same distances aft of the leading edge as that of the cavity in the step/cavity model. Results of surveys for determination of mean skin friction coefficient on the tiled surfaces by momentum analysis are given in Appendix A. Additional velocity surveys pertaining to the isolated step/cavity excrescence are given in Appendix C.

To qualify experimental velocity profiles and, thus, compare to or use widely accepted formulas for equilibrium turbulent boundary layer flow, several methods may be employed. The approach taken in the current study consisted of comparing skin friction coefficients determined by Preston tubes (see Ref. 93) over the smooth Formica plate side (the side of the step/cavity model) to the widely accepted Ludwig-Tillman⁸⁴ formula. Figure 29 shows the comparison between computed local skin friction coefficients. Included on Figure 29 is the White formula (see Ref. 45) and the Schultz-Grunow formula given by Schlichting.³³ Curves are divided for clarity of resolution.

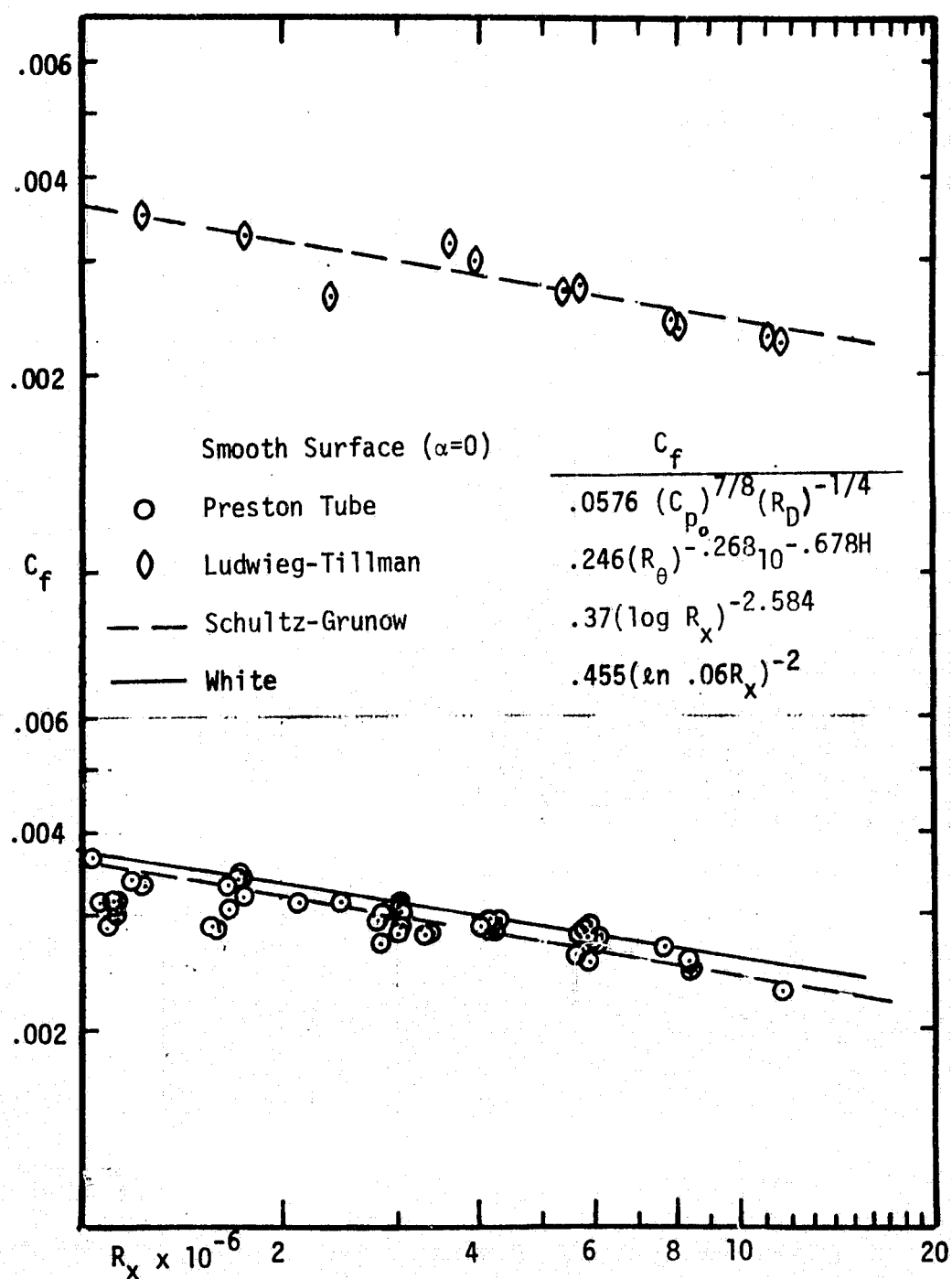


Fig. 29 Plate skin friction coefficient, C_f .

The momentum thickness, θ , and the shape parameter, H , necessary for using the Ludwig-Tillman formula, were determined by using velocity profiles recorded during this program. The Reynolds number, R_x , was determined based on distance from the leading edge and not corrected to represent the effective length of turbulent flow. On the upper scale of Fig. 29 at $R_x = 0.239 \times 10^7$, the skin friction coefficient ($C_f = 0.00261$) using the Ludwig-Tillman formula appears to be low. The data point corresponds to a tunnel dynamic pressure of 20 psf with the probe mechanism in the forward position ($X = 33.5$ in.). The velocity profile for this may be seen in Fig. C-5. It is remarked that the tunnel dynamic pressure, Q , is only an identifier and less than q_e for $\alpha = 0^\circ$. The value of Q was established by the tunnel operator based on control panel reading of plenum static pressure. Also, according to White⁴⁵, the Ludwig-Tillman formula may be accurate to $\pm 10\%$. It is believed, however, that the boundary layer was affected by an adverse pressure gradient. Neither Preston tube nor static pressure data on the plate surface was taken during the particular run in question but velocity profile for this run indicates an adverse pressure is probably the cause for an unusually low value for C_f at $R_x = 0.239 \times 10^7$. On the lower scale in Fig. 29, C_f by Preston tube measurements is scattered but generally agrees with the Schultz-Grunow and White formula. Both formulas are given on Fig. 29.

Shown on Figs. (30), (31), (32), and (33) are experimental data on the conventional inner-law nondimensional scales. The overlap formula in inner variables due to Betterman⁸⁷ is also shown. Only in Fig. 32, however, has Coles wake region correlation (see Ref. 57)

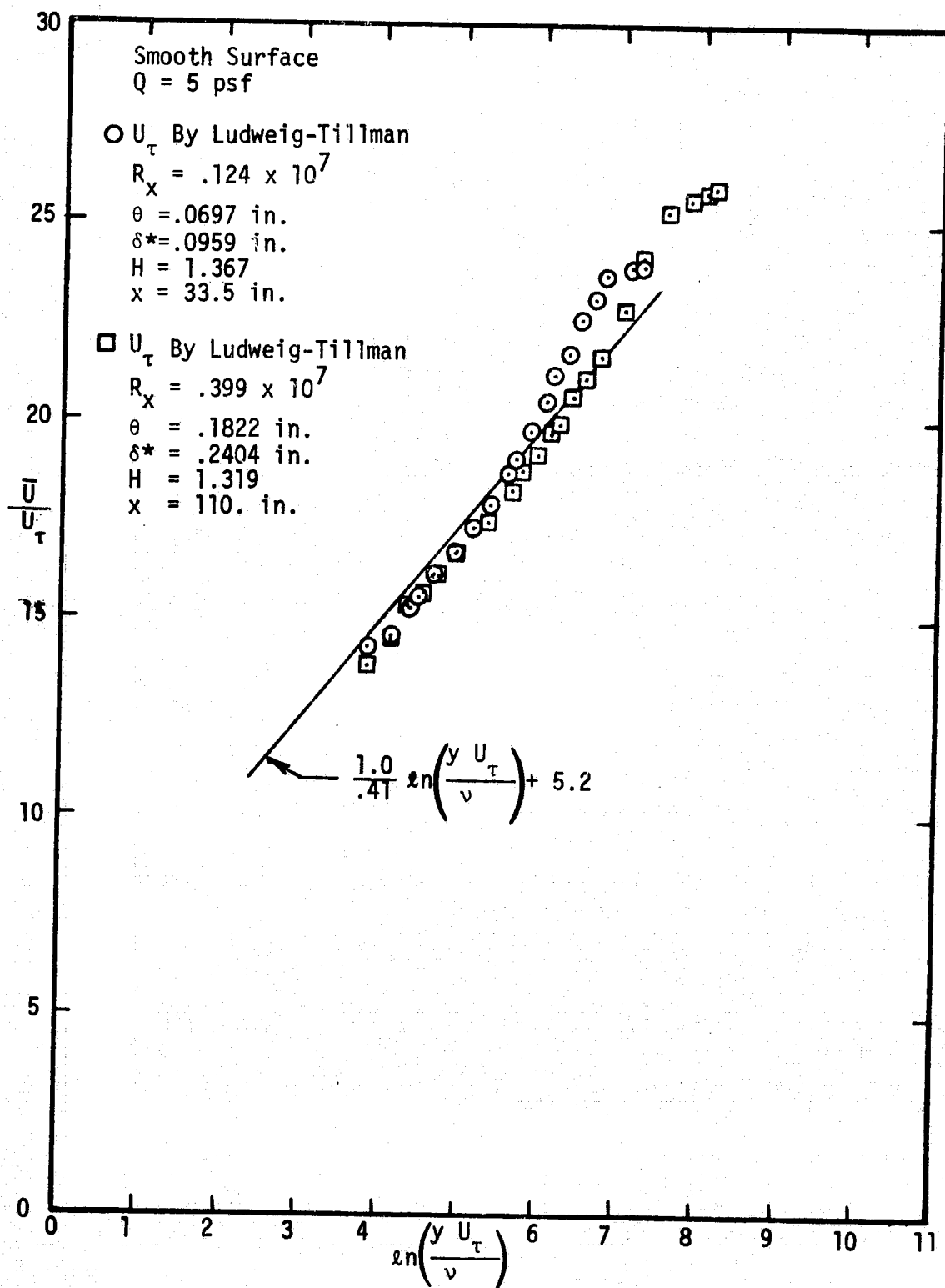


Fig. 30 Velocity profile correlation; $Q = 5 \text{ psf}$, front and rear positions.

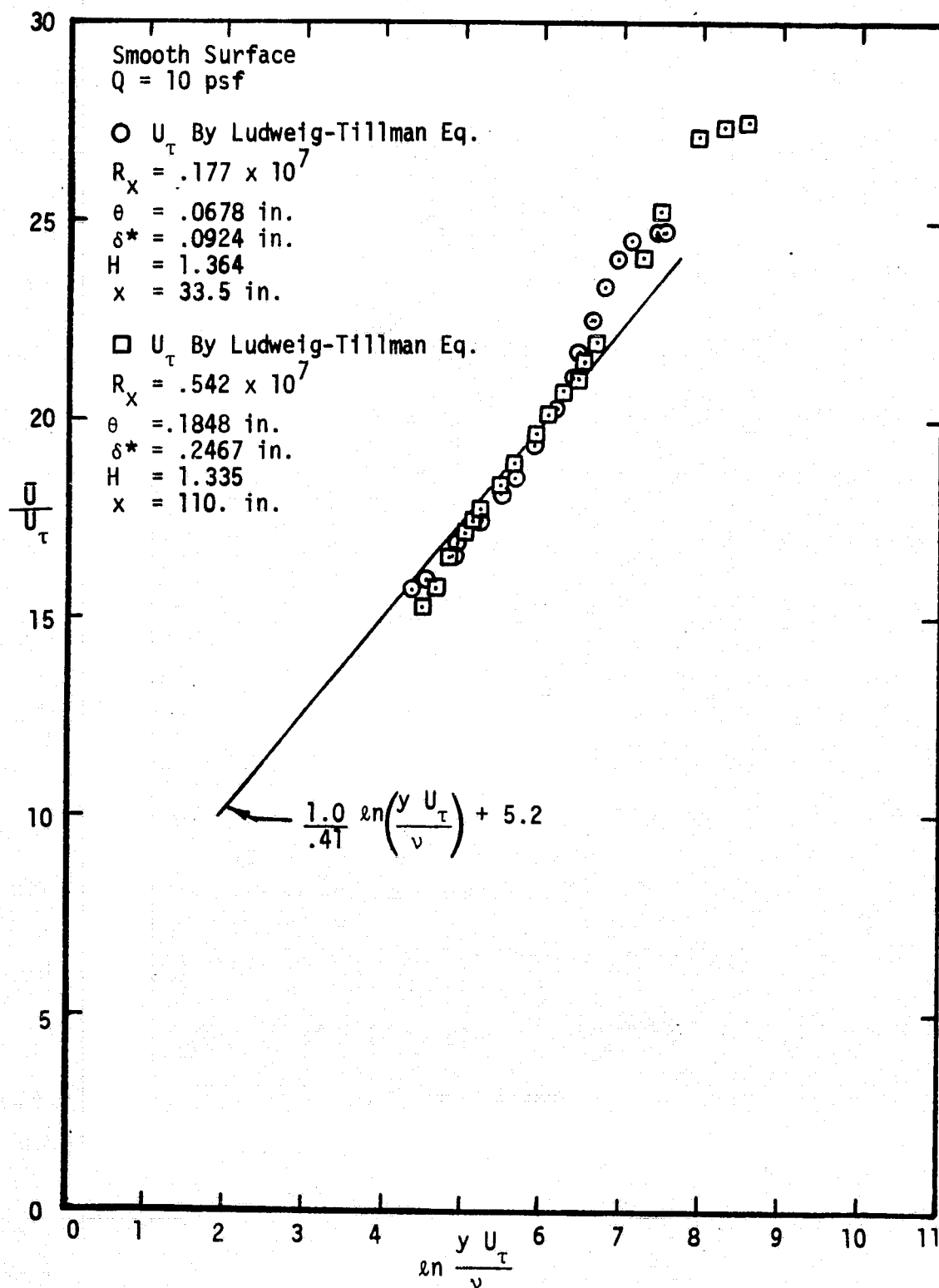


Fig. 31 Velocity profile correlation; $Q = 10 \text{ psf}$, front and rear positions.

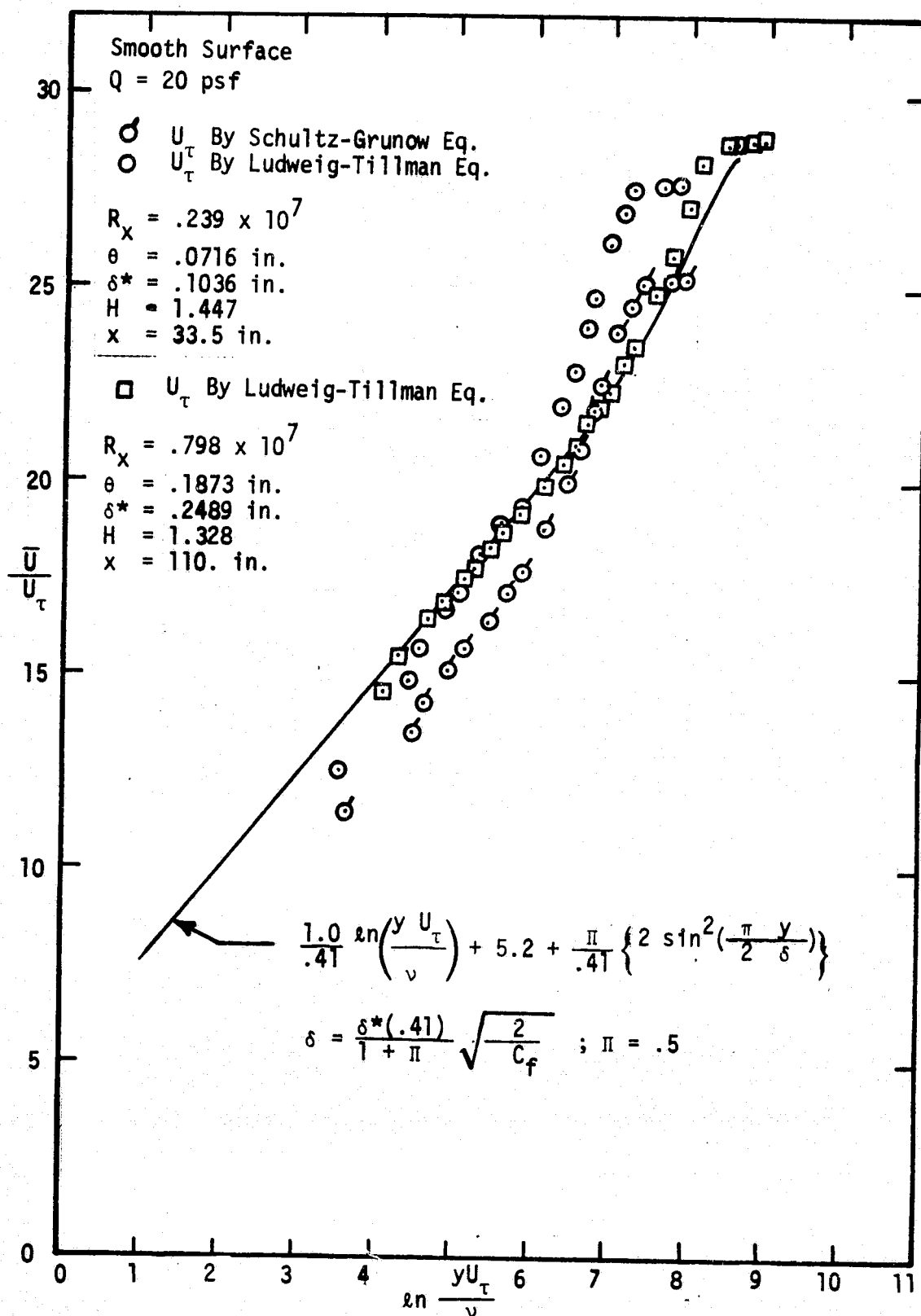


Fig. 32 Velocity profile correlation; Q = 20 psf, front and rear positions.

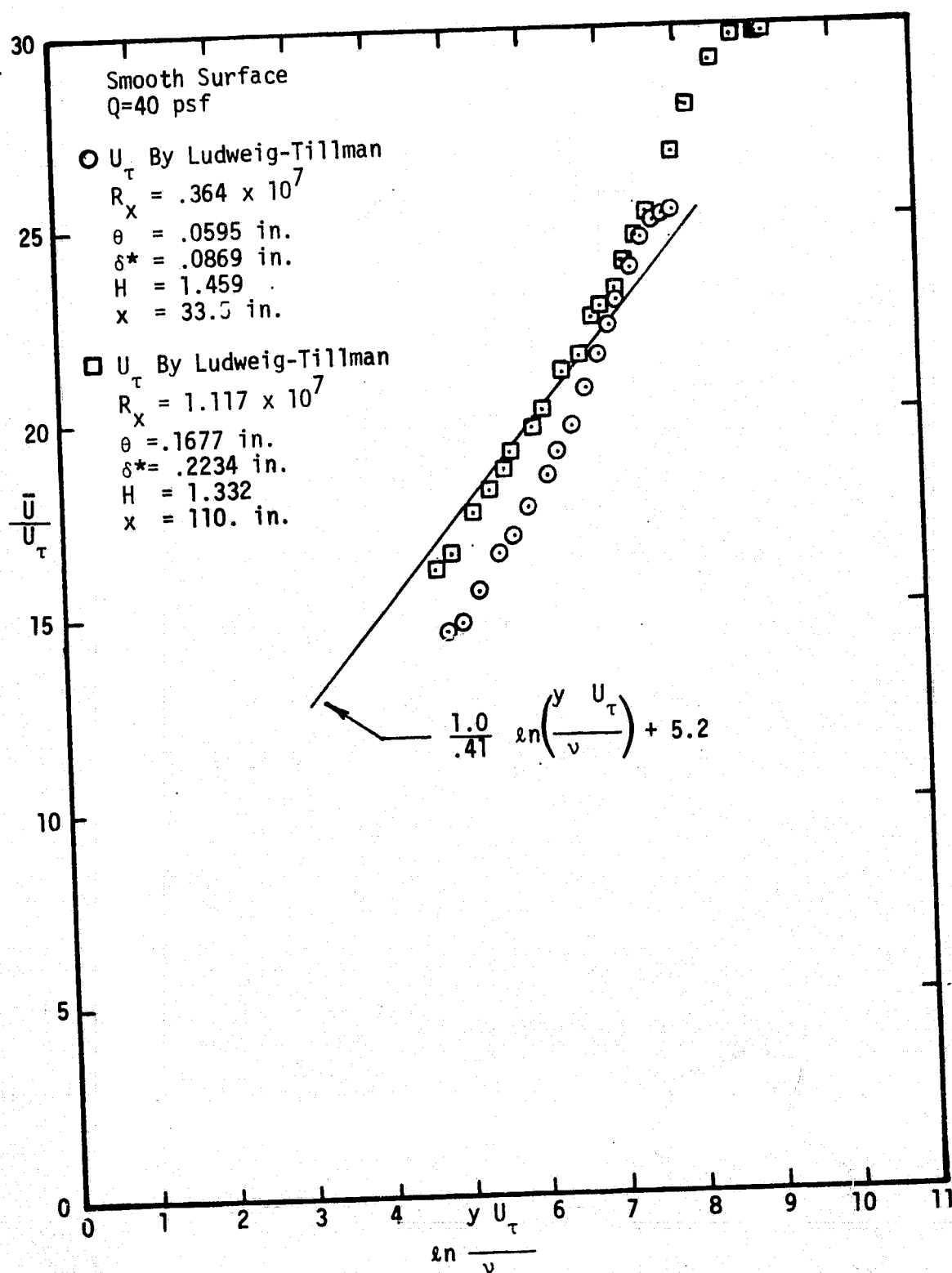


Fig. 33 Velocity profile correlation; Q = 40 psf, front and rear positions.

been added. Agreement between data and the smooth wall overlap region formula for equilibrium turbulent boundary layers is good for measurements made with the probe mechanism in the rear position. Because of inaccuracies in determining U_τ by Eq. (71) or by the method of Clauser⁸², the friction velocity was predicted by the relationship $U_\tau/U_e = \sqrt{C_f/2}$ and the Ludweigh-Tillman formula for C_f given on Fig. 29. This formula correlates the data for $Q = 5$ and 10 (Figs. 30 and 31) for the forward and rear positions and the rear position data for $Q = 20$ and 40 (Figs. 32 and 33, respectively). Correlation using the Schultz-Grunow equation given on Fig. 29 does not correlate the data well. Forward position data at $R_x = 0.364 \times 10^7$ ($Q = 40$) on Fig. 33 does not correlate well to the Betterman formula; however, the use of velocity profile at $Q = 40$ was not required in stepped/cavity correlations. It is suggested, however, that correlations for stepped/cavity momentum transfer (shown in a later section) should, where possible, be made with experimental reference profiles. By doing this it should be possible to predict stepped/cavity momentum transfer when the boundary layer is of a very general type or shape.

Velocity surveys were made, primarily, during the first tunnel entry. Some were repeated during the second entry when stepped cavity pressure measurements were made. As seen in Fig. 34, repeatability between the first entry (Run #135-1) and the second entry (Run #62) was excellent. Fig. 34 shows typical results. Also typical is the repeatability of turbulence intensity, Fig. 35, found to exist at different testing periods permitting the use of early entry velocity profile data with pressure data taken four months later. Free stream

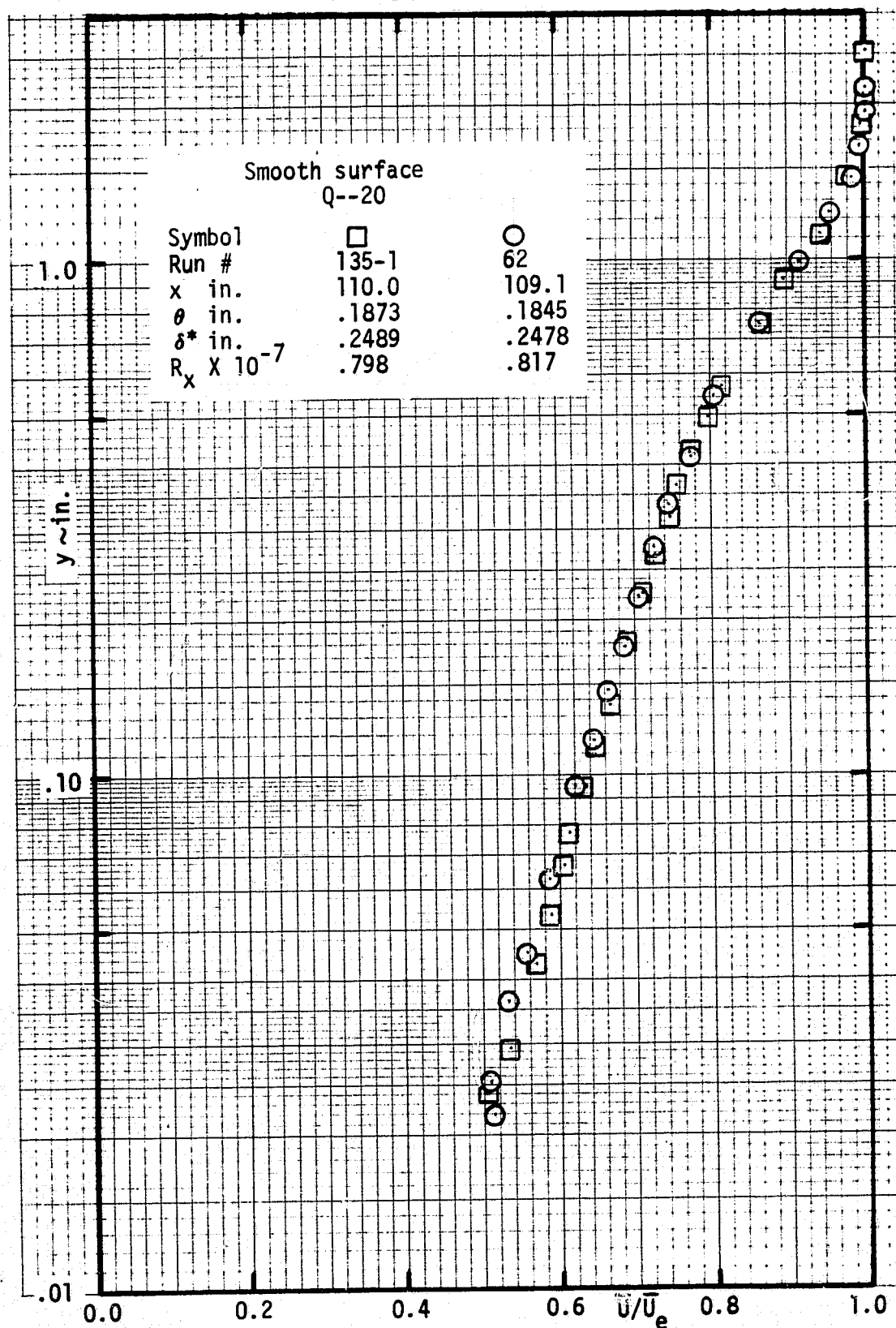


Fig. 34 Velocity survey repeatability between different entry dates;
Q = 20 psf, rear position.

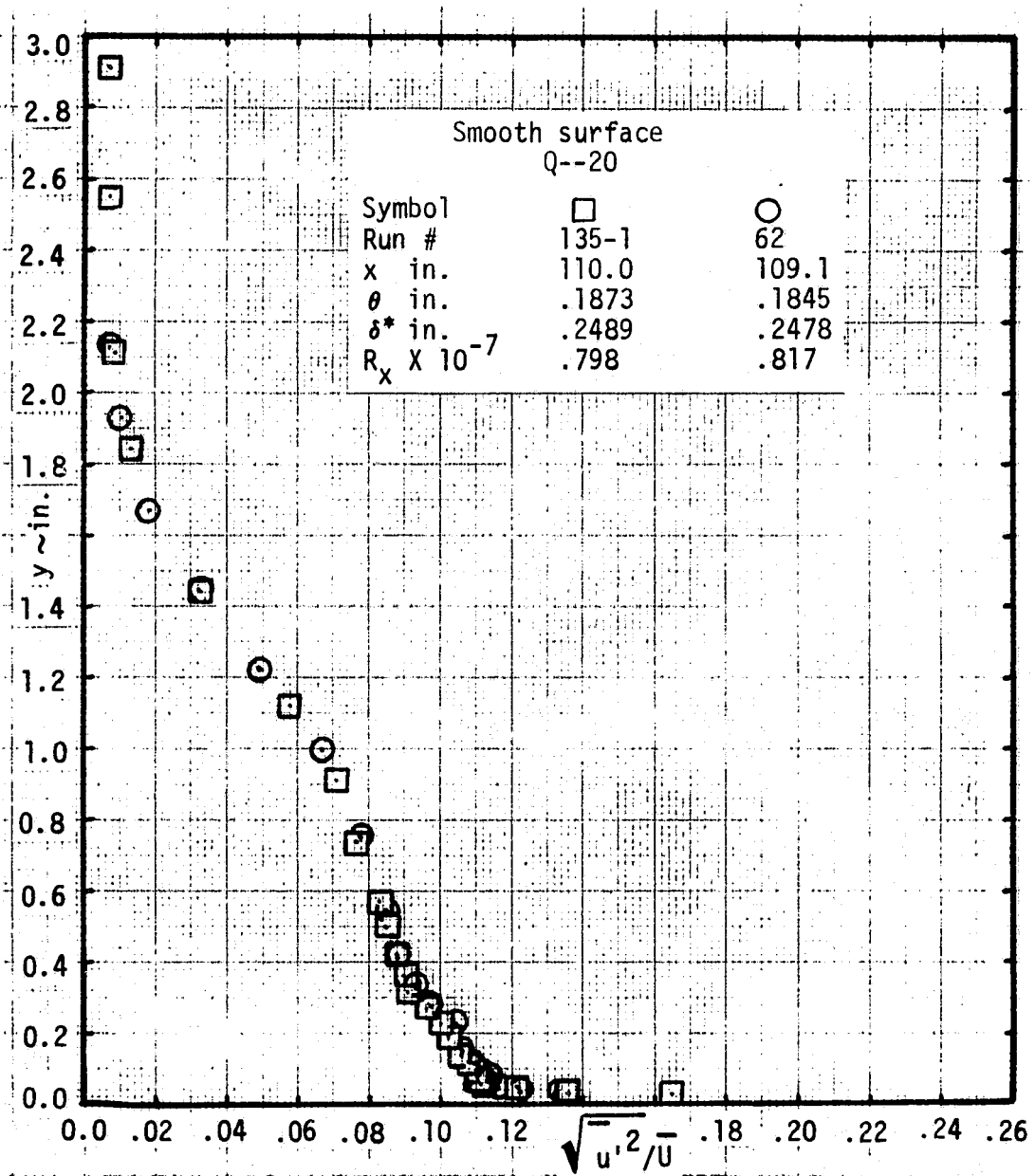


Fig. 35 Turbulence intensity survey repeatability; Q = 20 psf, rear position.

turbulence intensity is approximately 0.7%.

Shown in Fig. 36 are typical results of velocity profile measurements behind a level cavity with various depths. The velocity scale is translated for greater definition. Additional mean velocity profiles are shown in Appendix C. Slight differences are noticeable in profiles shown on Fig. 36 although no distinct differences are to be seen in mean velocity profiles. Whereas, in Fig. 37, turbulence intensity shows the effect of a cavity depth. For $d/b = 0.2$ a discontinuity near $y \approx 0.6$ inch may result from a resonant condition. Additional measurements to verify this were not made, unfortunately. Inset in Fig. 37 are turbulence intensity profiles near the surface at the distance 0.5 inch aft of the cavity rear edge used for depth effect profile measurements. It is difficult to discern the trend; although, an effect of depth on a level cavity is obvious. Attempts to correlate local turbulence intensity from measurements such as shown in Fig. 37 to cavity momentum transfer were unsuccessful.

Correlation of Momentum Transfer

Although not correlated to boundary layer parameters, the drag coefficients shown on Fig. 3 for level cavities have distinct characteristics depending on boundary layer depth, Reynolds number, and, perhaps, Mach number. Figure 38, however, presents drag coefficient variation for a level cavity with the boundary layer height to cavity width ratio. Cavity pressure integrations were used to predict pressure drag coefficient where available; although, some drag balance data are included when pressure data were not given.

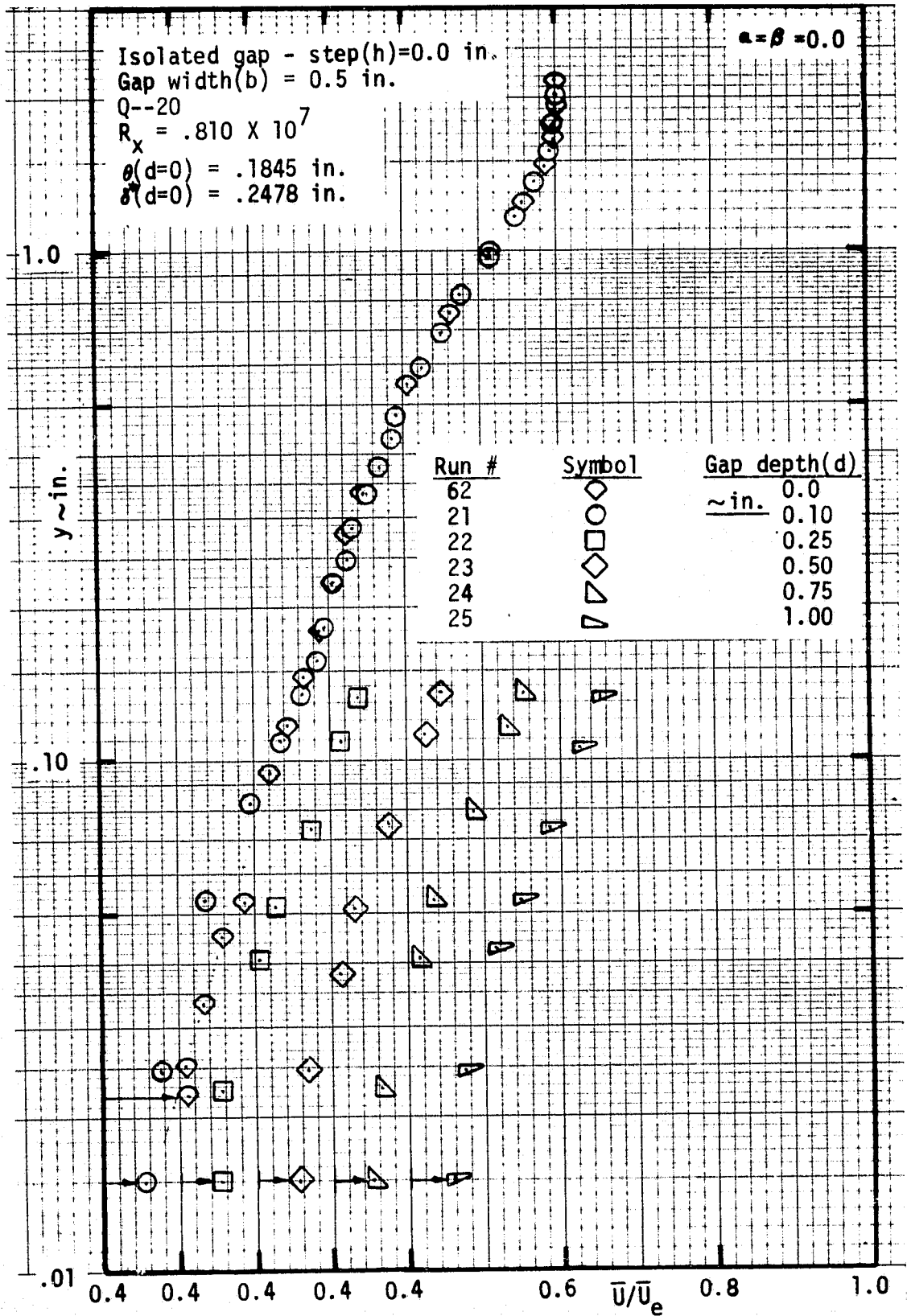


Fig. 36 Depth effect on level cavity velocity survey; $Q = 20$ psf, rear position.

Isolated gap - step(h)=0.0 in.

Gap width(b) = 0.5 in.

Q--20

$R_x = .810 \times 10^7$

$\theta(d=0) = .1845$ in.

$\delta^*(d=0) = .2478$ in.

Run #	Symbol	Gap depth(d)
62	◇	0.0
21	○	0.10
22	□	0.25
23	◇	0.50
24	△	0.75
25	▽	1.00

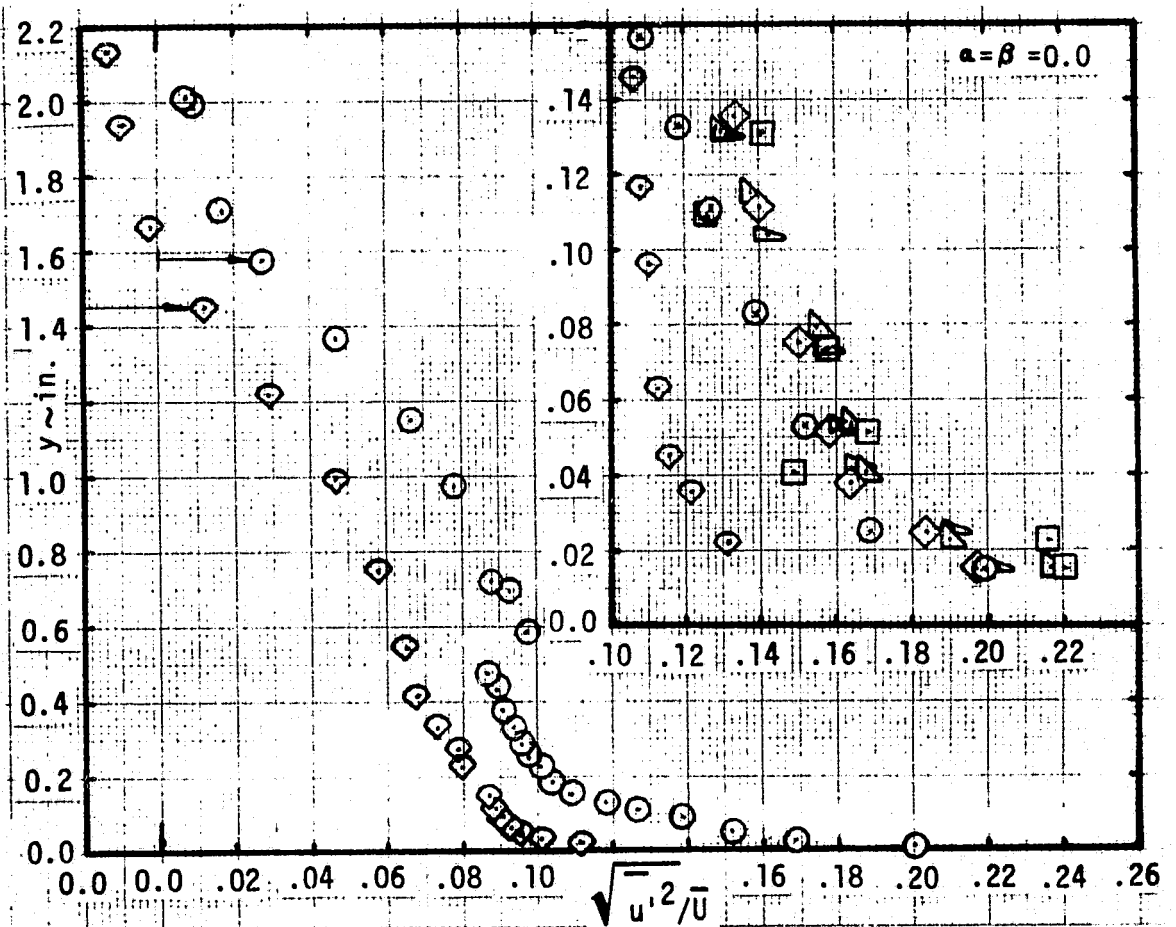
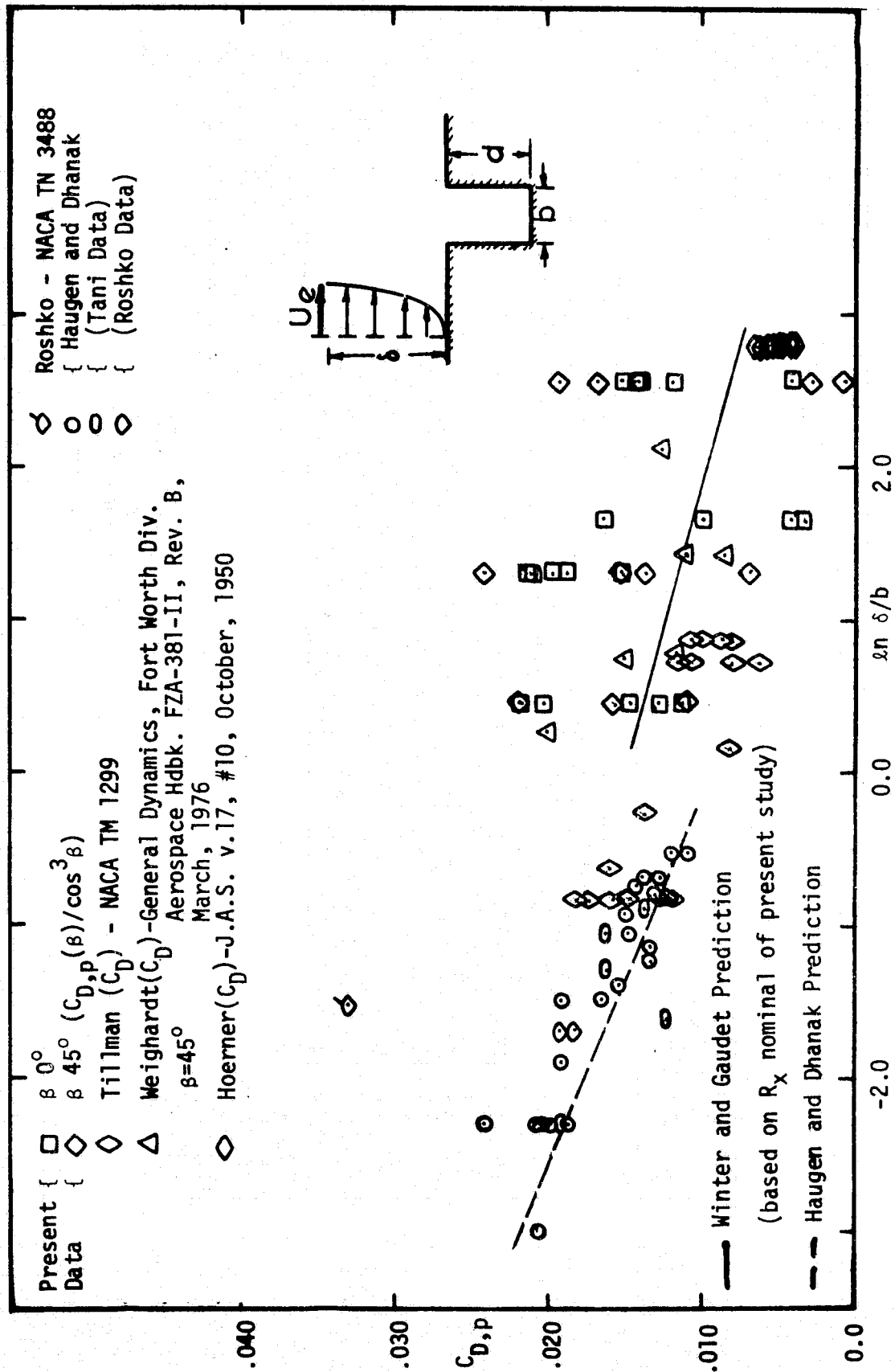


Fig. 37 Depth effect on level cavity turbulence intensity survey;
Q = 20 psf, rear position.

Fig. 38 Level cavity drag coefficient for various d/b .

Direct force measurement data are designated C_D and include a friction drag component where $C_{D,p}$ does not. This correlation scheme is essentially the same correlation scheme presented by Haugen and Dhanak³⁰; however, $\ln \delta/b$ instead of δ/b is used to compress the wide range of δ/b included. The logarithm scale also linearizes the two prediction methods shown in Fig. 38. Two observations are significant:

1. Drag coefficient data do not correlate to $\ln \delta/b$ or to δ/b for a level cavity.
2. For the level cavity, prediction methods (described in the literature review within this report) do not agree and ignore the effect of the cavity depth.

To determine the effect cavity depth has on momentum transfer, data from the present experimental test program are compared on the basis of the proposed model relating Eqs. (108) and (109) in the form shown on Figs. 39, 40, 41, 42, and 43 for cavity depths of 0.10, 0.25, 0.50, 0.75, and 1.00 inch, respectively. These comparisons are for the matrix of configurations shown on Fig. 5 and include the cavity configurations with a forward-facing step. Included also are results for $\beta = 0^\circ$ and $\beta = 45^\circ$ with the cavity model in both the forward and rear position on the level test-bed plate. Some data scatter is evident and may be attributed to data and data reduction method inaccuracies. Although liberal interpretation may be made of the change in pressure force integral with mean kinetic pressure, from all appearances the effect of cavity depth, d , and width, b , are accounted for by the curves shown on each of Figs. 39 through 43.

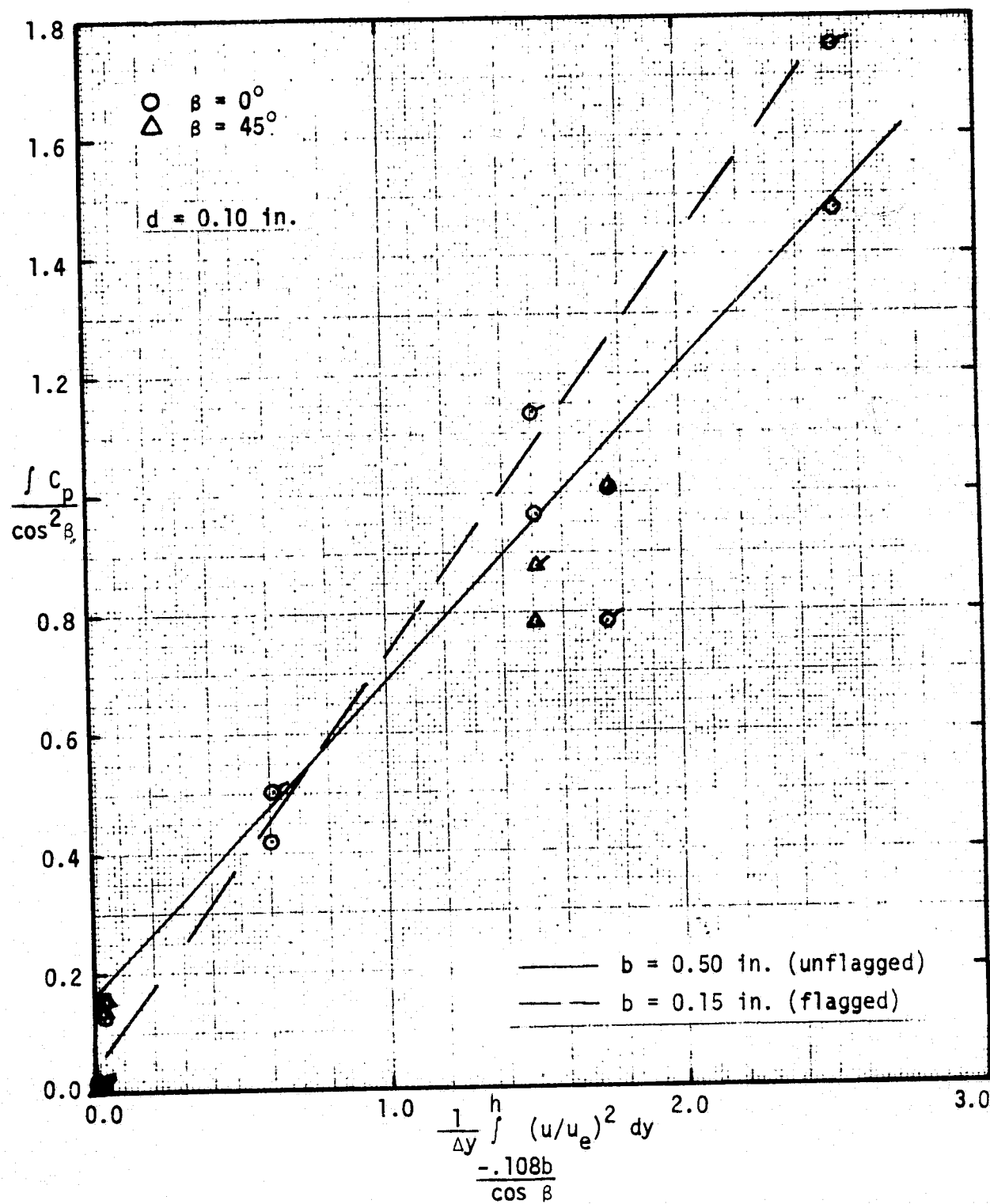


Fig. 39 Width parameter scale effects on stepped cavity correlation; $d = 0.10$ inch.

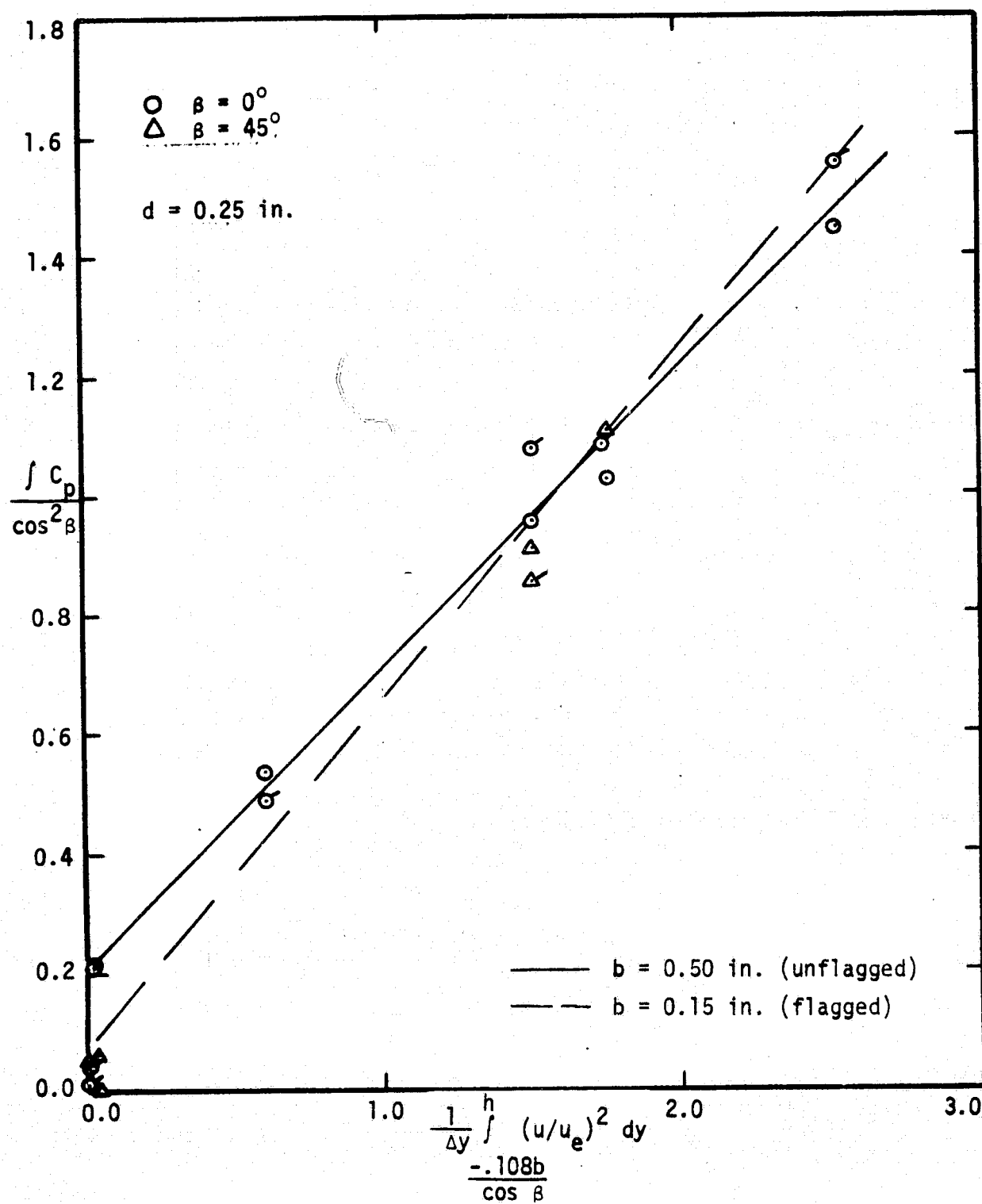


Fig. 40 Width parameter scale effects on stepped cavity correlation;
 $d = 0.25 \text{ inch.}$

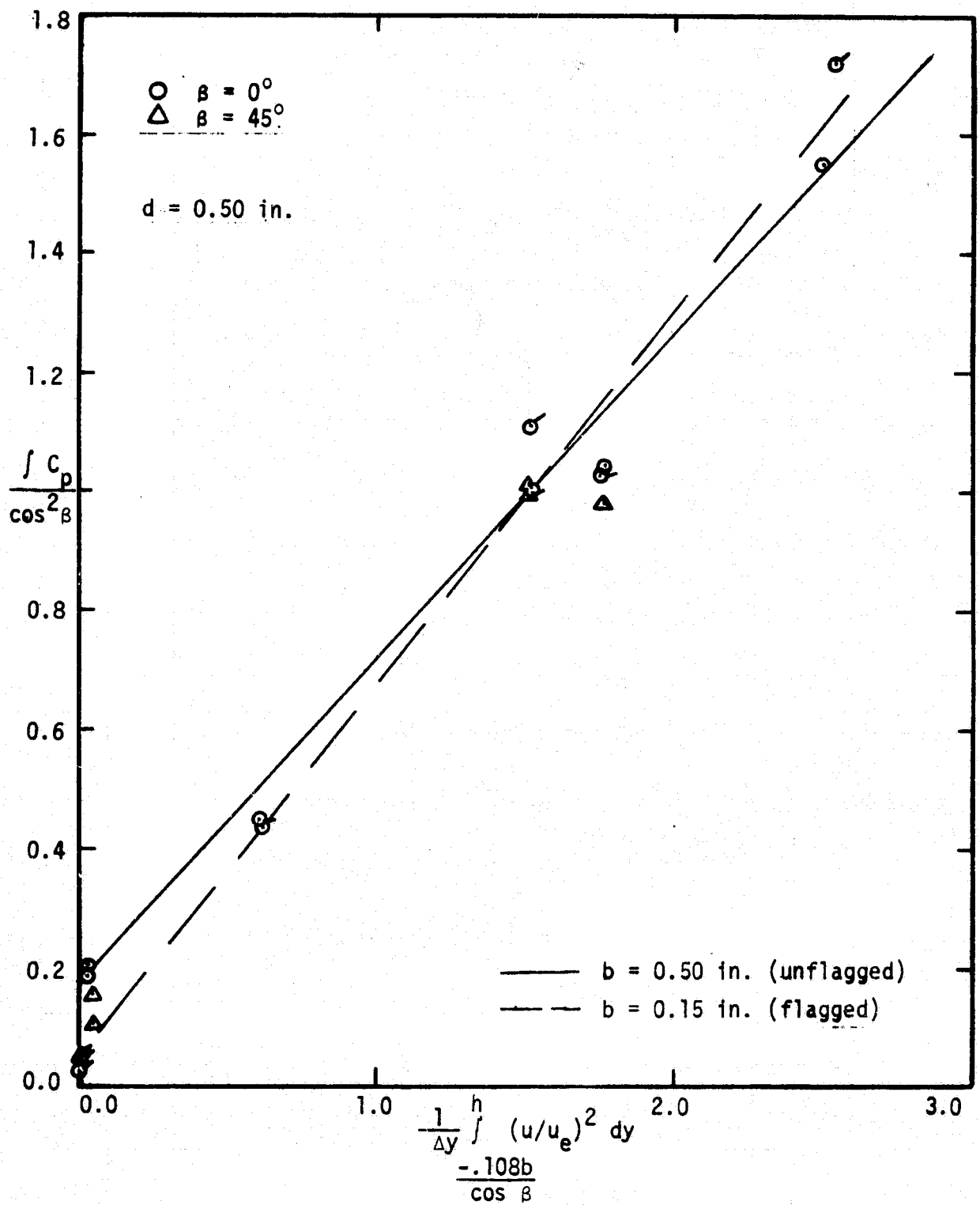


Fig. 41 Width parameter scale effects on stepped cavity correlation; $d = 0.50$ inch.

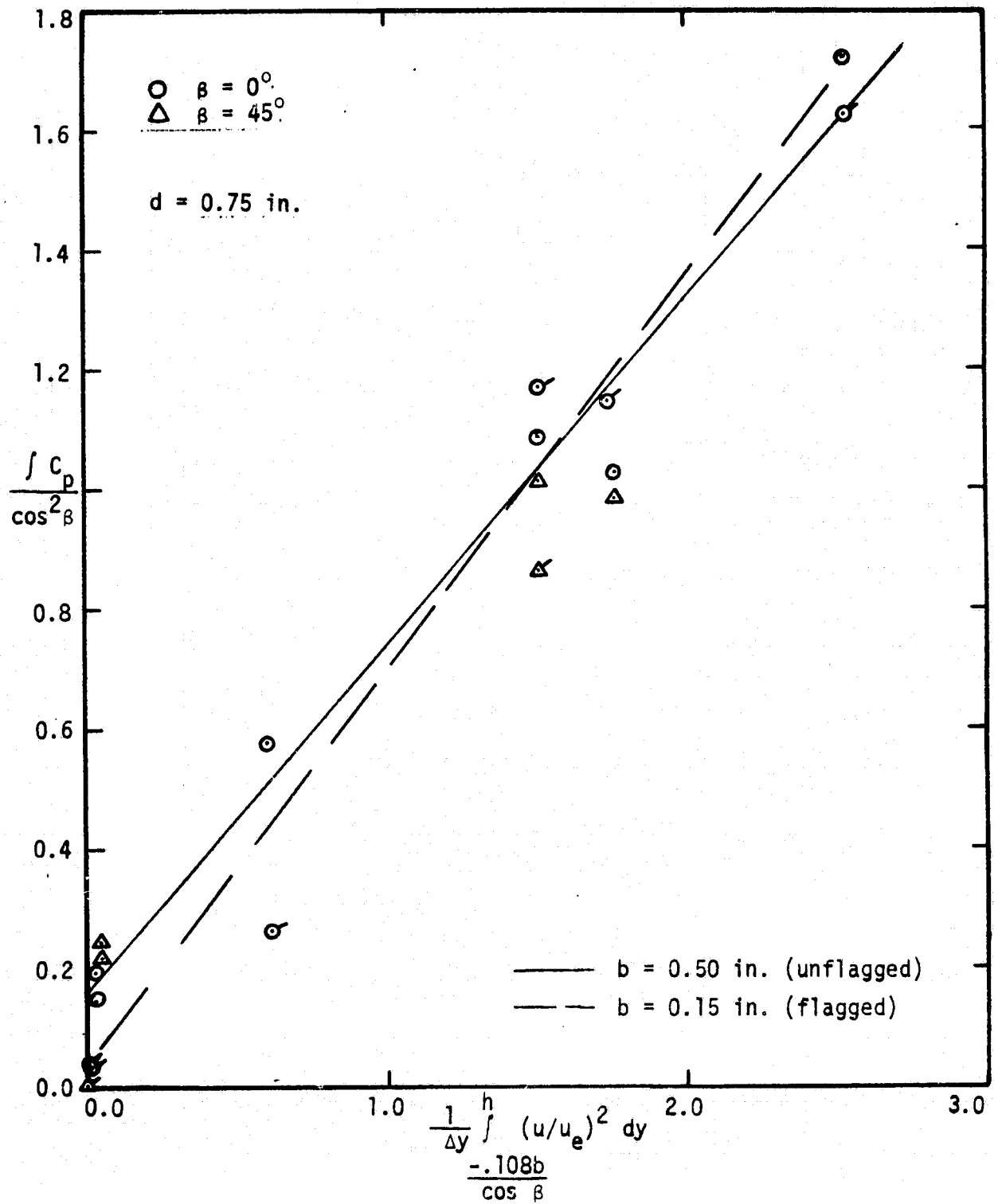


Fig. 42 Width parameter scale effects on stepped cavity correlation; $d = 0.75$ inch.

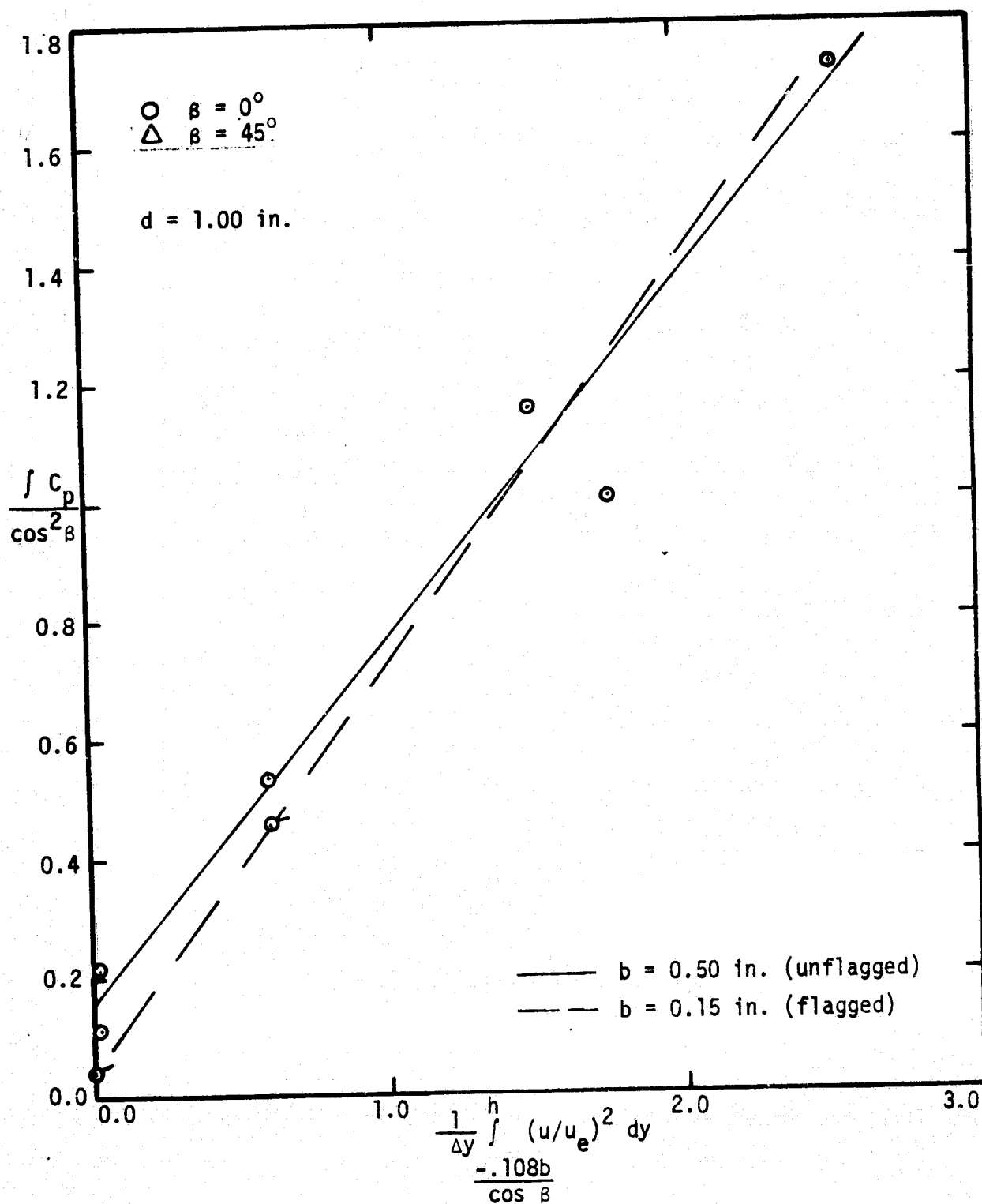
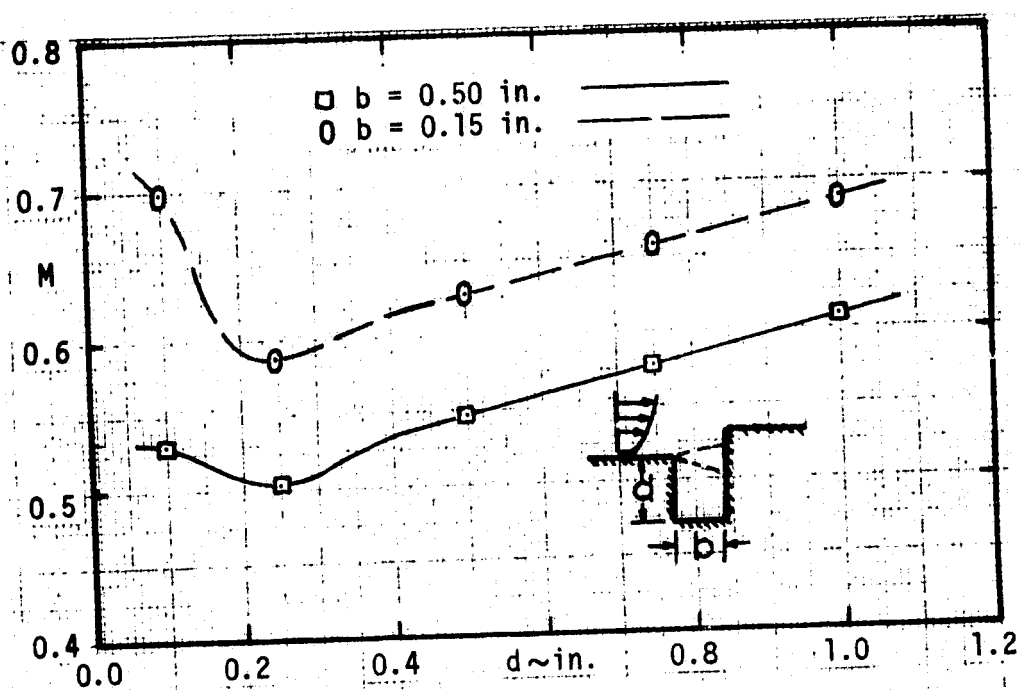


Fig. 43 Width parameter scale effects on stepped cavity correlation;
 $d = 1.00$ inch.

Ideally one curve should correlate all data; however, a cavity width parameter scale affect is unaccounted for in the correlation scheme. This width effect is further revealed in Fig. 44 where previously described straight line correlation curve slope and intercept variation with cavity depth are shown. Both the slope and intercept differ by approximately constant increments, with the exception being in the slope for a cavity depth of 0.1 inch.

Data shown in Figs. 39 through 43 near correlation curve origins corresponds to level cavity configurations. Because of the small magnitude of force contributed by level cavities compared to stepped/cavity configurations, more detail of the level cavity momentum transfer is desirable. This detail is given in Fig. 45 to expose the nature of the effect of depth on the momentum transfer for a level cavity. To give this detail, a correlation parameter group is given that is akin to that deduced by Good and Joubert⁶³ making use, however, of Eq. (93) and applied to cavities normal to the flow and at a skew to the flow direction ($\beta = 45^\circ$ for the present study). The cavity depth to momentum thickness, d/θ , provides geometry and boundary layer dependence. Assuming that b remains finite as d approaches zero, the momentum transfer by pressure is described, though roughly, by the solid-line curve on Fig. 45. Here again, however, a width effect is seen since narrow cavity correlation corresponds more nearly to the segmented line for the cavity model in the forward position on the level test-bed plate. Also, the $b = 0.50$ inch skewed cavity (with $\beta = 45^\circ$) in the forward position does not conform to the solid-line curve: this behavior is out of character for wide cavity



$$\frac{\int C_p}{\cos^2 \beta} = M \left(\frac{1}{\Delta y} \int_0^h (u/u_e)^2 dy \right) + N$$

$$\frac{-0.108b}{\cos \beta}$$

$$(\Delta y = .05 \text{ in.})$$

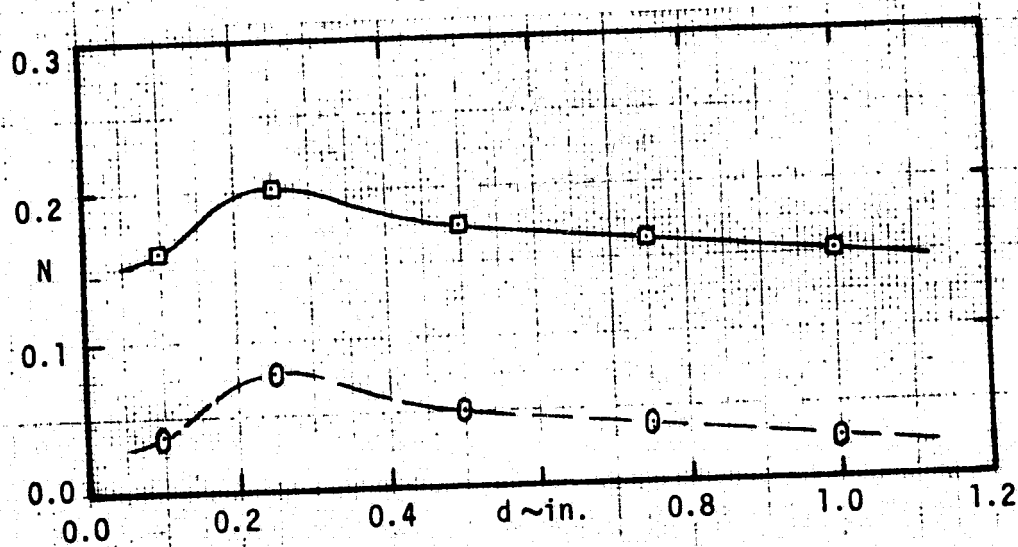


Fig. 44 Correlation slope and intercept width parameter scale effects on stepped cavities.

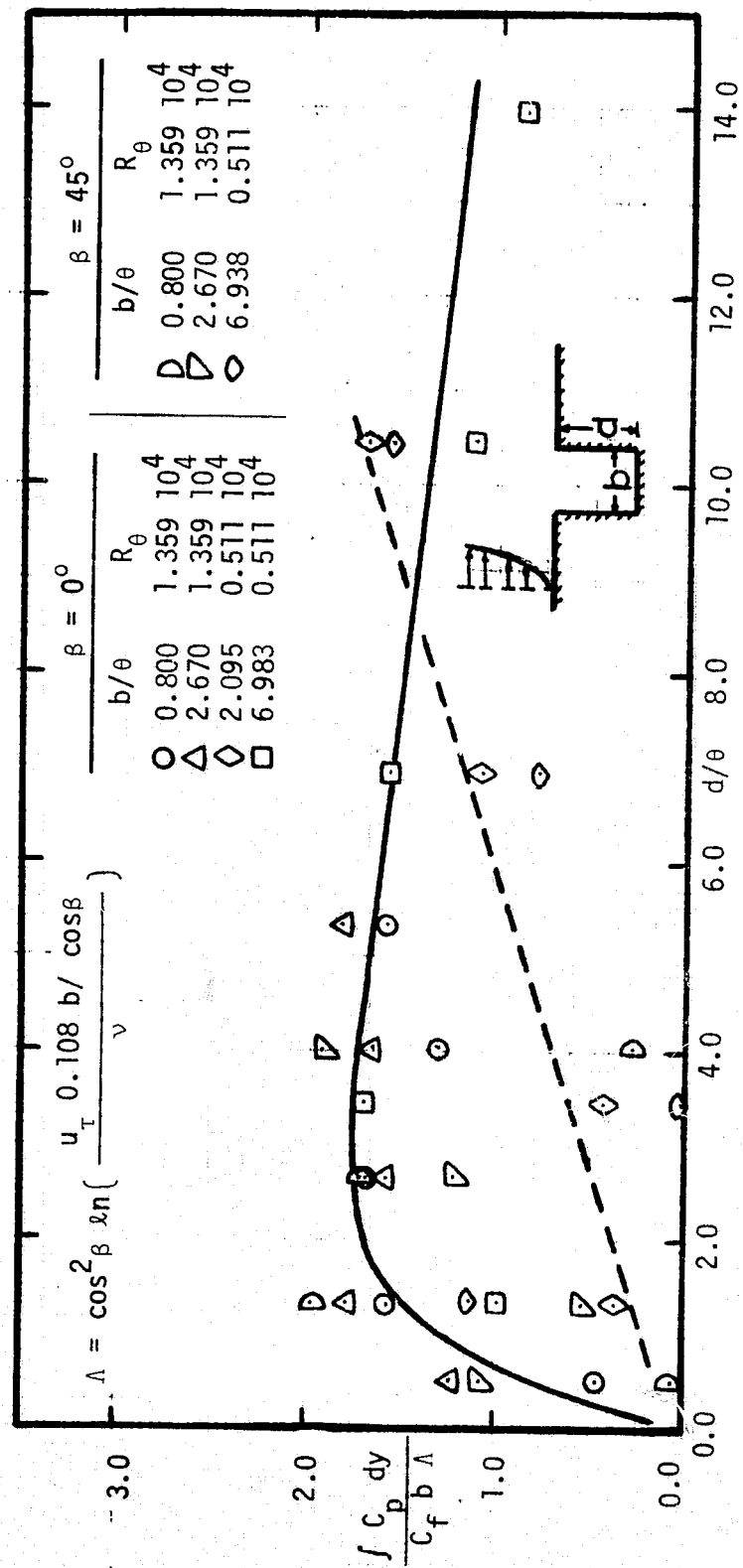


Fig. 45 Depth component effect on level cavity unification parameter correlation with boundary layer/width coupling.

configuration data.

Fig. 46 shows the kinetic pressure correlation for momentum to a simple forward-facing step. Correlation is good and may, incidentally, be deduced from Fig. 44 using the wide cavity ($b = 0.50$ inch) data.

Fig. 47 was constructed to analyze the limited amount of data for simple rearward facing steps. Data correlates to the formula deduced by Hoerner;⁷⁶ however, Tani et al²⁶ data do not. Limiting values for $C_{D,p}$ ($C_{D,p}$ at $\delta = 0.0$) due to Tanner⁷⁹ and Nash⁷⁷ are given to be 0.20 and 0.28, respectively. Data show that base pressures are not a constant and are considerably below theoretical limit values. Fig. 48 compares rearward-facing step data by and to correlation using the scheme proposed by Good and Joubert⁶³ and evaluated by Gaudet and Winter.²⁹ Correlation agreement is not good.

Surface Hot-Film Measurements

The surface hot-film sensor, located approximately 0.75 inches behind the cavity rear corner, was encased in aluminum and positioned with the longest dimension perpendicular to the flow direction. Because the hot-film sensor was not calibrated for mean or fluctuating shear stress, anemometer output voltage, V , whether average or RMS fluctuating component, is referenced to average or RMS component recorded when the cavity model had no step and no cavity gap. Thus, all voltages shown in Figs. 49 through 56 are relative to sensor voltage of the smooth flat-plate configuration. Run time was allowed for the cavity model to attain a steady-state temperature condition so that transient external temperature of the surrounding aluminum

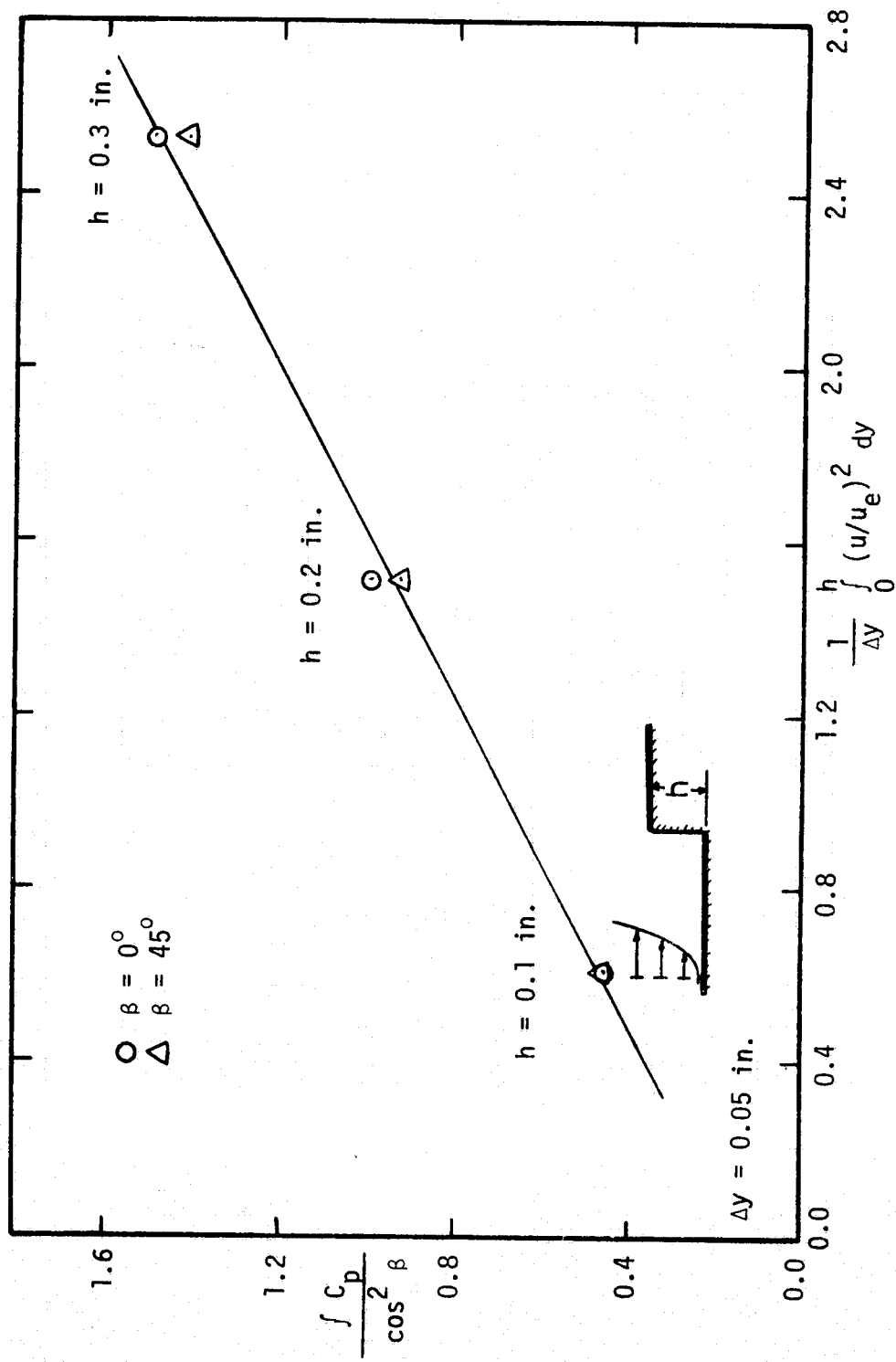


Fig. 46 Forward-facing step correlation.

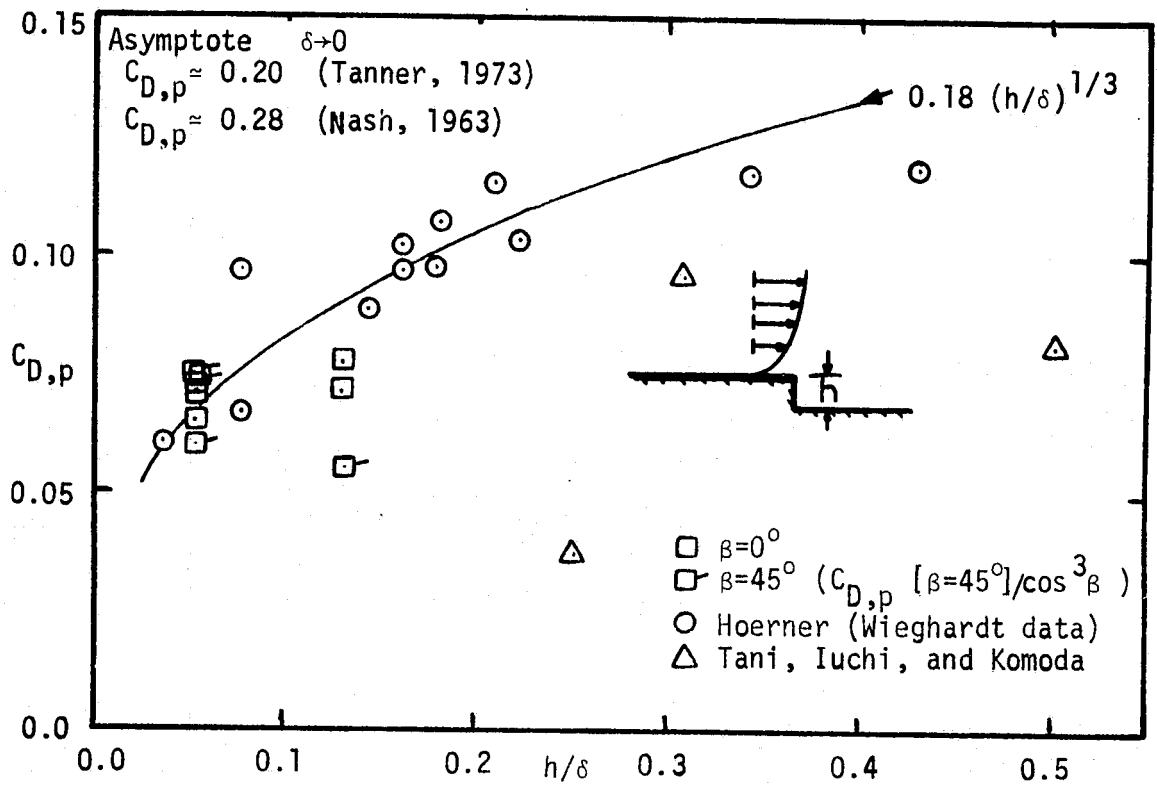


Fig. 47 Rearward-facing step correlation to h/δ .

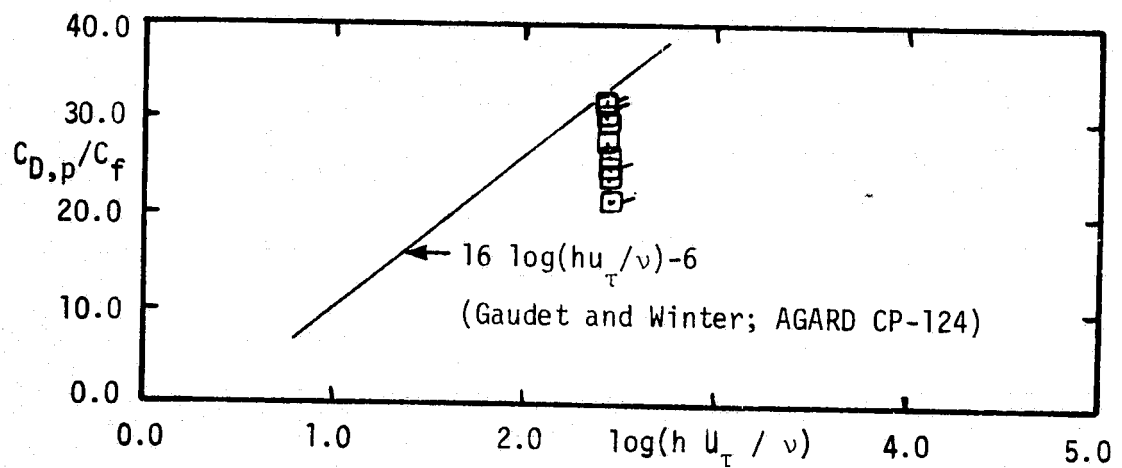


Fig. 48 Rearward-facing step correlation to $\log(hU_T/\nu)$.

environment was constant for the sensor. The sensor element was always flush to the surrounding surface, and height, depth, and width dimensions on Figs. 49 through 56 are given in inches.

Figure 49 depicts surface hot-film sensor measurement results of testing forward-facing steps without a cavity present. Also included is the rearward-facing step results where step height is -0.1 inch. As described previously, straight line segments connecting data of the linearized anemometry signals are strictly used to distinguish and not interpret or predict. The average component is minimum for the rearward-facing step and is approximately constant for forward-facing steps. This may indicate that the average shear stress is low and the sensor is within the separated region behind a stepdown. Average shear may be nearly constant atop the steps. Whereas; the fluctuating component is minimum for the level surface and larger for the -0.1 stepdown. The fluctuating component for forward-facing steps is larger than that for the level surface and an increase with increasing step height is evident. It is probable, however, that the fluctuating component is bounded and would reach a peak value dependent on the structure of the boundary layer. The reference boundary layer profile for the data shown on Fig. 49 is given on Figs. 32, 34, and 35 and in Appendix C on Fig. C-5. Literal interpretation of hot film sensor results presented regarding shear stress should be avoided because of difficulties involving single element anemometer output in a highly turbulent, separated, and/or reverse flow situation. Signals to voltmeters are rectified and meters may give fallacious indications of both mean and RMS voltage.

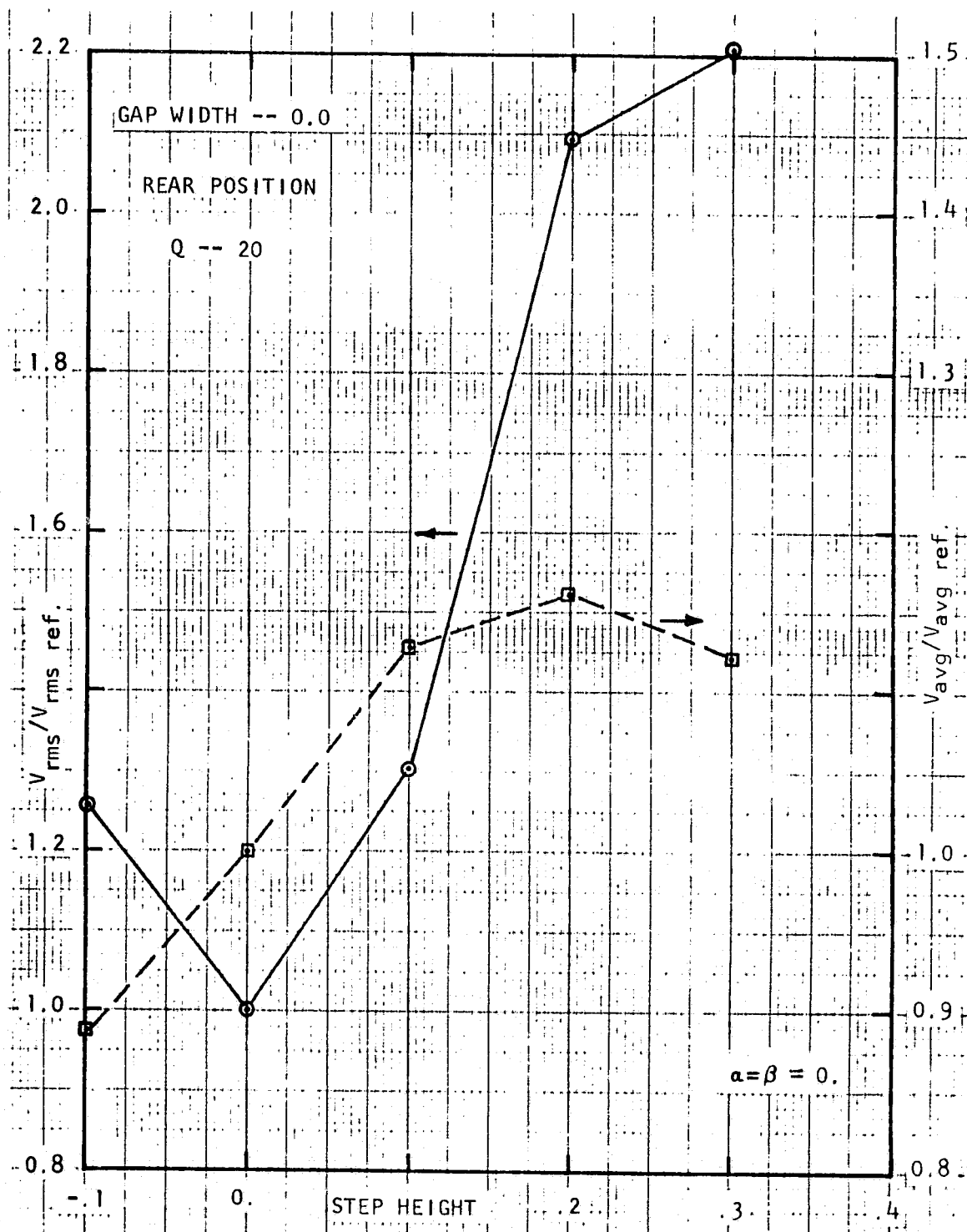


Fig. 49 Surface sensor mean and RMS components for a forward-facing step.

The most unusual finding with the present results is that mean and RMS components are often larger than smooth flat plate components. Kaul and Frost⁹¹ present data that show flow reattachment at approximately 7.5 step heights down stream of a rearward-facing step. Within the separated cell behind a stepdown, mean shear stress should be very low when compared to that of flat plate mean shear stress. In fact, within the large separation cell shear forces contribute a thrust force component as opposed to a drag force. At 12.5 step heights behind a rearward-facing step the flow may be reattached and formation of a new surface shear layer would be in progress. Flow redevelopment may occur over 18 to 20 step heights back of the step, and up to the point of equilibrium reattainment mean shear stress is lower than that on a smooth flat plate. Bitte and Frost⁷⁵ predict reattachment at less than four step heights behind the separation point aft of the forward-facing step. With $h = 0.3$ inch, the sensor should be within the cell. With $h = 0.2$ inch the sensor should be near the reattachment point, and for $h = 0.1$ inch the sensor should be behind the cell. For these three steps the shear stress should also be less than the smooth flat plate shear stress. The present findings using the sensor may be questioned with regard to using the sensor as a means of predicting local shear stress relative to smooth flat plate shear stress.

The results shown in Fig. 50 for surface film sensor RMS component bear some resemblance to pressure integral data presented on Fig. 22. The exception is in the relationship between the level and the backward-facing stepped/cavity. In Fig. 50, data for stepped/cavities

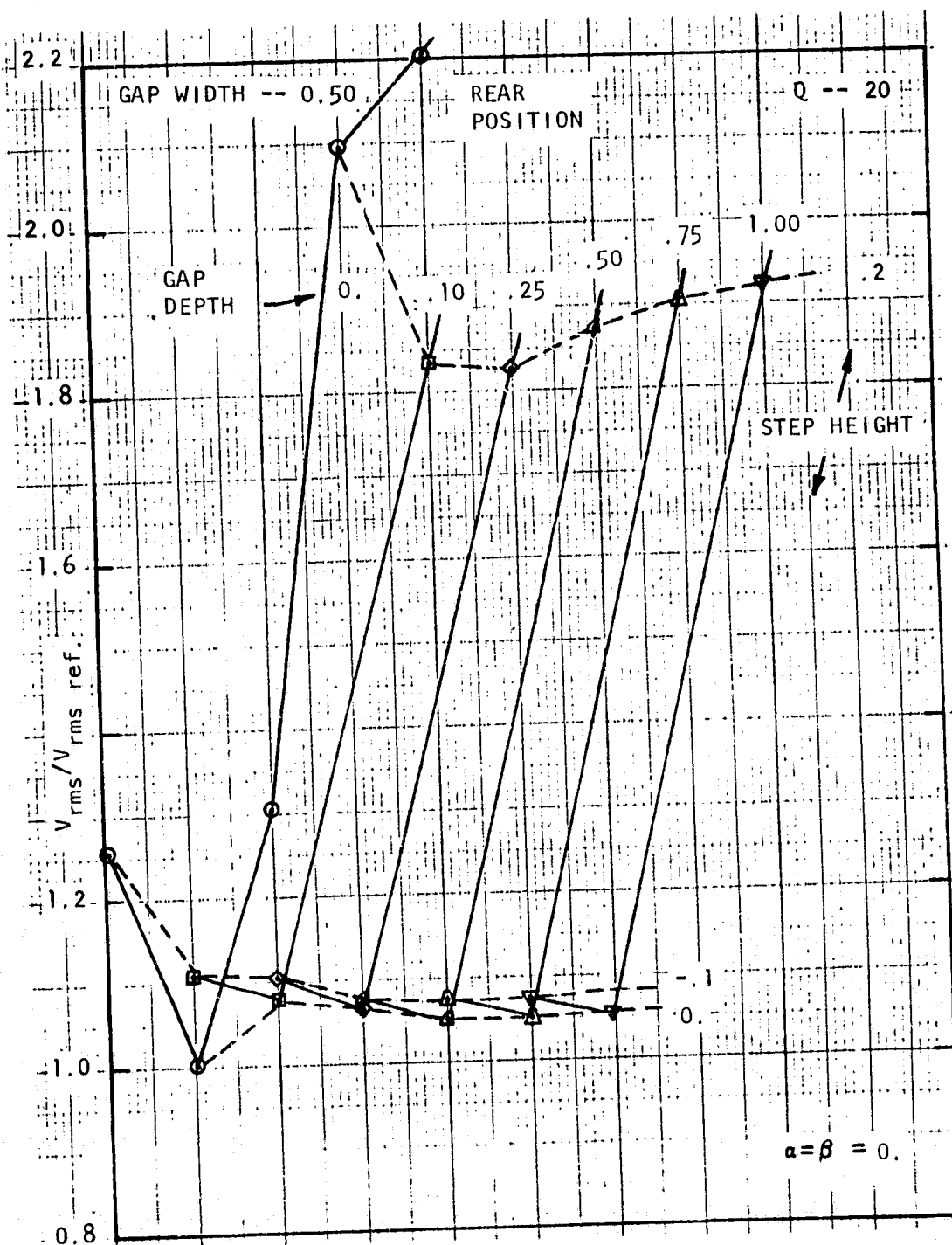


Fig. 50 Surface sensor RMS components for a stepped cavity; $b = 0.50$ inch, $Q = 20$ psf, rear position.

of constant step height are connected by segmented lines and solid lines connect data for a constant cavity gap depth. Similarly, results for the RMS component of voltage in Fig. 51 appear to resemble pressure integration results shown in Fig. 25. A third comparison between Fig. 52 and Fig. 24 show similarity between relative RMS voltage components and pressure integral used to predict momentum transfer to the $b = 0.50$ inch stepped/cavity in the forward position on the test-bed plate. It is believed that the surface sensor RMS component represents, though indirectly, the momentum transfer to the stepped/cavities tested; however, a comprehensive analysis using several surface sensors at other positions on the model would be necessary to ascertain the validity of this belief. In addition, pressure measurements and flow visualization techniques should be employed.

Figure 53 shows the effect of sensor placement on mean (average) and RMS sensor relative voltage for the sensor -0.1 inch below the front corner and 0.75 and 1.25 inches behind the backward-facing step wall. Two tunnel dynamic pressures ($Q = 20$ and $Q = 40$ psf) are indicated. For $h = -0.1$ and $d = 0.1$ inches, the surface behind the step wall is level. Little difference at the different Q is found when the sensor is 1.25 inches back; however, with the sensor 0.75 inch back, the mean and RMS components decrease with increase in Q . This behavior may be attributed to the structure of the base flow vortices within the separation cell behind the 0.1 inch down step. It is unlikely that data give a measure of the vortices strength since the strength of the previously described single large vortex may increase

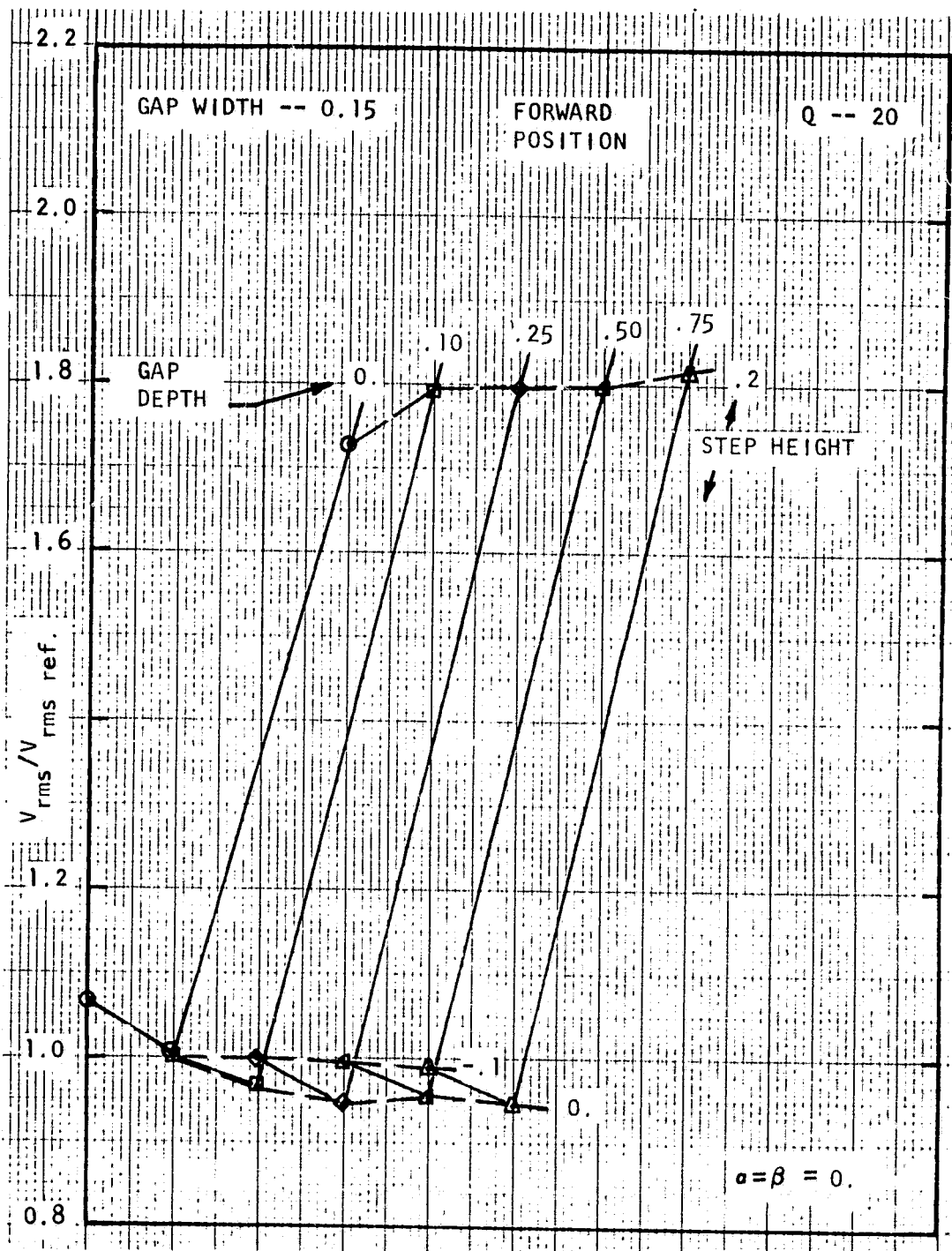


Fig. 51 Surface sensor RMS components for a stepped cavity; $b = 0.15$ inch, $Q = 20$ psf, forward position.

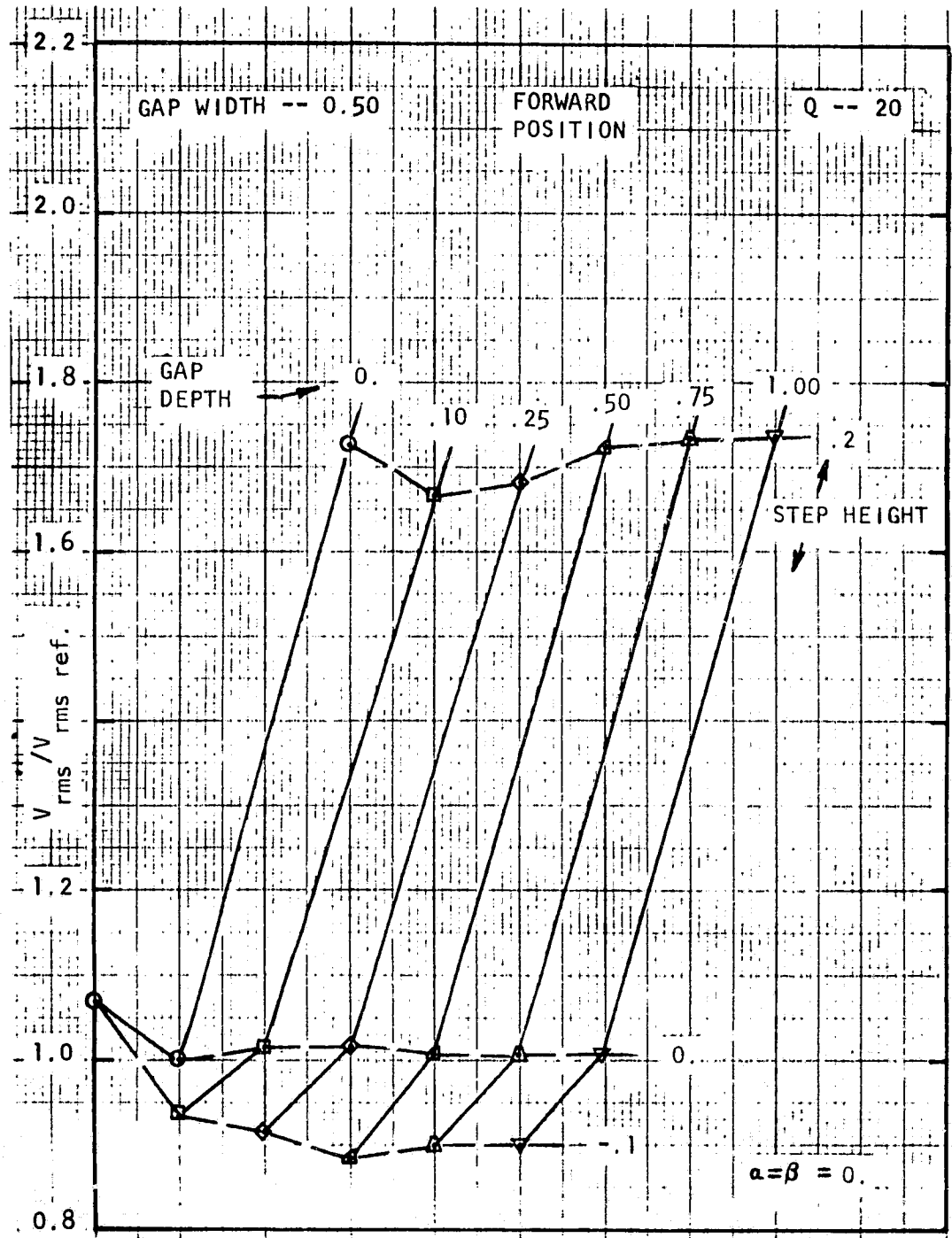


Fig. 52 Surface sensor RMS component for a stepped cavity;
 $b = 0.50$ inch, $Q = 20$ psf, forward position.

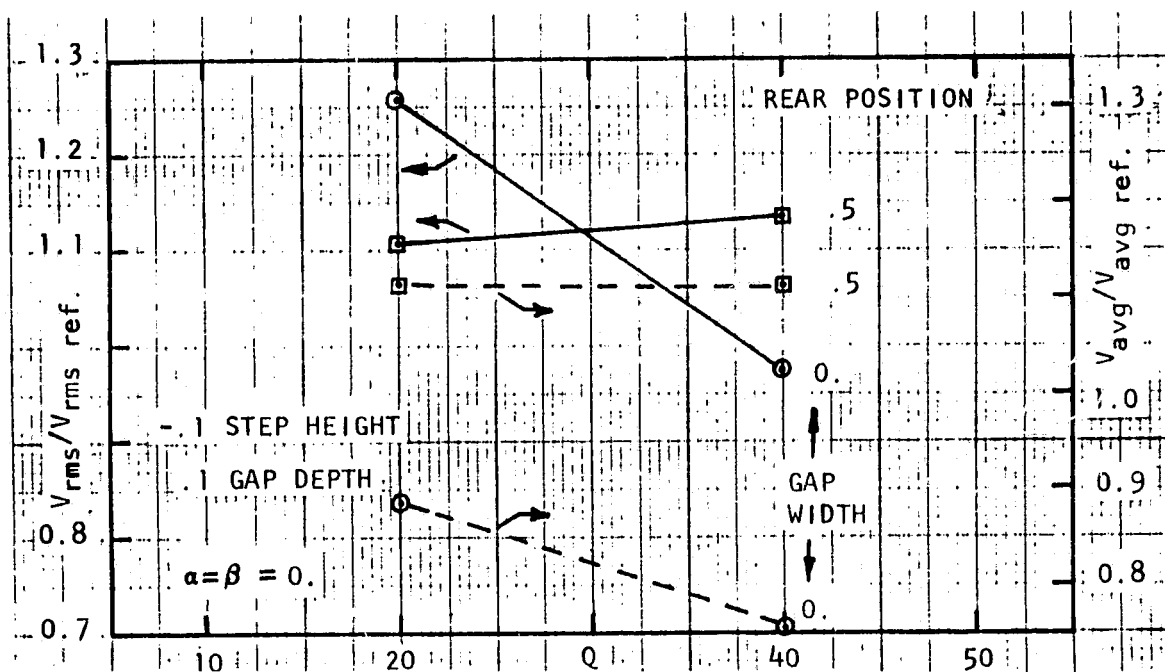


Fig. 53 Effect of position aft of rearward-facing step corner on surface sensor mean and RMS components at different tunnel Q .

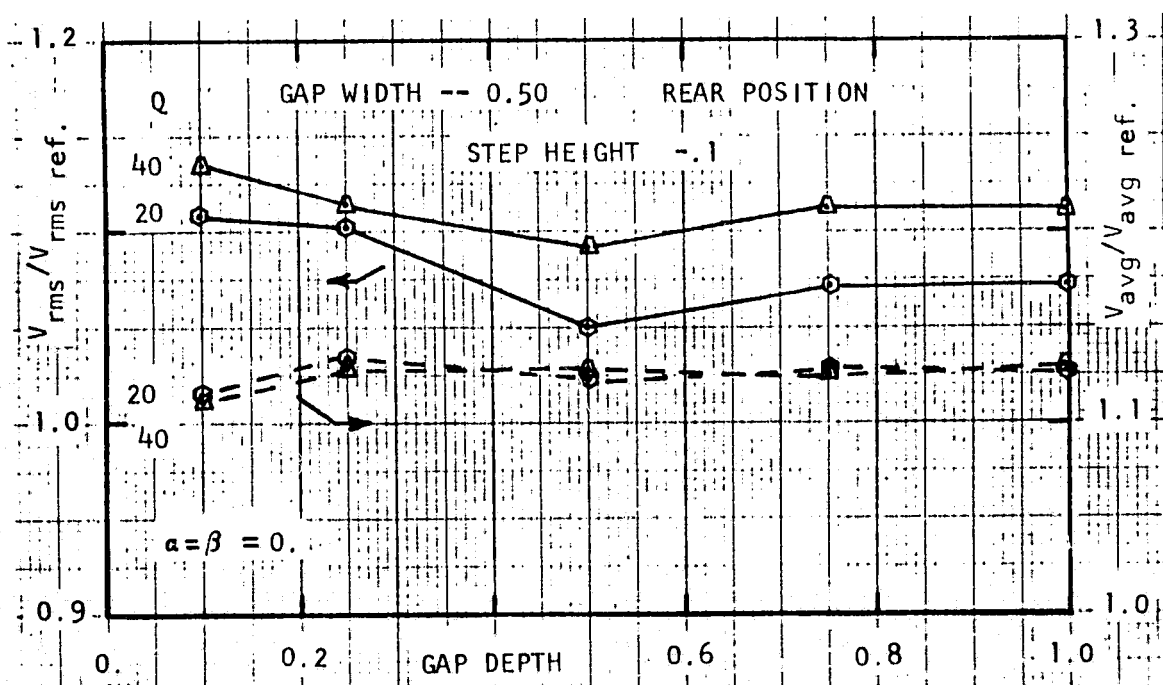


Fig. 54 Effect of different cavity gap depths on mean and RMS sensor voltage components; $Q = 20$ and 40 psf.

with increasing free stream velocity.

The effect of different cavity gap depths on the mean and the RMS sensor voltage components is shown in Fig. 54. A $b = 0.50$ inch cavity gap width behind a 0.10 inch step down is the configuration which was considered. Data indicate that the cavity depth has little effect on the flow over the backward-facing step. The separation cell extends over the cavity, and the cavity may only slightly influence the flow within the cell. The RMS component differs for $Q = 20$ and $Q = 40$ psf by approximately a constant increment. This difference may be attributed to a higher turbulence within the reattaching flow at higher velocity although proof of this will require a more thorough experiment. Data from Fig. 54 was taken with the sensor 12.5 step heights behind the rearward-facing wall.

With the sensor 7.5 step heights behind the rearward-facing 0.1 inch step both mean and RMS component of relative voltage decrease with increasing free-stream velocity. This is seen in Fig. 55 where only at $Q = 40$ are the mean and RMS components less than the smooth-flat plate mean and RMS voltages. Tunnel Q equal to 5, 10, 20, and 40 psf correspond approximately to $q_e = 6.7, 13.1, 26.7,$ and 52.4 psf, respectively.

Except for sensor data shown on Figs. 51 and 52, hot-film sensor data was for the cavity model in the rear position. Figure 56, however, shows the effect on mean and RMS relative voltage with change in sensor element position for the step/cavity model in the forward position on the test bed plate. At cavity gap widths of 0.0, 0.15, and 0.50 inches the sensor is 0.75, 0.90, and 1.25 inches behind the

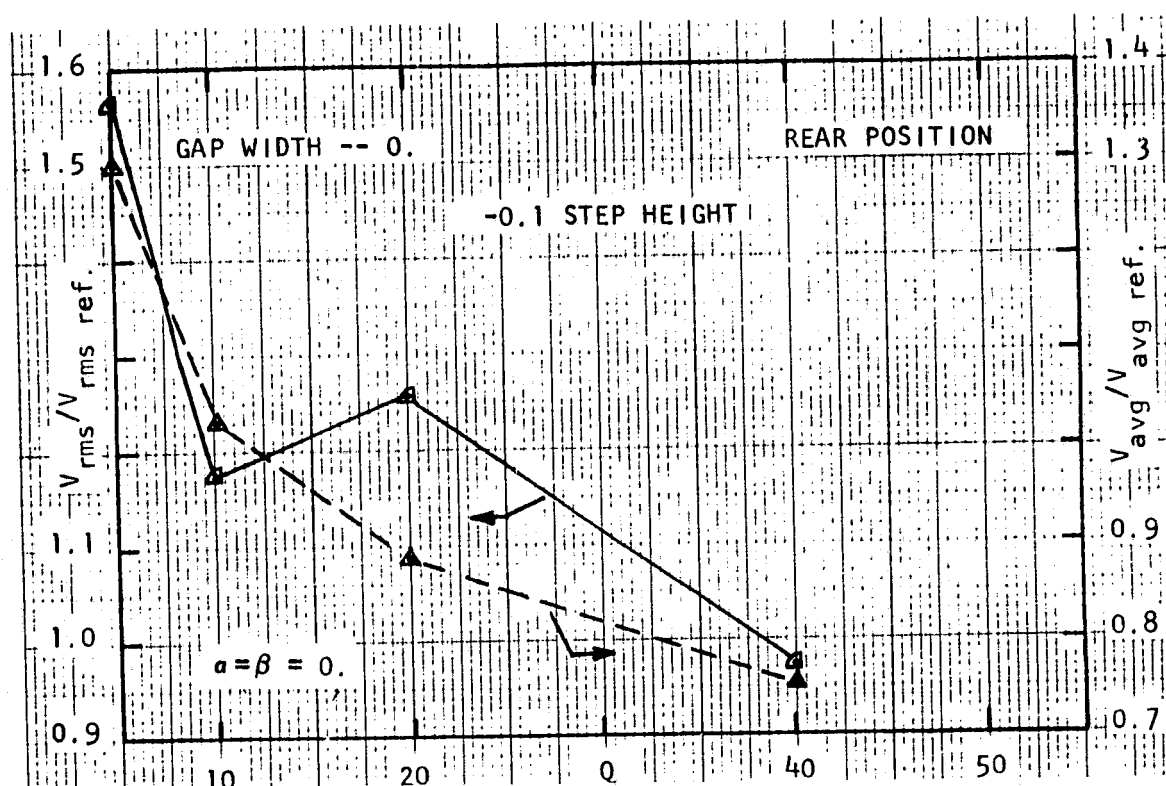


Fig. 55 Effect of tunnel Q on surface sensor for a rearward-facing step; sensor 8 step heights behind step.

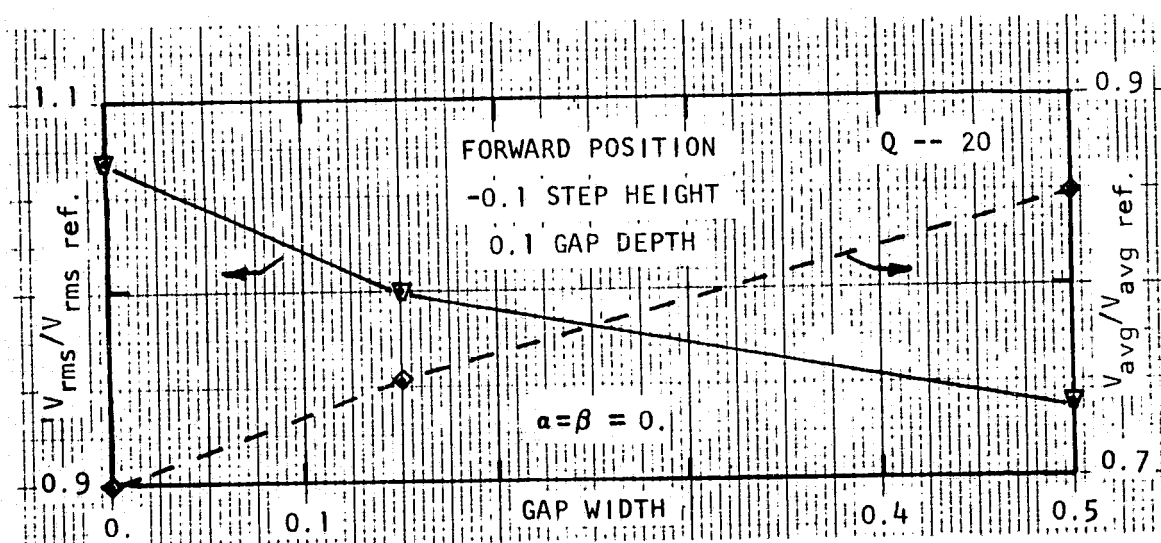


Fig. 56 Mean and RMS sensor components for different aft positions with a backward-facing step.

rearward-facing step wall. A decrease in RMS component and an increase in mean or average component with increasing cavity gap width is in agreement with data shown on Fig. 53 for $Q = 20$. The trend of increasing RMS with increasing sensor distance at $Q = 40$ shown on Fig. 53 is, however, different from findings at $Q = 20$. It is thus possible to argue that sensor mean component may be related to mean shear stress (the increase in shear after reattachment and during redevelopment with increase in distance behind the step down is expected).

Additional testing with surface hot-film sensors would be required, however, to establish quantitative understanding of the stepped/cavity flow and the influence of cavity depth, step height, and sensor placement.

CONCLUSIONS AND RECOMMENDATIONS

Conclusions

The following conclusions are drawn from the experimental and analytical findings of this study:

1. Pressure measurements taken along step/cavity walls provide data which can be used to predict momentum transfer to the step/cavity from the overriding boundary layer. A heretofore untested cavity model configuration matrix was used during experiments.
2. Correlation of experimental pressure measurement force coefficient to a kinetic pressure model developed using undisturbed velocity profile of the boundary layer is possible; however, adequate representation of the correlation to account for all effects of cavity depth and cavity width is not possible. Little improvement using inner-layer boundary layer parameters is possible to account for depth dependency and width size dependency on level cavities.
3. The kinetic pressure model is not possible for a rearward-facing step/cavity since shear layer impingement does not occur on the down stream wall. It is not possible to define an effective wall height necessary in applying the kinetic pressure model. For step/cavities used in experiments, separated flow from the forward corner reattached behind the rear corner on the level surface behind the cavity. Rearward-facing step drag coefficient found in experiments does,

however, agree with Hoerner's⁷⁶ correlation.

4. The momentum transfer to level cavities and stepped/cavities with cavity walls perpendicular to and skew to the flow direction is determined by a different mechanism than that which determines the momentum transfer to a rearward-facing wall step/cavity with flow attachment beyond the rear corner.
5. Surface hot-film sensor data shows similarity to momentum transfer data derived from pressure surveys. Clear and concise interpretations of surface hot-film sensor data is not possible, however, because necessary complementary studies of the pressure and velocity field behind step/cavity configurations were not conducted.
6. The kinetic pressure model developed for this study depends on prescribing a separated jet wake flow which matches the boundary layer at the upper edge of the jet shear layer. Momentum balancing was used to describe the shape of the separated jet wake by considering cavity geometry, cavity skew angle, and the mean velocity profile of an incompressible turbulent boundary layer. Additional considerations may be necessary to improve this model. It is not presently possible, however, to develop an accurate numerical solution for stepped/cavity flow without resorting to empiricism. Existing numerical solutions for forward-facing or rearward-facing steps depend on empirical correlations and are incapable of accurately predicting wall pressures.
7. With regard to tiled surface drag predictions, the kinetic

pressure model, when used with empirical protuberance drag data and a smooth surface drag prediction is suitable for predicting tiled-surface drag. The method of variable roughness-density phenomenology was not suitable for predicting the trend of mean shear-drag coefficient over the range of Reynold's numbers tested. It is expected that the kinetic pressure model may be used at Reynolds' numbers higher than those of this test program.

Recommendations

Some topics for further study are recommended in this section. These topics are primarily to further verify and expand the knowledge of stepped/cavity flow. Recommendations are to:

1. Map the entire velocity and pressure field around and in the stepped/cavity model.
2. Use flow visualization techniques to provide a record of separation and reattachment before, behind, and in the stepped/cavity model.
3. Develop a numerical method for predicting the surface pressure distribution about the corner of a semi-infinite two-dimensional block. Flow approaching the block should be of a general profile shape.
4. Design and test a stepped/cavity model similar to the model of this test program which may be used to get direct force measurements.
5. Investigate to determine if cavity resonance occurs and how

resonance affects step/cavity drag.

REFERENCES

- ¹Roshko, A., "Some Measurements of Flow in a Rectangular Cutout," NACA TN 3488, 1955.
- ²Fox, J., "Surface Pressure and Turbulent Airflow in Transverse Rectangular Notches," NASA TN D-2501, November 1955.
- ³Fox, J., "Flow Regimes in Transverse Rectangular Cavities," Proceedings of the 1965 Heat Transfer and Fluid Mechanics Institute, Stanford University Press, June 1965, pp. 230-247.
- ⁴Maul, D.J., and East, L.F., "Three-Dimensional Flow in Cavities," Journal of Fluid Mechanics, Vol. 16, 1963, pp. 620-632.
- ⁵Krishnamurty, K., "Acoustic Radiation From Two-Dimensional Rectangular Cutouts in Aerodynamic Surfaces," NACA TN D-3487, Aug. 1955.
- ⁶Plumbee, H.E., Gibson, J.S., and Lassiter, L.W., "A Theoretical and Experimental Investigation of the Acoustic Response of Cavities in an Aerodynamic Flow," WADD-61-75 (AD277803), March 1962.
- ⁷Quinn, Brian, "Flow in the Orifice of a Resonant Cavity," AIAA Student Journal, Vol. 1, No. 1, April 1963, pp. 1-5.
- ⁸Rossiter, J.E., "Wind Tunnel Experiments on the Flow over Rectangular Cavities at Subsonic and Transonic Speeds," A.R.C. R&M 3438, October 1964.
- ⁹Karamecheti, K., et al, "Some Features of an Edge-Tone Flow Field," NASA SP-207, July 1969, pp. 275-304.
- ¹⁰McGregor, O., Jr., Aerodynamic Drag of Two-Dimensional Rectangular Notches in Transonic and Supersonic Turbulent Flow (with Emphasis on the Effects of Self-induced Pressure Oscillations), Ph.D. Thesis, Aeronautical Engineering, University of Illinois, 1969.
- ¹¹McGregor, O.W., and White, R.A., "Drag of Rectangular Cavities in Supersonic and Transonic Flow Including the Effects of Cavity Resonance," AIAA J., Vol. 8, No. 11, November 1970, pp. 1959-1964.
- ¹²Fenton, D.L., and White, R.A., "Heat Transfer in Resonant Cavities Spanned by Low Speed, Turbulent, Shear Layers," Journal of Basic Engineering, ASME, September 1971, pp. 455-457.

¹³White, R.A., "Some Results on the Heat Transfer within Resonant Cavities at Subsonic and Supersonic Mach Numbers," Journal of Basic Engineering, ASME, December 1971, pp. 537-542.

¹⁴Bilanin, A.J., and Covert, E.E., "Estimation of Possible Excitation Frequencies for Shallow Rectangular Cavities," AIAA Journal, Vol. 11, No. 3, 1973, pp. 347-351.

¹⁵Hardin, Jay C., and Mason, Jean P., "A Vortex Model of Cavity Flow," 3rd AIAA Aero-Acoustics Conference paper 76-524, Palo Alto, CA., July 1976.

¹⁶Rockwell, D., "Prediction of Oscillation Frequencies for Unstable Flow Past Cavities," Journal of Fluids Engineering, ASME, June 1977, pp. 294-300.

¹⁷Sarohia, Virendra, "Experimental Investigation of Oscillations in Flow over Shallow Cavities," AIAA Journal, Vol. 15, No. 7, July 1977, pp. 984-991.

¹⁸East, L.F., "Aerodynamic Induced Resonance in Rectangular Cavities," Journal of Sound and Vibrations, Vol. 3, March 1966, pp. 277-287.

¹⁹Yu, Yung H., "Measurements of Sound Radiation from Cavities at Subsonic Speeds," 3rd AIAA Aero-Acoustics Conference paper 76-529, Palo Alto, CA., July 1976.

²⁰Mabey, Dennis, "Analysis and Correlation of Data on Pressure Fluctuations in Separated Flow," Journal of Aircraft, Vol. 9, No. 9, September 1972, pp. 642-645.

²¹Heller, Hanno H., and Bliss, Donald B., "The Physical Mechanism of Flow-Induced Pressure Fluctuations in Cavities and Concepts for Their Suppression," 2nd AIAA Aero-Acoustics Conference paper 75-491, Hampton, VA, March 1975.

²²Borland, C.J., "Numerical Prediction of the Unsteady Flowfield in an Open Cavity," 10th AIAA Fluid & Plasma Dynamics Conference paper 77-673, Albuquerque, N.M., June 1977.

²³Chin, E., Rafiinejad, D., and Seban, R.A., "Prediction of the Flow and Heat Transfer in a Rectangular Wall Cavity with Turbulent Flow," Journal of Applied Mechanics, Vol. 39, Series E, No. 2, June 1972, pp. 351-358.

²⁴Wieghardt, K., "Erhöhung des turbulenten Reibungswiderstandes durch Oberflächenstörungen," Forschungsbericht 1953, S W B, March 19, 1942 (also Jahrb., deutschen Luftfahrtforschung, 1943).

²⁵Tillmann, W., "Additional Measurements of the Drag of Surface Irregularities in Turbulent Boundary Layers," NACA TM 1299, January 1951.

²⁶Tani, I., Iuchi, M., and Komoda, H., "Experimental Investigation of Flow Separation Associated with a Step or a Groove," Aeronautical Research Institute, University of Tokyo, Report No. 364, April 1961.

²⁷Hoerner, S.F., Fluid Dynamic Drag, Published by the Author (148 Busted Drive, Midland Park, N.J.), 1965.

²⁸Charwat, A.F., Roos, J.N., Dewey, F.C., Jr., and Hitz, J.A., "An Investigation of Separated Flow - Part I: The Pressure Field," Journal of the Aerospace Sciences, June 1961, pp. 457-470.

²⁹Gaudet, L., and Winter, K.G., "Measurements of the Drag of Some Characteristic Aircraft Excesses Immersed in Turbulent Boundary Layers," AGARD CP-124 Aerodynamic Drag, April 1973.

³⁰Haugen, R.L., and Dhanak, A.M., "Momentum Transfer in Turbulent Separated Flow Past a Rectangular cavity," J. of Applied Mechanics, September 1966, pp. 641-646.

³¹Norton, D.J., and White, R.E., "Drag Characteristics of the Space Shuttle Orbiter TPS System," TEES-1086-TR-75-10, Texas A&M University, November 1975.

³²Norton, D.J., and White, R.E., "Experimental Subsonic Drag Properties of the Space Shuttle Orbiter TPS Tiles," Journal of Spacecraft and Rockets, Vol. 14, No. 3, March 1977, pp. 149-154.

³³Schlichting, H., Boundary Layer Theory, 4th ed., McGraw-Hill Book Co., New York, 1960, Chap. XXI.

³⁴Chang, P.K., Separation of Flow, Pergamon Press, Oxford, England, 1970, Chap. VII.

³⁵Charwat, A.F., Roos, J.N., Dewey, F.C., Jr., and Hitz, J.A., "An Investigation of Separated Flows - Part II: Flow in the Cavity and Heat Transfer," Journal of the Aerospace Sciences, July 1961, pp. 513-527.

³⁶Tollmien, Walter, "Calculation of Turbulent Expansion Processes," NACA TM 1085, September, 1945.

³⁷Abramovich, G.N., The Theory of Turbulent Jets, MIT Press, Cambridge MA., 1963.

³⁸Surber, T.E., "Estimation of Orbiter TPS Drag Increment," North American Rockwell SAS/AERO/73-720, February 1974.

³⁹Chapman, D.R., "A Theoretical Analysis of Heat Transfer in Regions of Separated Flow," NACA TN 3792, Oct. 1956.

⁴⁰Chung, P.M., and Viegas, J.R., "Heat Transfer at the Re-attachment Zone of Separated Laminar Boundary Layers," NASA TND-1072, Sept. 1961.

⁴¹Adams, J.C., Jr., "Numerical Calculation of Hypersonic Laminar Cavity Flows," AIAA/ASME 1974 Thermophysics and Heat Transfer Conference paper AIAA No. 74-707, Boston MA., July 1974.

⁴²Kistler, Alan L., and Tan, Felix C., "Some Properties of Turbulent Separated Flow," Boundary Layers and Turbulence, Proceedings of an International Symposium on Boundary Layers and Turbulence, The Physics of Fluids Supplement 1967, Kyoto, Japan, September 1966, pp. S165-S173.

⁴³Pai, S.I., Fluid Dynamics of Jets, D. Van Nostrand, Princeton, N.J., 1954.

⁴⁴Rajaratnam, N., Turbulent Jets, Development in Water Science #5, Elsevier, New York, N.Y., 1976.

⁴⁵White, Frank M., Viscous Fluid Flow, McGraw-Hill, Inc., New York, N.Y., 1974.

⁴⁶Batchelor, G.K., "Note on Free Turbulent Flows, with Special Reference to the Two-Dimensional Wake," Journal of the Aeronautical Sciences, Vol. 17, No. 7, July 1950, pp. 441-445.

⁴⁷Liepmann, Hans Wolfgang, and Laufer, John, "Investigations of Free Turbulent Mixing," NACA TN 1257, August 1947.

⁴⁸Elassar, R.J., and Pandolfini, P.P., "An Examination of Eddy Viscosity Models for Turbulent Free Shear Flows," Journal of Basic Engineering, ASME, December 1971, pp. 614-630.

- ⁴⁹Islam, Obaidul, A Study of Three-Dimensional Incompressible Free Turbulent Air Jets, Ph.D. Thesis, Mechanical Engineering, Arizona State University, 1969.
- ⁵⁰Corrsin, S., and Kistler, A.L., "The Free-Stream Boundaries of Turbulent Flows," NACA TN 3133, Jan. 1954.
- ⁵¹Townsend, A.A., The Structure of Turbulent Shear Flow, Cambridge University Press, New York, N.Y., 1956.
- ⁵²Hinze, J.O., Turbulence, McGraw-Hill Book Co., New York, N.Y., 1959.
- ⁵³Sforza, Pasquale M., Trentacoste, Nicholas, and Mons, Robert, "Turbulent Mixing: A Review, Revaluation, and Extension," AIAA 7th Aerospace Sciences Meeting paper 69-31, New York, N.Y., January 1969.
- ⁵⁴Chow, W.L., and Korst, H.H., "On the Flow Structure within a Constant Pressure Compressible Turbulent Jet Mixing Region," NACA TN D-1894, April 1963.
- ⁵⁵Camarata, F. Justin, "A Method for Determining the Effect of Initial Boundary Layer on Turbulent Free Shear Layer Velocity Profiles," Journal of Basic Engineering, December 1971, pp. 713-715.
- ⁵⁶Birch, S.F., Rudy, D.H., Bushnell, D.M., and Eggers, J.M., eds., "Free Turbulent Shear Flow: Volume I - Conference Proceedings/ Volume II - Summary of Data," NASA SP-321, July 1972.
- ⁵⁷Kline, S.J., Morkorin, M.V., Sovran, G., and Cockrell, D.J., eds., Computation of Turbulent Boundary Layers - 1968 AFOSR-IFP Stanford Conference, Vol. I - Methods, Predictions, Evaluation and Flow Structure, Stanford University, California, August 1968.
- ⁵⁸Gauntner, James W., Livingood, John N.B., and Hrycak, Peter, "Survey of Literature on Flow Characteristics of Single Turbulent Jet Impinging on a Flat Plate," NASA TN-D 5652, February 1970.
- ⁵⁹Tani, I., and Komatsu, Y., "Impingement of a Round Jet on a Flat Surface," Proceedings of the Eleventh International Congress of Applied Mechanics, H. Gortner, ed., Springer-Verlag, 1966, pp. 672-676.
- ⁶⁰Johnson, R.T., "An Approximate Model for the Static Operation of a Fluidic Amplifier Employing Axisymmetric Jets," Journal of Basic Engineering, ASME, March 1971, pp. 47-54.

⁶¹Beltaos, Spyridon, "Oblique Impingement of Plane Turbulent Jets," Journal of the Hydraulics Division, Proceedings of the American Society of Civil Engineers, Vol. 102, No. HY9, September 1976, pp. 1177-1192.

⁶²Bradshaw, P., and Galea, P.V., "Step-induced Separation of a Turbulent Boundary Layer in Incompressible Flow," Journal of Fluid Mechanics, Vol. 27, Part 1, 1967, pp. 111-130.

⁶³Good, M.C., and Joubert, P.N., "The Form Drag of Two-Dimensional Bluff-Plates Immersed in Turbulent Boundary Layers," Journal of Fluid Mechanics, Vol. 31, Part 3, 1968, pp. 547-582.

⁶⁴Plate, Erich J., Aerodynamic Characteristics of Atmospheric Boundary Layers, Chapter 4, AEC Critical Review Series, USAEC Technical Information Center, Oak Ridge, TN, March 1972.

⁶⁵Gaudet, L. et al, "Drag of Two-Dimensional Steps and Ridges Immersed in a Turbulent Boundary Layer at Subsonic and Supersonic Speeds," Royal Aeronautical Society Engineering Sciences Data Item No. 73028, October 1973.

⁶⁶Nash, J.F., and Bradshaw, P., "The Magnification of Roughness Drag by Pressure Gradient," Journal of the Royal Aeronautical Society, Vol. 71, January 1967, pp. 44-46.

⁶⁷Pallister, K.C., "Wind Tunnel Measurements of the Transonic Drag of Excrescences Immersed in a Turbulent Boundary Layer," ARA Report No. 37, Aircraft Research Association Limited, Bedford, England, December 1974.

⁶⁸Kovalenko, V.M., and Nesterovich, N.I., "The Drag of Ridges of Finite Length in a Turbulent Boundary Layer," Royal Aircraft Establishment Library Translation 1852, May 1975, N76-10410.

⁶⁹Wu, J.M., and Chen, C.H., "Experimental Study of Compressible Turbulent Boundary Layer Separation as Influenced by Upstream Disturbances," AIAA 8th Fluid and Plasma Dynamics Conference paper 75-830, Hartford, CT, June 1975.

⁷⁰Czarnecki, K.R., and Jackson, M.W., "Turbulent Boundary-Layer Separation due to a Forward-Facing Step," AIAA Journal, Vol. 13, No. 2, December 1975, pp. 1585-1591.

⁷¹Ota, Terukazu, and Itasaka, Masaaki, "A Separated and Reattached Flow on a Blunt Flat Plate," Journal of Fluids Engineering, Transactions

of the ASME, March 1976, pp. 79-86.

⁷²Robertson, J.M., and Taulbee, D.B., "Turbulent Boundary Layer and Separation Flow Ahead of a Step," Developments in Mechanics, Vol. 5, Proceedings of the 11th Midwest Mechanics Conference, Ames, Iowa, Iowa State University Press, 1969, pp. 171-190.

⁷³Taulbee, D.B., and Robertson, J.M., "Turbulent Separation Analysis Ahead of a Step," Journal of Basic Engineering, Transactions of the ASME, September 1972, pp. 544-550.

⁷⁴Raju, K.G. Ranga, Loeser, J., and Plate, E.J., "Velocity Profiles and Fence Drag for a Turbulent Boundary Layer Along Smooth and Rough Flat Plates," Journal of Fluid Mechanics, Vol. 76, Part 2, 1976, pp. 383-399.

⁷⁵Bitte, Juergen, and Frost, Walter, "Atmospheric Flow over Two-Dimensional Bluff Surface Obstructions," NASA CR-2750, October, 1976.

⁷⁶Hoerner, Sigward F., "Base Drag and Thick Trailing Edges," Journal of the Aeronautical Sciences, Vol. 17, No. 10, October 1950, pp. 622-628.

⁷⁷Nash, J.F., "An Analysis of Two Dimensional Turbulent Base Flow, Including the Effect of the Approaching Boundary Layer," ARC R&M No. 3344, July 1963.

⁷⁸McDonald, H., "Turbulent Shear Layer Re-Attachment with Special Emphasis on the Base Pressure Problem," The Aeronautical Quarterly, August 1964, pp. 247-280.

⁷⁹Tanner, M., "Theoretical Prediction of Base Pressure for Steady Base Flow," Progress in Aerospace Sciences, Vol. 14, Pergamon Press, Oxford, England, 1973, pp. 177-225.

⁸⁰Tanner, M., "The Pressure at the Reattachment Point in Subsonic Two-Dimensional Steady Base Flow," The Aeronautical Quarterly, Vol. XXVII, part I, February 1976, pp. 55-65.

⁸¹Kaul, U. K., and Frost, Walter, "Turbulent Atmospheric Flow Over a Backward-Facing Step," NASA CR-2749, October, 1976.

⁸²Clauser, F.H., "The Turbulent Boundary," Advances in Applied Mechanics, Academic Press, Inc., New York, N.Y., 1956, pp. 1-51.

⁸³Clauser, F.H., "Turbulent Boundary Layers in Adverse Pressure Gradients," Journal of the Aeronautical Sciences, V. 21, February 1954, pp. 91-108.

⁸⁴Ludwig, H., and Tillmann, W., "Investigations of the Wall Shearing Stress in Turbulent Boundary Layers," NACA TM 1285, May 1950.

⁸⁵Hama, F.R., "Boundary Layer Characteristics for Smooth and Rough Surfaces," Soc. Naval Architects and Marine Engineers, Transactions, Vol. 62, 1954, pp. 333-358.

⁸⁶Schlichting, H., "Experimental Investigation of the Problem of Surface Roughness," NACA TM 823, April 1937.

⁸⁷Betterman, D., "Contribution of L'Etude de la Convection Forcee Turbulente le Long de Plaques Rugueuses," International Journal of Heat and Mass Transfer, Vol. 9, 1966, pp. 153-164.

⁸⁸Dvorak, F.A., "Calculation of Turbulent Boundary Layers on Rough Surfaces in Pressure Gradient," AIAA Journal, Vol. 7, 1969, pp. 1752-1759.

⁸⁹Simpson, R.L., "A Generalized Correlation of Roughness Density Effects on the Turbulent Boundary Layer," AIAA Journal, Vol. 11, 1973, pp. 242-244.

⁹⁰Furuya, Y., Miyata, M., and Fujita, H., "Turbulent Boundary Layer and Flow Resistance on Plates Roughened by Wires," ASME Gas Turbine and Fluids Engineering Conference paper 76-FE-6, March 1976.

⁹¹Perry, A. E., Schofield, W.H., and Joubert, P. N., "Rough Wall Turbulent Boundary Layers," J. Fluid Mech., Vol. 37, 1969, pp. 383-413.

⁹²Plate, E.J., "The Drag on a Smooth Flat Plate with a Fence Immersed in Its Turbulent Boundary Layer", ASME 1964 Fluids Engineering Conference Paper 64-FE-17, Philadelphia, Pa., May 18-20, 1964.

⁹³Staff of Aerodynamics Division, N.P.L., "On the Measurement of Local Surface Friction on a Flat Plate by Means of Preston Tubes," Aero. Res. Council, London, Rep. and Mem. No. 3185, 1961.

⁹⁴Ludwig, H., "Instrument For Measuring the Wall Shearing Stress of Turbulent Boundary Layers," NACA TM 1284, May, 1950.

⁹⁵Bellhouse, B.J., and Schultz, D.L., "The Measurement of Skin Friction in Supersonic Flow by Means of Heated Thin Film Gages," A.R.C. R&M 3490, Aeronautical Res. Conn., Oct. 1965.

⁹⁶Brown, G.L., "Theory and Application of Heated Films For Skin Friction Measurement," Proc. of the 1967 Heat Transfer and Fluid Mechanics Institute, Stanford University Press, Stanford University, California, pp. 361-381.

⁹⁷McCormick, Michael E., Johnson, Bruce, and Lee, William M., "Effects of a Flexible Surface on Surface Shear-Stress Fluctuations Beneath a Turbulent Boundary Layer," Journal of Hydronautics, Vol. 6, No. 1, January 1972, pp. 62-64.

⁹⁸Pope, R.J., "Skin-Friction Measurements in Laminar and Turbulent Flows Using Heated Thin-Film Gages," AIAA Journal, Vol. 10, No. 6, June 1972, pp. 729-730.

⁹⁹Blinco, Paul H., and Simons, Daryl B., "Characteristics of Turbulent Boundary Shear Stress," Journal of the Engineering Mechanics Division, ASCE, Vol. 100, No. EM2, April 1974, pp. 203 - 220.

¹⁰⁰Rubesin, Morris W., Okuno, Arthur F., and Mateer, George G., "A Hot-Wire Surface Gage for Skin Friction and Separation Detection Measurements," NASA-TM-X-62465, July 1975.

¹⁰¹Murthy, V. Sreedhara, and Rose, W.C., "Direct Measurements of Wall Shear Stress by Buried Wire Gages in a Shock Wave-Boundary Layer Interaction Region," Paper 77-691, AIAA 10th Fluid and Plasmadynamics Conference, Albuquerque, N.M., June 1977.

APPENDIX A

TILED SURFACE DRAG PREDICTIONS

In the following discussions, a scheme is derived based on phenomenological or empirical drag data for use in predicting the experimental drag results obtained in tests on the multiple array of steps, gaps, and slots. This presentation expands and complements the treatment presented by Norton and White^{31,32} and includes additions to theories previously presented. Power-law and log-law velocity profiles are used to deduce the mean or effective kinetic pressure on a roughness and an account is given for considering the effective roughness density of distributed roughness. Pressure gradient effects on boundary layer profiles and drag are not considered although reference to these effects is made as they relate to individual roughnesses. Pressure gradient results were presented previously by Norton and White^{31,32}.

Tile Roughness Element Drag Using the Hoerner Independent Drag Coefficient Concept

The drag associated with a roughness element is given by

$$D = C_D q S \quad (A-1)$$

and is written in accordance with the notation of Hoerner²⁷ where C_D is the element drag coefficient based on the roughness element basic area S . Experience shows that the experimental data and empirical correlations presented by Hoerner account for drag of individual drag producing items in a reliable and often conservative way. Limitations on obtaining appropriate values for C_D occur because one must closely match the geometry for which Hoerner presents data. Furthermore, by using the free-stream kinetic pressure, q , and because C_D was obtained from tests where flat plates contained the tested element, the preceding formula for drag of roughness elements is applicable to flow over a flat plate.

Generally, as for aerodynamic surfaces, consideration must be given to effects of a pressure gradient. This consideration is often referred to as a drag "magnification" correction resulting from the pressure gradient along the boundary layer edge. The pressure gradient may also be responsible for modifications to the boundary layer profile which alters roughness element drag from the flat plate value. Considerations may be found in the drag magnification paper by Nash and Bradshaw⁶⁶ where not only boundary layer edge kinetic pressure but also the integral boundary layer momentum

thickness parameter are shown to have an influence on a roughness element drag different from that on a flat plate.

Experiments conducted on the stretch of test plate covered by an array of square tiles permitted all roughness elements to be associated with surface area that included the square tile, a gap before, and a slot beside the tile. Thus, on this surface area, S_{tile} , basis

$$D = C_D q \left(\frac{S}{S_{\text{tile}}} \right) S_{\text{tile}} \quad (\text{A-2})$$

With this representation, each roughness element, whether gap, slot, or step, may be viewed as if it contributed to total drag as a shear drag effect

$$\Delta C_f = C_D \left(\frac{S}{S_{\text{tile}}} \right) \quad (\text{A-3})$$

Because each tile arrangement tested had gaps and slots then approximately

$$S_{\text{tile}} = A_{\text{tile}} + (\text{gap width} \times \text{gap length}) + (\text{slot width} \times \text{slot length}) \quad (\text{A-4})$$

To systematically eliminate the effects local boundary layer growth and profile shape have on roughness element drag over the stretch of test plate, the independent drag coefficient may be introduced; however, the concept as described by Hoerner will be modified. The Hoerner independent drag concept is contingent on the general mechanism that a small protuberance or cavity element in a boundary layer experiences the same force as would the same element were it placed in a free flow of uniform kinetic pressure q_{eff} . As

for the element within the boundary layer, the kinetic pressure at the boundary layer edge is q . In addition, because a large number of tiles occurred over the stretch of test plate the cumulative drag effects due to numerous repetitive roughness elements can be accounted for as a periodic set and thus summed in the integral sense. Validity of this approach necessitates analysis of small roughnesses compared to boundary layer height and seldom enough to assure minimal alterations to a smooth surface turbulent boundary layer development yet often enough to justify integral summing as described. Therefore, the independent drag coefficient for flow over a flat plate may be introduced

$$C_{D_{ind}} = C_D \left(\frac{q}{q_{eff}} \right) \quad (A-5)$$

The equivalent average shear force increment due to a single roughness element is

$$\Delta \bar{C}_f = \frac{1}{x_2 - x_1} \int_{x_1}^{x_2} C_{D_{ind}} \left(\frac{q_{eff}}{q} \right) \left(\frac{S}{S_{tile}} \right) dx \quad (A-6)$$

where the surface between x_1 and x_2 forms the stretch of test plate of interest. Because, in the classical sense, more than one type of roughness element existed between x_1 and x_2 it may be appropriate to identify each type by subscript to describe the type. Namely, $\Delta \bar{C}_{f,step}$, $\Delta \bar{C}_{f,gap}$, and $\Delta \bar{C}_{f,slot}$ describe the type of roughness element equivalent shear force coefficient. Although steps and gaps or slots were integral with one another on tiles, it must be assumed for this analysis that combined elements may be treated separately. Doing so

is necessitated by the data given in Hoerner where no combined effect data for $C_{D_{ind}}$ appear. This is referred to as considering roughness in the classical sense. Table A-1 presents the element independent drag coefficients german to tile geometries tested.

Table A-1 Element Drag Properties

<u>Element type</u>	<u>$C_{D_{ind}}$</u>	<u>S</u>
Forward Step	0.40	(h)(a)
Rearward Step	0.22	(h)(a)
Slot	0.28	(d)(b)
Gap	0.014	(b)(b+a)

where $a = (A_{tile})^{1/2}$.

Independent drag coefficients, $C_{D_{ind}}$, were determined by Hoerner from measured step drag converted to coefficient form, C_D . Hoerner's coefficients are for elements exposed to incompressible flow representative of a power-law boundary layer profile having $n = 6$; however, direct application of the scheme proposed by Hoerner is not always proper. Because flow with boundary layers may correlate to more general logarithmic profiles or to $n = 7$ or 9 power-law profiles, modifications may be accomplished by use of an effective kinetic pressure representative of the boundary layer profile existing in the experimental study or in theoretical analysis. The boundary layer profile to use should be the profile at the location of the roughness element assuming, however, that the element has no effect on the

approaching boundary layer. As will be shown later, the approach basic to the Hoerner method utilizes this superposition of roughness drag and smooth plate drag, C_f , and in fact necessitates the assumption that no permanent modification to a smooth plate boundary layer occurs before or after a roughness element. Because of the way drag information was obtained experimentally for roughnesses presented by Hoerner, the change in shear stresses before and after roughness elements is included in drag coefficients. This is thought to account for modifications to shear forces in the proximity of a roughness element.

The concept of an independent drag coefficient may be applied by using

$$\frac{q_{\text{eff}}}{q} = \left(\frac{1}{k}\right) \int_0^k \left(\frac{U}{U_e}\right)^2 dy \quad (\text{A-7})$$

if, in addition, the effective roughness height, k , is defined properly. For the case of protuberances, k corresponds to protuberence height, h , above the smooth surface. This convenient but somewhat contrived practice of defining k for protuberences seems to afford accountability of the drag of a protuberence submerged in a boundary layer as judged by the success and acceptance within the aircraft and ship building industries. The equality of roughness height and protuberence height for an element is understandable from a physical point of view but geometrical similarity to protuberences presented by Hoerner is necessary. For shallow indentions Schlichting³³ has shown that a degree of similarity exists between the drag of the indention and a protuberence image counterpart projecting above a

smooth plate by the same amount which the indentation is below the smooth flat-plate surface. Accepting this premise of similarity, the gap and slot associated with each tile have a drag which can be derived using an effective kinetic pressure of a "similar" protuberence. For roughness elements of the indentation type it is possible to use observed trends in drag coefficient data and base k selection on the depth of the indentation. A limit is imposed on k such that k be less than or equal to the depth beyond which the observed drag coefficient is unchanged based on change with depth. Thus, for a single type of roughness element spread in equal intervals over a relatively long stretch of test surface, the equivalent shear coefficient is

$$\Delta \bar{C}_f = \frac{1}{x_2 - x_1} \int_{x_1}^{x_2} C_{D_{ind}} \left(\frac{S}{S_{tile}} \right) \left(\frac{1}{k} \right) \int_0^k \left(\frac{U}{U_e} \right)^2 dy dx \quad (A-8)$$

where the innermost integral is a yet to be determined function of x and the turbulent boundary layer profile which exists over the test surface between x_1 and x_2 . By adding the individual roughness element equivalent shear coefficients and the average smooth flat plate skin friction coefficient, an approximation to the net drag coefficient over the stretch of tiles between x_1 and x_2 may be found.

This drag analysis, leading to Eq. (A-8), could be accomplished by forming the summation of discrete roughness element drag to dispense with the formulation requiring the outermost integral. The approach would be more general and, in fact, would be necessary if the test surface had consisted of roughness elements that were not repeated at many equally spaced intervals. Experimental conditions which could prevent direct use of Eq. (A-8) include compressible flow, very close

element spacing, nonuniform tile size or spacing, an unpredictable equivalent roughness height, or an erratic velocity-profile distribution at stations along the plate. The latter could result in an inability to adequately describe the local velocity profile because of inadequate profile measurements. This could result if disturbances to the boundary layer were caused by roughness induced perturbations from elements before or behind the roughness element of interest. By restricting roughness elements to be small in comparison to the boundary layer depth, limitations on successful use of Eq. (A-8) may not be severe when proved by agreement with drag predictions obtained from momentum measurements at the ends of the test surface of interest.

To employ Eq. (A-8), $(\frac{U}{U_e})^2$ must be evaluated. For each roughness element, $C_{D_{ind}}$, S , S_{tile} , and k are constant over the test surface. One way of representing the velocity profile is to assume a power-law profile

$$\frac{U}{U_e} = \left(\frac{y}{\delta}\right)^{\frac{1}{n}} \quad (A-9)$$

Then,

$$\left(\frac{1}{k}\right) \int_0^k \left(\frac{U}{U_e}\right)^2 dy = \left(\frac{1}{k}\right) \int_0^k \left(\frac{y}{\delta}\right)^{\frac{2}{n}} dy = \left(\frac{n}{n+2}\right) \left(\frac{k}{\delta}\right)^{\frac{2}{n}} \quad (A-10)$$

Based on experimental evidence that Eq. (A-9) represents the velocity distribution well, it is possible to consider for a smooth flat plate (one without a pressure gradient) a boundary layer that correlates well with the form

$$\frac{U}{U_\tau} = (C) \left(\frac{y U_\tau}{\nu} \right)^{\frac{1}{n}} \quad (\text{A-11})$$

over a large part of the boundary layer. Equation (A-9) and the definition of the incompressible momentum thickness gives

$$\theta = \frac{n\delta}{(n+1)(n+2)} \quad (\text{A-12})$$

Thus, from Eq. (A-11) the local smooth-flat-plate friction coefficient is

$$C_f = \frac{2nD}{(n+2)(n+3)} R_x^{\frac{-2}{n+3}} \quad (\text{A-13})$$

where

$$D = \left\{ \frac{(n+2)(n+3)}{n} \right\}^{\frac{n+1}{n+3}} C^{\frac{-2n}{n+3}} \quad (\text{A-14})$$

However, rewriting Eq. (A-13)

$$D = \frac{(n+2)(n+3)}{2n} C_f R_x^{\frac{2}{n+3}} \quad (\text{A-15})$$

where one may represent the skin friction coefficient for a flat plate with White's⁴⁵ correlation

$$C_f = \frac{.455}{[\ln(.06 R_x)]^2} \quad (\text{A-16})$$

Using the momentum equation (zero pressure gradient)

$$\frac{d\theta}{dx} = \frac{C_f}{2} \quad (A-17)$$

applied with Eq. (A-12), the boundary layer thickness becomes

$$\delta = D R_x^{\frac{-2}{n+3}} x \quad (A-18)$$

Therefore, from Eq. (A-18), Eq. (A-15), and Eq. (A-16)

$$\frac{\delta}{x} = \frac{(.455)(n+2)(n+3)}{2n[\ln(.06R_x)]^2} \quad (A-19)$$

Assuming the power-law velocity profile holds, Eq. (A-8) may be reduced with Eq. (A-10) since

$$\left(\frac{1}{k}\right) \int_0^k \left(\frac{U}{U_e}\right)^2 dy = N' [\ln(.06R_x)]^{\frac{4}{n}} \left(\frac{k}{x}\right)^{\frac{2}{n}} \quad (A-20)$$

where

$$N' = \frac{n}{n+2} \left\{ \frac{4.396 n}{(n+2)(n+3)} \right\}^{\frac{2}{n}} \quad (A-21)$$

For a roughness element, Eq. (A-8) may be integrated to give

$$\Delta \bar{C}_f = N C_{D_{ind}} \left(\frac{S}{S_{tile}}\right) \left\{ \ln(.06 \bar{R}_x) \right\}^{\frac{4}{n}} \frac{k}{x_2 - x_1} \left\{ \left(\frac{x_2}{k}\right)^{\frac{n-2}{n}} - \left(\frac{x_1}{k}\right)^{\frac{n-2}{n}} \right\}$$

or

$$\Delta \bar{C}_f = \frac{C_{D_{ind}} \frac{S}{S_{tile}}}{1 - \left(\frac{2}{n}\right)^2} \left\{ \frac{2n(\ln(.06 \bar{R}_x))^2}{(.455)(n+2)(n+3)} \right\} \frac{\frac{2}{n} \left[\left(\frac{x_2}{k}\right)^{1-\frac{2}{n}} - \left(\frac{x_1}{k}\right)^{1-\frac{2}{n}} \right]}{\left[\frac{x_2}{k} - \frac{x_1}{k}\right]} \quad (A-22)$$

where \bar{R}_x is the mean Reynolds number representing the flow between x_1 and x_2 and

$$N = \frac{n}{n-2} N' \quad (A-23)$$

For $n = 6$, $N = 0.8050$; for $n = 7$, $N = 0.8013$; and for $n = 9$, $N = 0.8048$.

Although not specifically mentioned to now, it is necessary to reference x_1 and x_2 to the origin or virtual origin of turbulent flow. Where the difference $x_2 - x_1$ appears, any reference suffices; however, in the last term of Eq. (A-22) and in defining \bar{R}_x , turbulent flow ordinates must be used. This consideration arises in practice principally because of the assumption of a completely turbulent boundary layer and especially for the present analysis because of the wind-tunnel model design used to make drag measurements. Comparison is to be made between the measurements and the theories developed to account for distributed roughnesses. The basis for comparison between measured and predicted drag may be made consistent by using comparable references. That is, since the plate model had no roughness on the droop nose and pressure gradients were not evaluated there, it was necessary to establish a virtual origin of the rough, turbulent boundary layer which developed over the flat test plate. This was accomplished by assuming the form of growth of momentum thickness over the rough turbulent portion to be

$$\theta = G(\text{Re}_{x'})^{\frac{6}{7}} \quad (\text{A-24})$$

where G is an undetermined constant and

$$x' = x - x'_0 \quad (\text{A-25})$$

From measurements of θ at $x = x_1$ and at $x = x_2$, G may be eliminated and the virtual origin of turbulent flow, x'_0 , may be estimated. In actuality the last term in Eq. (A-22) requires $x_2 - x'_0$ replace x_2 and $x_1 - x'_0$ replace x_1 . Although $U_{e1} = U_{e2}$, for completeness an average velocity is used. This average velocity is defined as

$$\bar{U}_e = \frac{U_{e1} + U_{e2}}{2} \quad (\text{A-26})$$

to eliminate or to account for pressure gradient in the mean sense, and a reference ordinate is

$$\bar{x} = \frac{(x_2 - x'_0) + (x_1 - x'_0)}{2} = \frac{(x_2 + x_1)}{2} - x'_0 \quad (\text{A-27})$$

So, the mean Reynolds number becomes

$$\bar{R}_{\bar{x}} = \bar{U}_e \frac{\bar{x}}{\nu} \quad (\text{A-28})$$

A somewhat different result is predicted when the inner integral of Eq. (A-8), which reduces to Eq. (A-10), uses nominal values of D and R_x for Eq. (A-18). This approach was used by Norton and White³² with $n = 7$, $R_x = 1 \times 10^7$, and $D = 0.381$ giving $\delta \approx 0.0152 x$ from Eq. (A-18). In addition a value of $\delta \approx 0.016 x$ corresponding to $n = 6$ as suggested by Hoerner was used by Norton and White³² for

comparison to experimental measurements. With the above information for $n = 7$,

$$\left(\frac{1}{k}\right) \int_0^k \left(\frac{U}{U_e}\right)^2 dy \approx 2.58 \left(\frac{k}{x}\right)^{\frac{2}{7}} \quad (\text{A-29})$$

Since $\frac{n}{n+2} \left(\frac{x}{\delta}\right)^{\frac{2}{n}} = 2.58$ nominally for $n = 7$. For $n = 6$,

$$\left(\frac{1}{k}\right) \int_0^k \left(\frac{U}{U_e}\right)^2 dy \approx 3.0 \left(\frac{k}{x}\right)^{\frac{2}{6}} \quad (\text{A-30})$$

Correspondingly, Eq. (A-8) yields

$$\Delta \bar{C}_f = \frac{C_{D_{\text{ind}}} \frac{S}{S_{\text{tile}}}}{1 - \left(\frac{2}{n}\right)^2} \{K\} \frac{\left[\left(\frac{x_2}{k}\right)^{1 - \frac{2}{n}} - \left(\frac{x_1}{k}\right)^{1 - \frac{2}{n}}\right]}{\left[\frac{x_2}{k} - \frac{x_1}{k}\right]} \quad (\text{A-31})$$

where K represents the nominal value of x/δ raised to the $2/n$ power.

Over the range of Reynold's numbers tested, δ/x from Eq. (A-19) is preferred to nominal values of δ/x previously cited. A third relationship based on law-of-the-wake computations for a smooth turbulent flat plate is

$$\frac{\delta}{x} \approx \frac{0.14}{(R_x)^{1/7}} \quad (\text{A-32})$$

This relationship relies on a power-law analysis to fit computations (see White²⁵ p. 495) and gives overly conservative approximations of \bar{C}_f which will be described later. A fourth analysis may also be

deduced if it is known that the test surface is of the "fully-rough-surface" type. Knowing this, one may use either

$$C_f = (1.4 + 1.61 \ln \frac{x}{k})^{-2} \quad (A-33)$$

from White⁴⁵ or

$$C_f = (2.87 + 1.69 \ln \frac{x}{k_s})^{-2.5} \quad (A-34)$$

from Schlichting³³.

The friction coefficients from Eq. (A-33) and Eq. (A-34) are within five percent of each other above $\frac{x}{k} = 500$; however, both refer to a uniformly roughened surface. In Eq. (A-33), k is the average roughness for protuberence and in Eq. (A-34) k_s is the equivalent sand-grain roughness. Generally, however, k does not equal k_s . As with previously developed power-law formulations it is necessary to find

$$\frac{\delta}{x} = \frac{(n+2)(n+3)}{2n} C_f \quad (A-35)$$

for use with Eq. (A-10) and Eq. (A-8). It is noteworthy that trends in experimental data preclude the use of Eq. (A-33) or Eq. (A-34) to find $\frac{\delta}{x}$. Observed values of $\frac{\delta}{x}$ do not exceed 3.0% for the roughest case tested which for $n = 7$ gives $C_f \approx 0.0047$ from Eq. (A-35) and a corresponding $\frac{x}{k} \approx 3500$ from Eq. (A-33). However, observed values of the equivalent shear coefficient for this same test case are approximately 0.0060 which, for the power-law analysis (Eq. (A-35)) gives $\frac{\delta}{x} \approx 3.9\%$. With this observation it appears that the tiled surfaces tested do not correspond to uniformly roughened surfaces. Further, it has been observed that there is noticeable change in \bar{C}_f with \bar{R}_x which

does not correspond to a fully roughened surface flow.

An alternative to the velocity profile representation given by Eq. (A-9) is to use the inner boundary layer variables such that

$$\frac{U}{U_e} = g(U_e, U_\tau, \nu, \text{ and } y) \quad (\text{A-36})$$

For such a representation near the surface

$$\left(\frac{U}{U_e}\right)_S = \frac{yU_\tau}{\nu} \frac{U_\tau}{U_e}, \quad 0 < y < \delta_S \quad (\text{A-37})$$

and

$$\left(\frac{U}{U_e}\right)_T = \left[A \ln \frac{yU_\tau}{\nu} + B\right] \frac{U_\tau}{U_e}, \quad y > \delta_S \quad (\text{A-38})$$

where δ_S is the viscous sublayer height. Thus for $\delta_S < k$,

$$\frac{q_{\text{eff}}}{q} = \frac{1}{k} \int_0^k \left(\frac{U}{U_e}\right)^2 dy = \frac{1}{\delta_S} \int_0^{\delta_S} \left(\frac{U}{U_e}\right)_S^2 dy + \frac{1}{k-\delta_S} \int_{\delta_S}^k \left(\frac{U}{U_e}\right)_T^2 dy \quad (\text{A-39})$$

Upon integrating with Eq. (A-37) and Eq. (A-38)

$$\begin{aligned} \frac{q_{\text{eff}}}{q} = \left(\frac{U_\tau}{U_e}\right)^2 & \left\{ \frac{(\delta_S U_\tau / \nu)^2}{3} + 2A^2 - 2AB + B^2 + \left[\frac{2AB}{k-\delta_S} - \frac{2A^2}{k-\delta_S}\right] \left[k \ln \frac{kU_\tau}{\nu} \right. \right. \\ & \left. \left. - \delta_S \ln \frac{\delta_S U_\tau}{\nu}\right] + \frac{A^2}{k-\delta_S} \left[k \ln^2 \frac{kU_\tau}{\nu} - \delta_S \ln^2 \frac{\delta_S U_\tau}{\nu}\right] \right\} \quad (\text{A-40}) \end{aligned}$$

Taking $A = 2.44$ and $B = 5.2$ after Betterman⁸⁷ and with the approximation that there be immediate transition from the viscous sublayer to the inner logarithmic layer

$$\delta_s = 11.065 \frac{v}{U} \quad (A-41)$$

and

$$\frac{q_{eff}}{q} = C_f \left\{ 27.191 - \frac{522.473 \frac{v}{U_e \sqrt{C_f}}}{k - \frac{15.648v}{U_e \sqrt{C_f}}} + \frac{2.9768k}{k - \frac{15.648v}{U_e \sqrt{C_f}}} \left[2.2623 \ln \frac{kU_e \sqrt{C_f}}{v} \right. \right. \\ \left. \left. \ln^2 \frac{kU_e \sqrt{C_f}}{v} \right] \right\} \quad (A-42)$$

Comparison to experiments using this "log-law" analysis is simplified with Eq. (A-42) where k , \bar{U}_e (replacing U_e), \bar{v} , and \bar{R}_x for computing C_f from Eq. (A-16) are used. The resulting $\frac{q_{eff}}{q}$ becomes $\frac{\bar{q}_{eff}}{q}$ and Eq. (A-8) takes the simplified form

$$\Delta \bar{C}_f = C_{D_{ind}} \frac{S}{S_{tile}} \frac{\bar{q}_{eff}}{q} \quad (A-43)$$

Whatever method is used for computing $\frac{q_{eff}}{q}$, the equivalent skin friction coefficient becomes

$$\bar{C}_f = C_f + \Delta \bar{C}_{f,steps} + \Delta \bar{C}_{f,gap} + \Delta \bar{C}_{f,slot} \quad (A-44)$$

For theoretical computations, C_f is determined with Eq. (A-16) which, over the range of Reynolds numbers \bar{R}_x tested, is a better fit and approximately 5% greater than the F. Schultz-Grunow formula given by Schlichting³³

$$C_f = \frac{0.370}{(\log_{10} \bar{R}_x)^{2.584}} \quad (A-45)$$

used by Norton and White^{31,32} in a slightly different analysis with the experimental data. For the test plate in the horizontal, zero-angle position, a very slight favorable pressure gradient existed based on boundary layer edge values, velocities differed by less than 4.0% at probing locations; however, over the stretch of test plate for which the skin friction analysis applies the pressure gradient was nominally zero at zero angle. Differing tunnel conditions caused slight differences in kinematic viscosity (less than 2.0%) between data sets used; however, flat plate results are approximated by averaging velocities and kinematic viscosities at each appropriate test dynamic pressure condition. Using identical independent parameters for comparing test and theory eliminates the slight differences previously mentioned.

For Preston tube computations, the integrated mean value of C_f between probing stations on a smooth flat surface results in comparable values of \bar{C}_f . The formula developed by the staff of N.P.L.,⁹³

$$C_f = \frac{0.0576}{R_D^{1/4}} (C_{p_0})^{\frac{7}{8}} \quad (A-46)$$

is applicable to the 0.122 inch outer diameter tubes used. The C_{p_0} is based on tube pressure and the associated static pressure: R_D is the Reynolds number based on local flow conditions and tube diameter. Other experimental data shown were determined from the formula

$$\bar{C}_f = \frac{1}{x_2 - x_1} \int_{x_1}^{x_2} C_f dx = \frac{1}{x_2 - x_1} \int_{x_1}^{x_2} 2 \frac{d\theta}{dx} = \frac{2(\theta_2 - \theta_1)}{x_2 - x_1} \quad (A-47)$$

$$\theta = \int_0^{\delta} \frac{U}{U_e} \left(1 - \frac{U}{U_e}\right) dy \quad (\text{A-48})$$

was determined from velocity measurements. Results of each theoretical analysis make use of Eq. (A-16) and an appropriate prediction of roughness drag on a mean shear basis. Figure A-1 shows the experimental data and theoretical predictions. The superposition of smooth flat plate shear coefficient and the summation of equivalent shear coefficients computed using a logarithmic velocity profile over predicts (is conservative) the roughest case tested by approximately 8.5% based on the theory. Steps are the predominant drag producing features and Norton and White³¹ show that the height of the steps for Case D are such as to provide, with the log-law analysis, an effective kinetic pressure approximating more nearly a $n = 9$ power-law profile than a $n = 7$ profile. Because of this and the trend in power-law theoretical predictions shown, it is not surprising that the log-law overpredicts the experimental data for Case D. Three "power" formulations differing principally in the approximation formulas used to compute $\frac{\delta}{x}$ are shown. Formulas used to compute that portion of drag due to the roughness elements are indicated and the power-law exponent, n , is indicated. For Cases C and D, differences between experiment and theory are believed to be within the accuracy of measurements and accuracy of the independent drag coefficient concept of roughness drag prediction. Noteworthy is the fact that Eq. (A-22) with $n = 6$ and $n = 7$ bracket the data, none of the predictions have significant error compared to experiment, and predictions of C_f tend to be flatter for

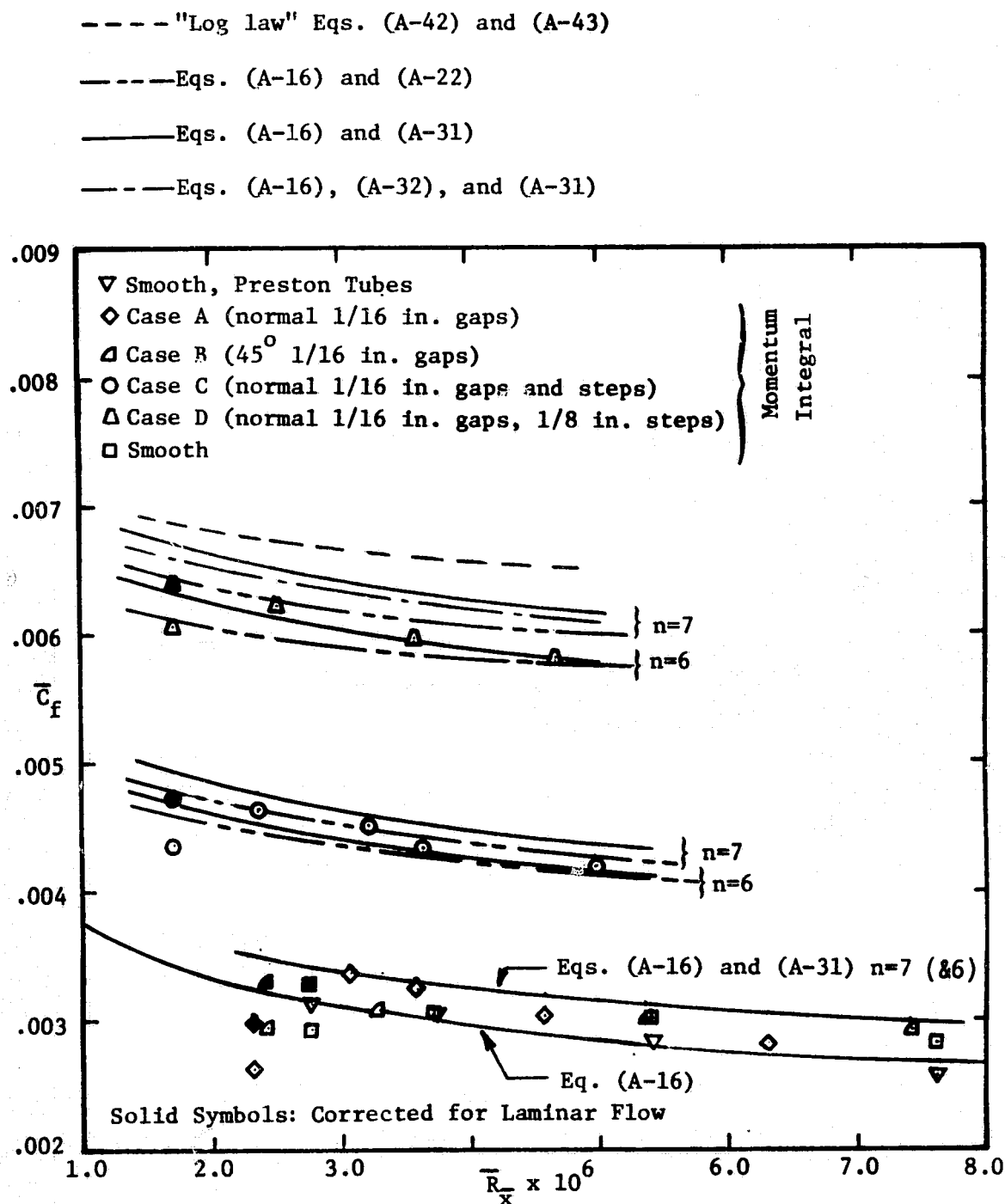


Fig. A-1 Average skin friction coefficient compared to empirical method predictions.

the \bar{R}_x than do the experimental data trend. Furthermore, the $n = 6$ predictions appear to fit the data better at the higher values of \bar{R}_x which is somewhat unexpected. Finally, for Cases A and B, experimental values of \bar{C}_f may be slightly greater than smooth plate values but not to a significant degree nor definitely. The predictions with $n = 6$ for Cases A and B differ too little from $n = 7$ to present in graphical form and differences are well within measurement accuracy. Laminar-flow corrections are based solely on the fit of the curve shape determined by Eq. (A-16) using experimental data at highest \bar{R}_x to give a constant increment to the momentum integral smooth surface data at the lowest \bar{R}_x . This increment is uniformly applied to tiled surface data at the same tunnel dynamic pressure (5.0 psf).

Theoretical results show that the roughness drag increment increases with increasing Reynolds number understandably on the basis of a thinner boundary layer given a fixed position, x . Further, the increment in roughness drag after removing smooth plate drag is nominally 119% for Case D over Case C for $n = 7$ and nominally 124% additional for Case D over Case C for $n = 6$. These increments may be explained by noting that step height changes by a factor of two between Case D and Case C and for the power-law analysis the step drag increment for this halving of step height is proportional to

$$\left(\frac{1}{2}\right)^{\frac{2+n}{n}}.$$

Additional analysis may be seen for the tiled configurations and the smooth surface in the work of Norton and White^{31,32}. Note that the difference between power-law analysis with $n = 6$ for the Cases

A and B and the Case C is less than experimental "best fit" difference between the same cases. This indicates an unfavorable interference exists experimentally which cannot be accounted for in the independent drag method theory. In addition, although the error band is approximately 5.0%, the modified Hoerner method appears to overestimate the gap and slot (no steps present) effective shear coefficient.

Tile Roughness Element Drag
Using the Betterman/Dvorak Law
of the Wall Roughness Density Concept

A different analysis of the tiled surface can be employed by considering a log-law velocity profile with a roughness displacement term

$$\frac{U}{U_\tau} = A \ln \frac{yU_\tau}{\nu} + B - \frac{\Delta U_1}{U_\tau} \quad (A-49)$$

where, according to Clauser⁸² and Hama⁸⁵ $\frac{\Delta U_1}{U_\tau}$ depends on the roughness Reynolds number $\frac{kU_\tau}{\nu}$. Based on the velocity defect analysis of Clauser, Betterman⁸⁷ writes the defect equation for velocity profile

$$\frac{U - U_e}{U_\tau} = A \ln \frac{y}{\Delta} - 0.4 \quad (A-50)$$

where

$$\Delta = \frac{\delta^*}{\frac{\sqrt{C_f}}{\sqrt{2}}} = \frac{U_e \delta^*}{U_\tau} \quad (A-51)$$

Eliminating $\frac{U}{U_\tau}$ gives

$$\frac{\sqrt{2}}{\sqrt{C_f}} = A \ln \frac{U e^{\delta^*}}{U_\tau} + B - 0.4 - \frac{\Delta U_1}{U_\tau} \quad (A-52)$$

Suggested values of the constants are $A = 2.44$ and $B = 5.2$ although slightly different values of B appear in some analyses.

Clauser has also shown that the displacement term $\frac{\Delta U_1}{U_\tau}$ takes the form

$$\frac{\Delta U_1}{U_\tau} = A \ln \frac{k U_\tau}{U} + C(\lambda) \quad (A-53)$$

where $C(\lambda)$ is some function of roughness density and geometry and according to Betterman⁸⁷ and to Dvorak⁸⁸

$$\begin{aligned} C(\lambda) &= 12.24 \ln \lambda - 17.35 \quad ; \quad 1 < \lambda \leq 4.68 \\ C(\lambda) &= -2.85 \ln \lambda + 5.95 \quad ; \quad \lambda > 4.68 \end{aligned} \quad (A-54)$$

The quantity λ is defined as the ratio of the total surface to the roughness area. This definition is somewhat nebulous and in much of the data presented by Dvorak,⁸⁸ the parameter λ could as well have been based on the surface area and the roughness frontal area normal to the flow. This occurs because in most of the data used by Dvorak, overhead and frontal area were the same. Simpson⁸⁹ and Furuya⁹⁰ suggest

$$C(\lambda_k) = -2.85 \ln \lambda_k + 9.68 \quad ; \quad \lambda_k > 4.68 \quad (A-55)$$

based principally on three-dimensional short angle roughnesses.

With Eq. (A-53), Eq. (A-52) becomes

$$\frac{\sqrt{2}}{\sqrt{C_f}} = 2.44 \ln \left(\frac{\delta^*}{k} \frac{\sqrt{2}}{\sqrt{C_f}} \right) + 4.8 - C(\lambda_k) \quad (A-56)$$

To apply Eq. (A-56) to the tiled surface it is necessary to determine suitable mean values of δ^* and λ_k or k . Because the dominant feature of the tiles surface is the step height, a consistent bookkeeping procedure for use with Eq. (A-56) was devised where trial and error solutions for k (more properly \bar{k}) could be determined. Cases C and D had step heights of 0.0625 inch and 0.125 inch, respectively, so that values of \bar{k} less than these values would not be proper. Based on an analogy similar to Eq. (A-24), $\bar{\delta}^*$ could be approximated from measured values of δ^* . Therefore, Eq. (A-56) becomes

$$.41 \frac{\sqrt{2}}{\sqrt{C_f}} - \ln \frac{\sqrt{2}}{\sqrt{C_f}} = \ln \left[\frac{\bar{\delta}^*(\bar{\lambda}_k)^{1.168}}{E \bar{k}} \right] \quad (A-57)$$

where $E = 1.602$ using the second Eq. (A-54) and $E = 7.389$ using Eq. (A-55). Consideration of the tiled surface requires $\bar{\lambda}_k > 4.68$ and by defining $\bar{\lambda}_k$ by

$$\bar{\lambda}_k = \frac{\sqrt{S_{\text{tile}}}}{\bar{k}} \quad (A-58)$$

then the effective protuberence roughness height may be determined by

$$\bar{k} = G \left\{ \frac{\bar{\delta}^*}{e^{[.41 \frac{2}{\bar{C}_f} - \ln \frac{2}{\bar{C}_f}]} } \right\}^{.46125} \quad (A-59)$$

Here $\bar{\delta}^*$ is in inches: the value of G required for acceptable values of \bar{k} comes from Eq. (A-54) and is

$$G = 2.124 \quad (\text{A-60})$$

Using experimental data shown in Fig. (A-1) and experimental values of $\bar{\delta}^*$, the effective protuberence roughness of the tiled surface with steps was determined to be

$$\bar{k} = 0.90h + .028 \quad , \text{ inches} \quad (\text{A-61})$$

where h is in inches. For computational purposes, to predict \bar{C}_f for tiled surfaces with steps, an interpolation formula for $\bar{\delta}^*$ is

$$\bar{\delta}^* = \bar{\delta}_{\text{smooth}}^* + 0.917h \quad (\text{A-62})$$

where all heights are in inches. Some reasonably accurate formula for $\bar{\delta}_{\text{smooth}}^*$ are

$$\frac{\bar{\delta}_{\text{smooth}}^*}{x} = \frac{.0193}{(R_x)^{1/7}} \quad (\text{A-63a})$$

according to Hoerner²⁷

$$\frac{\bar{\delta}_{\text{smooth}}^*}{x} = \frac{.01738}{(R_x)^{.139}} \quad (\text{A-63b})$$

according to Schlichting³³ or

$$\frac{\bar{\delta}_{\text{smooth}}^*}{x} = \frac{.018}{(R_x)^{1/7}} \quad (\text{A-63c})$$

according to White⁴⁵. There is little difference in these formulae and by combining Eqs. (A-63a) and (A-62) a comparison to experimental values, Fig. (A-2), shows good correlation to experimental data. With the exception of $\bar{\delta}^*$, the right side of Eq. (A-57) contains constants for a stepped tile configuration. Comparing \bar{C}_f predicted by Eq. (A-57) to experimental data, however, shows on Fig. (A-3) that the magnitude is approximately correct but the trend of decreasing \bar{C}_f with R_x is not predicted with Eq. (A-52). Recall that a log-law analysis with the modified Hoerner method shown in Fig. (A-1) does predict the proper trend.

This analysis, based on roughness density effect correlation by Betterman⁸⁷ and Dvorak⁸⁸ to account for log-law velocity profile displacement, has been shown to agree in magnitude with experiment but fail to predict the trend in experimental measurements. The principle reason which is believed to be the cause of failure of the theory to show the data trend is that in the experiments the velocity profile is mainly modified locally near the surface and does not exhibit the behavior of density-correlated flow over protuberances. The boundary layer is thought to attach alternately to raised and unraised smooth tile surfaces after a region of locally separated flow before and behind a forward step and behind a rearward step. The streamwise distribution of surface pressure as shown by Norton and White³¹ alternately increases and decreases before and after a forward step to modify the boundary layer and produce a non-equilibrium, non-similar wall velocity profile. The effect at the outer edges of the boundary

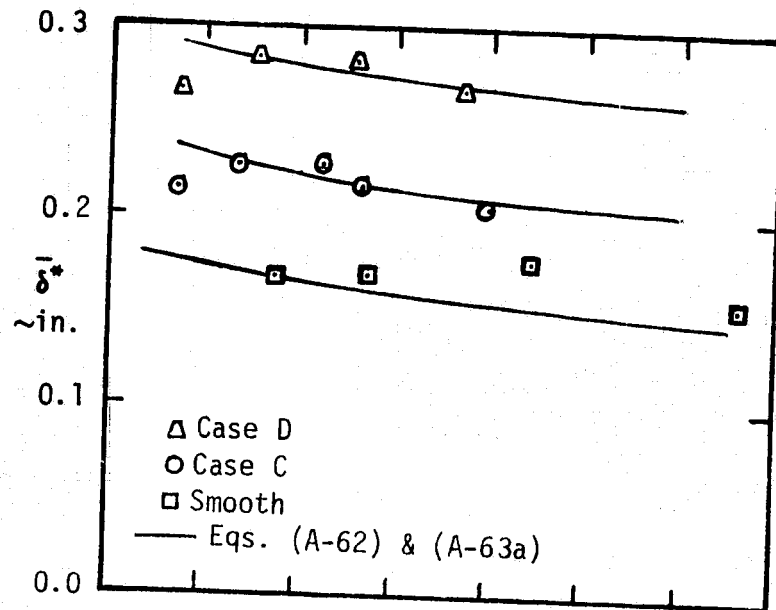


Fig. A-2 Average displacement thickness prediction compared to experiment for tiled surfaces - dependency on Reynolds number.

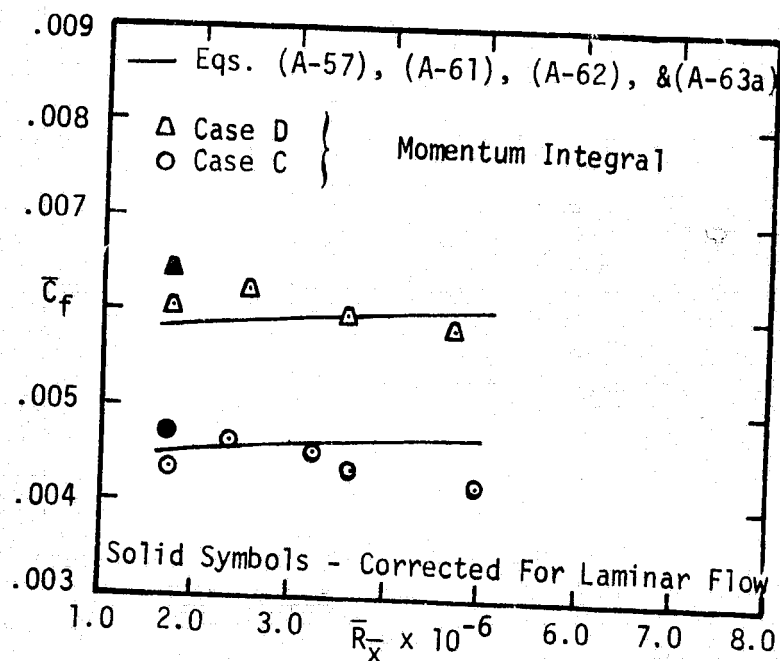


Fig. A-3 Comparison of average skin friction by variable roughness density phenomenology to experiment - dependency on Reynolds number.

layer may appear much as does boundary layer flow over a slight and slowly undulating, wavy wall but concrete proof of this is not available. For the type of roughness tested it appears that analysis with predictions suited to isolated roughness elements within a smooth plate is a better representation. Flow is not of the fully-rough-surface type with respect to gaps and steps. By the modified Hoerner method, alterations from smooth surface conditions to the shear force on approaches to and in the wake of the step, gap, and slot arrangements are accounted for within the drag coefficients of the individual roughness elements.

APPENDIX B

PRESSURE SURVEYS

Presented in this appendix are corrected, stepped cavity pressure coefficient distributions on the cavity model walls for the model in both the rear and forward position on the flat, horizontal test bed used in this study. Also presented are typical uncorrected horizontal surface pressure coefficient distributions for the model in the rear position which were used to establish corrections to rear position pressure data. Corrections put pressure coefficient distributions for the cavity walls on a reference basis of free stream static pressure as found on the model surface when no step or cavity is present. The same type correction was made to the model pressure coefficients when the model was in the forward position. Pressure coefficient distributions were used to derive the nondimensional, net-force-coefficient parameter, $\int C_p$. All pressures were for a tunnel Q of 20 psf.

Figures B-1 and B-2 show the uncorrected pressure coefficient, $C_p^+ = (p - p_{ref})/q_e$. The cavity was closed and level. For Fig. B-1, $\beta = 0^\circ$; $\beta = 45^\circ$ for Fig. B-2. The scale on C_p^+ is enlarged compared to a great majority of C_p plots; so, the C_p^+ to C_p correction is very small. Because of the way $\int C_p$ is found, no correction is required for level cavities. What appears to be scatter is actually perturbation caused by local surface effects. The slight differences between least squares mean and reference orifice pressure for flow aligned pressure orifices is probably due to small undulation in the Formica

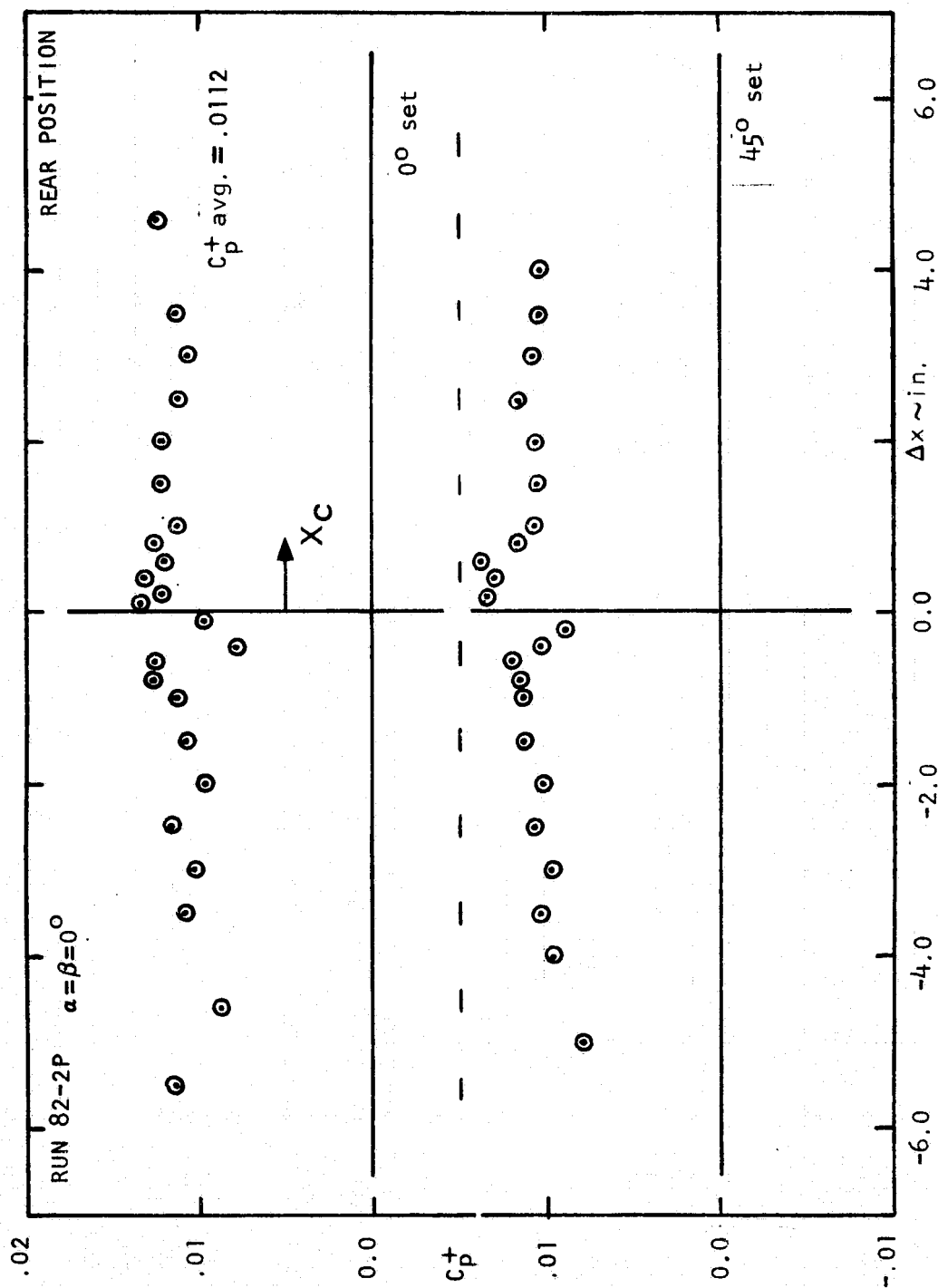


Fig. B-1 Cavity model surface pressure coefficients;
 $h=b=0.0$, $\alpha=\beta=0^\circ$, reference orifice ahead of
 model.

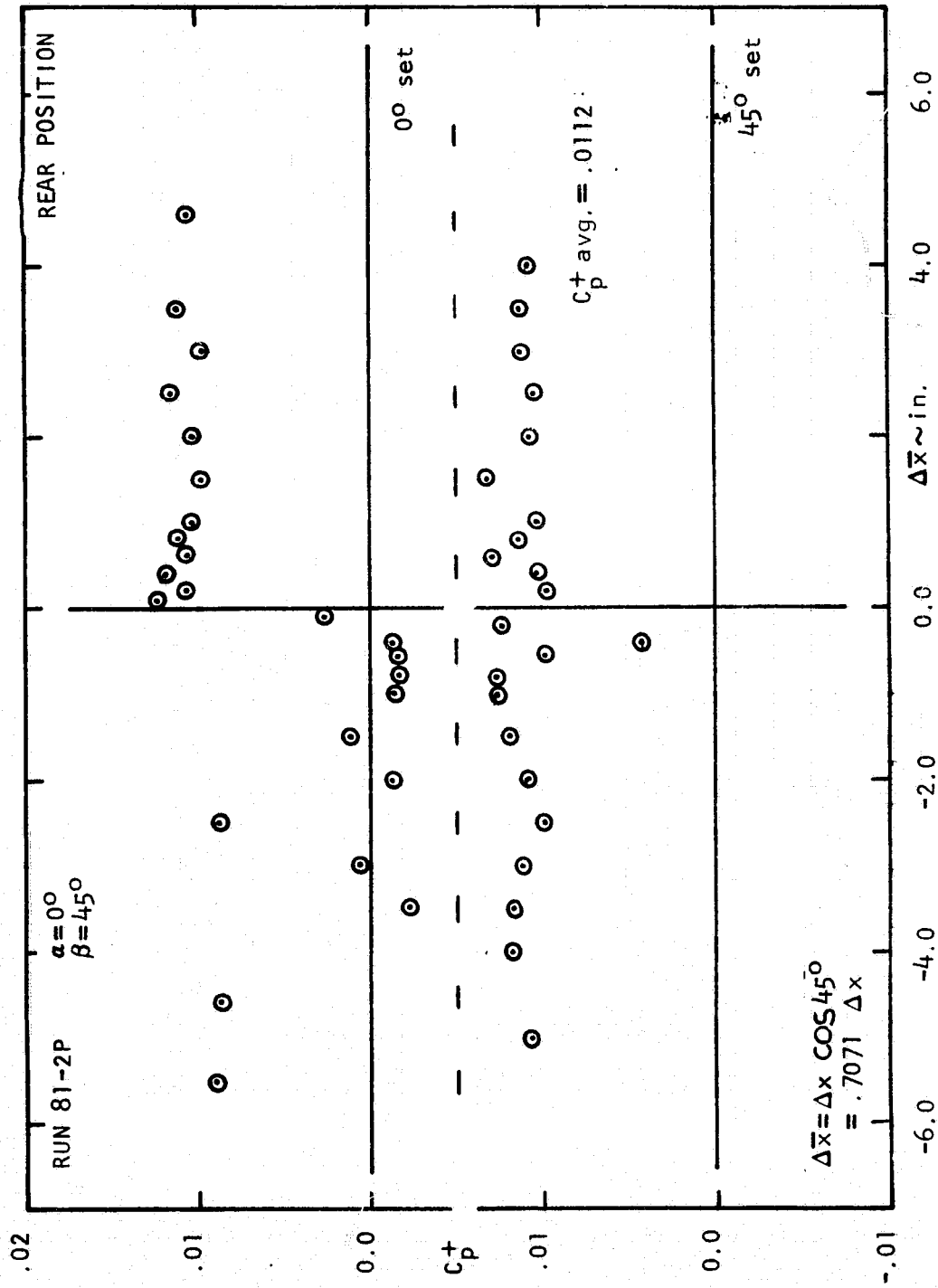


Fig. B-2 Cavity model surface pressure coefficients;
 $h=b=0.0$, $\alpha = 0^\circ$, $\beta = 45^\circ$, reference orifice
 ahead of model.

surface and/or a slightly recessed cavity model. Local perturbations in surface pressures are due to cavity model part interfaces. Skewed pressure orifices show more perturbation for $\beta = 0^\circ$ and $\beta = 45^\circ$ due, perhaps, to spanwise perturbations in the flow with transition from Formica to aluminum surfaces. This, however, was not thoroughly investigated, but only flow aligned pressure orifices were used in step/cavity momentum correlation analysis.

Figure B-3 shows data for the model in the rear position with $b = 0.50$ inch and $\beta = 0^\circ$. Figure B-4 is for the model in the rear position with $b = 0.15$ inch and $\beta = 0^\circ$. Figure B-5 is for steps without cavities at $\beta = 0^\circ$ and the model in the rear position; whereas, Fig. B-6 is for $\beta = 45^\circ$. In Fig. B-7 the rear position model has $b = 0.50$ inch and $\beta = 45^\circ$; Fig. B-9 has $b = 0.15$ inch and $\beta = 45^\circ$.

Figure B-9 shows pressure coefficient data for the model in the forward position with $b = 0.15$ inch and $\beta = 0^\circ$. In Fig. B-10 the model is in the forward position on the test bed plate and the cavity gap width, b , is 0.50 inch. For Fig. B-10, $\beta = 0^\circ$. Figure B-11 shows pressure coefficient data for $b = 0.50$ inch and $\beta = 45^\circ$. The model was in the forward position. The distinction between level cavities or forward-facing stepped cavities and rearward-facing stepped cavities is that the former have positive pressure on the forward-facing cavity wall where the latter have negative pressures over both walls making up the stepped/cavity.

Analysis of these data has been included in the main body of this report.

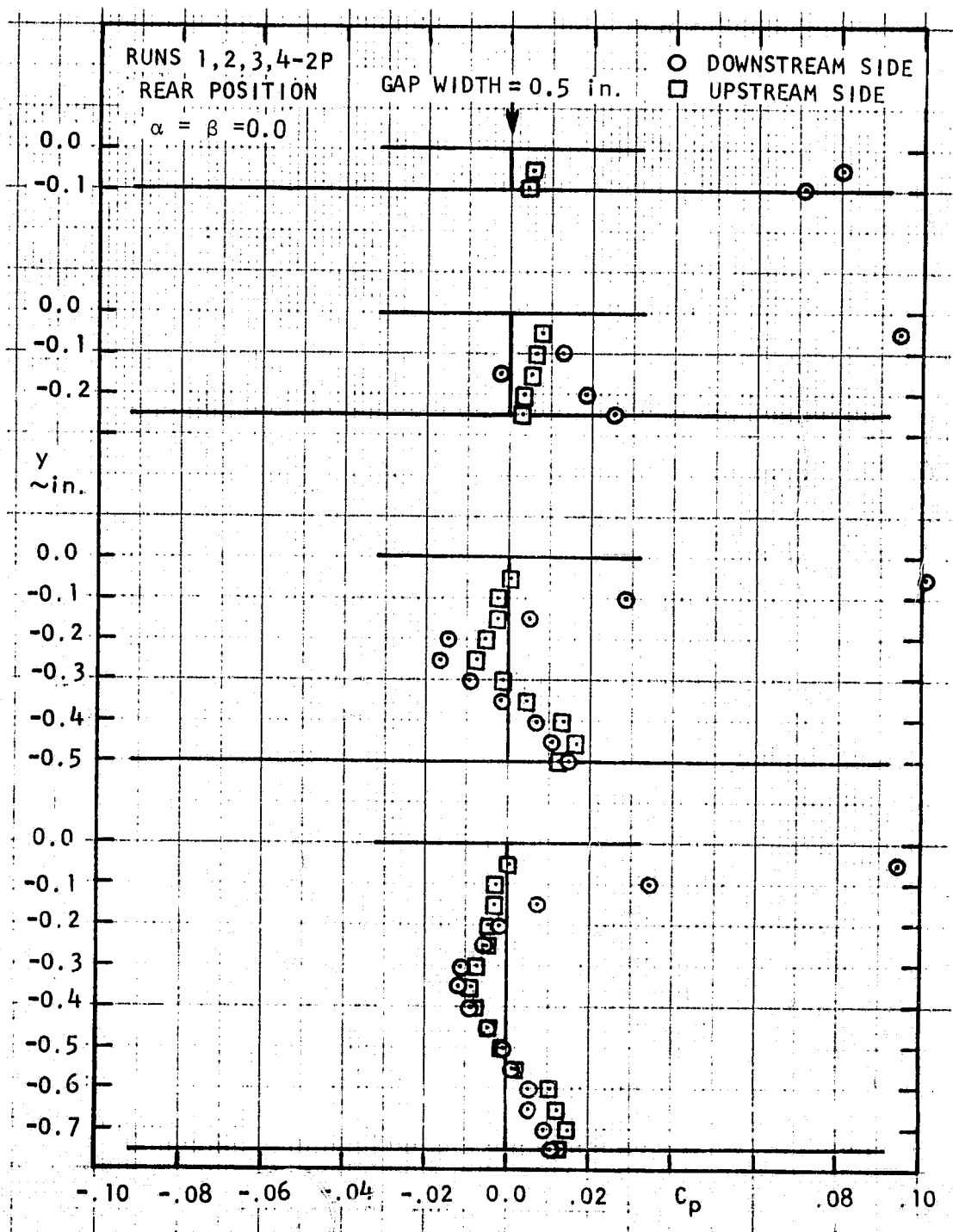


Fig. B-3 Step/cavity wall pressure coefficients for various steps and cavity gap depths; $b=0.5$ inch, $\beta=0^\circ$, rear position.

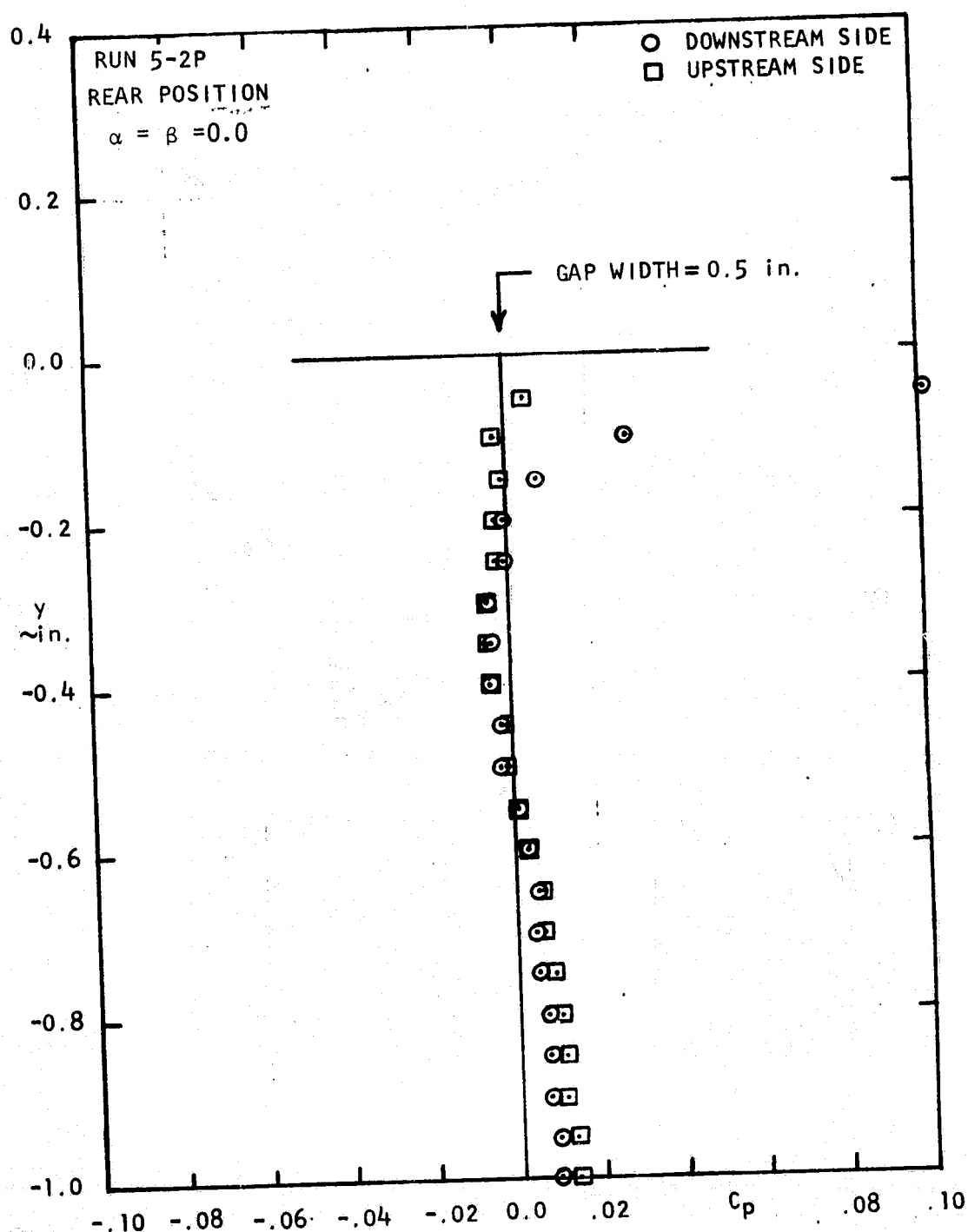


Fig. B-3 continued.

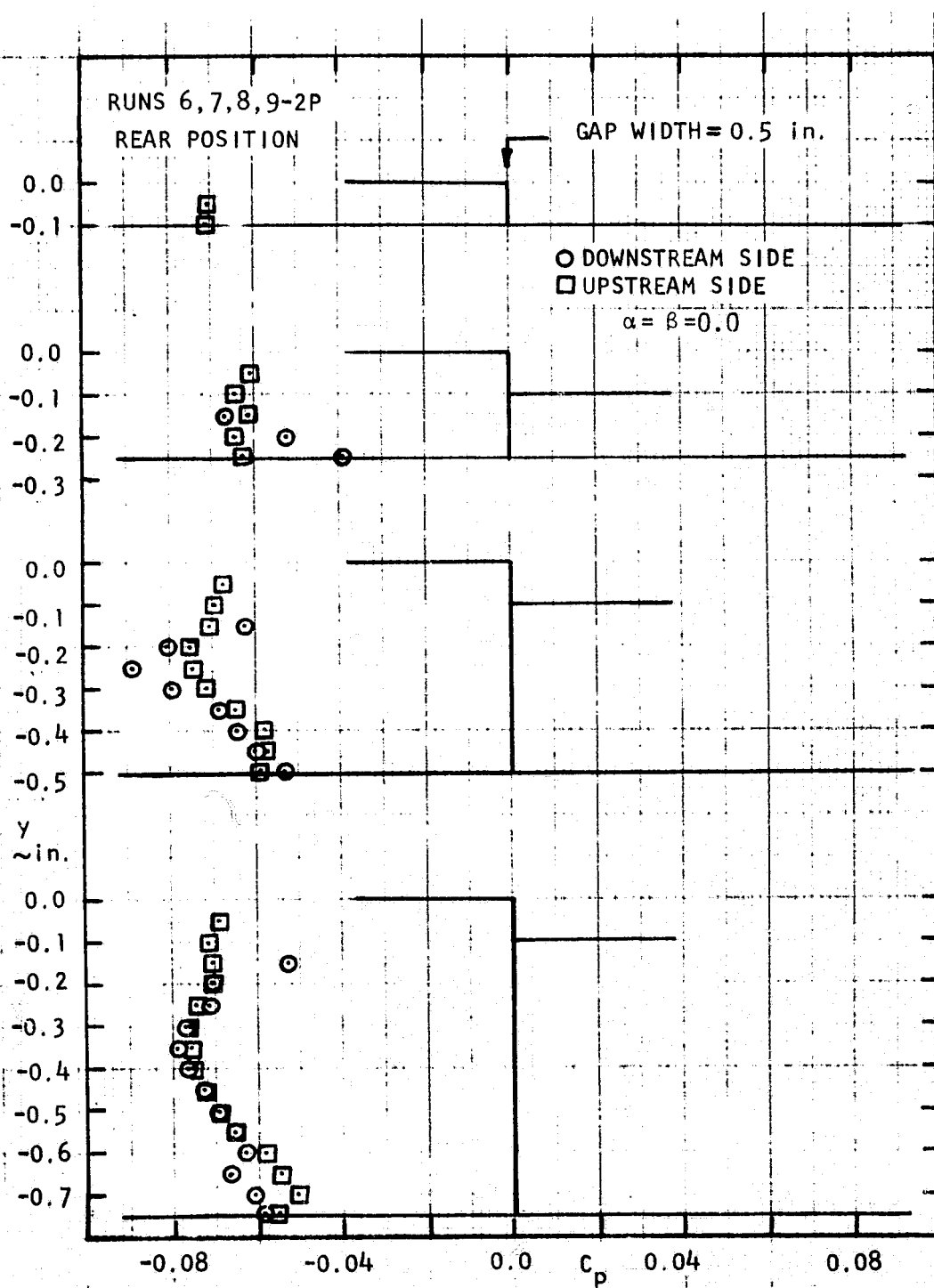


Fig. B-3 continued.

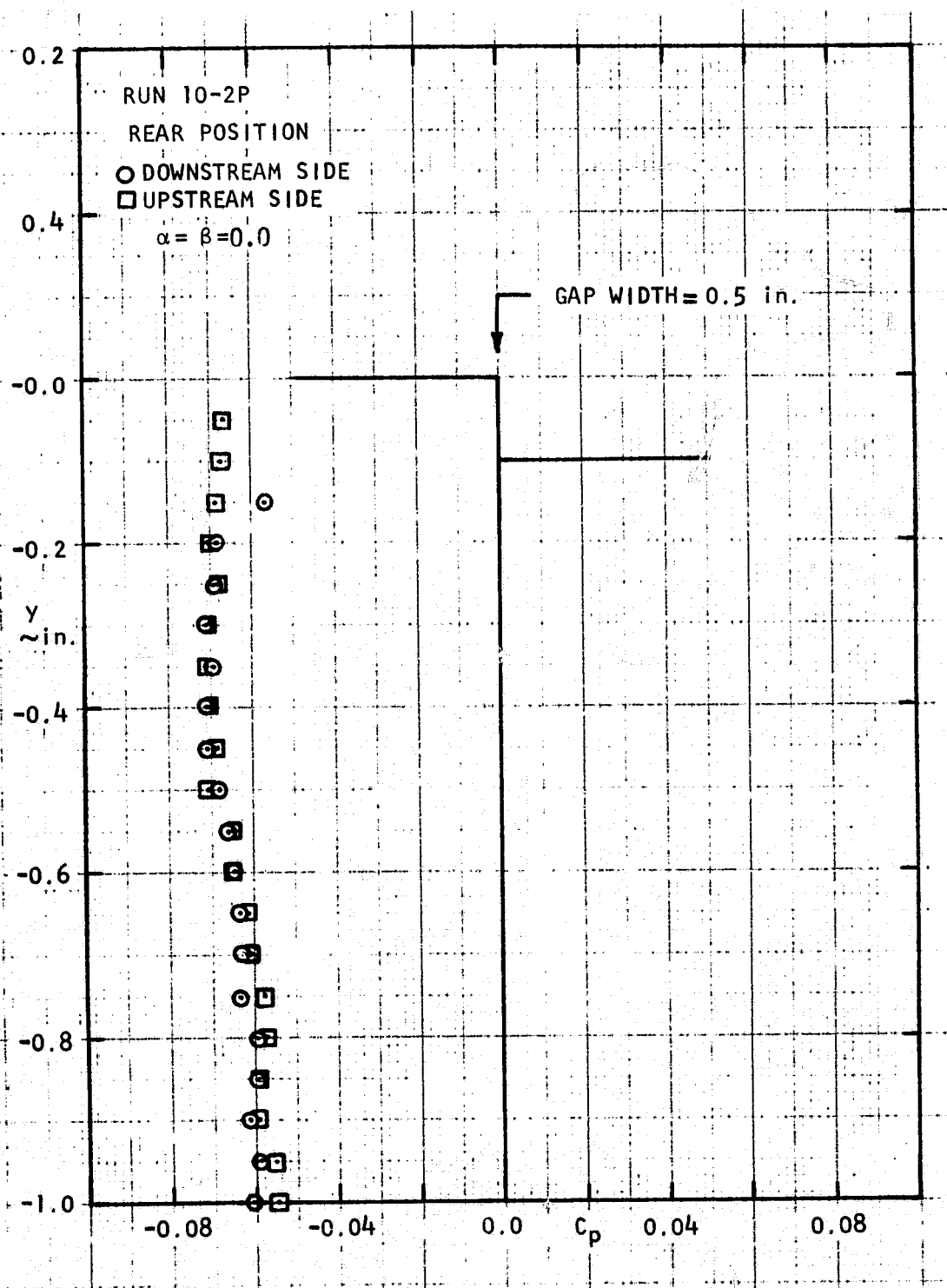


Fig. B-3 continued.

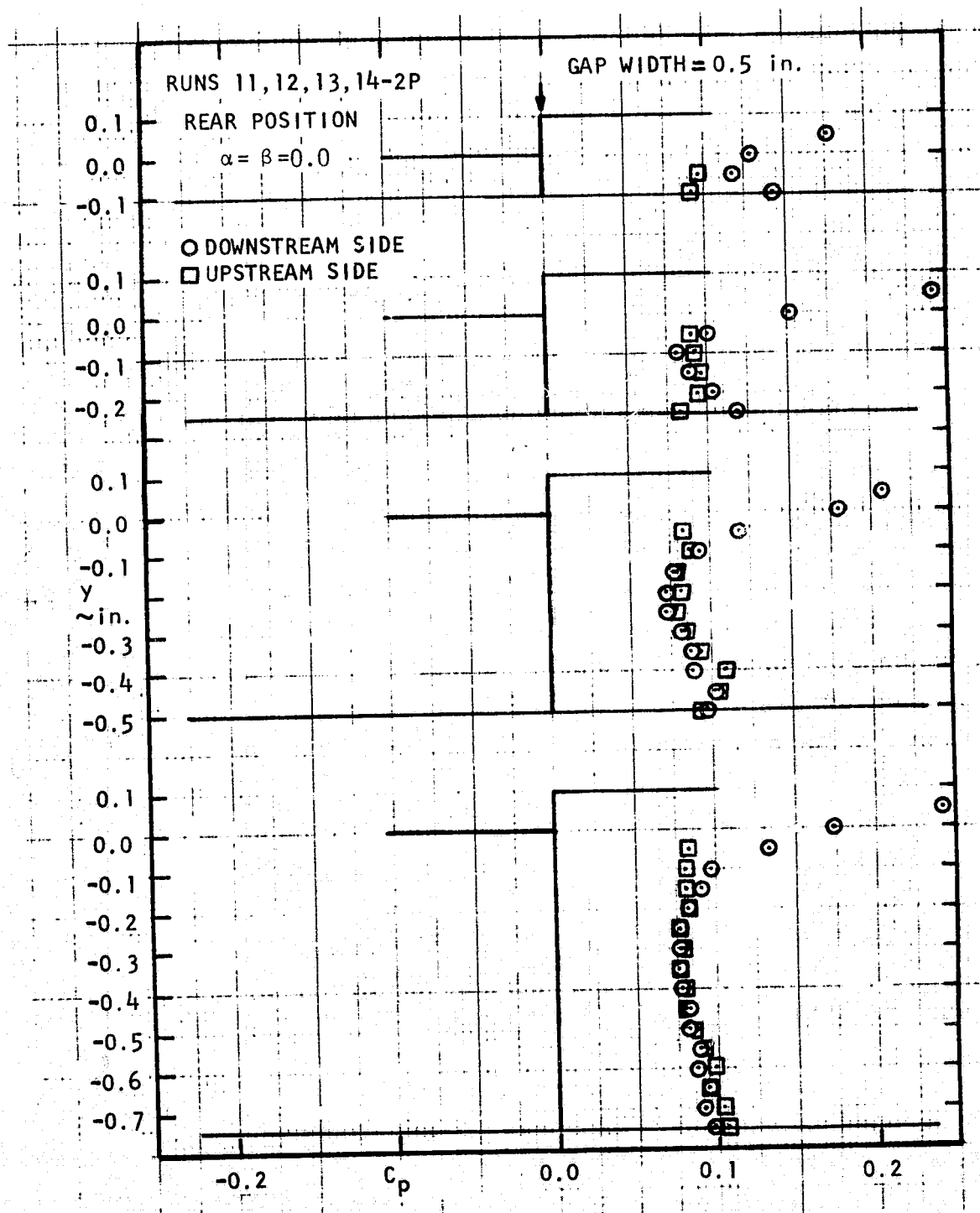


Fig. B-3 continued.

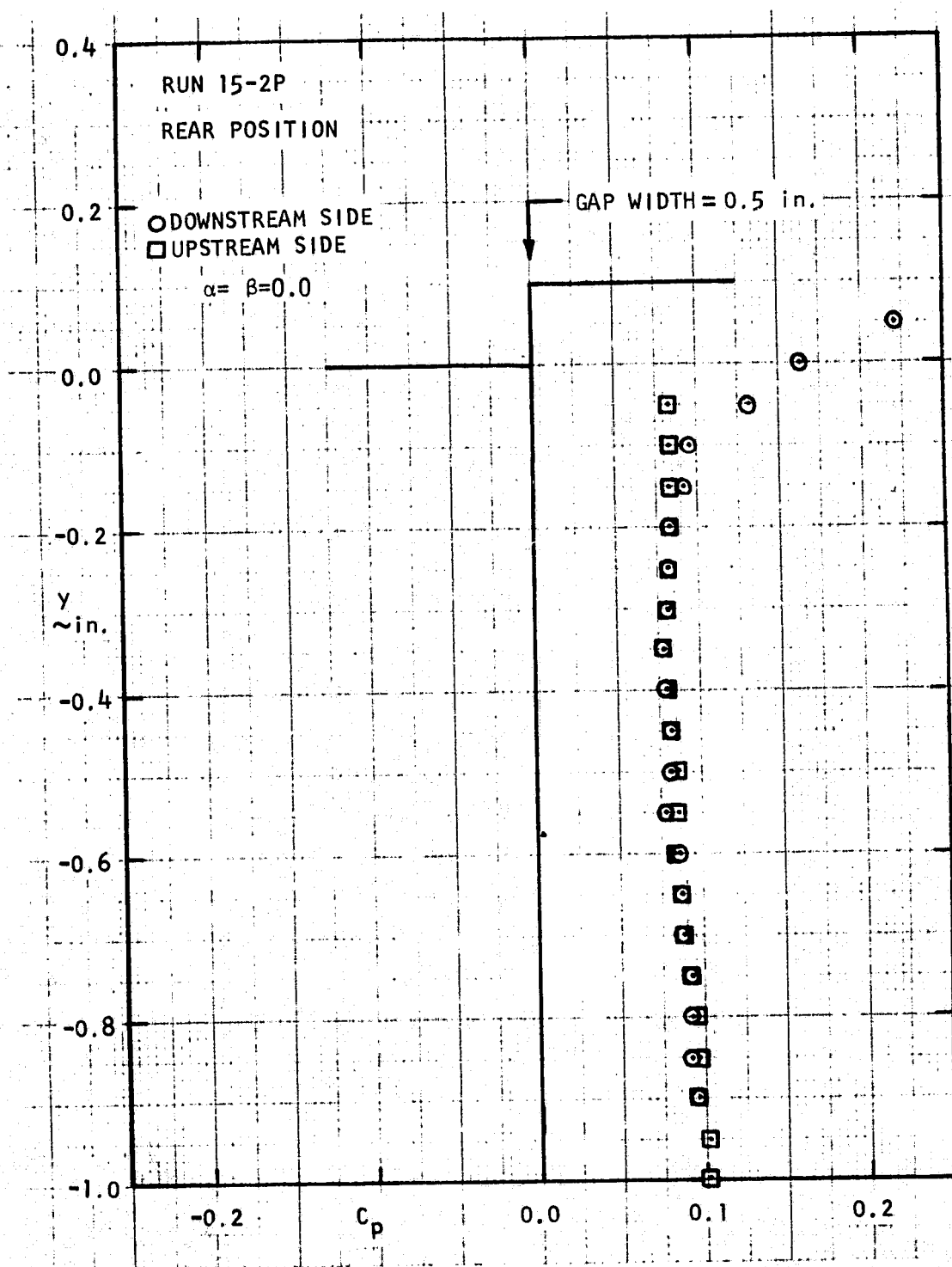


Fig. B-3 continued.

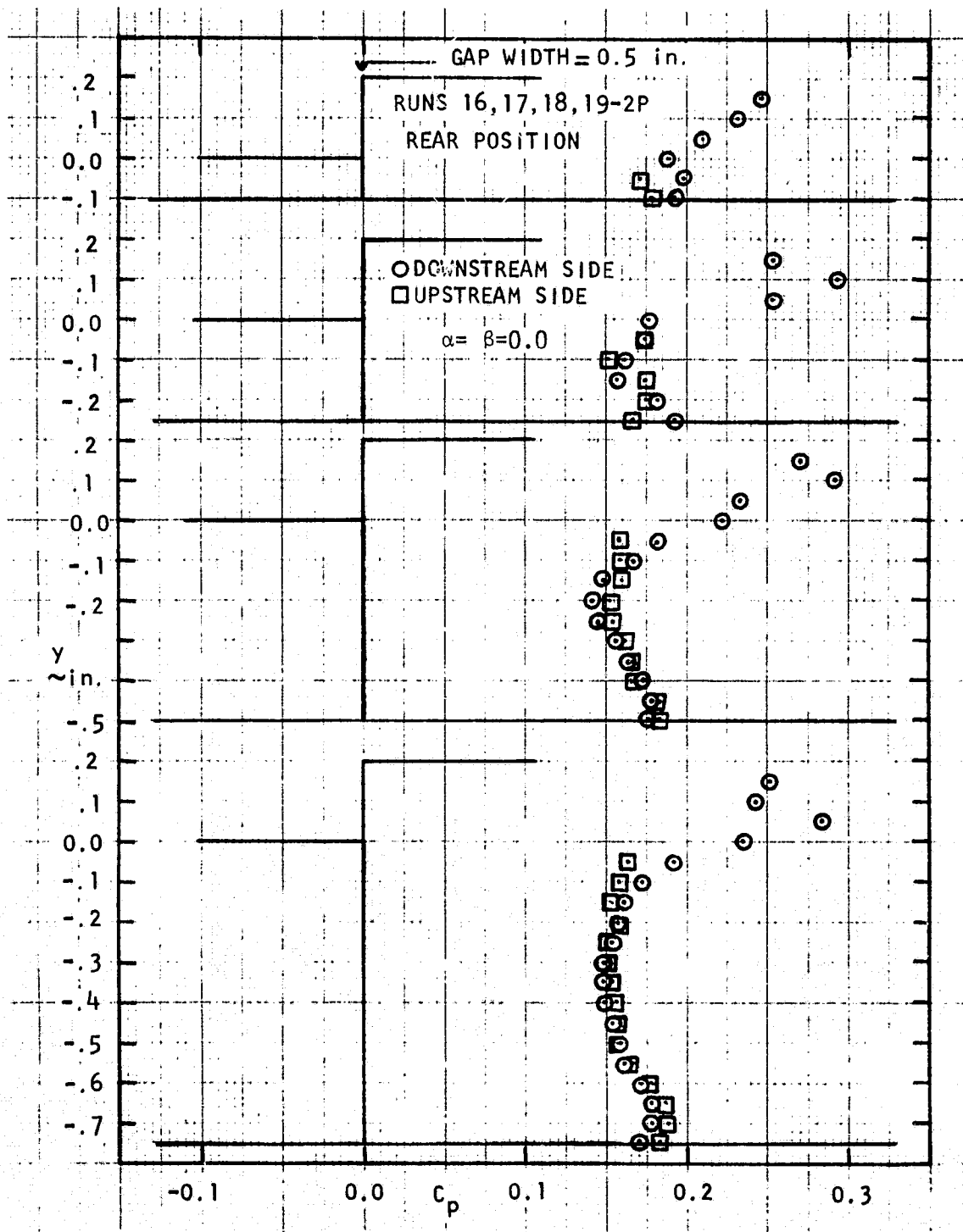


Fig. B-3 continued.

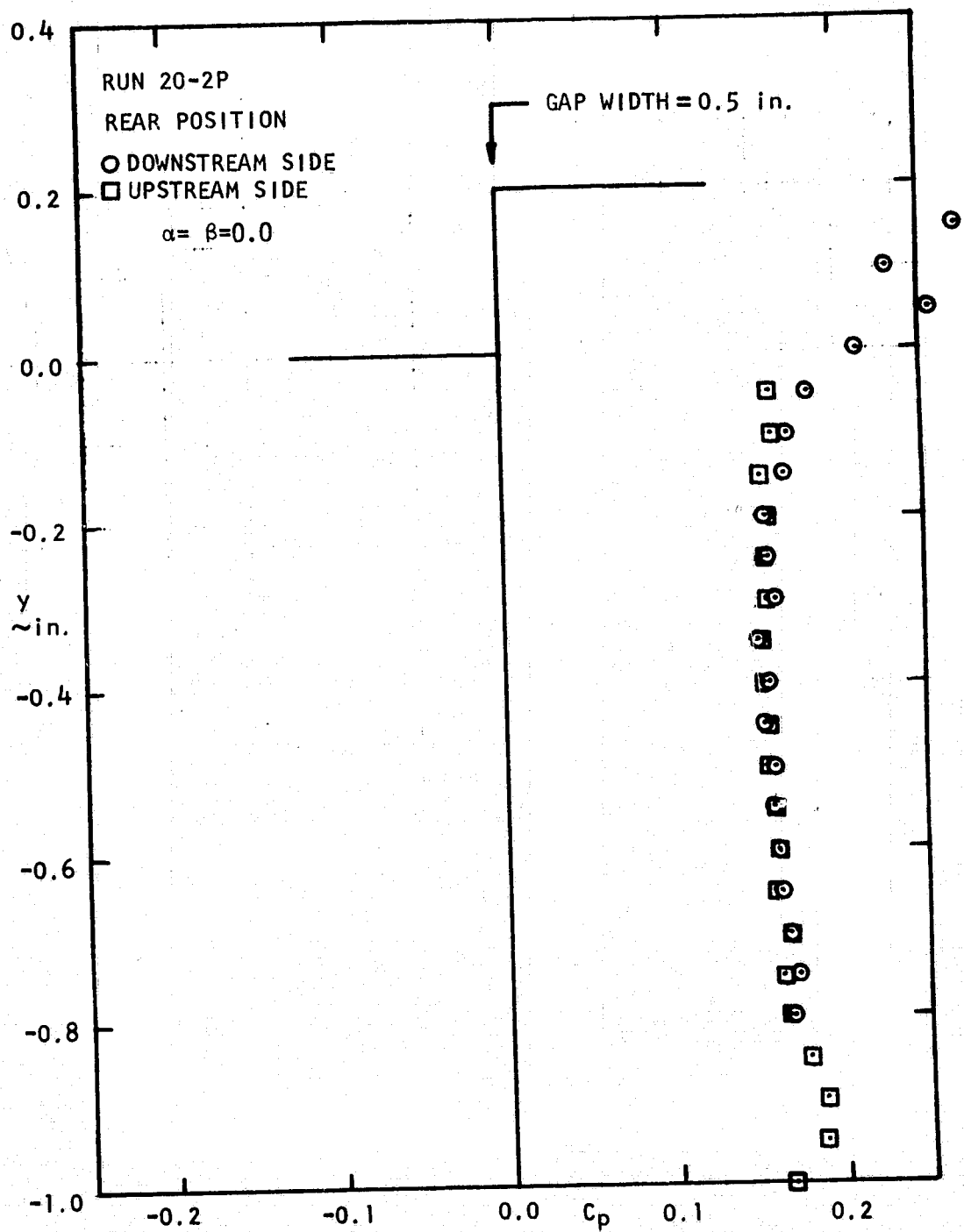


Fig. B-3 continued.

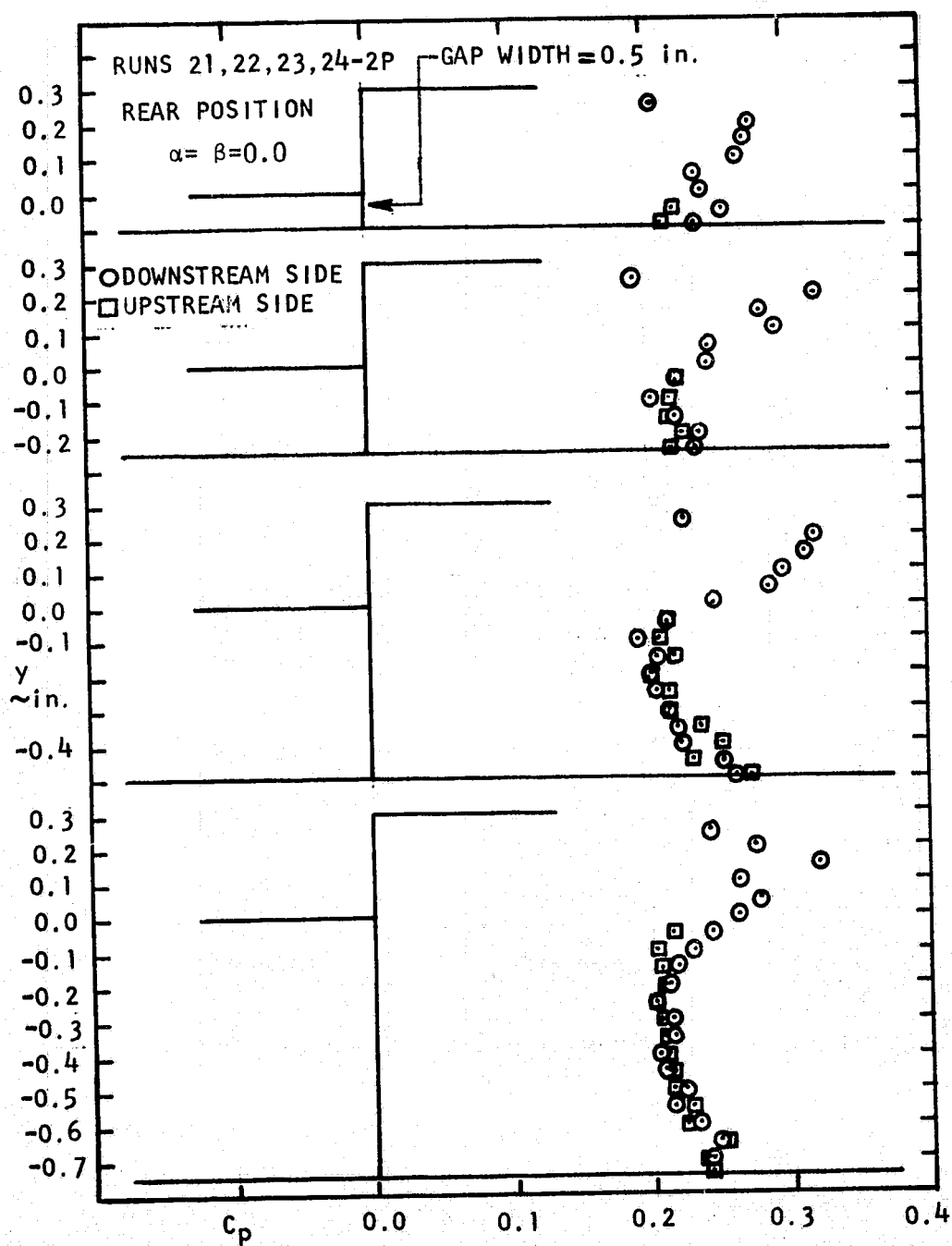


Fig. B-3 continued.

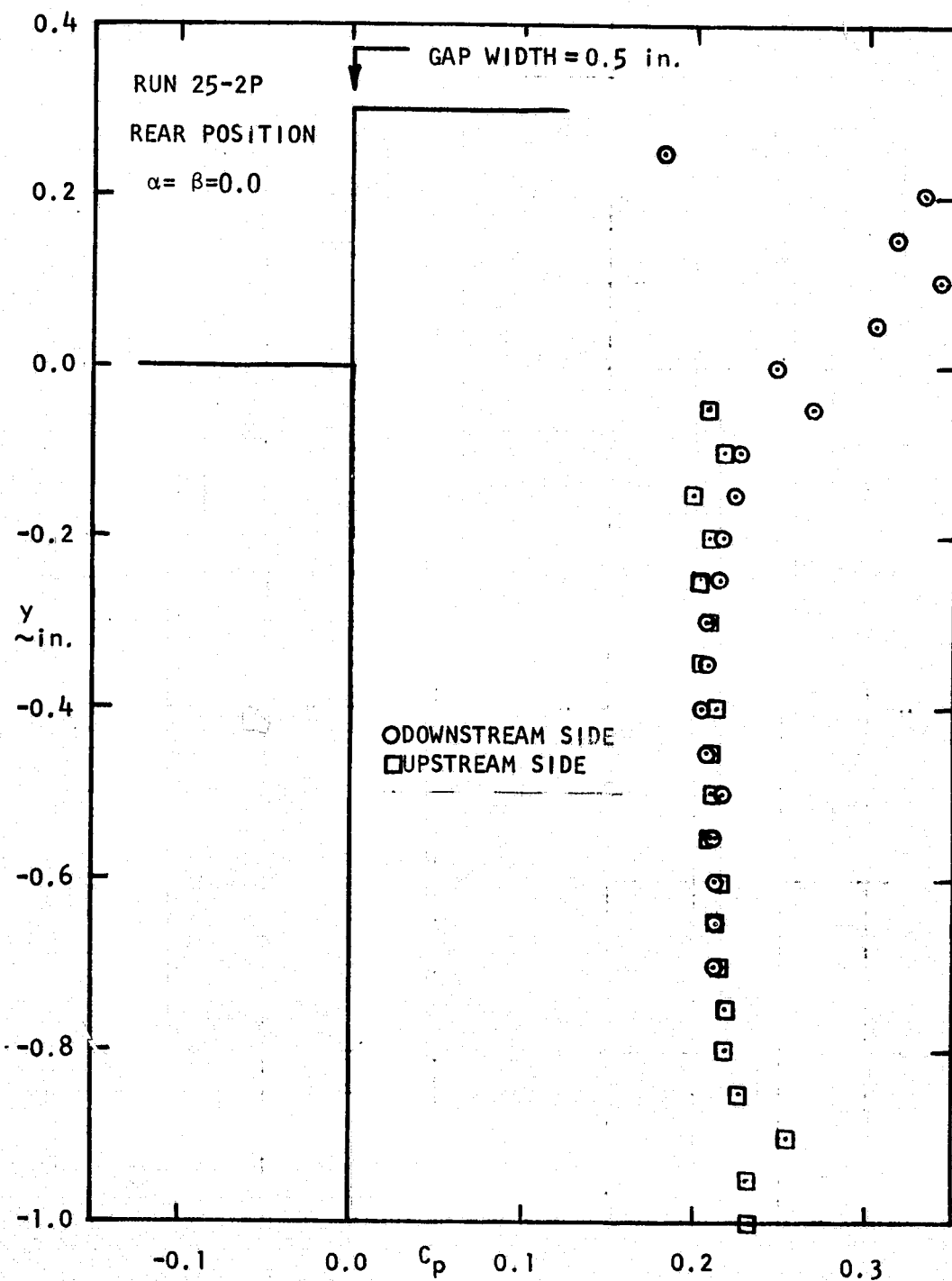


Fig. B-3 continued.

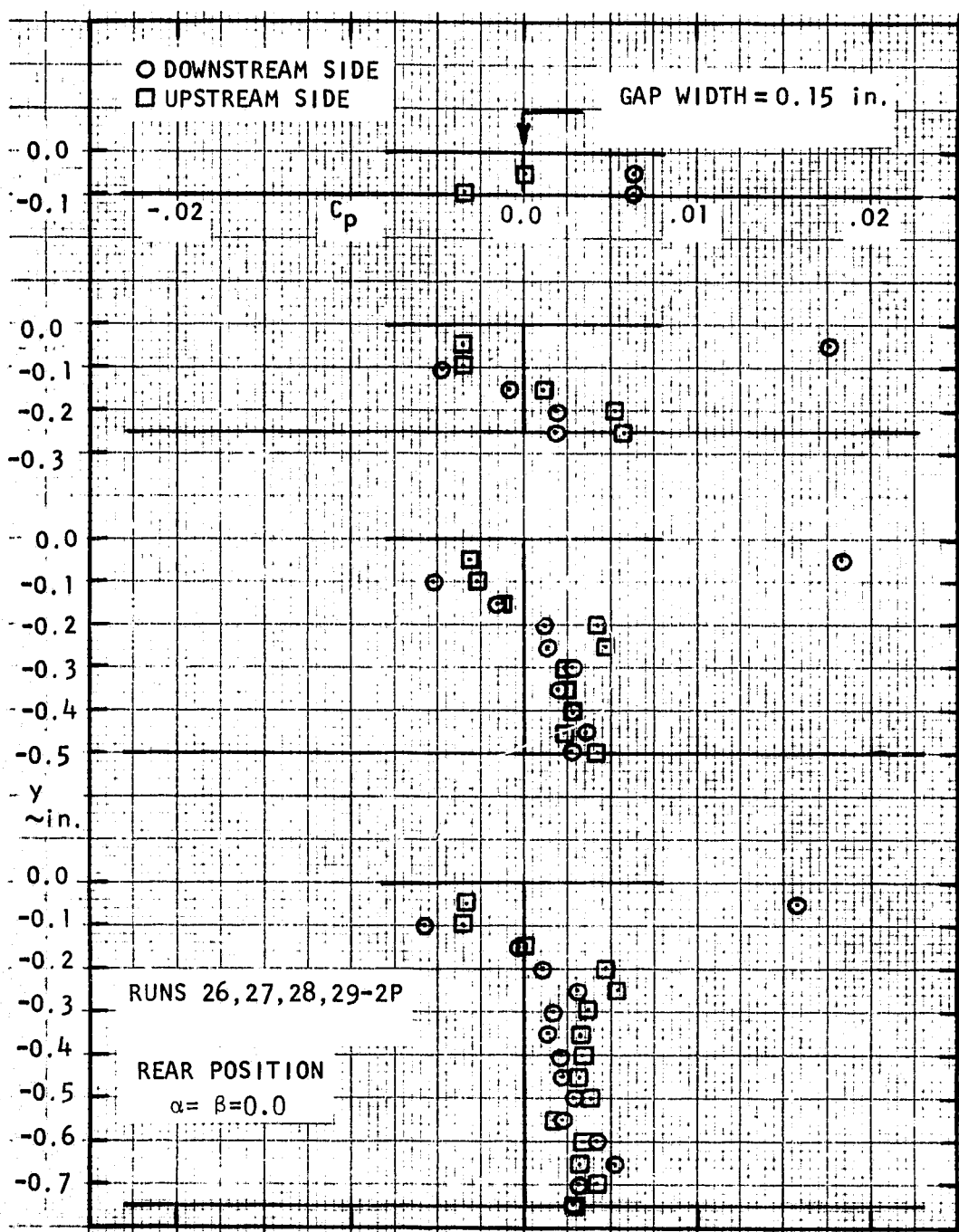


Fig. B-4 Step/cavity wall pressure coefficients for various steps and cavity gap depths; $b=0.15$ inch, $\beta=0^\circ$, rear position.

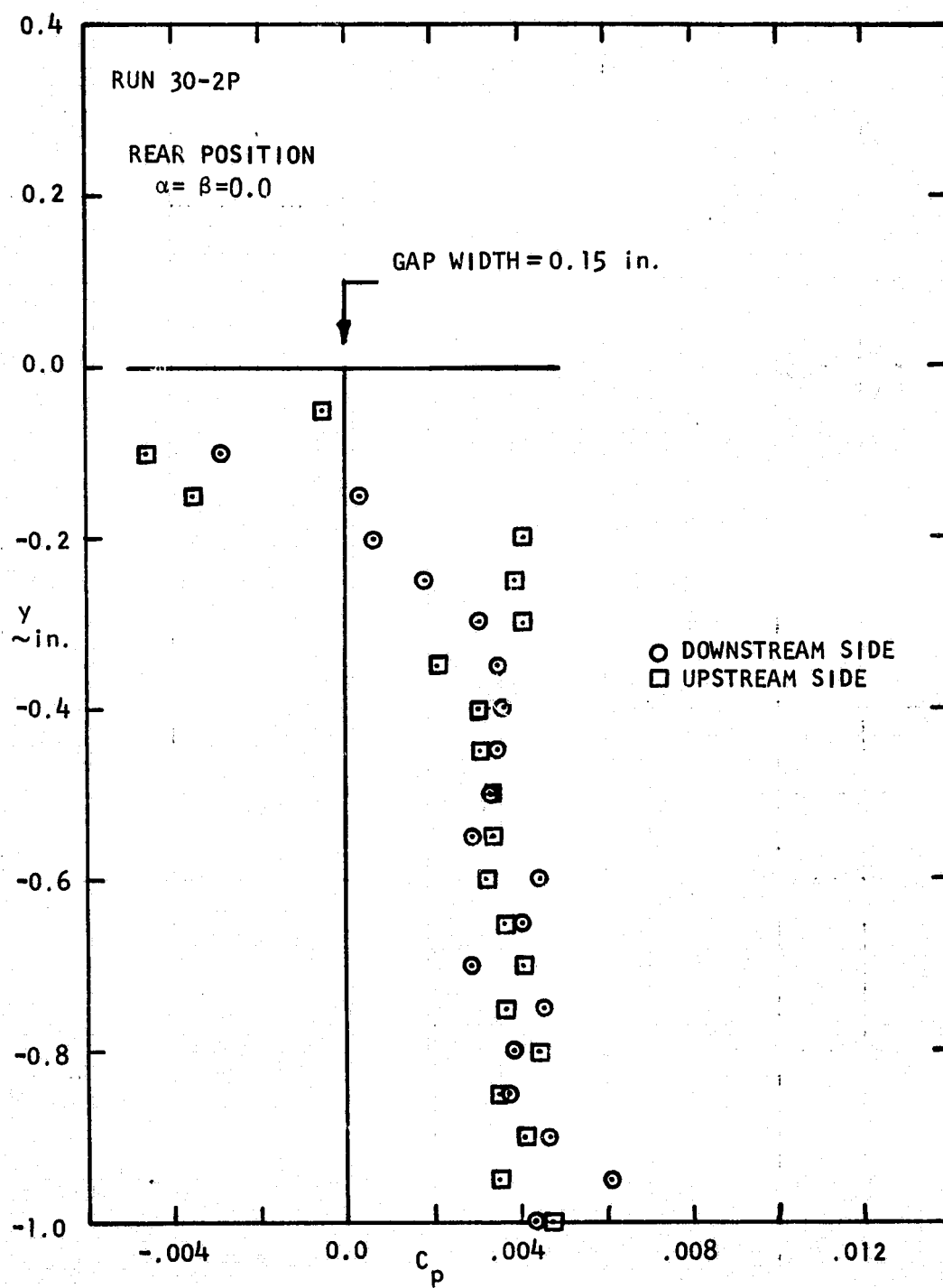


Fig. B-4 continued.

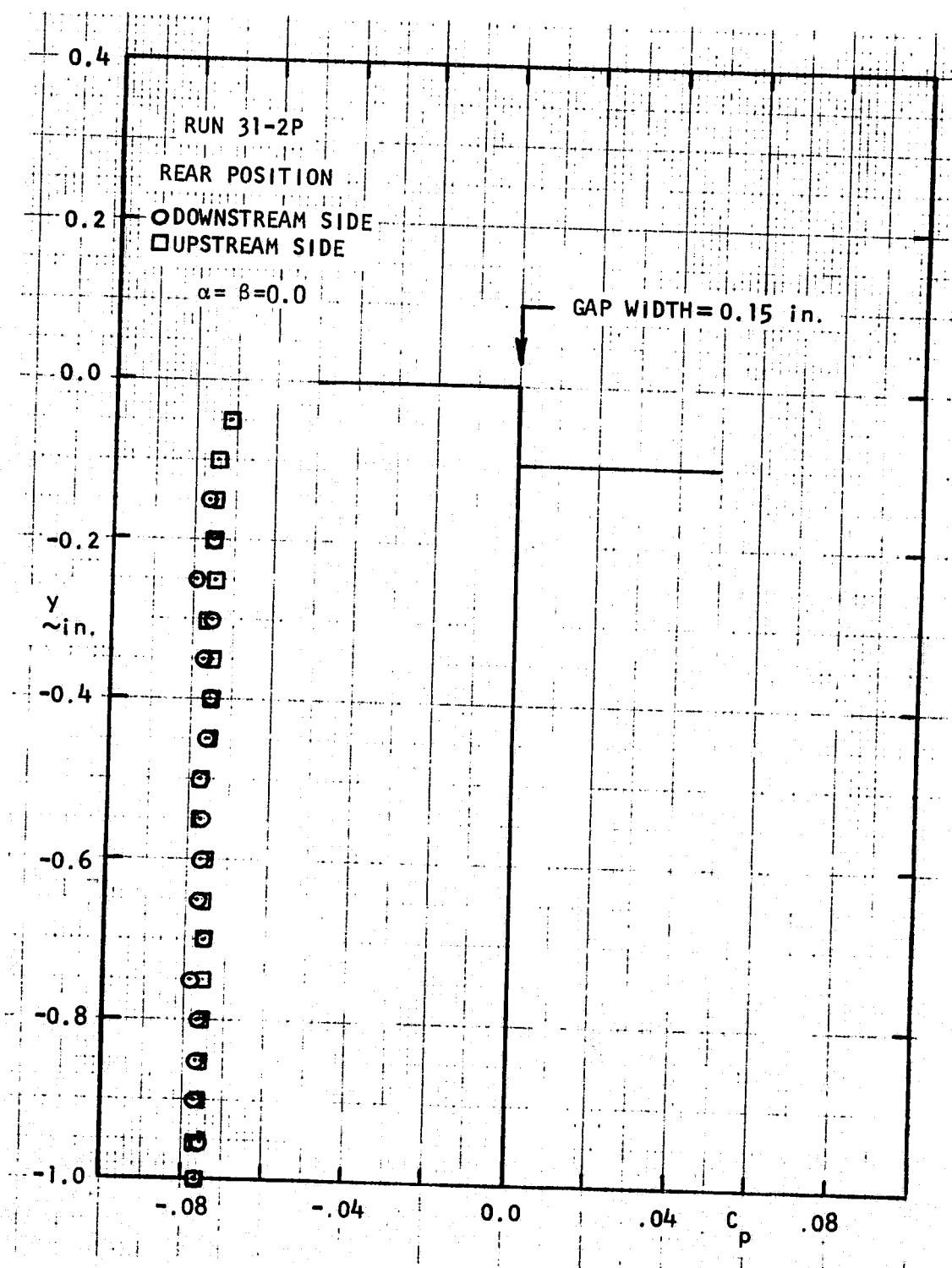


Fig. B-4 continued.

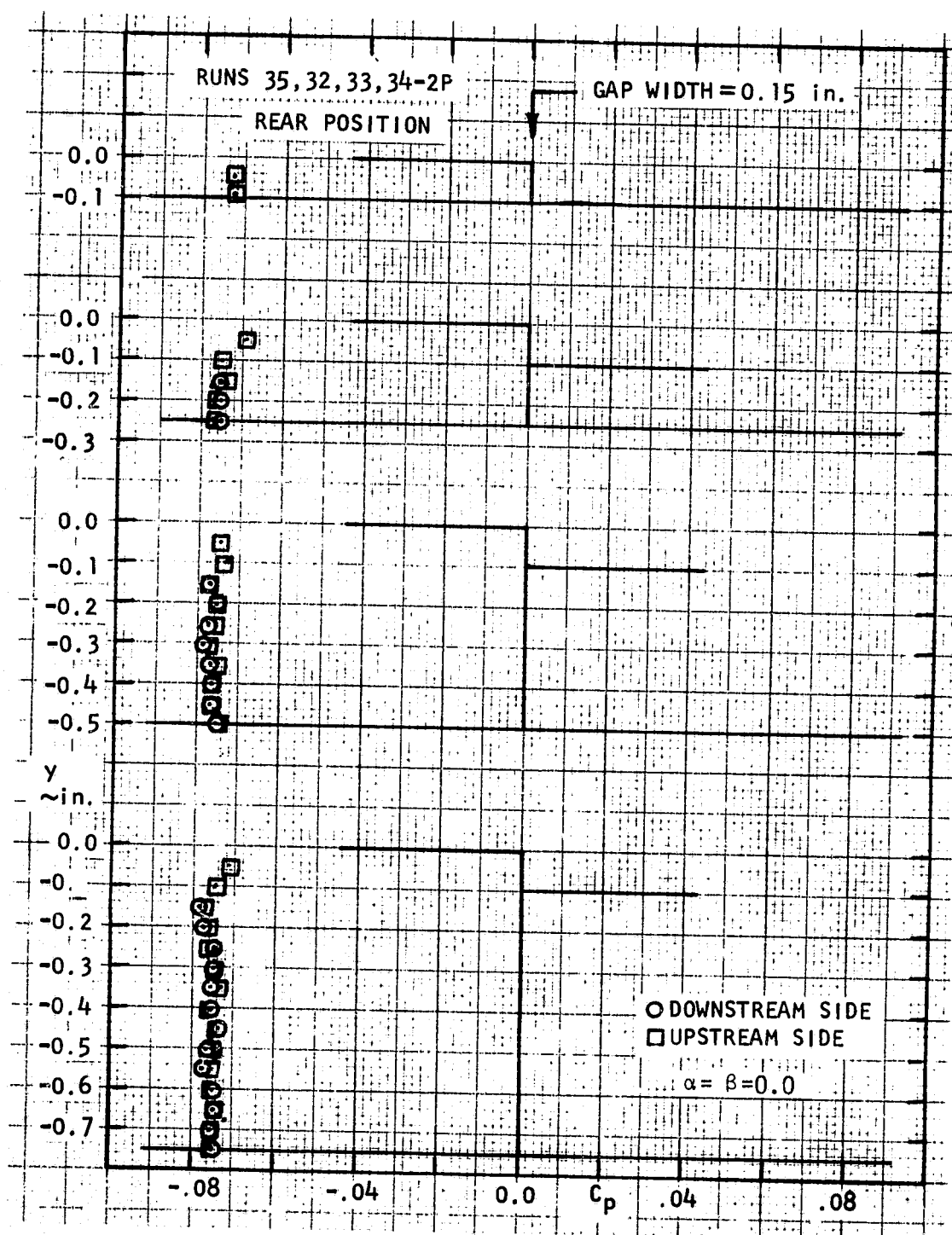


Fig. B-4 continued.

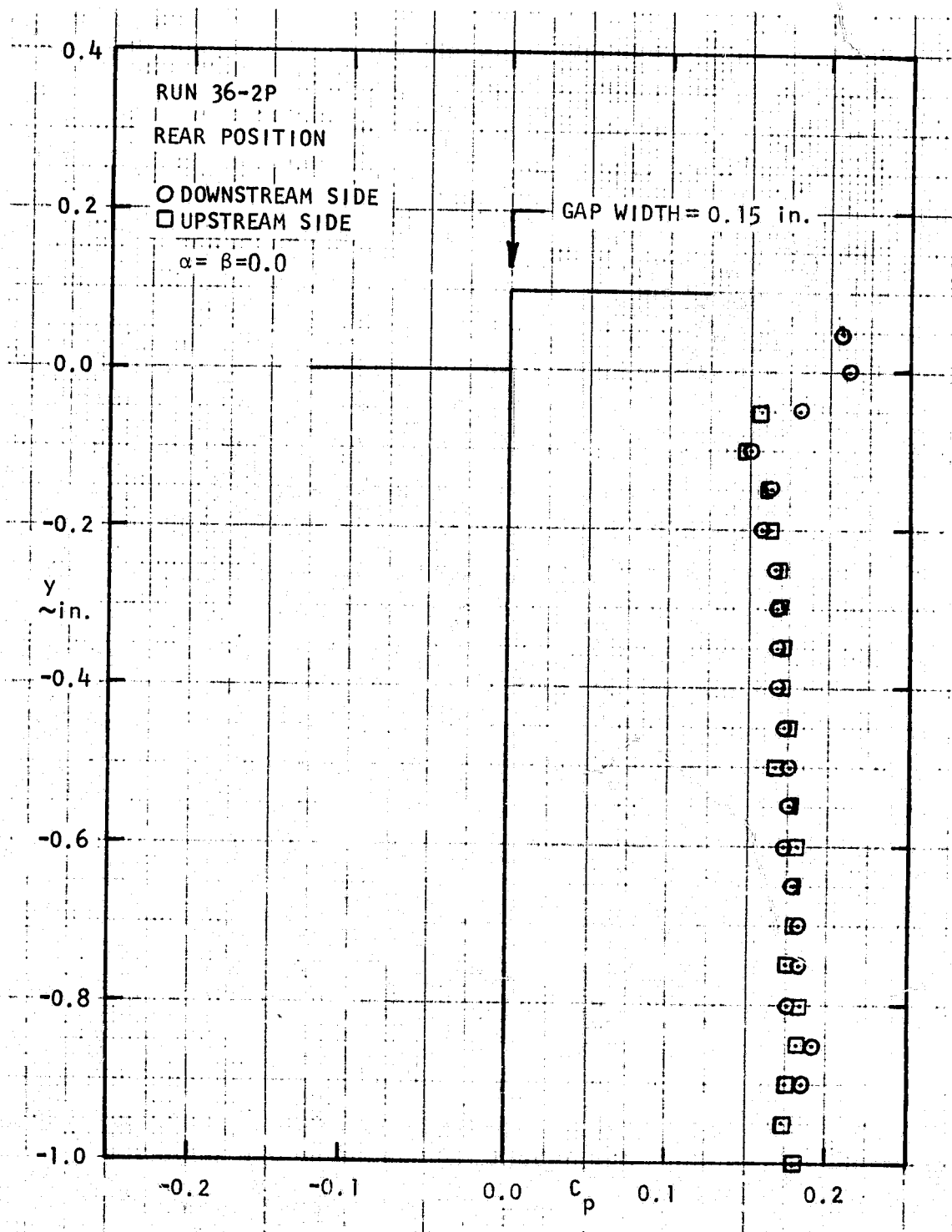


Fig. B-4 continued.

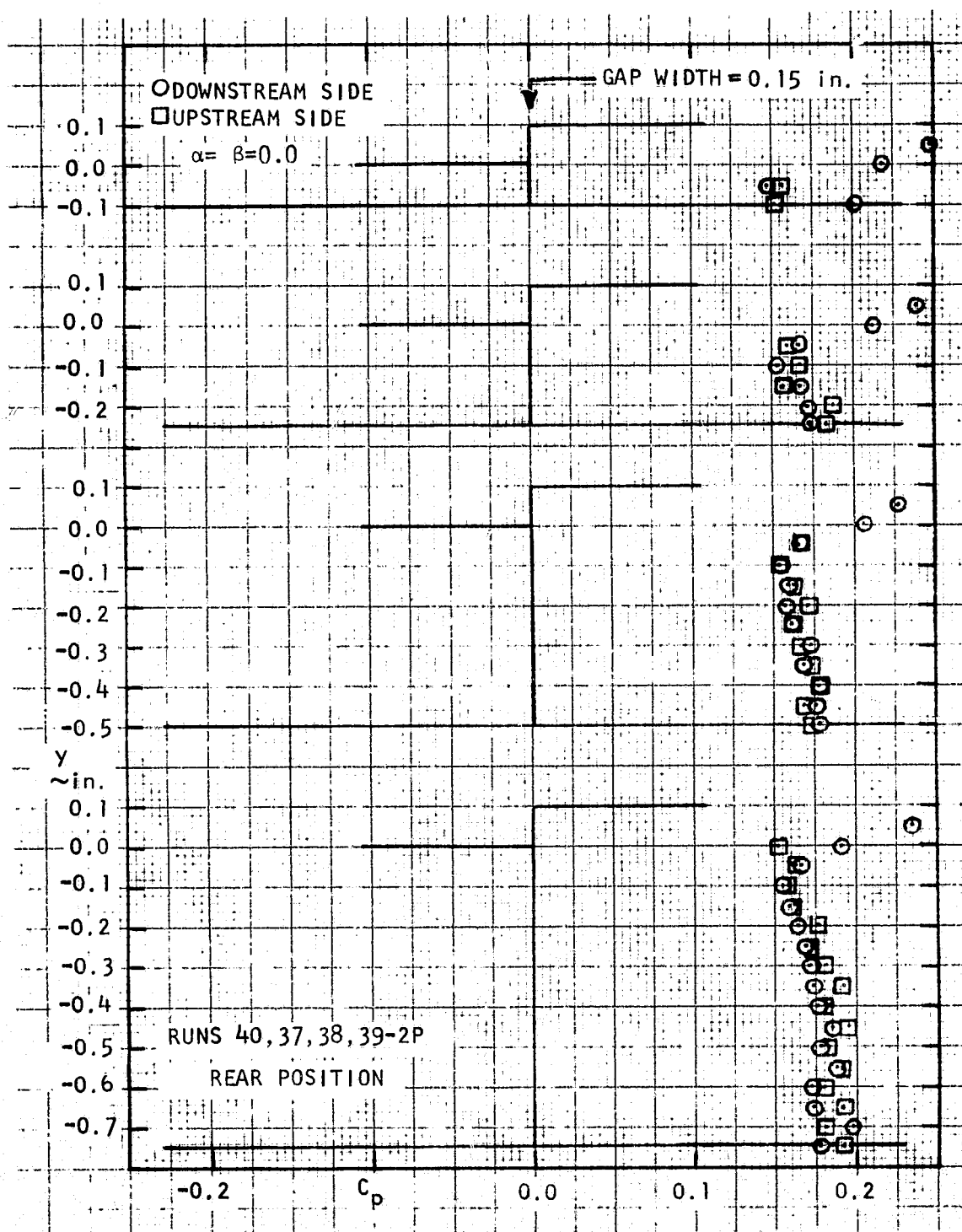


Fig. B-4 continued.

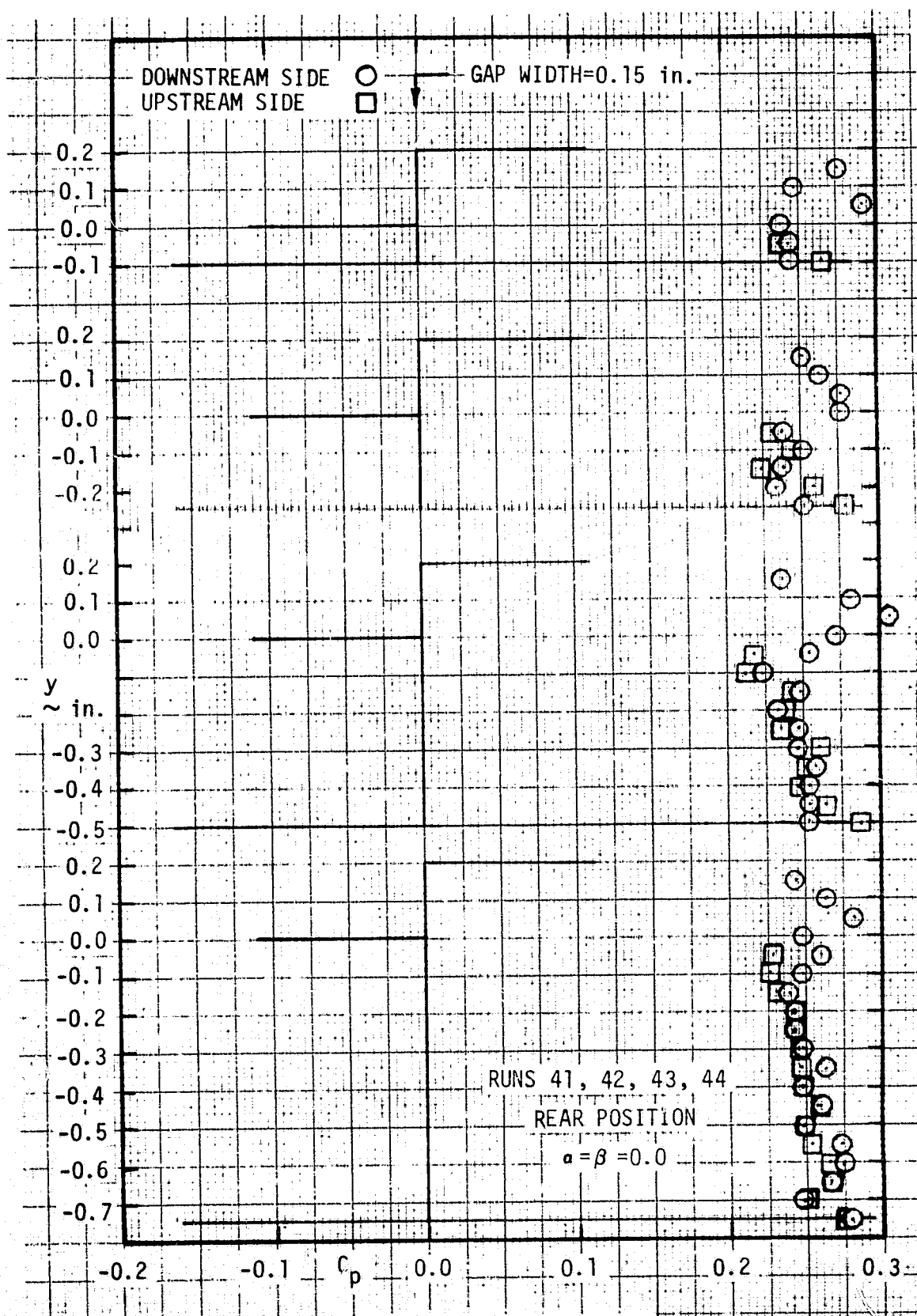
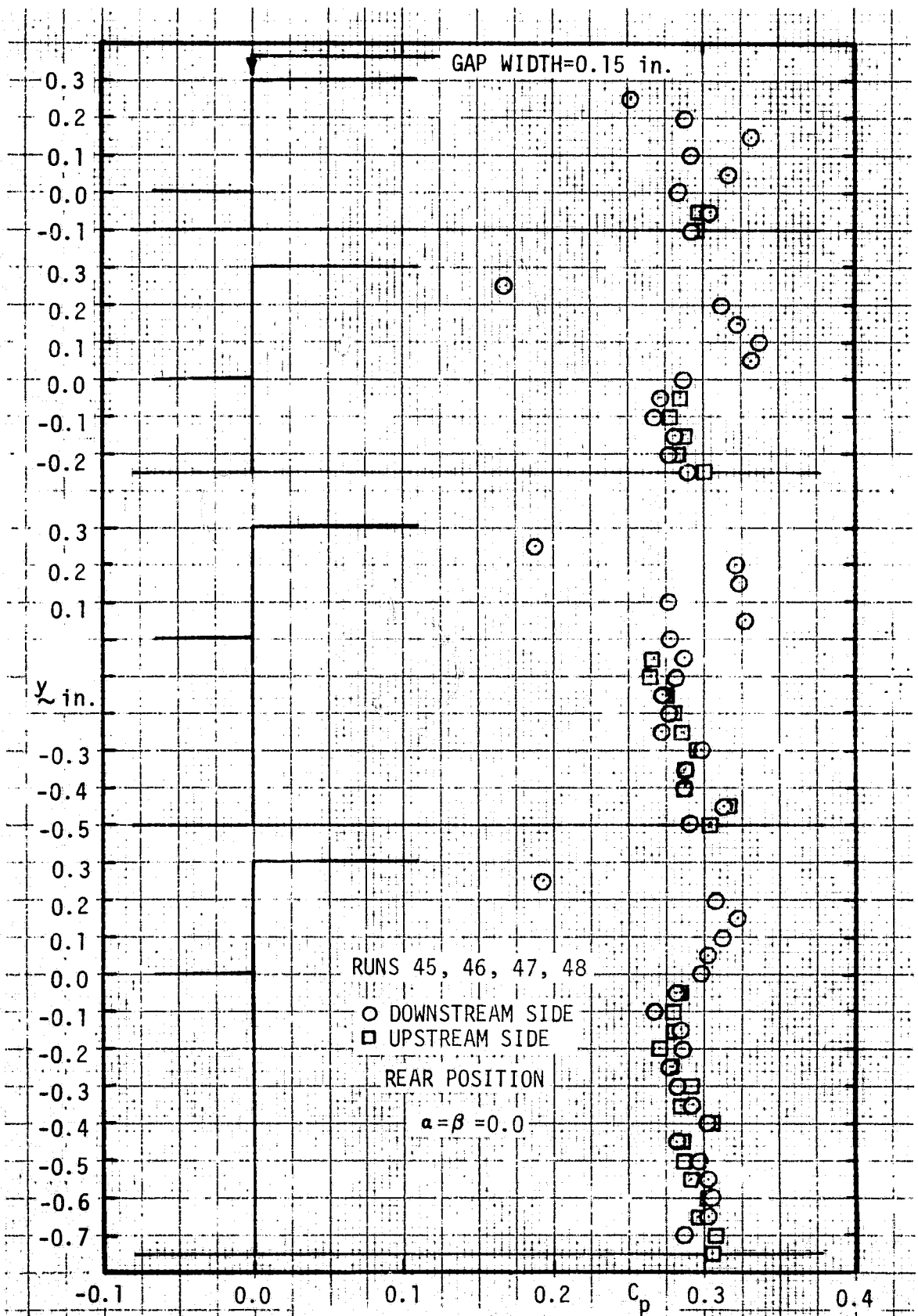


Fig. B-4 continued.



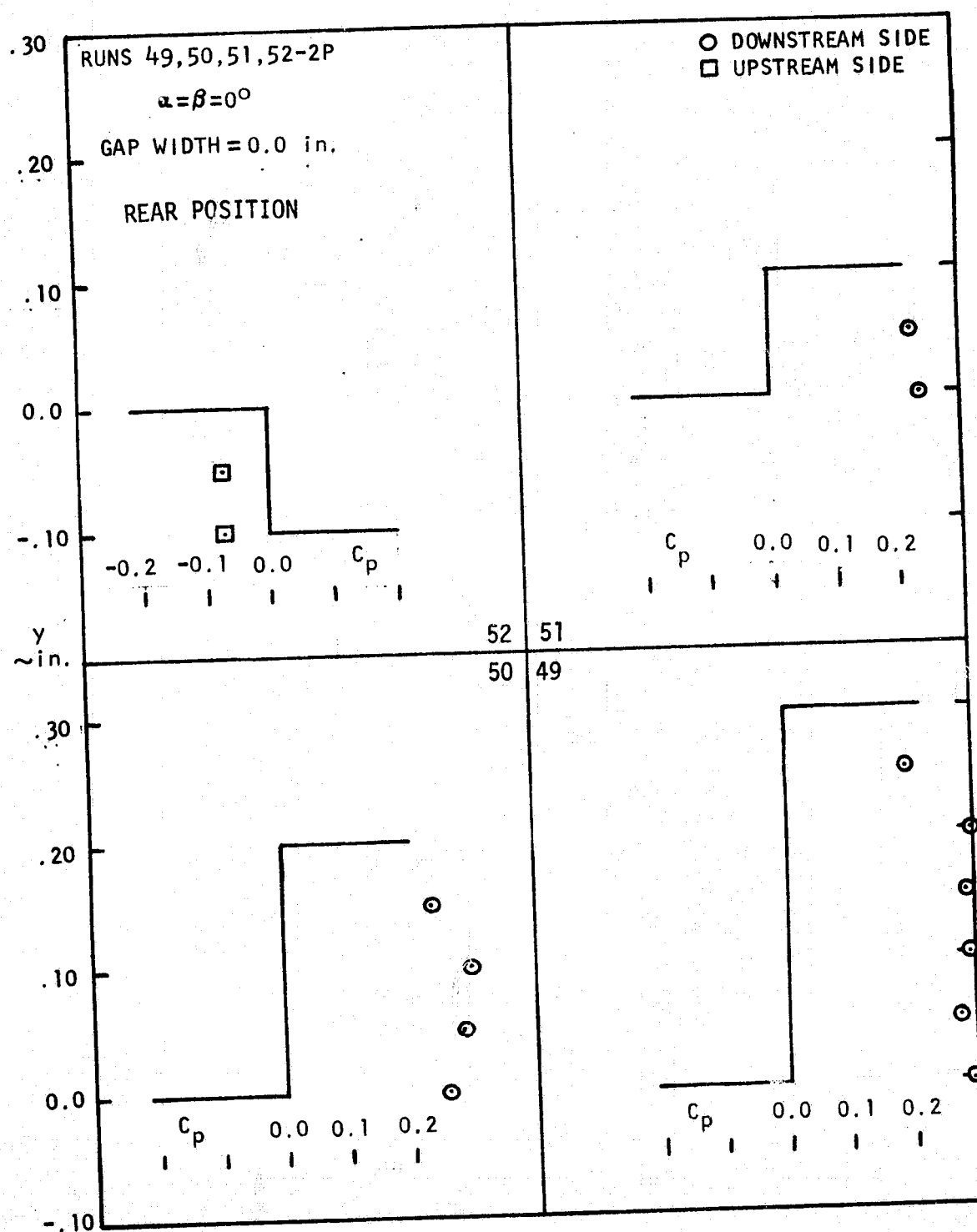


Fig. B-5 Step wall pressure coefficients; $\beta = 0^\circ$, rear position.

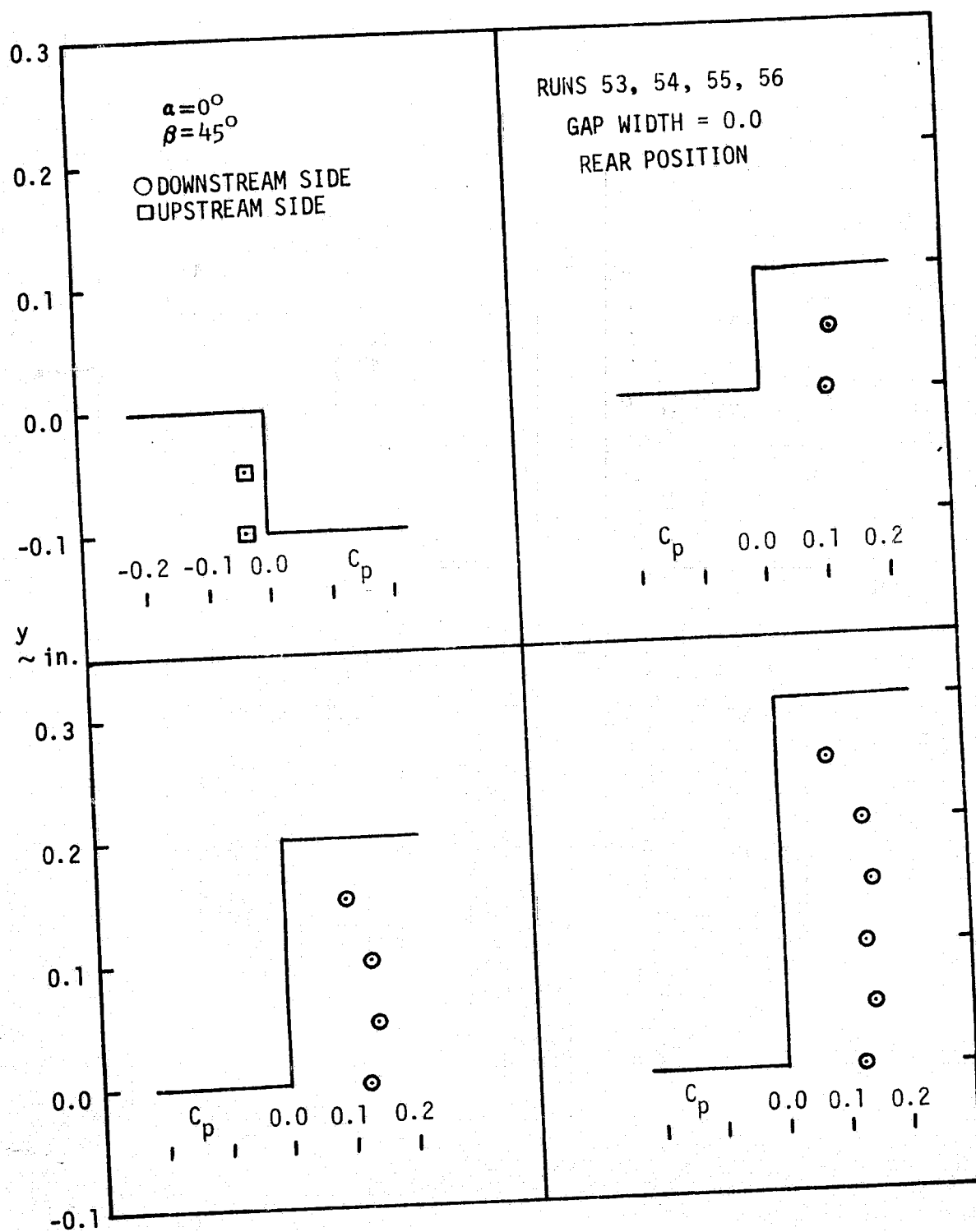


Fig. B-6 Step wall pressure coefficients; $\beta = 45^\circ$, rear position.

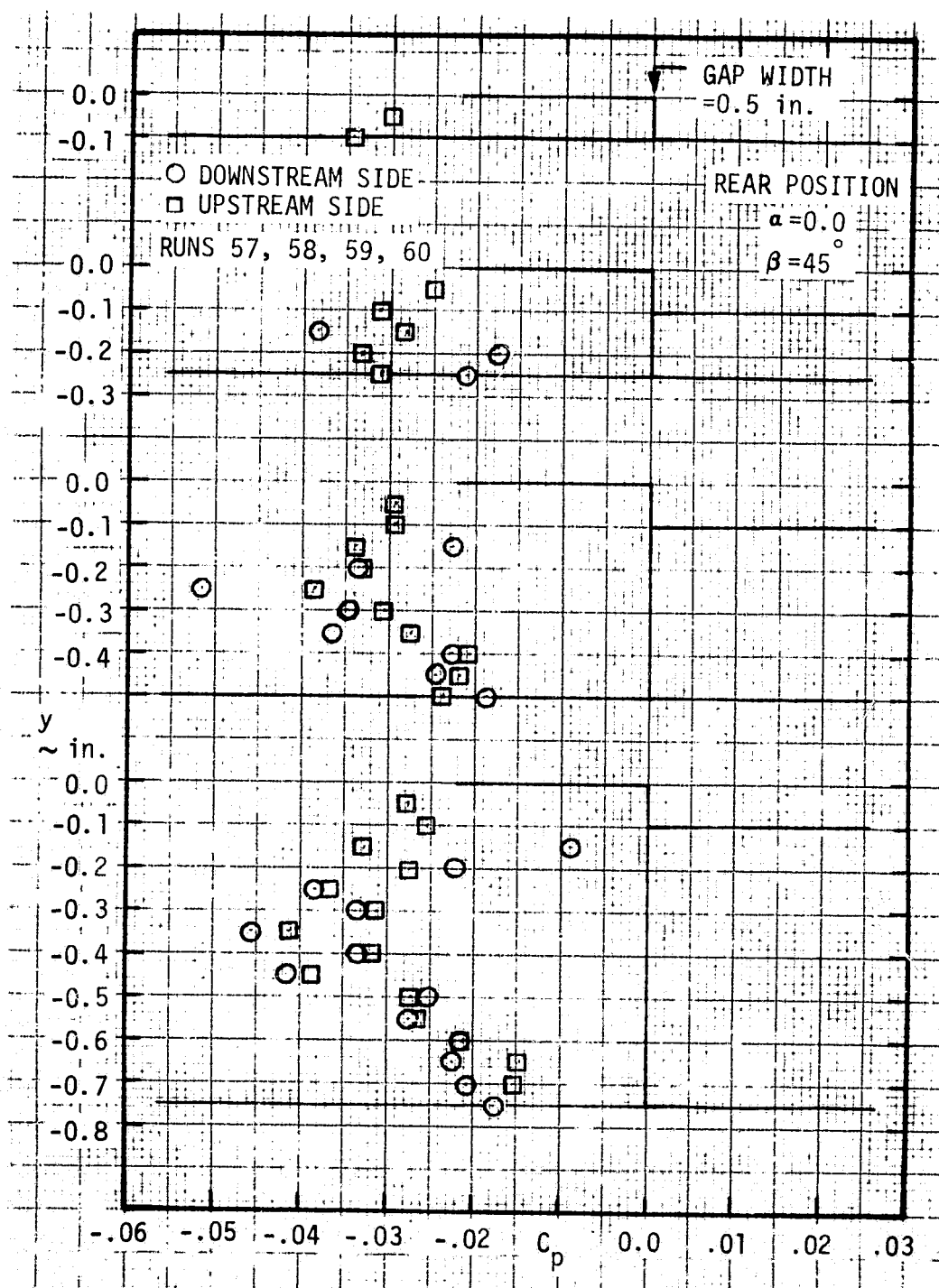


Fig. B-7 Step/cavity wall pressure coefficients for various steps and cavity gap depths; $b=0.5$ inch, $\beta=45^\circ$, rear position.

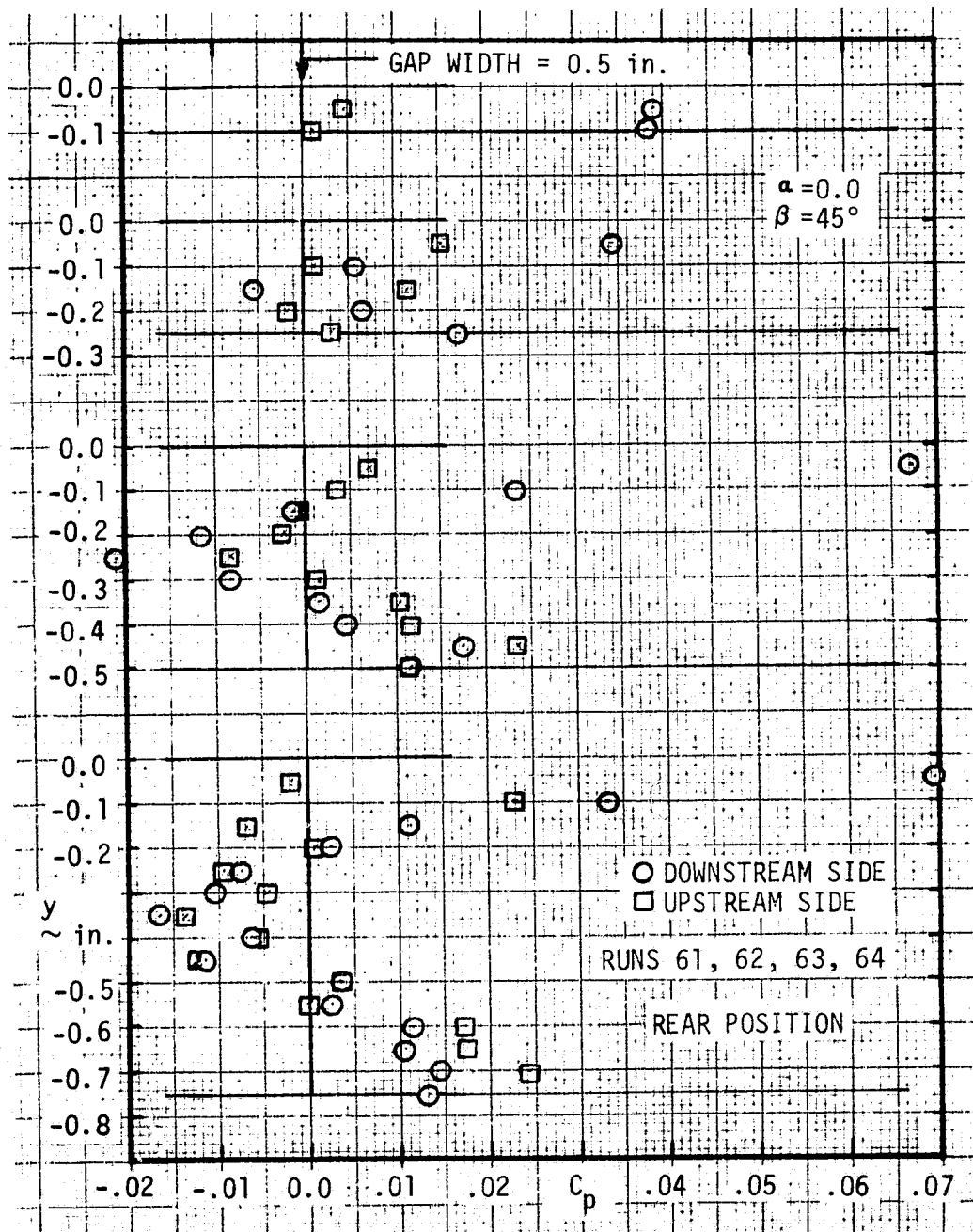


Fig. B-7 continued.

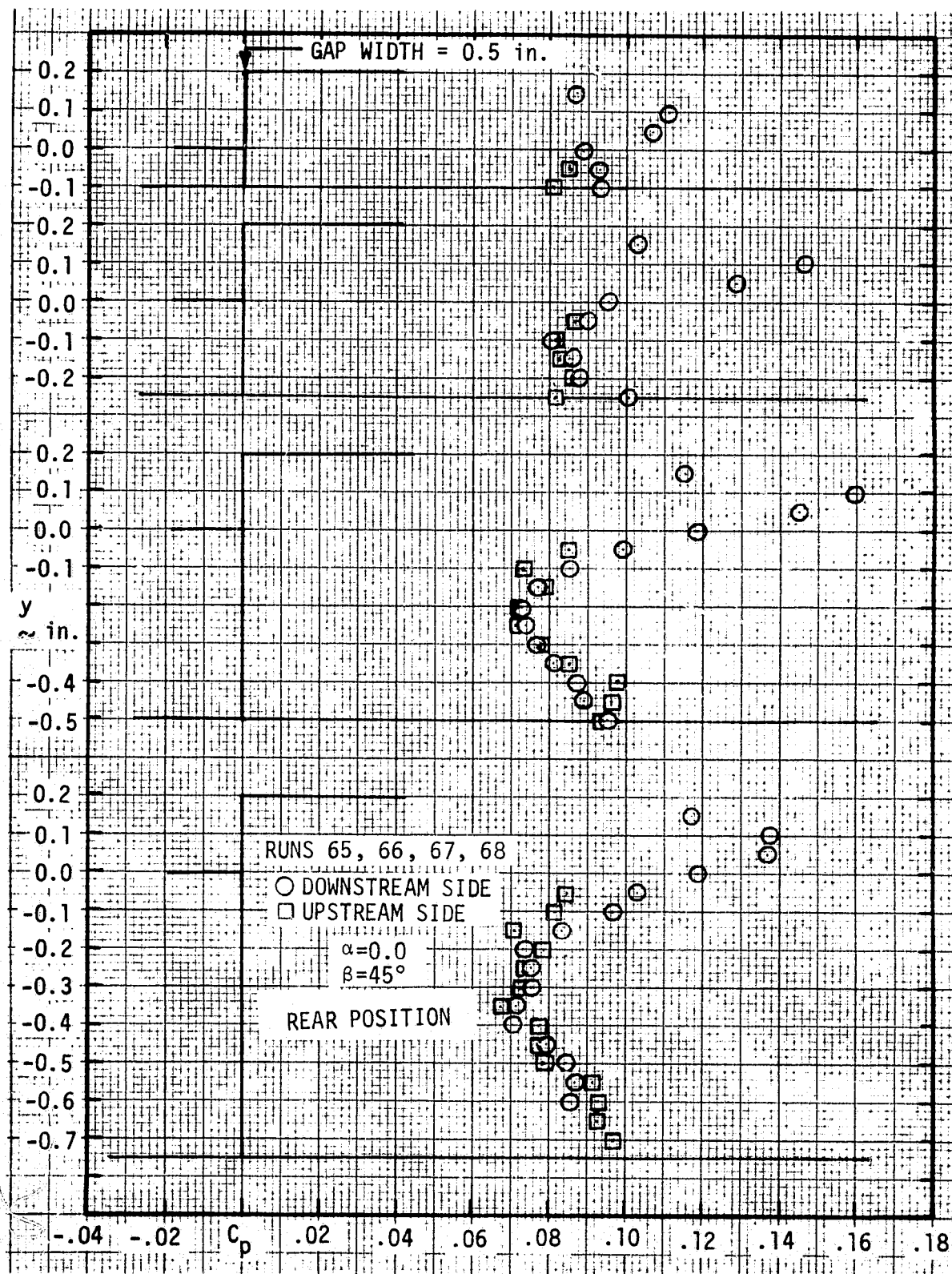


Fig. B-7 continued.

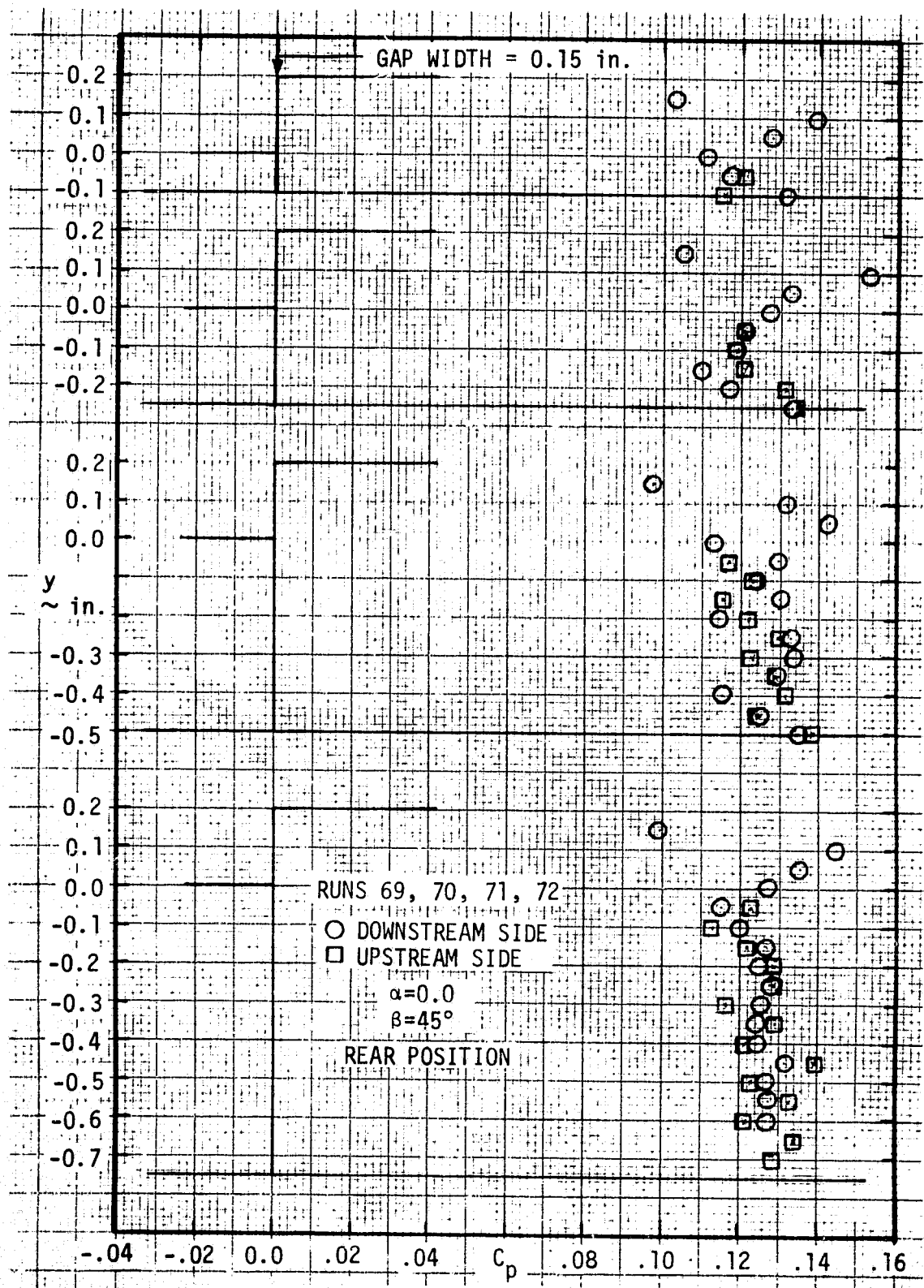


Fig. B-8 Step/cavity wall pressure coefficients for various steps and cavity gap depths; $b=0.15$ inch, $\beta=45^\circ$, rear position.

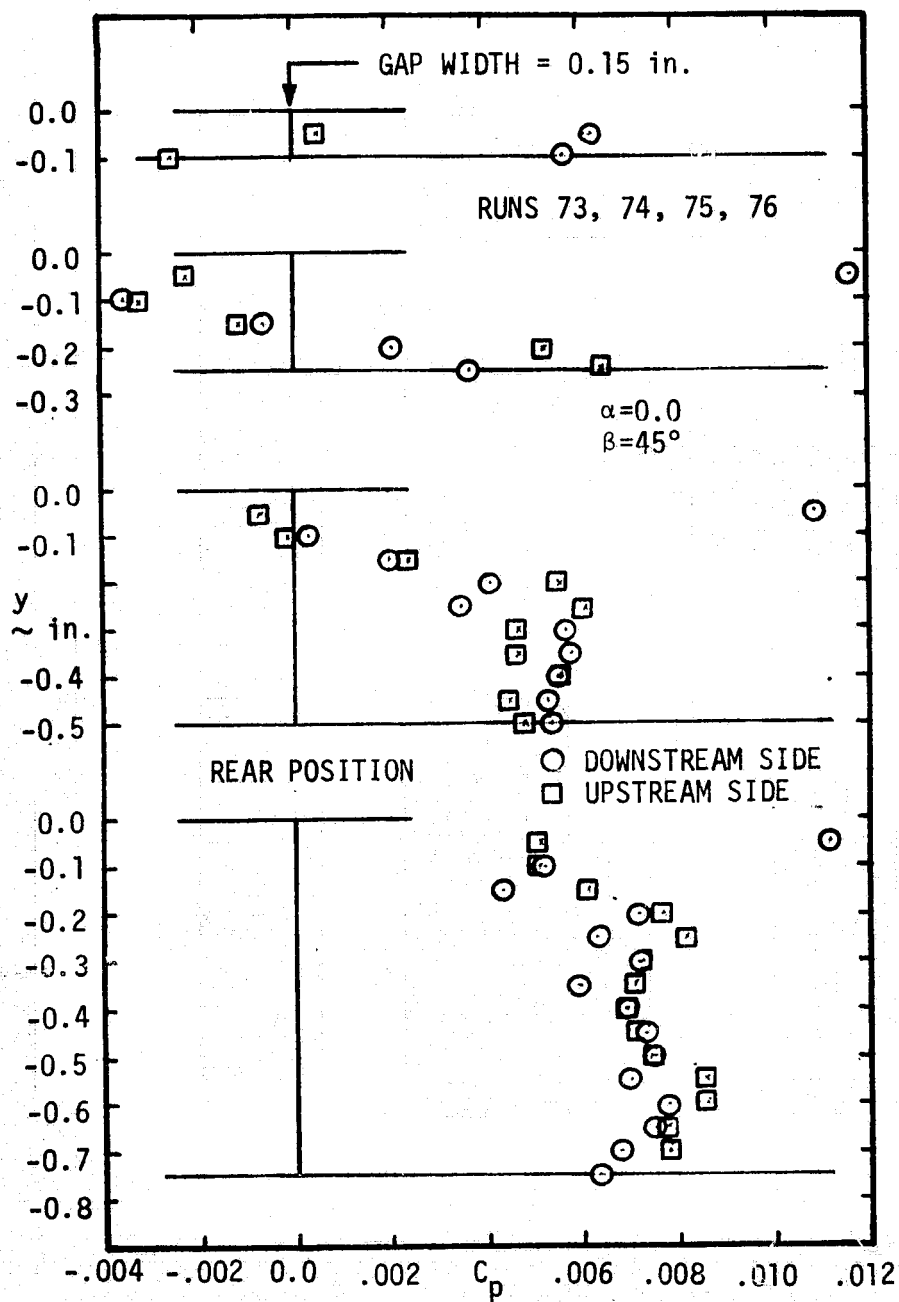


Fig. B-8 continued.

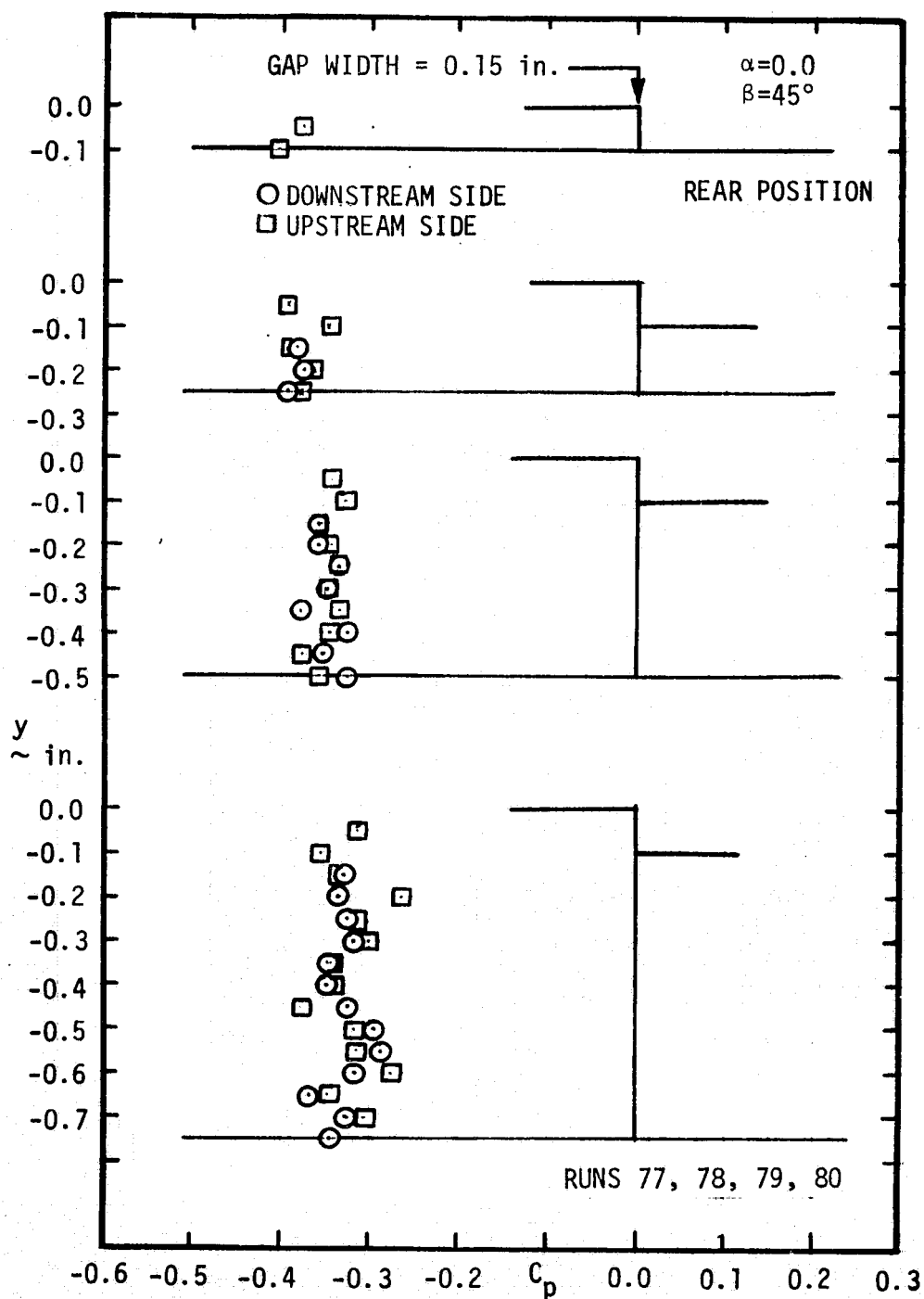


Fig. B-8 continued.

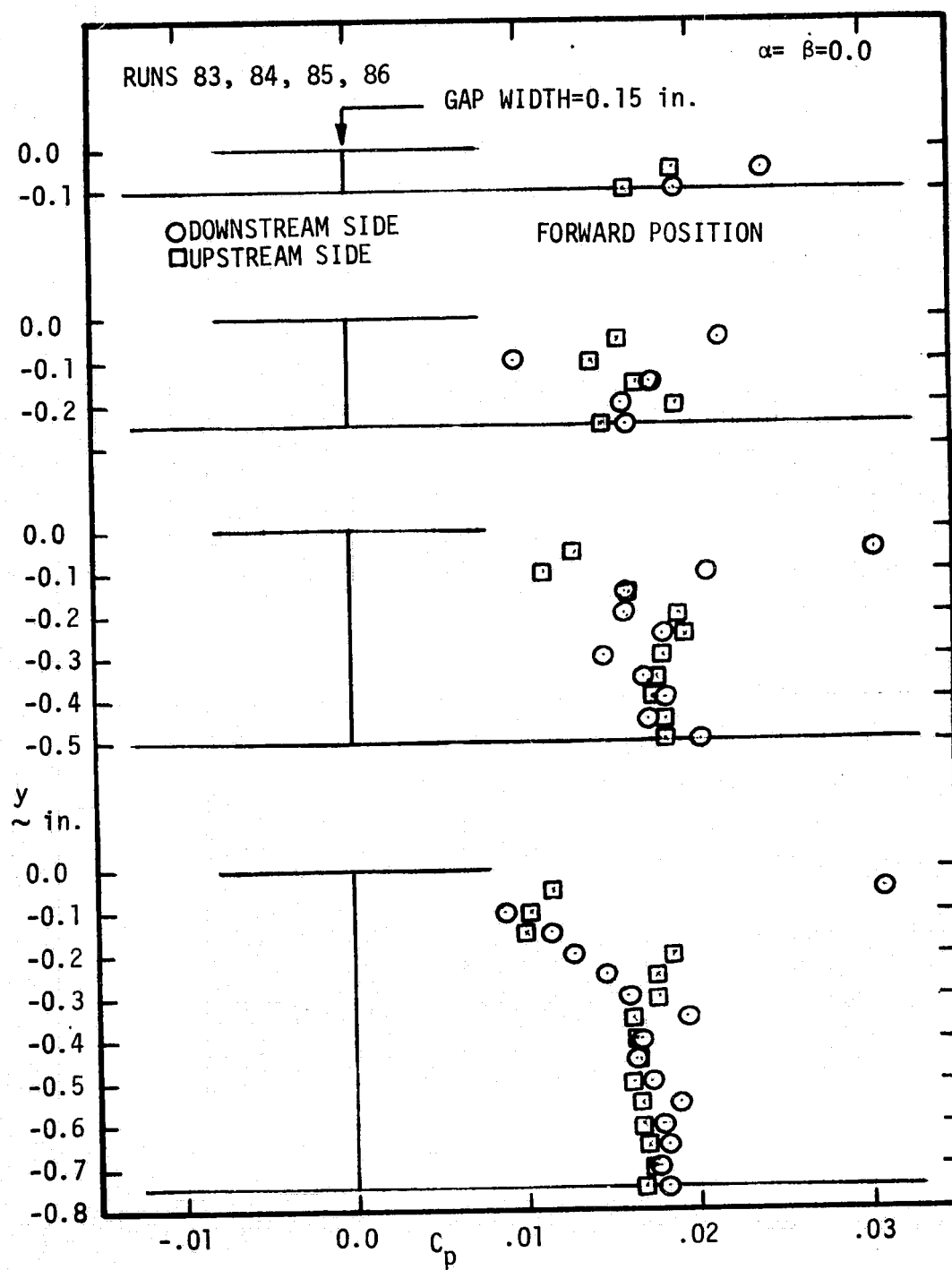


Fig. B-9 Step/cavity wall pressure coefficients for various steps and cavity gap depths; $b=0.15$ inch, $\beta=0^\circ$, forward position.

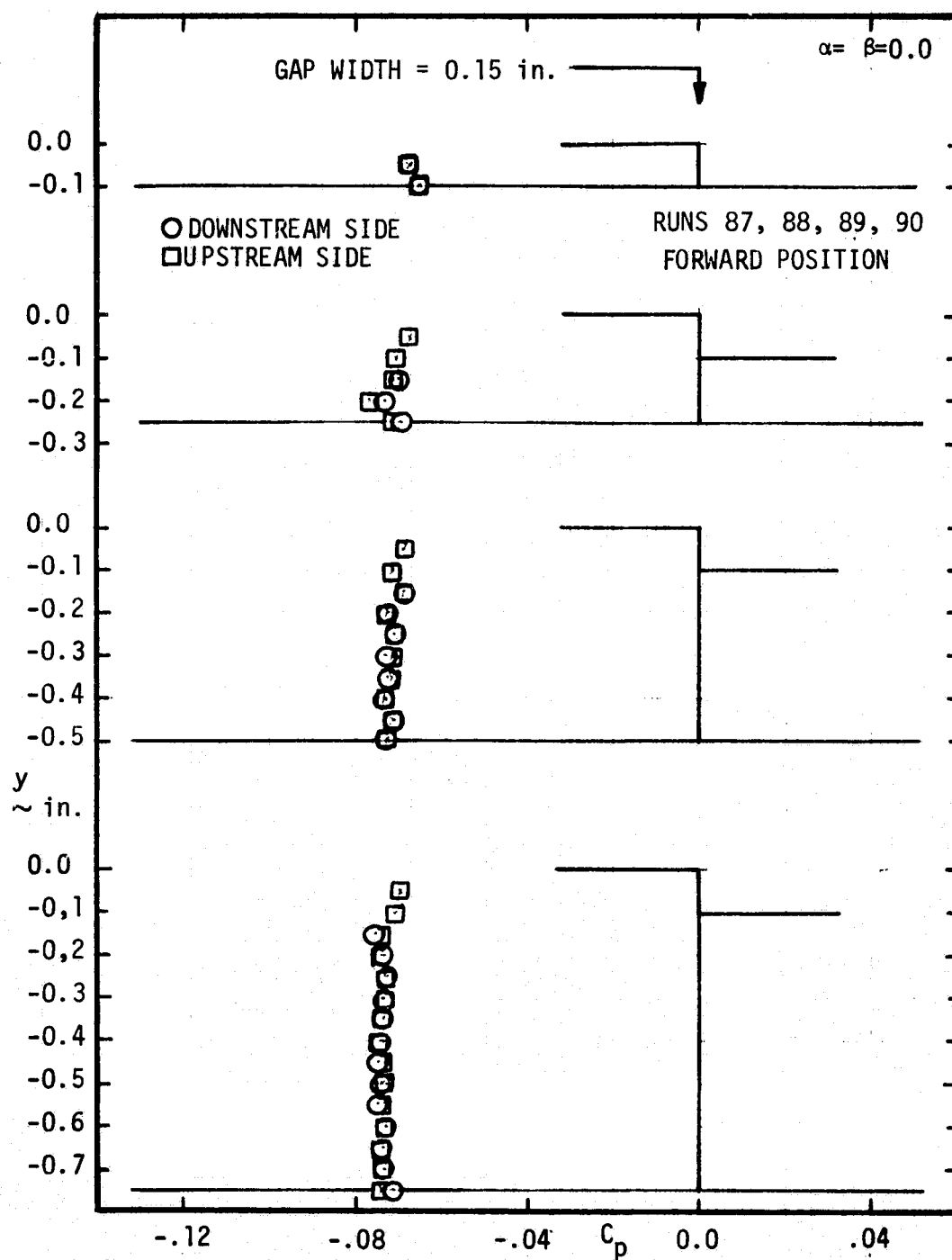


Fig. B-9 continued.

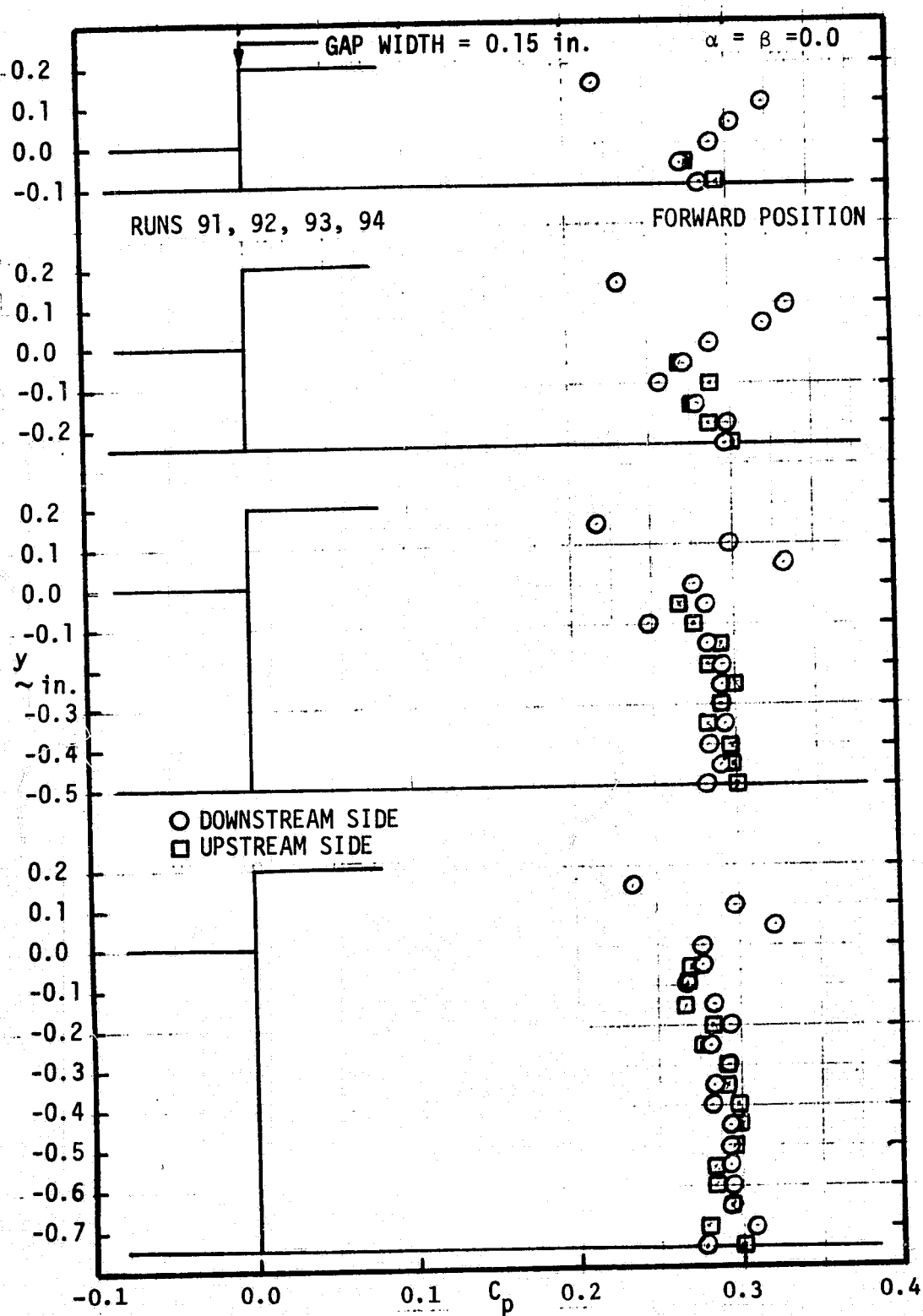


Fig. B-9 continued.

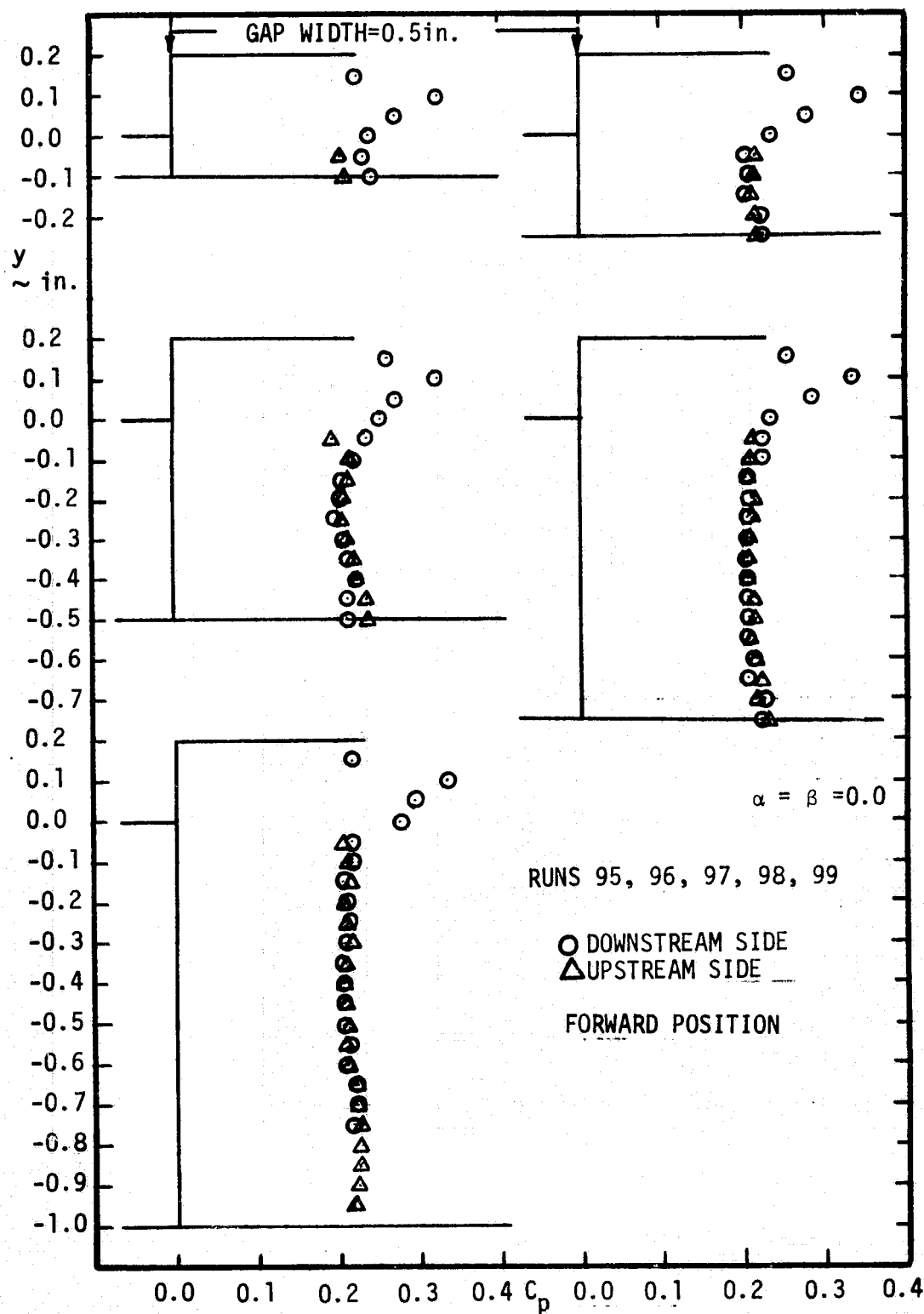


Fig. B-10 Step/cavity wall pressure coefficients for various steps and cavity gap depths; $b=0.5$ inch, $\beta=0^\circ$, forward position.

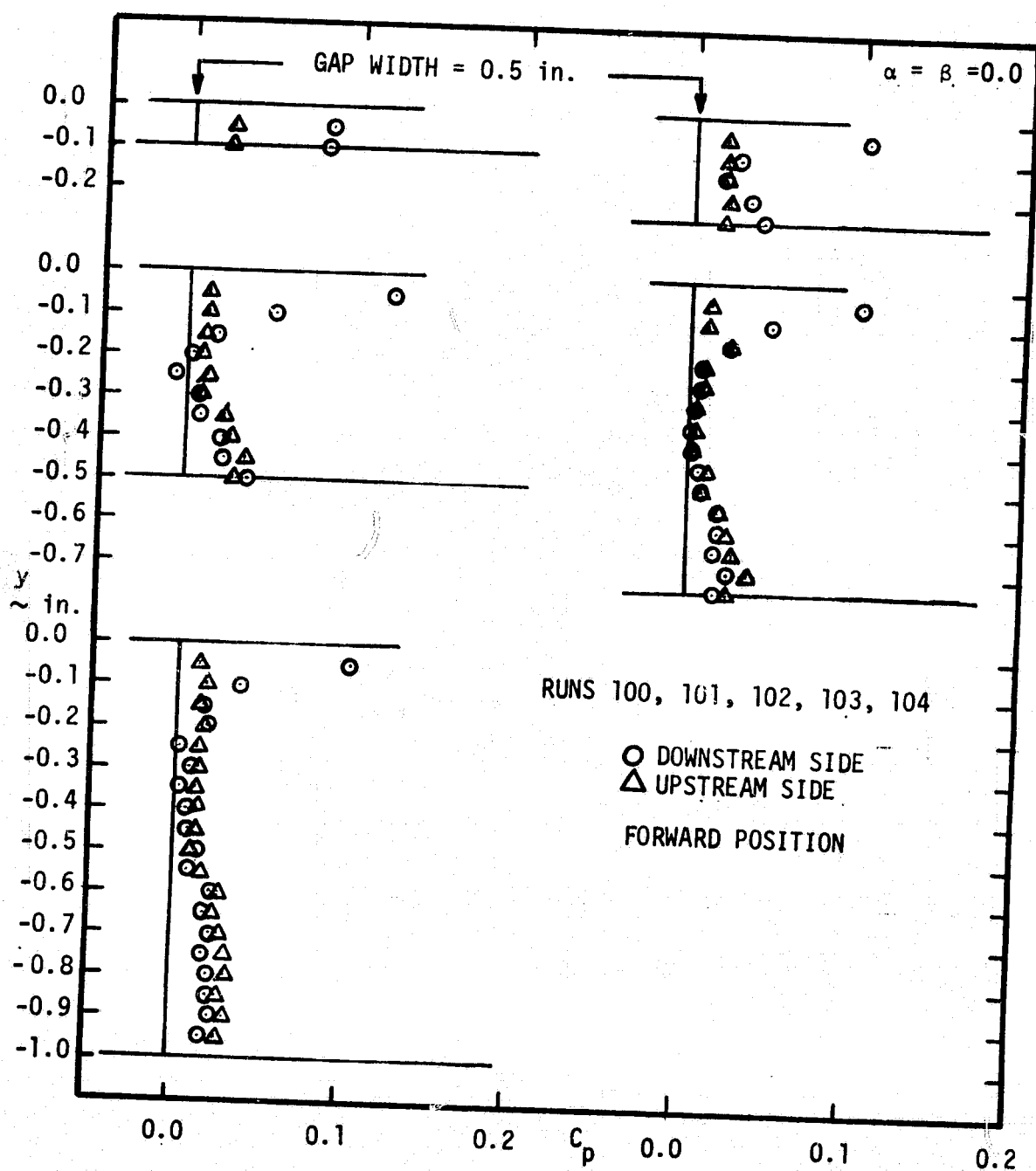


Fig. B-10 continued.

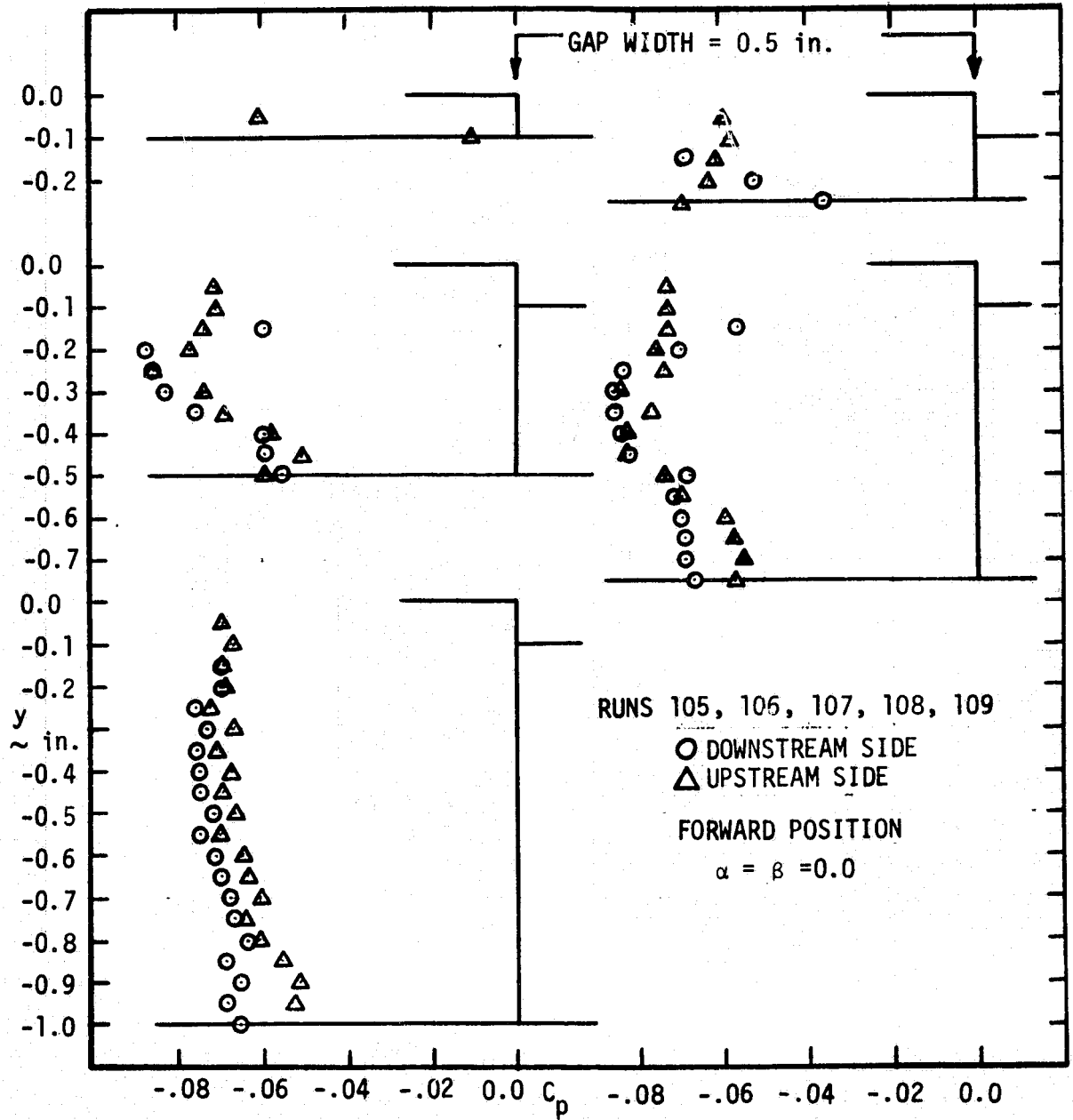


Fig. B-10 continued.

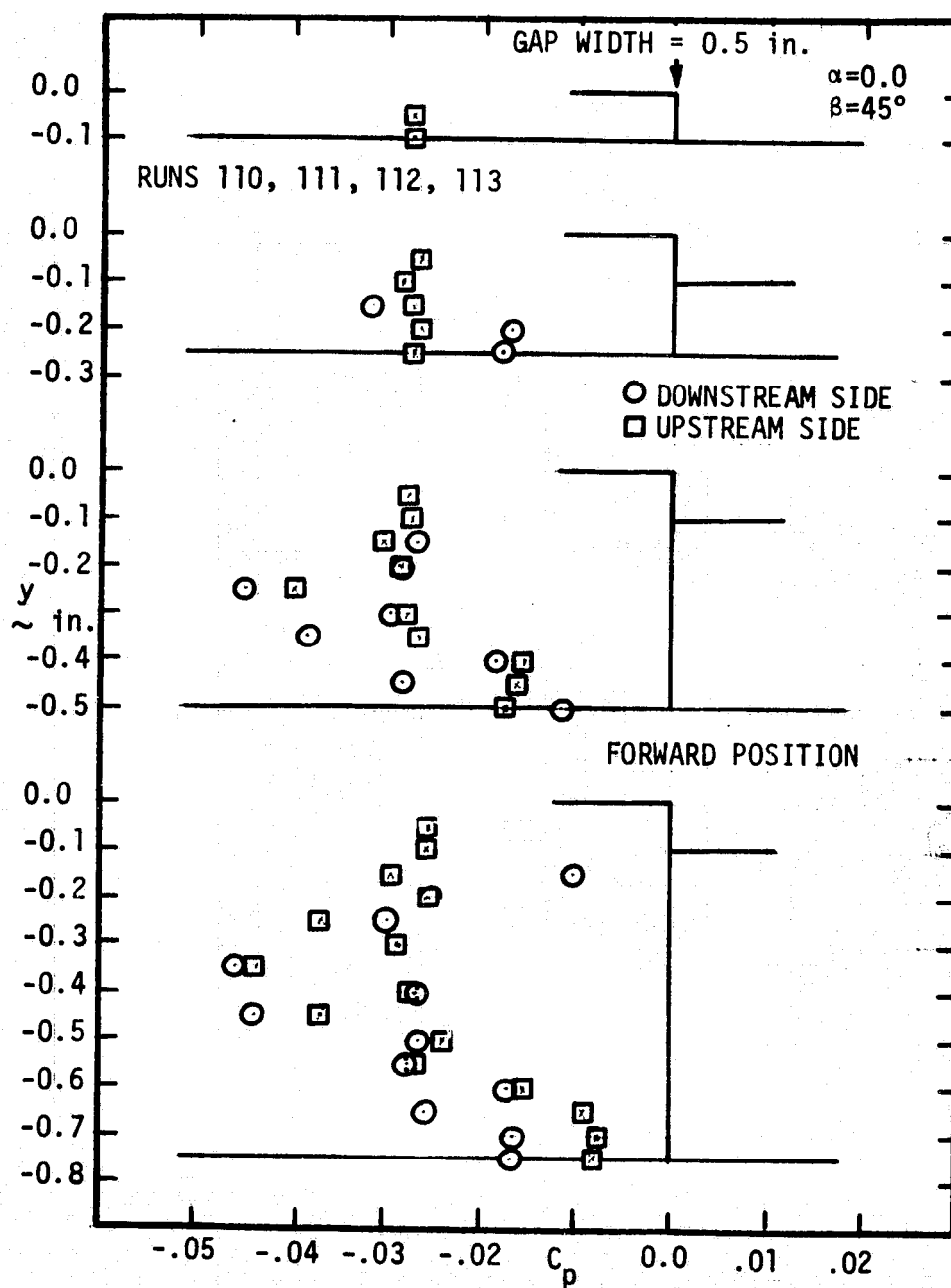


Fig. B-11 Step/cavity wall pressure coefficients for various steps and cavity gap depths; $b = 0.5$ inch, $\beta = 45^\circ$, forward position.

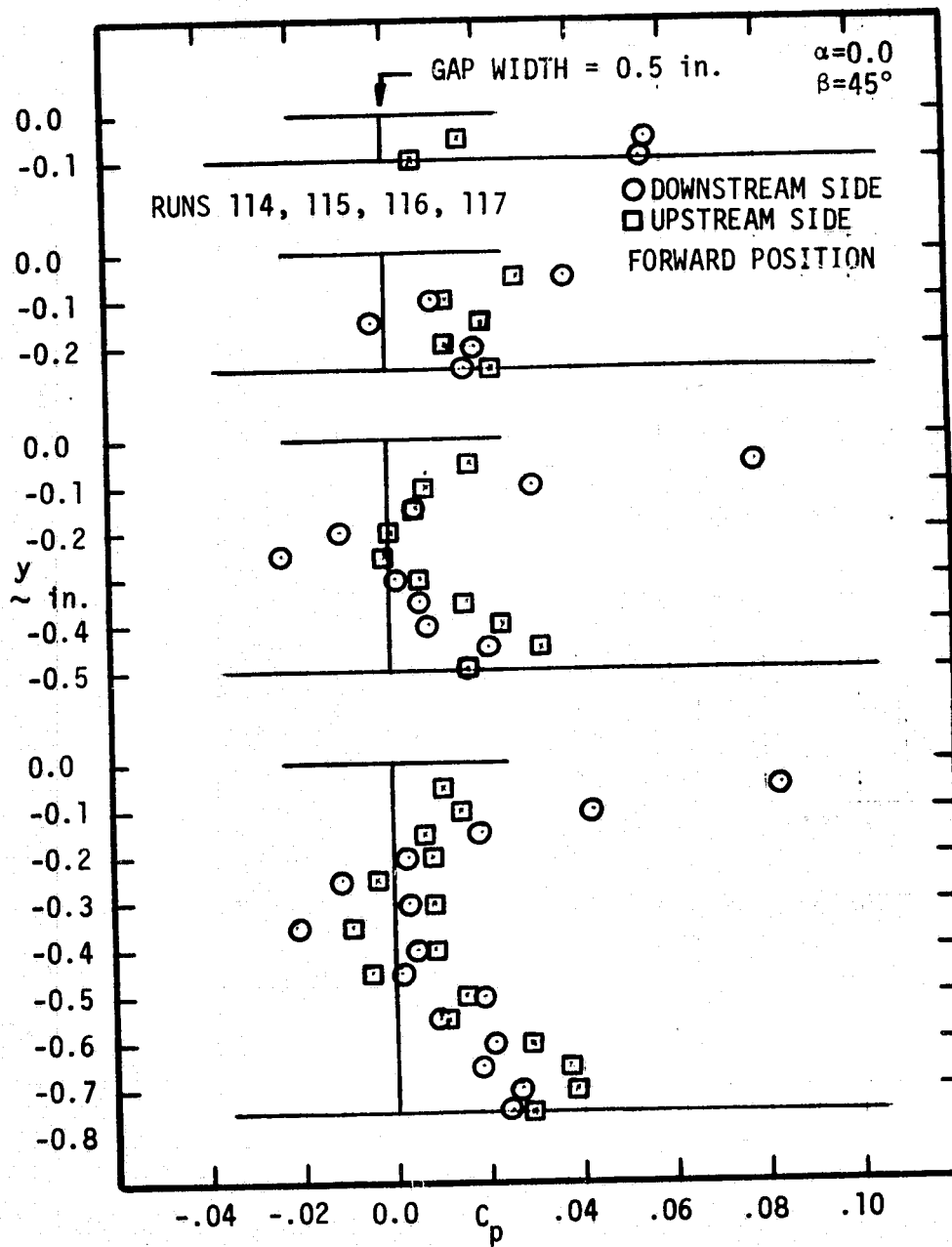


Fig. B-11 continued.

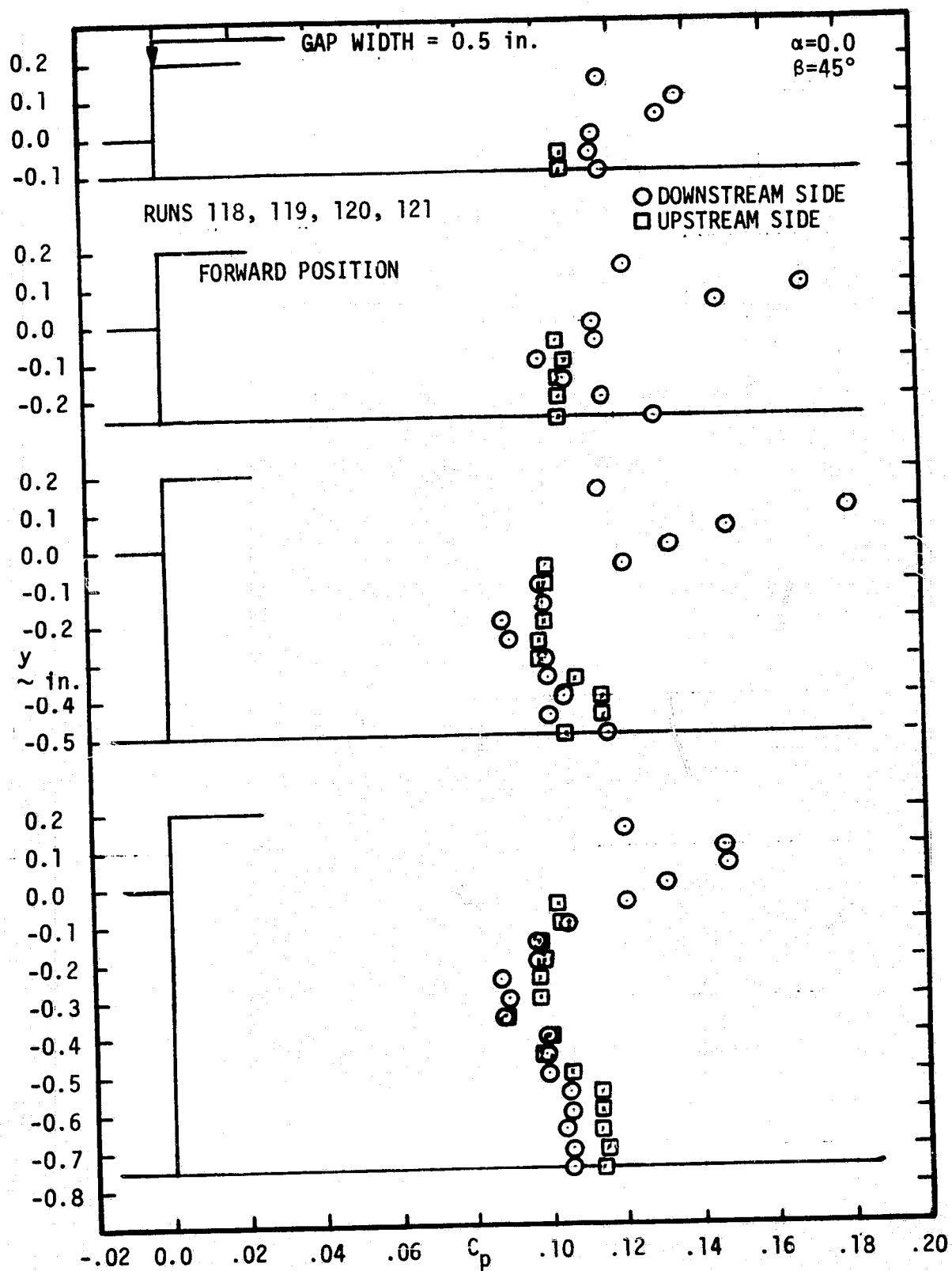


Fig. B-11 continued.

APPENDIX C

VELOCITY SURVEYS

Velocity surveys presented in this appendix were used to compute skin friction coefficient and to evaluate the universality of the velocity profiles. An additional reason for including velocity profiles is to enable future use of the data contained in the main body of this report and in other appendices which require velocity profile information. Mean velocity and turbulence intensity profiles have been included. The values for dynamic pressure given on the following figures is a reference value used as an identifier. The correlation between tunnel Q and q_e is that $Q = 5, 10, 20$, and 40 psf correspond to $q_e = 6.7, 13.1, 26.7$, and 52.4 psf, respectively.

Figures C-1 and C-2 are for $Q = 5$. In Fig. C-1 mean velocity in the front and in the rear position are shown. Turbulence intensity is shown in Fig. C-2. Similar profiles for mean velocity and turbulence intensity for $Q = 10, 20$, and 40 are shown on Figs. C-3 and C-4, C-5 and C-6, and C-7 and C-8, respectively. Figure C-9 shows the effect of depth on mean velocity for a level cavity with $b = 0.50$ inch at $Q = 10$ psf. For the test run numbered 61, the hot film probe was 0.90 inch forward of the cavity front corner. For $d \neq 0.0$ the probe was 0.50 inch behind the cavity rear corner. The corresponding turbulence intensity is shown in Fig. C-10.

Another mean velocity profile set shown on Fig. C-11 was with a cavity gap width equal to 0.065 inch. Probing was 0.90 inch before the front cavity corner for $d = 0.0$ inch and 0.50 inch behind the rear

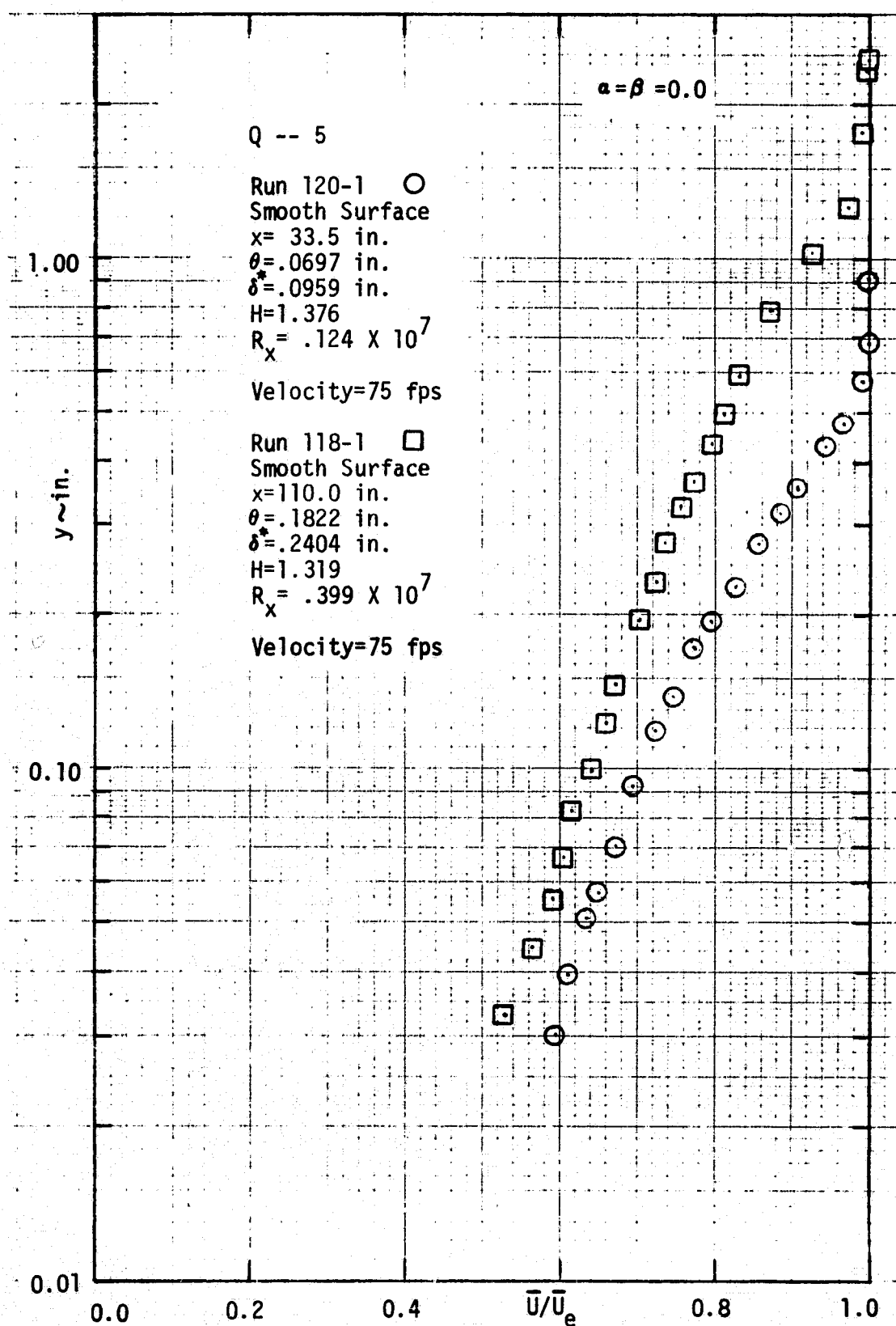


Fig. C-1 Velocity survey; Q = 5 psf

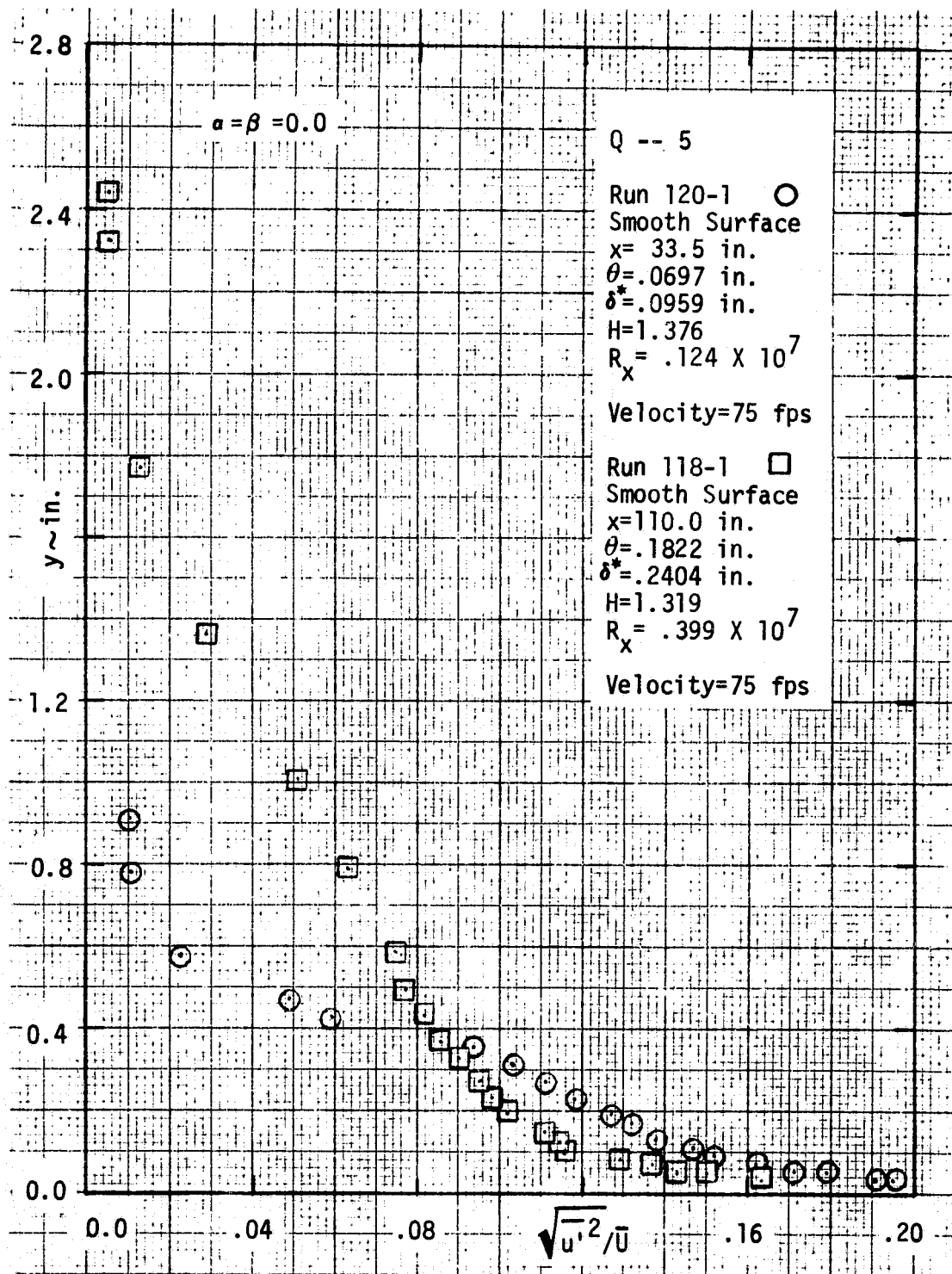
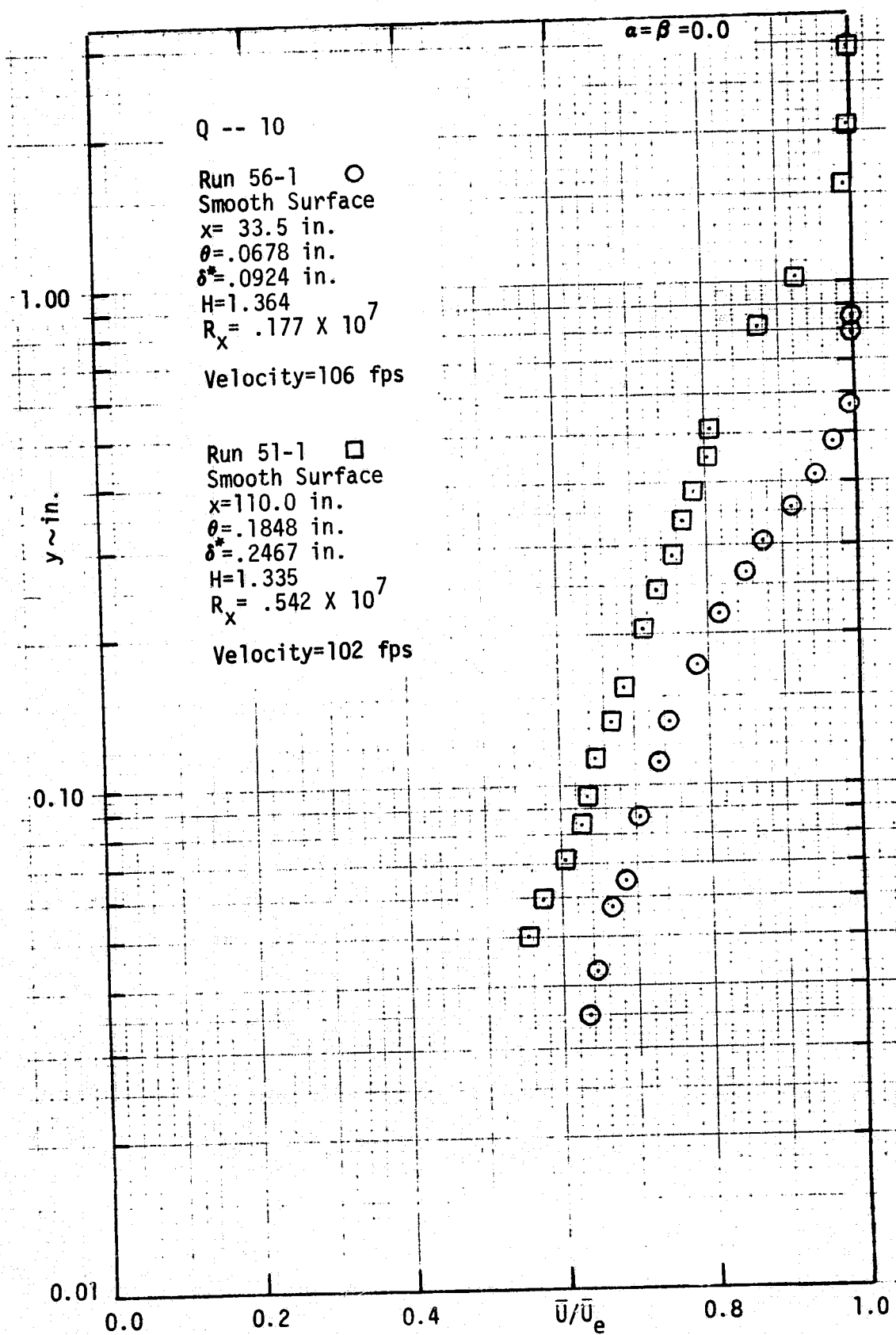


Fig. C-2 Turbulence intensity; $Q = 5$ psf

Fig. C-3 Velocity survey; $Q = 10$ psf

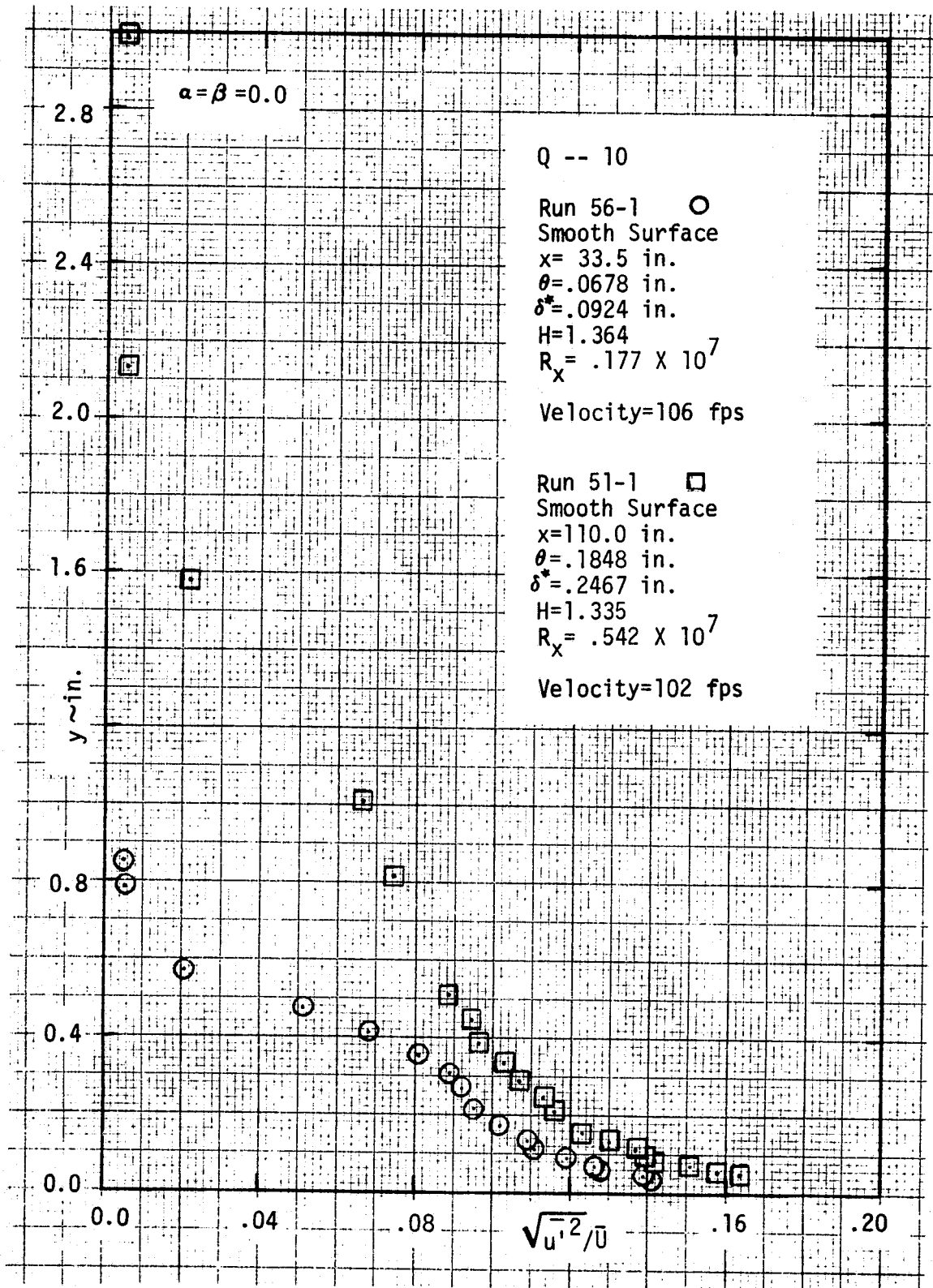
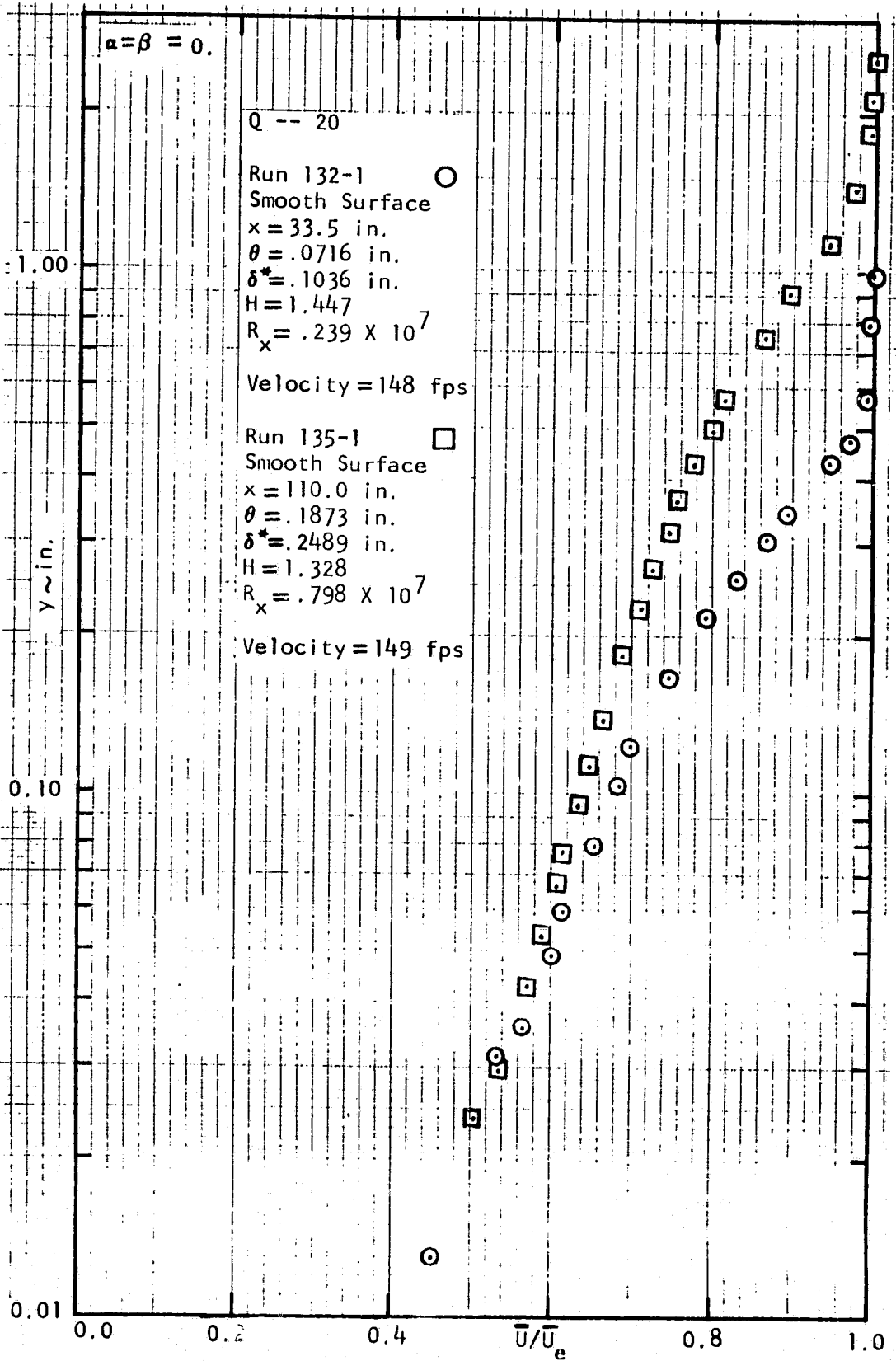


Fig. C-4 Turbulence intensity; Q = 10 psf

Fig. C-5 Velocity survey; $Q = 20$ psf

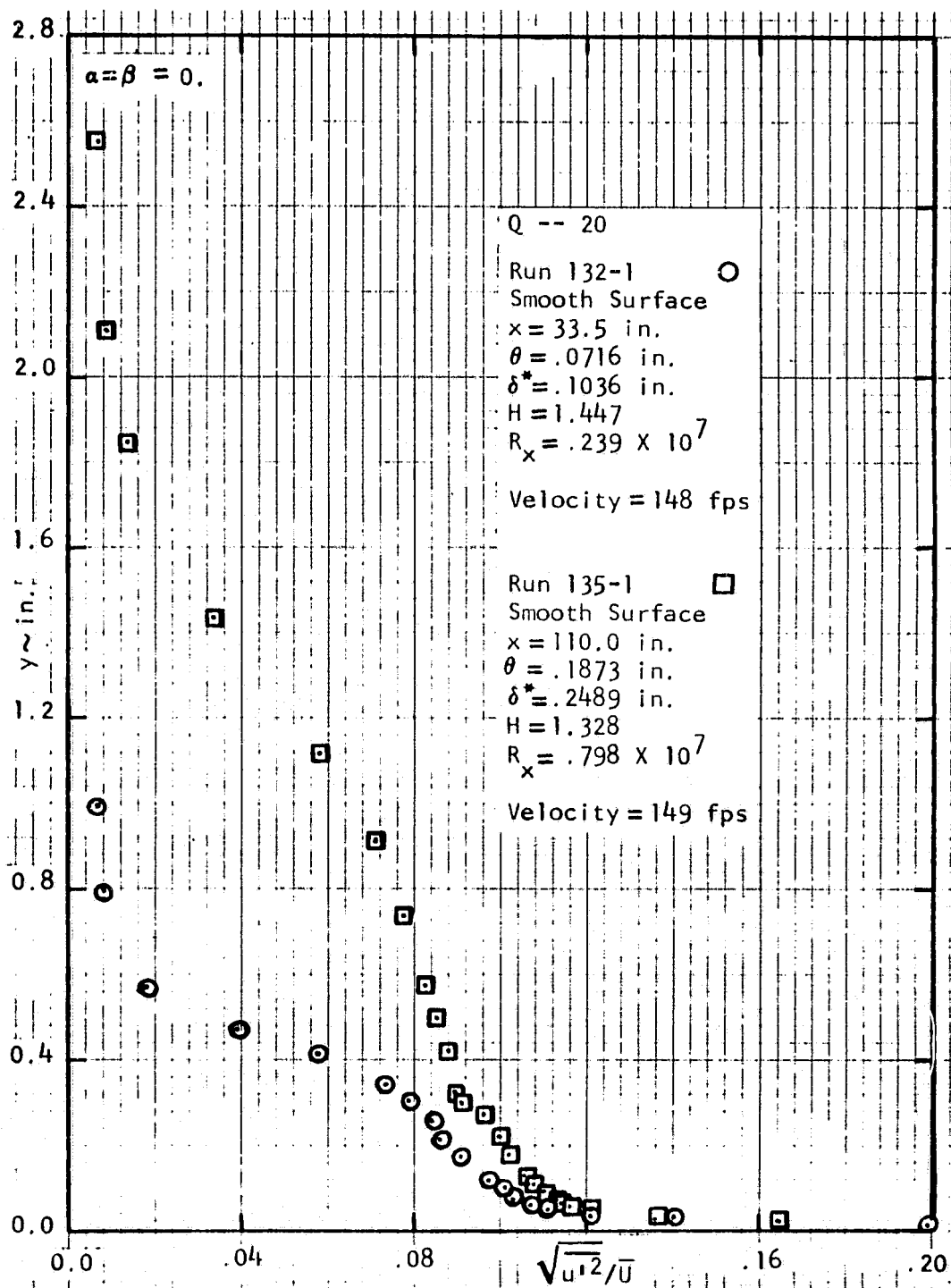
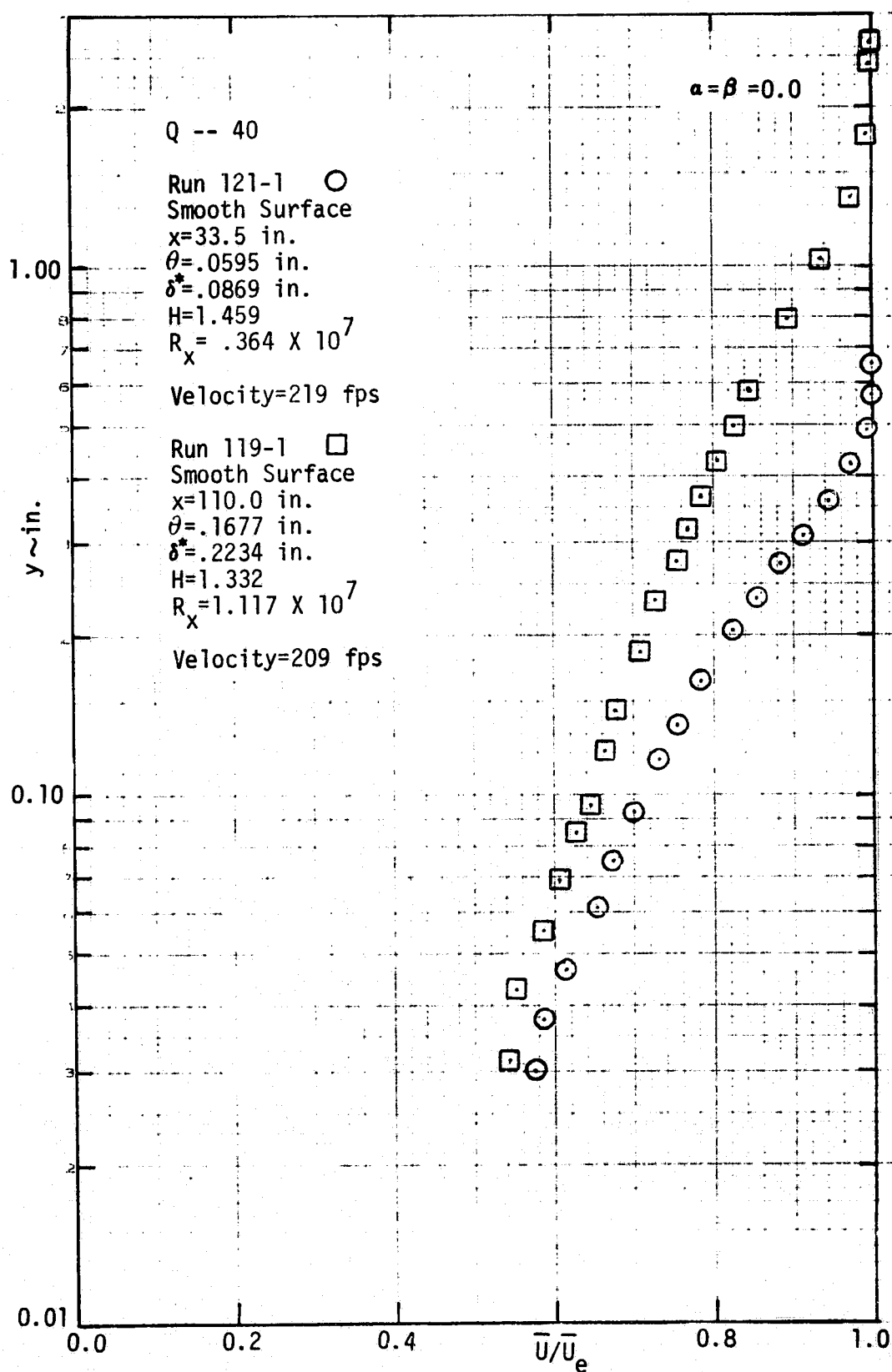


Fig. C-6 Turbulence intensity; Q = 20 psf

Fig. C-7 Velocity survey; $Q = 40$ psf

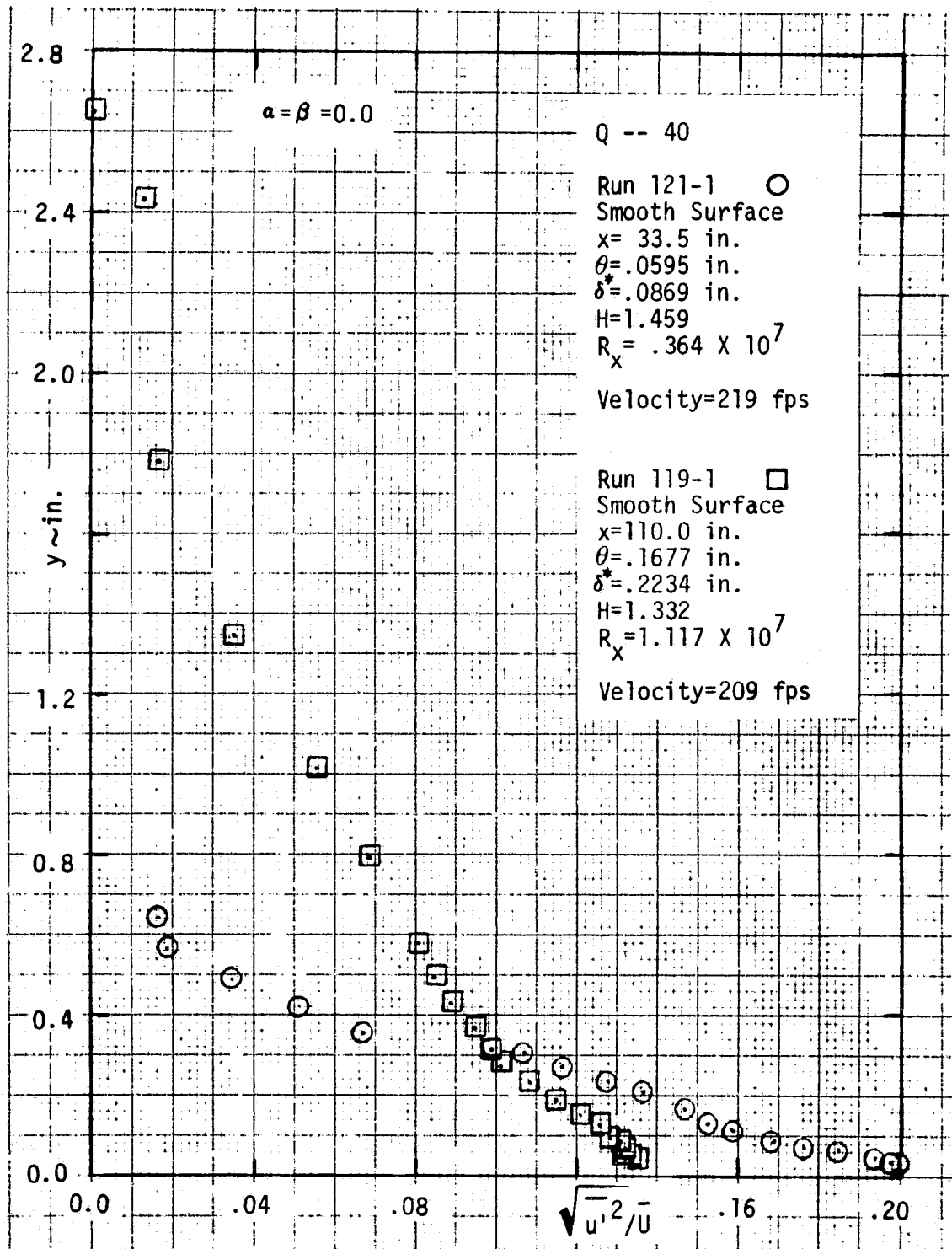


Fig. C-8 Turbulence intensity; Q = 40 psf

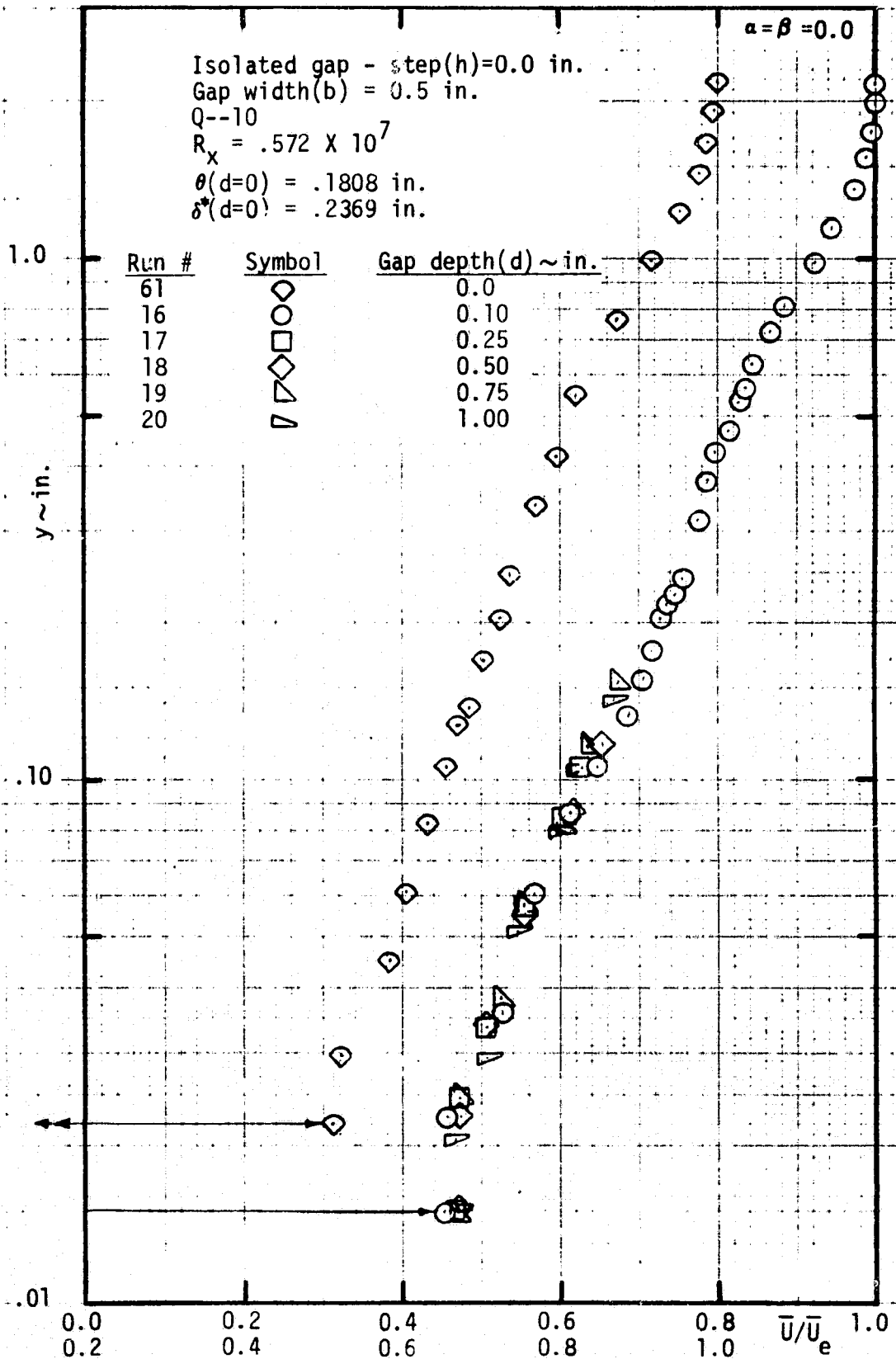


Fig. C-9 Velocity survey behind a $b = 0.5$ inch level cavity;
 rear position, $Q = 10$ psf

Isolated gap - step(h)=0.0 in.

Gap width(b) = 0.5 in.

Q=10

$R_x = .572 \times 10^7$

$\theta(d=0) = .1808$ in.

$\delta^*(d=0) = .2369$ in.

Run #	Symbol	Gap depth(d) ~ in.
61	○	0.0
16	○	0.10
17	□	0.25
18	◇	0.50
19	△	0.75
20	▽	1.00

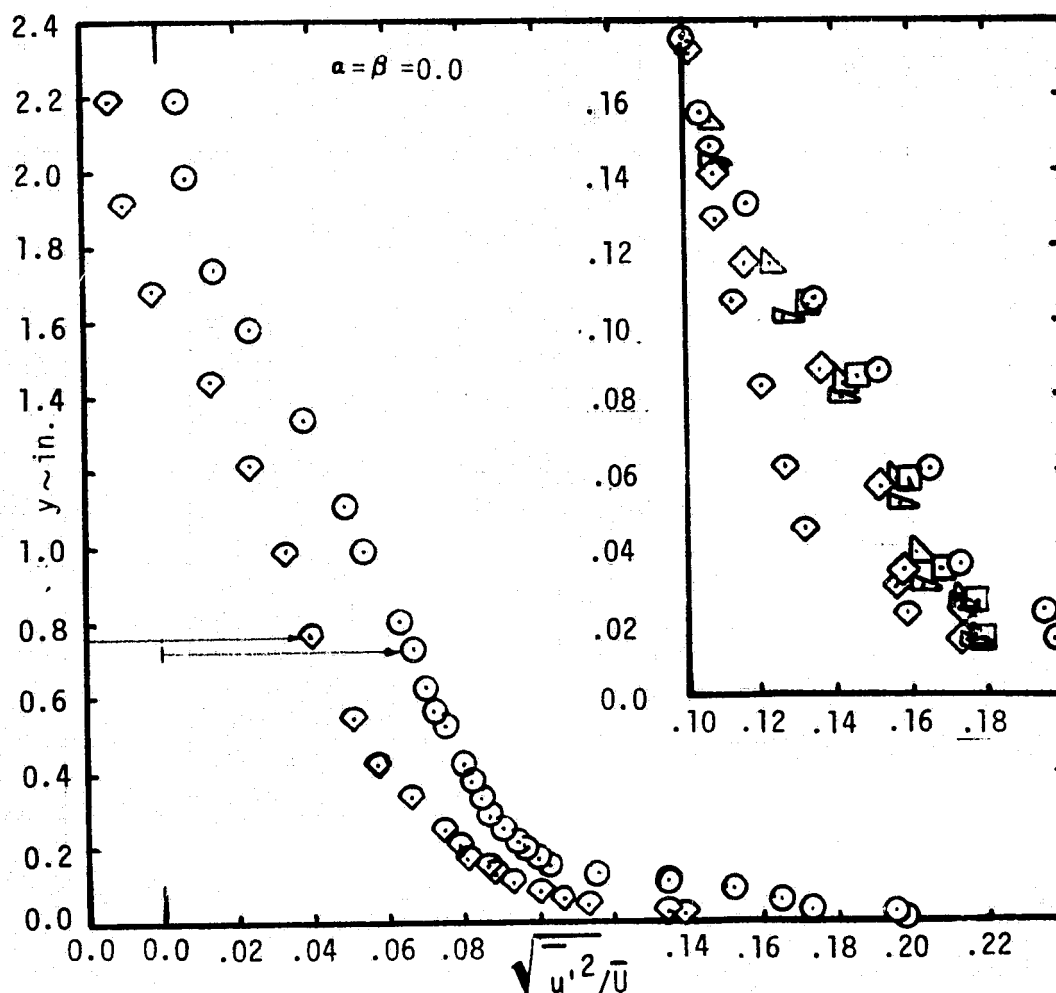


Fig. C-10 Turbulence intensity behind a $b = 0.5$ inch level cavity; rear position, $Q = 10$ psf

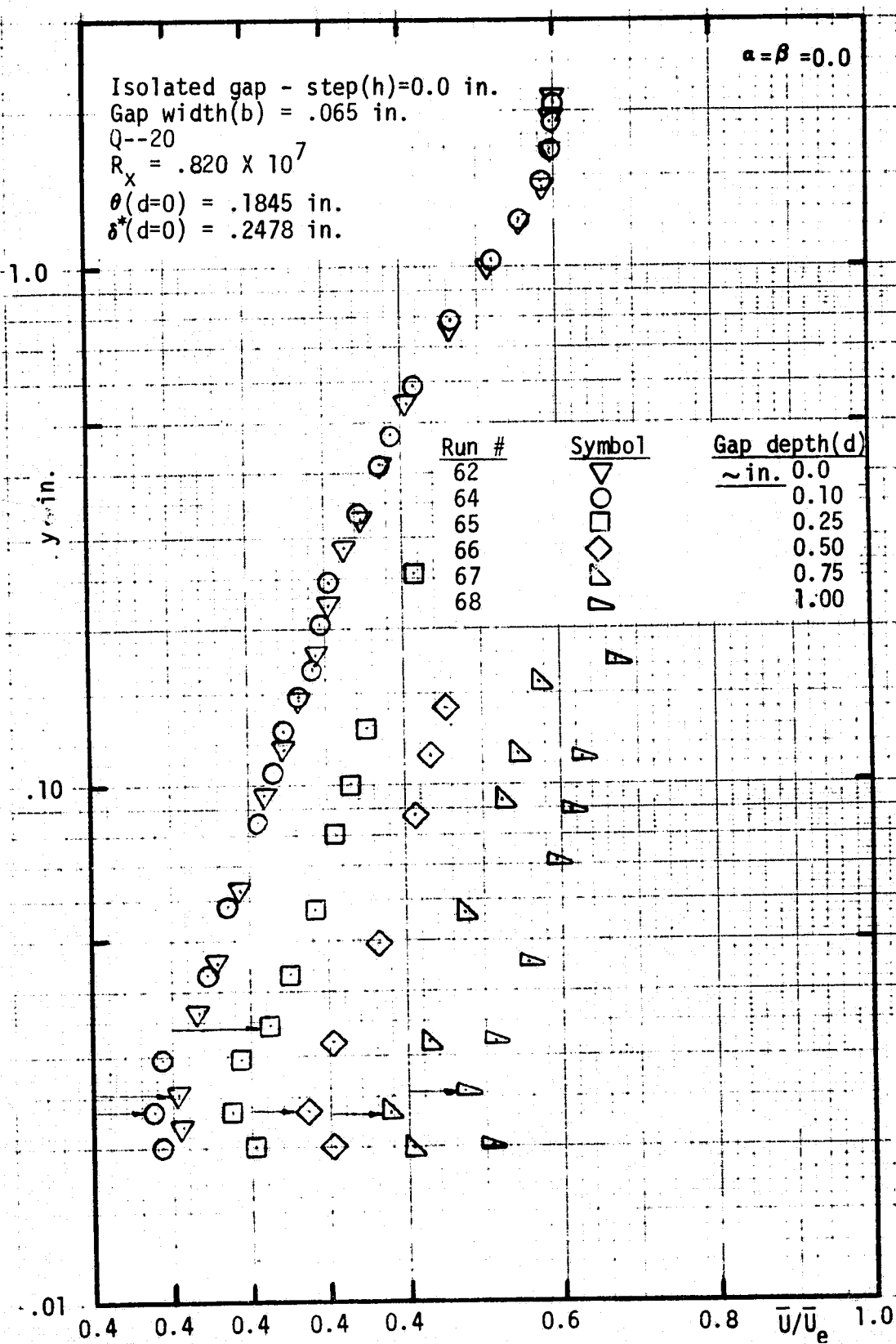


Fig. C-11 Velocity survey behind a $b = 0.065$ inch level cavity;
 rear position, $Q = 20$ psf

cavity corner for $d \neq 0.0$. The turbulence intensity profile (corresponding to mean velocity of Fig. C-11) is shown in Fig. C-12.

For $Q = 40$ psf the effect of cavity depth on the flow behind a level cavity is shown in Fig. C-13. For this mean velocity data the cavity gap width was 0.50 inch. Probing stations were the same as for Fig. C-9.

Finally, the turbulence intensity (corresponding to mean velocities shown on Fig. C-9) is shown on Fig. C-14.

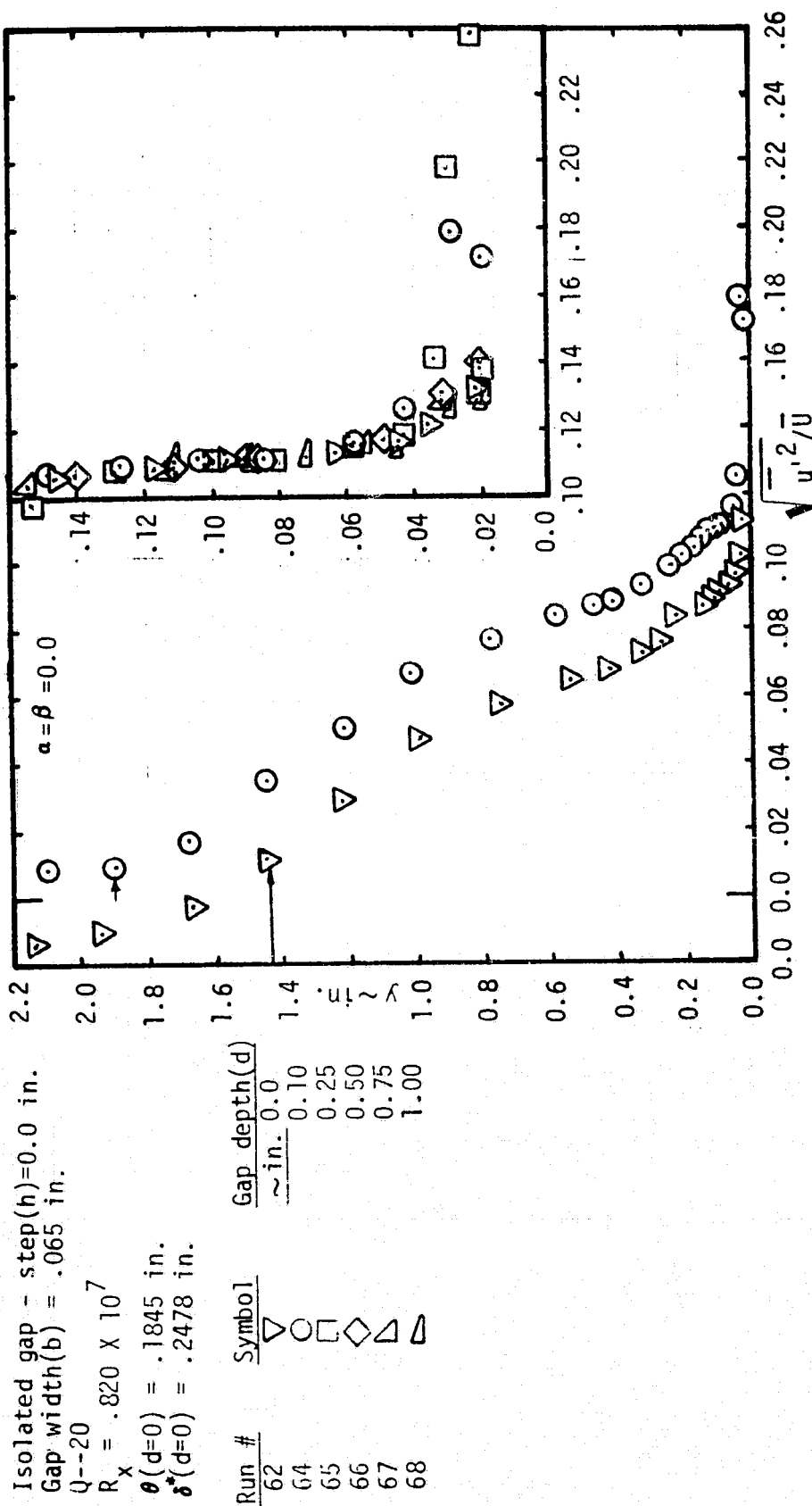


Fig. C-12 Turbulence intensity behind a $b = 0.065$ level cavity;
 rear position, $Q = 20$ psf

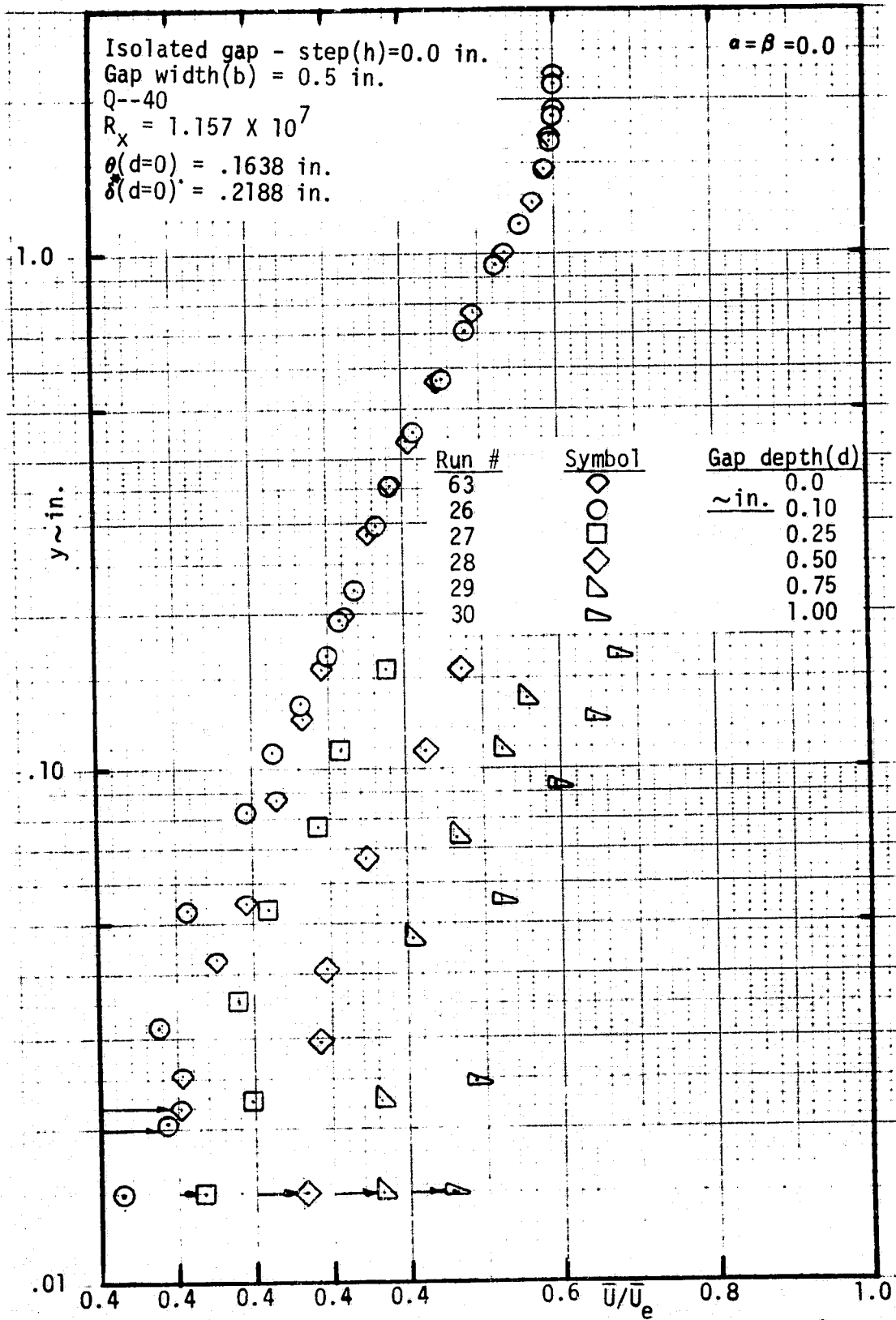


Fig. C-13 Velocity survey behind a $b = 0.5$ inch level cavity;
 rear position, $Q = 40$ psf.

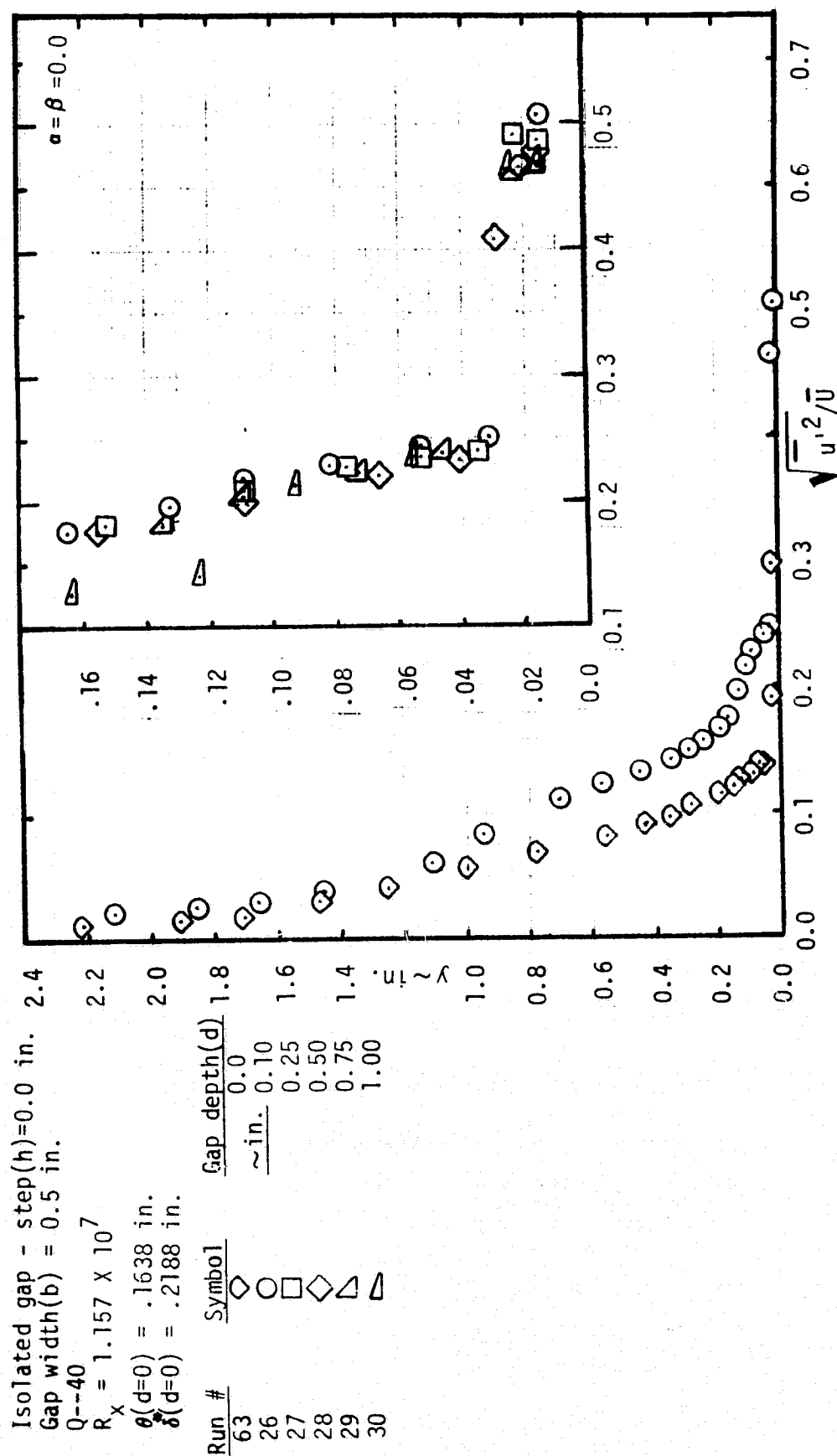


Fig. C-14 Turbulence intensity behind a $b = 0.5$ inch level cavity;
 rear position, $Q = 40$ psf.